NUMERICALLY ACCURATE RANS/PDF AND LES/PDF CALCULATIONS OF TURBULENT FLAMES

A Dissertation

Presented to the Faculty of the Graduate School

of Cornell University

in Partial Fulfillment of the Requirements for the Degree of

Doctor of Philosophy

by

Haifeng Wang

May 2010

NUMERICALLY ACCURATE RANS/PDF AND LES/PDF CALCULATIONS OF TURBULENT FLAMES

Haifeng Wang, Ph.D.

Cornell University 2010

Numerically accurate probability density function (PDF) calculations of turbulent jet flames are performed in the Reynolds-averaged Navier-Stokes (RANS) context. First, the effect is investigated of the time-averaging of the mean feedback quantities from the particle solver to the RANS solver on the bias errors that are caused by feeding the noisy mean quantites extracted from a finite number of particles back into the calculations. The time-averaging of the feedback quantities leads to approximately the same convergent results as those without time-averaging, while it reduces the bias errors significantly for the same number of particles per cell. Second, the particle time-series from the PDF calculations are analyzed, for the first time, to investigate the local extinction and re-ignition in the Sandia piloted flame E, and the auto-ignition in the Cabra hydrogen/nitrogen lifted jet flame. The particle time-series provide deep insight into the complicated combustion processes in these flames and demonstrate the capability of the models to represent these processes.

Next, different types of weak second-order splitting schemes applicable to the stochastic differential equations from the composition PDF method are developed and validated, which, for the first time, makes the composition PDF calculations second-order accurate in time in contrast to first-order accuracy in all previous composition PDF practices.

Finally, the current RANS/PDF capability is advanced to the large eddy sim-

ulations (LES) with the composition PDF method. A new high-performance PDF code, called HPDF, is developed with the following attributes: second-order accuracy in space and time; scalable up to at least 4096 cores; supporting Cartesian and polar cylindrical coordinate systems; parallelizable by domain decomposition in two dimensions; and it has a general interface to facilitate coupling to different existing LES (or RANS) codes etc. The new HPDF code is combined with an existing LES code, and the first set of LES/PDF calculations based on the new code is performed. The numerical convergence of the HPDF code is verified. The overall good agreement of the LES/PDF results with the experimental data is observed. The new LES/PDF capability establishes the basis for the future LES/PDF work to consider more advanced models, realistic chemistry, differential diffusion etc.

BIOGRAPHICAL SKETCH

Haifeng Wang was born in April 1977, in Yancheng, China. He received his Bachelor degree in Engineering Thermophysics from the University of Science and Technology of China (USTC) in 2000. In August 2002, he married Haixia Ji. He and his wife came to the Unite States in 2005. He enrolled in the Ph.D. program at Cornell University in August 2005, majoring in Mechanical Engineering, and received his master degree in June 2008. He has accepted a postdoc position with Professor Stephen B. Pope at Cornell University after graduation.

To my wife Haixia Ji

ACKNOWLEDGEMENTS

I am most grateful to my Ph.D. advisor, Professor Stephen B. Pope, for his patience, outstanding guidance and constant help. He directs me to develop critical thinking, judging and decision making toward a rigorous researcher. I am also grateful to Professors David A. Caughey and Alexander B. Vladimirsky for their suggestions and help to my Ph.D. study and for serving in my special committee. I want to thank all professors at Cornell who taught me courses, especially Professor Franklin K. Moore who provided a lot of advice about my course project which led to a journal publication.

I appreciate my colleagues for their discussions and suggestions. They are the current members and affiliates of the Turbulence and Combustion Group at Cornell, Ms. Sharadha Viswanathan, Mr. Pavel P. Popov, Mr. David H. Rowinski, Dr. Konstantin A. Kemenov, Mr. Varun Hiremath, Mr. Parvez Sukheswalla, Dr. Steven R. Lantz, and the previous group members, Dr. Renfeng R. Cao, Dr. Zhuyin Ren, Dr. Liuyan Lu, and Dr. Randall J. McDermott. I want to thank the consulting group from Cornell Center for Advanced Computing, especially Dr. Steven R. Lantz, for their tremendous help in high-performance computing.

I am sincerely grateful to my wife, our parents, brothers and sisters for their endless love, encouragement and support. I wish to remember my father who passed away during my study at Cornell. My father has the deepest influence on my growing. His leaving is the greatest loss of my life. His spirit, however, will live forever in my heart.

I finally wish to thank all my friends for their friendship and enormous help.

TABLE OF CONTENTS

LIST OF TABLES

LIST OF FIGURES

CHAPTER 1

INTRODUCTION

1.1 Background

The global demand for energy increases rapidly. According to the International Energy Outlook 2009 of the Energy Information Administration (EIA)[1], the global consumption of the primary energy (fossil fuels, nuclear, renewables etc.) grew by 67 percent from 1980 to 2006, and a 44 percent growth is projected from 2006 to 2030 [1]. In the United States, the energy consumption grew by 27 percent from 1980 to 2008, and it is projected to grow by 15 percent over the period from 2008 to 2035 [2]. This rapid growth is expected to continue in the future. Hence the development of sustainable energy, its secure supply and efficient use will be the major efforts of the world development.

Among the primary energy sources, fossil fuels (natural gas, liquid petroleum, coal etc.) are the most significant energy supplies. The percentage of the primary energy consumption against years is plotted in Figure 1.1 based on the data from EIA [1, 2]. The left plot of Figure 1.1 shows the percentage of the energy consumption worldwide from 1980 to 2006 and the projections to 2030. The percentage consumption of the most significant fuels (liquids — including biofuels[2], natural gas and coal) are 90%, 86%, and 83% in 1980, 2006, and 2030, respectively. The percentage of the biofuels is estimated to be not greater than five percent in the period of years shown in the figure. Hence the share of the fossil fuels of the worldwide energy consumption is expected to be greater than

[1]The Energy Information Administration (http://www.eia.doe.gov/) is the statistical agency of the Department of Energy.

[2]The separate data for the liquid petroleum and the biofuels are not available.

78 percent up to 2030. The slight decrease of fossil fuels is due to the increase of nuclear power and renewables (wind, solar, hydropower, etc.). The right plot of Figure 1.1 shows the percentage of the energy consumption in the United States from 1980 to 2035. The percentage of fossil fuels is 89%, 84%, and 78% in 1980, 2008 and 2035, respectively. Fossil fuels are expected to be a significant supply of the energy sources in the foreseeable future.

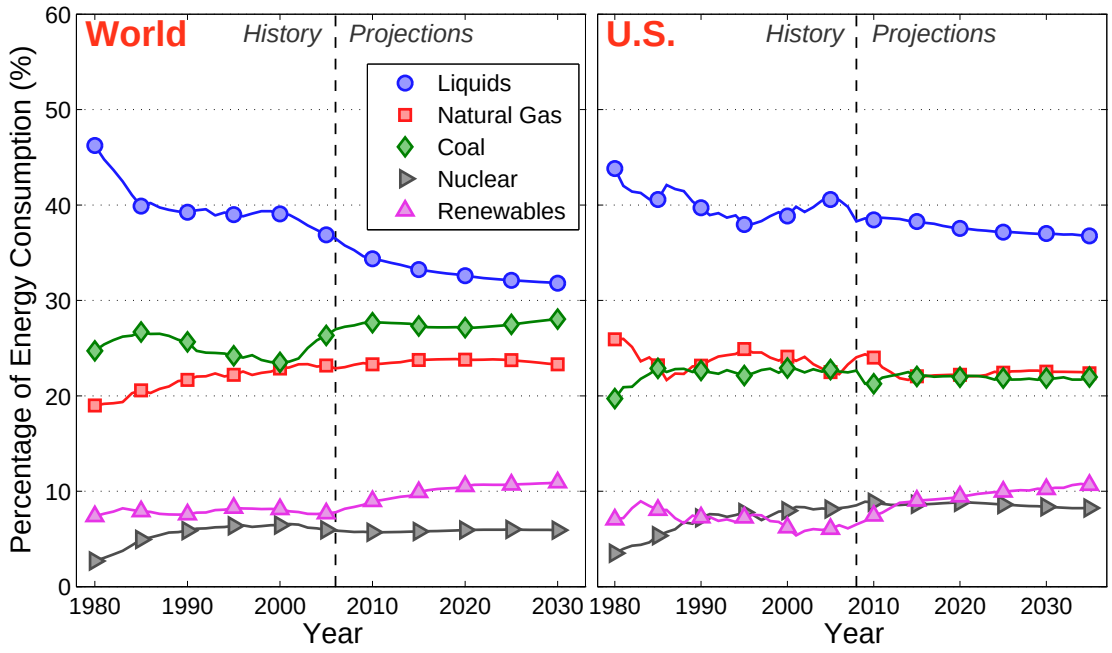

Figure 1.1: Percentage of the consumption of the primary energy (liquids — including biofuels, natural gas, coal, nuclear, and renewables) worldwide (left) and in the United States (right). (Source: U.S. Energy Information Administration, Jan 2010)

Combustion of fossil fuels causes severe environmental problems: global warming, pollution etc. Hence the study of combustion science is crucial to the thorough understanding of the combustion processes of fossil fuels. The knowledge acquired in turn helps in the control of combustion processes by designing clean and efficient combustion devices.

1.2 Study of turbulent combustion

Almost all combustion in engineering applications (electric plants, transportation vehicles etc.) occurs in turbulent flows. Turbulence is one of the unresolved classical physics problems. The reactive flow adds one level of complexity to turbulence by chemical reaction and makes the problem much harder. The chemical reaction occurs between the fully mixed mixture of fuel and oxidizer at the molecular level, and interacts with turbulence at very small scales. The strong interaction between turbulence and chemistry is an extremely challenging problem in the study of turbulent combustion.

The study of turbulent combustion falls mainly into two categories: experiments and modeling. Much work has been done experimentally to investigate turbulence, chemistry and their interactions. Measurements of a series of turbulent flames in canonical flows have been archived in the TNF workshop[3], which was initiated to facilitate the international collaborations among experimental and computational researchers in turbulent combustion. The experimental work on turbulent combustion provides excellent validation for modeling, as well as revealing interesting behaviors of turbulence and turbulent combustion.

The modeling of turbulence is divided into different categories based on the levels of description of turbulence. A full description of turbulence can be achieved by the direct numerical simulation (DNS) of the Navier-Stokes (NS) equations. Many studies have been done in this direction, e.g. DNS of homogeneous isotropic turbulence [3], of fully-developed pipe flow [4], and of jet flow [5]. The DNS studies provide deep insight into turbulence, and are highly valu-

[3]International Workshop on Measurement and Computation of Turbulent Non-premixed Flames (http://www.sandia.gov/TNF/abstract.html).

able for inspiring and validating turbulence models. DNS resolves all scales of turbulent flows, and hence is very expensive computationally. DNS only of simple, low to moderate Reynolds-number flows is affordable with current computer capability. This restricts the applicability of DNS in engineering applications.

To meet the urgent modeling requirement of engineering applications, different levels of reduced description of turbulence are established: the statistical modeling and the large-eddy simulation (LES). The Reynolds-averaged Navier-Stokes (RANS) is a widely used statistical modeling approach. In this approach, the Navier-Stokes equations are averaged to describe the evolution of the statistics (usually only low-order moments) of the flow fields. Turbulence models, such as the k-ε model and the Reynolds-Stress model (RSM), are constructed to close the unknown terms in the RANS equations. All scales of turbulent motion are averaged in RANS and hence all scales are modeled. RANS has been a dominant approach for turbulence modeling in the last 50 years, and has received some great success in engineering applications.

The probability density function (PDF) methods [6, 7] account for the evolution of the PDF of the flow fields (rather than just of the low-order moments as in RANS), and hence all statistical moments of the flow fields are known through the modeling although the low moments are of primary interest for engineering applications.

RANS and the PDF methods model turbulence as a single-scale or a few-scale problem, which naturally is not expected to be accurate for most turbulent flows with a wide range of scales. LES [7, 10] is an attractive approach with incomplete but increased description of turbulence compared to RANS or the

PDF methods. In LES, the large scales of turbulence are resolved explicitly with the contribution of small scales being modeled. Different methods can be used to separate the large scales and the small scales, e.g. the low-pass spatial filtering [7], the projection onto local basis functions [8]. The filtering operation is the dominant approach for LES. Recently, Pope [9] developed an alternative foundation for LES based on self-conditioned fields, rather than on filtering. Several advantages are provided by this method over the traditional LES based on filtering as illustrated in [9]. LES is a very promising research tool for turbulence and turbulent combustion in the near future, which largely benefits from the rapid development of the computer technologies and the availability of large parallel computing clusters, such as TeraGrid[4].

The modeling of turbulent combustion can be carried out in three levels too: DNS, statistical modeling and LES. As expected, DNS of turbulent combustion is extremely expensive even for simple geometry flows with simple chemistry. Large efforts of turbulent combustion modeling have been made in the statistical modeling and LES. In RANS, closure is also required for the reaction source terms. Different turbulent combustion models have been proposed in the past for the closure, e.g., the PDF methods [6], the flamelet model [11], and the conditional moment closure (CMC) [12]. Among them, the PDF methods have proved to be most successful in accounting for turbulence-chemistry interactions. LES of turbulent combustion also requires the closure of reaction source terms because of the occurrence of reaction at the small, un-resolved scales. Almost all turbulent combustion models developed in the RANS context can be extended straightforwardly to LES. The combined LES/PDF study of turbulent combus-

[4]"TeraGrid is an open scientific discovery infrastructure combining leadership class resources at eleven partner sites to create an integrated, persistent computational resource" (http://www.teragrid.org/).

tion is a popular research area currently and is expected to be so in the near future.

The modeling approaches developed for turbulence and turbulent combustion usually lead to a set of closed partial differential equations (PDEs), ordinary differential equations (ODEs), and (or) stochastic differential equations (SDEs). With proper initial and boundary conditions, these equations can be solved numerically with discretization. The numerical results generated are estimates of the exact solutions. It is important to appreciate the difference between the numerical solutions and the exact solutions. The latter are almost always unknown in engineering applications. All the numerical results involve inevitably different kinds of numerical errors which contribute to the discrepancies between the numerical solutions and the exact solutions as well as the errors in the modeling. The evaluation of numerical properties (e.g., numerical convergence, accuracy) of a numerical simulation is an essential procedure to make the numerical results convincing and useful. Unfortunately, not all simulations reported in the literature have been able to meet this requirement before the numerical results are analyzed.

In this thesis work, PDF methods are employed to study turbulent combustion problems in conjunction with RANS and LES. Extensive efforts have been made to verify the numerical convergence and accuracy of the numerical results before they are analyzed and conclusions are drawn.

1.3 Overview of chapters

The development of the chapters in this thesis is summarized in this section. Each of chapters 2 to 5 corresponds to a published or submitted journal article.

Chapter 2 explores the numerical accuracy and convergence of a combined RANS/PDF method in terms of the bias errors. The RANS equations are solved by the finite volume method and the PDF transport equation [6] is solved by the Lagrangian Monte Carlo particle method [6]. The coupling of the finite-volume method and particle method is described in [13, 14]. The hybrid finite-volume/particle algorithms have been implemented in a FORTRAN code called HYB2D [13, 14], mainly for statistically axisymmetric and stationary problems. The numerical accuracy and convergence of the code have been explored extensively in [13, 14], and a series of studies of turbulent non-premixed jet flames have been performed using this code, e.g., [15, 16, 17, 18, 19]. In the hybrid algorithm, there is feedback of the extracted statistics from the particles to the flow calculations. Due to a limited number of particles (usually on the order of 100 particles per grid cell), the feedback statistics extracted from the particles involve significant statistical errors, which lead to bias errors. For statistically stationary problems, time-averaging (Section 2.2.2) of the feedback quantities can be performed to reduce the statistical errors, and hence reduce the bias errors.

This study provides a thorough understanding of the reduction of the bias errors by time-averaging the feedback quantities, particularly the mean fluctuating velocity. The convergence tests, accomplished by varying the number of particles per cell and with all other parameters fixed for two different flames,

indicate that both feedback with and without time-averaging lead to the first-order convergence of the bias errors with respect to the number of particles per cell and to approximately the same converged results when the number of particles per cell tends to infinity (Section 2.3). However, the feedback mean fluctuating velocity with time-averaging involves much smaller bias errors than those without time-averaging, and therefore many fewer particles are needed in the former case to achieve the same accuracy as in the latter case. The source of the bias errors due to the velocity correction is analyzed (Section 2.2.3). The influence of the turbulence model constant $C_{\omega 1}$ is discussed as well as the connection of the current results with the previous ones (Sections 2.3.3 and 2.4).

Chapter 3 applies the HYB2D code, which is fully tested and well understood, to the study of local extinction and re-ignition in the Sandia piloted flame E [20] and of auto-ignition in the Cabra H_2/N_2 lifted flame [21]. Flame extinction and ignition are very complicated combustion phenomena in turbulent combustion. Studies of these phenomena are helpful to a deep understanding of flame stability, turbulence-flame interactions etc. These phenomena are extremely challenging to turbulent combustion models. The PDF methods [6] have proved to be the only successful models to predict both extinction and ignition processes in turbulent combustion reasonably well. The PDF calculations of these two flames have been performed successfully before, e.g. [22, 23, 18, 19] for flame E and [21, 17, 24] for the Cabra flame. Previous PDF calculations mainly looked at the Eulerian statistics (e.g., mean and variance of temperature and species mass fractions) and single-time particle distributions (e.g., scatter plots of particle temperature and species mass fractions in the mixture fraction space, conditional PDFs etc.). These statistics are of primary interest in engineering applications, and provide good insights into the models' behavior during

extinction and ignition.

This work provides a deeper understanding of extinction and ignition, and the model capability to represent these phenomena by looking at the Lagrangian time-series of particles. Due to the Lagrangian nature of the Monte Carlo particle method [6], it is straightforward to extract the time-series of the particles which represent the history of the particle evolution in the physical and composition spaces. The unsteady extinction and ignition processes are revealed much better by the particle evolution than by the single-time snapshot of particles. The particle time-series of the flame E and the different re-ignition mechanisms in it are discussed in Section 3.4, and the particle time-series of the Cabra flame and the different stages of combustion from the jet-nozzle to the downstream in it are discussed in Section 3.5. The roles of the mixing and reaction during re-ignition and auto-ignition are discussed in Section 3.6.

The HYB2D code that is used in the studies of Chapters 2 and 3 is based on RANS/PDF. LES attracts a lot of attention recently in studies of turbulence and turbulent combustion. It is urgently needed to develop the algorithms and codes suitable for LES/PDF studies of turbulence and turbulent combustion problems. The next two chapters (Chapters 4 and 5) develop the LES/PDF capability for future studies.

Chapter 4 develops the weak second-order splitting schemes for the Lagrangian Monte Carlo particle methods for the composition PDF transport equation. LES always solves unsteady three-dimensional problem, which requires time accurate solutions of the LES equations in addition to many other requirements, such as grid resolution, spatial accuracy, and numerical stability. For statistically stationary problems, the time-accuracy in RANS is less im-

portant because the numerical solutions after the statistically stationary state are independent of time. In LES, the numerical solutions are always time-dependent even for statistically stationary problems. Hence numerically accurate integration of the LES equations and the particle equations is crucial for the success of the LES/PDF calculations. The composition PDF method has been implemented previously in both RANS and LES in several research codes (e.g., [23, 25, 26]) and commercial codes (e.g., ANSYS FLUENT). In all previous composition PDF calculations, only first-order temporal accuracy is achieved due to the lack of the second-order splitting schemes for the coupled particle SDE system consisting of an SDE for the particle position and a random ODE for the particle compositions. Different weak second-order splitting schemes for this coupled SDE system are developed in Section 4.5. Second-order convergence of the different splitting schemes is validated for a one-dimensional test case, and the comparisons are made of the different splittings in terms of accuracy and efficiency in Section 4.6. A general methodology for generating test cases for the Monte Carlo method is developed in Section 4.4 based on the method of manufactured solutions (MMS) [27, 28].

In Chapter 5, a new PDF code called HPDF is developed and the first LES/PDF calculation of DLR Flame A [29, 30] based on the new code is presented. Both the first-order and second-order accurate splitting schemes developed in Chapter 4 are implemented in the code. The grid convergence and temporal convergence of the HPDF code are verified in Section 5.3. The numerical results are analyzed and compared in Section 5.4 to address the following issues: the effect of the LES grid resolution (Section 5.4.1); the numerical consistency between the LES and PDF (Section 5.4.2); and the effect of time integration schemes (Section 5.4.4). The numerical results are also compared with the ex-

perimental data [29, 30] to show the capability of the LES/PDF code. This work establishes the basis of the future LES/PDF work to consider realistic chemistry with many species, differential-diffusion, advanced numerical models etc.

In Chapter 6, conclusions are drawn and future work on LES/PDF is discussed.

REFERENCES

[1] International Energy Outlook 2009, Energy Information Administration, Office of Integrated Analysis and Forecasting, U.S. Department of Energy, Washington, DC 20585 (http://www.eia.doe.gov/oiaf/ieo/index.html).

[2] Annual Energy Outlook 2010 Early Release Overview, Energy Information Administration, Office of Integrated Analysis and Forecasting, U.S. Department of Energy, Washington, DC 20585 (http://www.eia.doe.gov/oiaf/aeo/index.html).

[3] V. Eswaran, S.B. Pope, Direct numerical simulations of the turbulent mixing of a passive scalar, *Phys. Fluids* 31 (1988) 506-520.

[4] J.G.M. Eggels, F. Unger, M.H. Weiss, J. Westerweel, R.J. Adrian, R. Friedrich, F.T.M. Nieuwstadt, Fully-developed turbulent pipe-flow – a comparison between direct numerical-simulation and experiment, *J. Fluid Mech.* 268 (1994) 175-209.

[5] B. J. Boersma, G. Brethouwer, F. T. M. Nieuwstadt, A numerical investigation on the effect of the inflow conditions on the self-similar region of a round jet, *Phys. Fluids* 10(4) (1998) 899-909.

[6] S.B. Pope, PDF methods for turbulent reactive flows, *Prog. Energy Combust. Sci.* 11 (1985) 119-192.

[7] S.B. Pope, Turbulent Flows, Cambridge University Press, Cambridge, 2000.

[8] S.B. Pope, Large-eddy simulation using projection onto local basis functions, in: Fluid Mechanics and the Environment: Dynamical Approaches, Ed. J.L. Lumley, Springer, pp. 239-265, 2001.

[9] S.B. Pope, Self-Conditioned Fields for Large-Eddy Simulations of Turbulent Flows, *J. Fluid Mech.* (2010), to be published.

[10] P. Sagaut, Large eddy simulation for incompressible flows, Springer-Verlag, 2001.

[11] N. Peters, Laminar diffusion flamelet models in non-premixed turbulent combustion, *Prog. Energy Combust. Sci.* 10 (1984) 319-339.

[12] R.W. Bilger, Conditional moment closure for turbulent reacting flow, *Phys. Fluids A* 5(2) (1993) 436-444.

[13] M. Muradoglu, P. Jenny, S.B. Pope, D.A. Caughey, A consistent hybrid finite-volume/particle method for the PDF equations of turbulent reactive flows, *J Comput. Phys.* 154 (1999) 342-371.

[14] M. Muradoglu, S.B. Pope, D.A. Caughey, The hybrid method for the PDF equations of turbulent reactive flows: consistency conditions and correction algorithms, *J Comput. Phys.* 172 (2001) 841-878.

[15] M. Muradoglu, K. Liu, S.B. Pope, PDF modeling of a bluff-body stabilized turbulent flame, *Combust. Flame* 132 (2003) 115-137.

[16] K. Liu, S.B. Pope, D.A. Caughey, Calculations of bluff-body stabilized flames using a joint PDF model with detailed chemistry, *Combust. Flame* 141 (2005) 89-117.

[17] R.R. Cao, S.B. Pope, A.R Masri, Turbulent lifted flames in a vitiated coflow investigated using joint PDF calculations *Combust. Flame* 142 (2005) 438-453.

[18] R.R. Cao, S.B Pope, The influence of chemical mechanisms on PDF calculations of nonpremixed piloted jet flames *Combust. Flame* 143 (2005) 450-470.

[19] R.R. Cao, H. Wang, S.B. Pope, The effect of mixing models in PDF calculations of piloted jet flames. *Proc. Combust. Inst.* 31 (2007) 1543-1550.

[20] R.S Barlow, J.H. Frank, Effects of turbulence on species mass fractions in methane-air jet flames, *Proc. Combust. Inst.* 27 (1998) 1087-1095.

[21] R. Cabra, T. Myhrvold, J.-Y. Chen, R.W. Dibble, A.N. Karpetis, R.W. Barlow, Simultaneous laser Raman-Rayleigh-Lif measurements and numerical modeling results of a lifted turbulent H-2/N-2 jet flame in a vitiated coflow, *Proc. Combust. Inst.* 29 (2002) 1881-1888.

[22] J. Xu, S.B. Pope, PDF calculations of turbulent nonpremixed flames with local extinction, *Combust. Flame* 123 (2000) 281-307.

[23] R.P. Lindstedt, S.A. Louloudi, E.M. Vaos, Joint scalar probability density function modeling of pollutant formation in piloted turbulent jet diffusion

flames with comprehensive chemistry, *Proc. Combust. Inst.* 28 (2000) 149-156.

[24] A.R. Masri, R. Cao, S.B. Pope, G.M. Goldin, PDF Calculations of Turbulent Lifted Flames of H2/N2 issuing into a vitiated co-flow, *Combust. Theory Modelling* 8 (2004) 1-22.

[25] H.F. Wang, Y.L. Chen, PDF modelling of turbulent non-premixed combustion with detailed chemistry, *Chem. Eng. Sci.* 59(16) (2004) 3477-3490.

[26] V. Raman, H. Pitsch, A consistent LES/filtered-density function formulation for the simulation of turbulent flames with detailed chemistry, *Proc. Combust. Inst.* 31(2) (2007) 1711-1719.

[27] P.J. Roache, Code verification by the method of manufactured solutions, *J. Fluids Eng.* 124(1) (2002) 4-10.

[28] C.J. Roy, Review of code and solution verification procedures for computational simulation, *J. Comput. Phys.* 205 (2005) 131-156.

[29] W. Meier, R.S. Barlow, Y.-L. Chen, and J.-Y. Chen, Raman/Rayleigh/LIF measurements in a turbulent CH4/H-2/N-2 jet diffusion flame: Experimental techniques and turbulence-chemistry interaction, *Combust. Flame* 123 (2000) 326-343.

[30] Ch. Schneider, A. Dreizler, J. Janicka, Flow field measurements of stable and locally extinguishing hydrocarbon-fuelled jet flames, *Combust. Flame* 135 (2003) 185-190.

CHAPTER 2

TIME-AVERAGING STRATEGIES IN THE FINITE-VOLUME/PARTICLE HYBRID ALGORITHM FOR THE JOINT PDF EQUATION OF TURBULENT REACTIVE FLOWS*

Abstract

The influence of time-averaging on bias is investigated in the finite-volume/particle hybrid algorithm for the joint PDF equation for statistically-stationary turbulent reactive flows. It is found that the time-averaging of the mean fluctuating velocity (TAu) leads to the same variances of the fluctuating velocity before and after the velocity correction, whereas without TAu the estimates are different, and an additional numerical dissipation rate is introduced for the turbulent kinetic energy (TKE). When 100 particles per cell are used without TAu, a large bias error is found to be involved in the unconditional statistics of the statistically-stationary solutions of two tested turbulent flames, the Cabra H_2/N_2 lifted flame and the Sandia piloted flame E. The use of TAu reduces this bias dramatically for the same number of particles per cell. The conditional statistics in these flames, however, are hardly affected by TAu. To a large extent, the effect of the bias error on the unconditional statistics is similar to the effect of increasing the model constant $C_{\omega 1}$ in the stochastic turbulence frequency model.

*Haifeng Wang, Stephen B. Pope, Time averaging strategies in the finite-volume/particle hybrid algorithm for the joint PDF equation of turbulent reactive flows, *Combustion Theory and Modelling* 12(3) (2008) 529-544.

2.1 Introduction

The probability density function (PDF) method [1, 2] has achieved considerable success in the numerical simulation of turbulent combustion problems. Some complicated turbulent combustion phenomena (e.g., local extinction and re-ignition) can be predicted quantitatively [3, 4, 6, 5]. The success of the PDF method benefits from the parallel development of physical models and numerical methods. The physical models include the PDF transport equation and the corresponding stochastic differential equations (SDEs) [1, 2], models for the Lagrangian velocity, turbulence frequency [8] and acceleration [9], and mixing models [10]. Numerical methods include the Monte Carlo particle method [1, 11, 12], and the hybrid finite-volume (FV)/particle method [13, 14, 15, 16]. It is very important to ensure and demonstrate the numerical accuracy of computed results, so as to eliminate numerical error as a possible source of discrepancies between model calculations and experimental measurements. In this work, the numerical accuracy of the PDF calculations is further tested and related to previous work [5, 6, 15, 17].

The PDF calculations considered here are performed by using a code called HYB2D which implements the consistent hybrid finite-volume (FV)/particle solution algorithm for the joint PDF transport equation [15]. During the development of the PDF solution algorithms, from the stand-alone particle/mesh method (implemented in the code PDF2DV) [3, 18] to the current hybrid method [15], the numerical error has been carefully evaluated [18, 15, 12]. Compared to the stand-alone particle/mesh method, the hybrid method reduces the bias dramatically [15]. In order to understand better the bias error reduction in the hybrid method, the influence of the time-averaging technique on the bias is re-

investigated. Time-averaging is a powerful technique to reduce the statistical error [18] and to some extent the bias [15, 14]. We show here that the time-averaging of the mean fluctuating velocity can reduce the bias dramatically. In the hybrid method [15], the fluctuating velocity is a property of each particle. Due to statistical error, the mass-weighted mean of the fluctuating velocity from particles is not zero, and a velocity correction is performed for the fluctuating velocity of each particle by subtracting an estimate of the mean fluctuating velocity. Mean quantities such as the mean fluctuating velocity, which are estimated from the particles and fed back into the particle solver, are referred to as particle-to-particle quantities.

One motivation for the current work is to investigate the impact of time-averaging on calculations of the Sandia piloted flames, since time-averaging of particle-to-particle quantities was not used in some previously reported calculations [5, 6]. Various test cases indicate that only the time-averaging of the mean fluctuating velocity in the particle-to-particle quantities reduces the bias significantly, and the time averaging of the other particle-to-particle quantities has a negligible effect on the final solution. Hence only the influence of the time-averaging of the mean fluctuating velocity on the bias is discussed in this work.

In the following section, the hybrid algorithm in HYB2D is briefly summarized, the time-averaging strategies are described, and then the bias due to the velocity correction is analysed. In Section 2.3, the effect of time-averaging on the bias involved in the unconditional and condition statistics is evaluated for two test cases, the Cabra H_2/N_2 lifted flame [19] and the Sandia piloted flame E [20]. The choice of the value of the model constant $C_{\omega 1}$ and its interaction with

numerical error are discussed in Section 2.4. Conclusions are drawn in the final section.

2.2 Time-averaging in HYB2D

2.2.1 Summary of HYB2D

The hybrid method (implemented in the code HYB2D) [15] solves the transport equation for the joint PDF of velocity, turbulence frequency and composition for turbulent combustion problems. The finite volume (FV) method is used to solve the mean conservation equations for mass, momentum, and energy and the mean equation of state; and the particle method is used to solve the transport equation of the joint PDF of the fluctuating velocity, turbulence frequency and composition. The FV part provides the mean fields of velocity, density and pressure to the particle part and obtains all the Reynolds stresses, the turbulent fluxes and the mean chemical source term from the particle part. The hybrid method is consistent at the level of the governing partial differential equations. At the numerical level, the consistency conditions are identified, and the correction algorithms are devised in [15], where the details of the hybrid solution algorithm can be found.

2.2.2 Time-averaging technique

HYB2D is applicable to statistically-stationary flows by using a pseudo-time marching method. The PDF is represented by an ensemble of particles. Starting

from some initially specified properties, the method marches the particles in time steps Δt to approach the statistically-stationary solution. At a given time step, the mean fields are estimated from the particles. A statistical error which varies as $N_{pc}^{-1/2}$ [1] (where N_{pc} is the number of particles per cell) is involved in the estimate of mean fields. After the statistically-stationary state is reached, this error can be reduced by time-averaging [18]. For a quantity used solely for output, time-averaging reduces statistical error, but not bias. Part of the origin of bias is from statistical fluctuations in quantities fed back into the calculations. Hence the use of time-averaging to reduce these fluctuations reduces the bias. Following [15], the time-averaging scheme is defined, for a mean field Q, as

$$Q_{TA}^{j} = \left(1 - \frac{1}{N_{TA}^{j}}\right) Q_{TA}^{j-1} + \frac{1}{N_{TA}^{j}} Q^{j}, \tag{2.1}$$

where Q_{TA}^{j} and Q^{j} are the time-averaged and instantaneous values evaluated on the j-th time step, and N_{TA}^{j} is a time-averaging parameter to be specified, which is abbreviated to N_{TA} when it is not necessary to explicitly show the dependence on j. Note that $N_{TA}^{j} = 1$ corresponds to no time-averaging, and in general we have $N_{TA}^{j} \geqslant 1$.

Two different types of quantities in HYB2D are time-averaged: first, output quantities for postprocessing such as conditional or unconditional means and rms of temperature, species mass fractions; and, second, quantities which are fed back into the calculations, such as turbulent fluxes, and the mean chemical source term.

For output quantities, the time-averaging strategy used is called the uniform-time-averaging (UTA). UTA is turned on after the statistically-stationary state has been reached (indicated here as the time step j_0). By turning on UTA, the time-averaged quantities for the output at the j-th time step ($j > j_0$)

become

$$
\begin{aligned}
Q_{TA}^{j} &= \frac{1}{j - j_0 + 1} \sum_{i=j_0}^{j} Q^i \\
&= \left(1 - \frac{1}{j - j_0 + 1}\right) \frac{1}{j - j_0} \sum_{i=j_0}^{j-1} Q^i + \frac{1}{j - j_0 + 1} Q^j \qquad (2.2) \\
&= \left(1 - \frac{1}{j - j_0 + 1}\right) Q_{TA}^{j-1} + \frac{1}{j - j_0 + 1} Q^j.
\end{aligned}
$$

It may be seen that Equation (2.2) corresponds to the general definition of time-averaging (Equation 2.1) with N_{TA}^{j} specified as $N_{TA}^{j} = j - j_0 + 1$. The statistical error involved in the time-averaged output quantities scales as $(N_{pc} N_{TA}^{j})^{-1/2}$ for $\Delta t N_{TA}^{j}$ large compared to the correlation time of the statistical error [18, 13], so the statistical error of the output can be reduced by using UTA for many time steps and for a fixed number of particles per cell N_{pc}. Usually, for a typical run, more than 5000 steps ($N_{TA}^{j} > 5000$) are time-averaged uniformly to reduce the statistical error. The UTA of the output quantities, however, cannot reduce the bias involved in the solution which scales as N_{pc}^{-1} [18, 12].

Time-averaging of the feedback quantities is able to reduce the bias because of the reduced statistical fluctuations in these quantities. In the hybrid algorithm, there are three categories of feedback fields to be time-averaged [17]. The first category is the mean quantities from particles fed back into the evolution of particles (referred as particle-to-particle quantities, e.g., mean fluctuating velocity and turbulence frequency). The second category consists of the particle mean fields passed to the FV solver (e.g., Reynolds stresses, turbulent fluxes). The last category consists of the FV fields. A different strategy called moving-time-averaging (MTA) is used for these feedback quantities. The time-averaging scheme (Equation 2.1) is used with a different specification of the parameter N_{TA}^{j}. Initially, all the time-averaging strategies (MTA and UTA with

$N_{TA}^j = 1$) are disabled to make the transient process most rapid. After a certain number of time steps, a statistically-stationary state is reached, which is determined by monitoring the time series of particle ensemble mean quantities. This statistically-stationary state involves bias. By using MTA, the statistical error and the bias are reduced gradually, so the previous statistically-stationary state changes on a time scale of $T_{TA} = N_{TA}\Delta t$ and a different statistically-stationary state is approached. In order to reduce the statistical error and bias, N_{TA}^j is increased gradually, but it is limited to a specified maximum N_{max}, i.e., $N_{TA}^j = \min[1 + 0.25 \times \max(j - j_0, 0), N_{max}]$ where j_0 is the time step from which MTA is used. This upper limit N_{max} is imposed so that the time scale T_{TA} is not too large to allow the time-averaged quantities to follow any residual transients. On time step j ($j > j_0$), the time-averaged quantity Q_{TA}^j is

$$\begin{aligned} Q_{TA}^j &= \left(1 - \frac{1}{N_{TA}^j}\right) Q_{TA}^{j-1} + \frac{1}{N_{TA}^j} Q^j \\ &= \sum_{i=j_0}^{j} \frac{1}{N_{TA}^i} \left[\prod_{k=i+1}^{j} \left(1 - \frac{1}{N_{TA}^k}\right)\right] Q^i. \end{aligned} \tag{2.3}$$

so the contribution of Q^i to Q_{TA}^j is weighted by $\frac{1}{N_{TA}^i}\left[\prod_{k=i+1}^{j}\left(1 - \frac{1}{N_{TA}^k}\right)\right]$. In HYB2D, the value of N_{max} is different for different categories of feedback quantities, i.e., the value of $N_{max} = 500$ [17, 23] is used for the particle-to-particle quantities, and $N_{max} = 5$ [17] is used for the particle-to-FV quantities and for the FV fields. In previous work [17, 23], these values were deemed to provide satisfactory performance, but they may not be optimal.

The procedure of using the time-averaging in HYB2D during the time marching is the following. Initially, all the time-averaging strategies are turned off to make the transient process most rapid. After the statistically-stationary state is approximately reached, MTA is turned on to reduce the statistical error and the bias of the stationary solution. With more than 5000 steps of MTA,

a statistically-stationary solution with less bias is obtained. Then, UTA of the output quantities is turned on to further reduce the statistical error involved in these quantities. With another 5000 steps of UTA, the output quantities are sufficiently time-averaged and are ready for the postprocessing: then the run terminates.

2.2.3 Bias due to the velocity correction

The condition of zero mean density-weighted fluctuating velocity ($\langle \rho \mathbf{u} \rangle / \langle \rho \rangle = 0$, where angle brackets denote mathematical expectation) is identified as one of the three independent consistency conditions in the hybrid algorithm [15]. The fluctuating velocity is a property of a particle in the current PDF algorithm. The mass weighted ensemble mean of the particle fluctuating velocity $\widetilde{\mathbf{u}}$ pertaining to a FV cell, on a particular time step, is defined as

$$\widetilde{\mathbf{u}} = \sum_{k=1}^{N} \mathbf{u}^{(k)} m^{(k)} \Big/ \sum_{k=1}^{N} m^{(k)} \ , \tag{2.4}$$

where $\mathbf{u}^{(k)}$ and $m^{(k)}$ are the fluctuating velocity and mass of the kth particle in the cell, and N is the number of particles in the cell. Due to statistical and truncation errors, the ensemble mean $\widetilde{\mathbf{u}}$ is not zero exactly. A velocity correction is needed to enforce the consistency condition, e.g.,

$$\mathbf{u}^{(k)} = \mathbf{u}^{(k)^*} - \widetilde{\mathbf{u}^*}, \tag{2.5}$$

where the star denotes the uncorrected velocity. In the above correction, the ensemble mean $\widetilde{\mathbf{u}^*}$, which is random due to the finite number of particles, provides an estimate of the expectation of $\widetilde{\mathbf{u}^*}$. The ensemble mean of Equation (2.5) yields

$$\widetilde{\mathbf{u}} = \widetilde{\mathbf{u}^*} - \widetilde{\mathbf{u}^*} = 0, \tag{2.6}$$

showing that this velocity correction makes $\widetilde{\mathbf{u}}$ identically zero.

Alternatively, the time-averaged ensemble mean of the particle fluctuating velocity, denoted as $\widetilde{\mathbf{u}^*}_{TA}$, provides a better estimate of the expectation of $\widetilde{\mathbf{u}^*}$, and the following correction algorithm can be used [15]

$$\mathbf{u}^{(k)} = \mathbf{u}^{(k)^*} - \widetilde{\mathbf{u}^*}_{TA}. \tag{2.7}$$

For this correction, we obtain

$$\widetilde{\mathbf{u}} = \widetilde{\mathbf{u}^*} - \widetilde{\mathbf{u}^*}_{TA}, \tag{2.8}$$

and

$$\langle\widetilde{\mathbf{u}}\rangle = 0, \tag{2.9}$$

since, in the statistically-stationary state considered, we have $\langle\widetilde{\mathbf{u}^*}\rangle = \langle\widetilde{\mathbf{u}^*}_{TA}\rangle$. Thus, for this correction, and for non-trivial time averaging (i.e., $N_{TA} > 1$), $\widetilde{\mathbf{u}}$ is not identically zero, but it has zero expectation.

To understand the above two correction algorithms (Equation 2.5 and Equation 2.7), we consider the influence of the corrections on the variance of the fluctuating velocity $\mathrm{var}(u_i)$. For simplicity we perform the analysis for a single component of velocity, which we denote by u. In the limit of $N_{TA} \to \infty$, $\widetilde{u^*}_{TA}$ tends to $\langle u^*\rangle$, and it immediately follows from Equation (2.7) that

$$\mathrm{var}(u) = \mathrm{var}(u^*). \tag{2.10}$$

Hence, the correction (Equation (2.7)) is unbiased in the sense that the variances of fluctuating velocity evaluated before and after the correction are the same as $N_{TA} \to \infty$.

The correction Equation (2.5) yields

$$\mathrm{var}(u) = \mathrm{var}(u^*) + \mathrm{var}(\widetilde{u^*}) - 2\mathrm{cov}(u^*, \widetilde{u^*}), \tag{2.11}$$

where cov() denotes covariance. If we assume that the particles in a cell are statistically identical with equal mass $m^{(k)}$, and that the velocities associated with different particles are uncorrelated, it can be verified that

$$\mathrm{var}(\widetilde{u^*}) = \frac{1}{N_{pc}}\mathrm{var}(u^*), \tag{2.12}$$

$$\mathrm{cov}(u^*, \widetilde{u^*}) = \frac{1}{N_{pc}}\mathrm{var}(u^*). \tag{2.13}$$

Thus Equation 2.11 becomes

$$\mathrm{var}(u) = \left(1 - \frac{1}{N_{pc}}\right)\mathrm{var}(u^*), \tag{2.14}$$

showing that the correction Equation (2.5) is biased in the sense that, for finite N_{pc}, it decreases the variance of the fluctuating velocity.

Now we turn our attention to the expectations of the turbulent kinetic energy (TKE) k^* and k evaluated before and after the velocity correction, respectively,

$$\begin{aligned} \langle k^* \rangle = \frac{1}{2}\langle \widetilde{u_i^* u_i^*} \rangle &= \frac{1}{2}(\langle \widetilde{u_i^* u_i^*} \rangle - \langle \widetilde{u_i^*} \rangle \langle \widetilde{u_i^*} \rangle) + \frac{1}{2}\langle \widetilde{u_i^*} \rangle \langle \widetilde{u_i^*} \rangle \\ &= \frac{1}{2}\sum_{i=1}^{3} \mathrm{var}(u_i^*) + \frac{1}{2}\langle \widetilde{u_i^*} \rangle \langle \widetilde{u_i^*} \rangle, \end{aligned} \tag{2.15}$$

$$\begin{aligned} \langle k \rangle = \frac{1}{2}\langle \widetilde{u_i u_i} \rangle &= \frac{1}{2}(\langle \widetilde{u_i u_i} \rangle - \langle \widetilde{u_i} \rangle \langle \widetilde{u_i} \rangle) + \frac{1}{2}\langle \widetilde{u_i} \rangle \langle \widetilde{u_i} \rangle \\ &= \frac{1}{2}\sum_{i=1}^{3} \mathrm{var}(u_i) + \frac{1}{2}\langle \widetilde{u_i} \rangle \langle \widetilde{u_i} \rangle. \end{aligned} \tag{2.16}$$

The underlying assumption involved in the above equations are that all the particles in the same cell are statistically identical so the variance of fluctuating velocity of each particle is the same. In the above analysis, we observe that both corrections (Equation 2.5 and Equation 2.7) yield $\langle \widetilde{u_i} \rangle = 0$, so from Equation (2.15) and Equation (2.16), we have

$$\langle k \rangle - \langle k^* \rangle = \frac{1}{2}\sum_{i=1}^{3} [\mathrm{var}(u_i) - \mathrm{var}(u_i^*)] - \frac{1}{2}\langle \widetilde{u_i^*} \rangle \langle \widetilde{u_i^*} \rangle. \tag{2.17}$$

For correction Equation (2.7), the first term on the right-hand side of the above equation disappears due to Equation (2.10), so Equation (2.17) reduces to

$$\langle k \rangle - \langle k^* \rangle = -\frac{1}{2}\langle \widetilde{u_i^*} \rangle \langle \widetilde{u_i^*} \rangle. \tag{2.18}$$

It can be seen that the correction Equation (2.7) removes the mean kinetic energy contained in the TKE evaluated before the correction. For finite N_{TA} the analysis is more involved, but the bias shown in Equation (2.18) is likely to remain, albeit of a small magnitude.

For the correction Equation (2.5), however, the first term on the right-hand side of Equation (2.17) does not disappear, and by substituting Equation (2.14) into Equation (2.17), we have

$$\langle k \rangle - \langle k^* \rangle = -\frac{1}{2N_{pc}} \sum_{i=1}^{3} \mathrm{var}(u_i^*) - \frac{1}{2}\langle \widetilde{u_i^*} \rangle \langle \widetilde{u_i^*} \rangle. \tag{2.19}$$

For each time step Δt, the correction Equation (2.5) corresponds to a fractional step for the variation of TKE, i.e.

$$\left\langle \frac{dk}{dt} \right\rangle \Bigg|_{\text{correction}} = \frac{\langle k \rangle - \langle k^* \rangle}{\Delta t} = -\varepsilon_n - \frac{\langle \widetilde{u_i^*} \rangle \langle \widetilde{u_i^*} \rangle}{2\Delta t}, \tag{2.20}$$

where $\varepsilon_n = \frac{1}{2N_{pc}\Delta t} \sum_{i=1}^{3} \mathrm{var}(u_i^*) > 0$. In addition to removing the mean kinetic energy contained in the TKE evaluated before the correction, the correction Equation (2.5) introduces a numerical dissipation ε_n which reduces the TKE. As N_{pc} tends to infinity, ε_n tends to zero, so the two corrections (Equation 2.5 and Equation 2.7) are consistent in this limit. If the physical dissipation ε and the numerical dissipation ε_n are linearly related, the total dissipation rate of TKE ε_{tot} in the computation is the sum of them

$$\varepsilon_{tot} = \varepsilon + \varepsilon_n. \tag{2.21}$$

To summarize, the correction Equation (2.7) produces zero expectation of the fluctuating velocity and conserves its variance, and removes the mean kinetic

energy from the TKE evaluated before the correction. Although the correction Equation (2.5) produces identically zero ensemble mean of the fluctuating velocity, it reduces the variance of the velocity. As a consequence, it introduces a numerical dissipation term in the TKE evolution, in addition to removing the mean kinetic energy contained in the TKE evaluated before the correction.

2.3 Influence of time-averaging on bias

To quantify the influence of the time-averaging of mean fluctuating velocity on bias, two test cases, the Cabra H_2/N_2 lifted flame [19] and the Sandia piloted flame E [20], are performed and described in the following subsections.

2.3.1 Cabra lifted H_2/N_2 jet flame

The Cabra lifted H_2/N_2 jet flame has been investigated using the hybrid FV/particle PDF method in [7]. The details of the current simulation are the same as those in [7], i.e., the H_2/O_2 reaction mechanism (the Li mechanism or the Mueller mechanism used in [7]), the EMST model (C_ϕ = 1.5), the simplified Langevin model, the stochastic frequency model with $C_{\omega 1}$ = 0.65, the calculated inlet velocity profiles, the number of particles per cell N_{pc}=100. Any differences in the details of the simulation from [7] are mentioned below.

The test cases shown below use the same models and parameters (EMST, Li mechanism, coflow temperature T_c = 1033K) as those used in Figure 16 of [7], except for the values of C_ϕ, N_{pc}, and the time-averaging of the mean fluctuating velocity. The value of C_ϕ used here is 1.5 rather than 2.0 in Figure 16 of [7]. The

influence of C_ϕ on the results with T_c = 1033K is negligible (see Figure 8 in [7]). The value of N_{pc} varies from 100 to 250 in these test cases. For each value of N_{pc}, two cases are compared, one case with all quantities time-averaged (denoted as TAu), and the other with all quantities except the mean fluctuating velocity time-averaged (denoted as NoTAu). Figure 2.1 shows the mean axial velocity $\widetilde{U}$, the mean turbulence frequency $\widetilde{\omega}$, the Reynolds stresses $\widetilde{uu}$, $\widetilde{uv}$, and the means and rms of the mixture fraction and temperature plotted against N_{pc}^{-1} at the location $(x, r) = (15D, 1D)$ in the Cabra lifted H_2/N_2 jet flame, where (x, r) are the axial and radial coordinates, and D is the diameter of the fuel jet nozzle. Serval observations can be made from the figure. First, the results by the two methods (TAu and NoTAu) vary linearly with N_{pc}^{-1}, reflecting the expected scaling of the bias [12, 18]. Second, when extrapolated to $N_{pc} \to \infty$ (i.e., $N_{pc}^{-1} = 0$) the two methods (TAu and NoTAu) yield almost the same results, indicating the convergence of both methods to the same solution. Third, the slopes of the results obtained with TAu are much smaller in magnitude than those obtained by NoTAu, implying that TAu reduces the bias in the hybrid algorithm dramatically compared to the NoTAu case. Fourth, with TAu, all the results obtained with different values of N_{pc} (from 100 to 250) fall inside the ±5% error lines, so the value of N_{pc} = 100 used in [7] is a reasonable choice for the simulations. Last, with NoTAu, $\langle uu \rangle$ decreases with increasing N_{pc}^{-1}, consistent with the argument related to numerical dissipation ε_n (Equation 2.20). However, this is generally true for upstream locations, e.g., $x \leqslant 35D$. At downstream locations, $\langle uu \rangle$ may increase with increasing N_{pc}^{-1}. Comparing the results reported in [7] with the current results, we confirm that the presented results with TAu and N_{pc} = 100 are consistent with those in [7].

Figure 2.1 demonstrates that TAu has a substantial effect on the bias involved

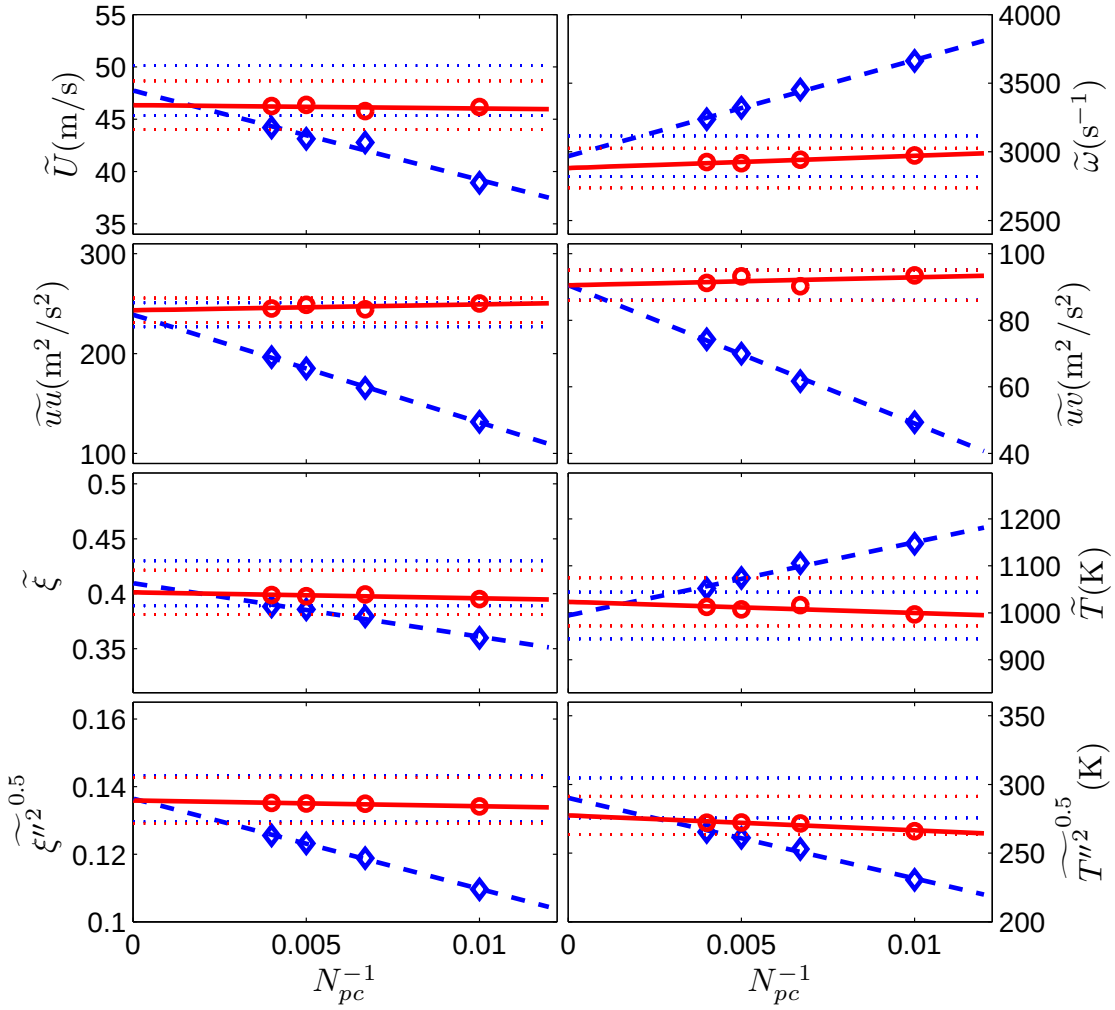

Figure 2.1: PDF calculations of the means of the axial velocity $\widetilde{U}$, the turbulence frequency $\widetilde{\omega}$, the Reynolds stress $\widetilde{uu}$, $\widetilde{uv}$, and the means and rms of the mixture fraction and temperature against N_{pc}^{-1} at the location of $(15D, 1D)$ in the Cabra lifted H_2/N_2 jet flame. (Circle: TAu; Diamond: NoTAu; Solid or dashed lines: linear least square fit; Dotted lines: ±5% error)

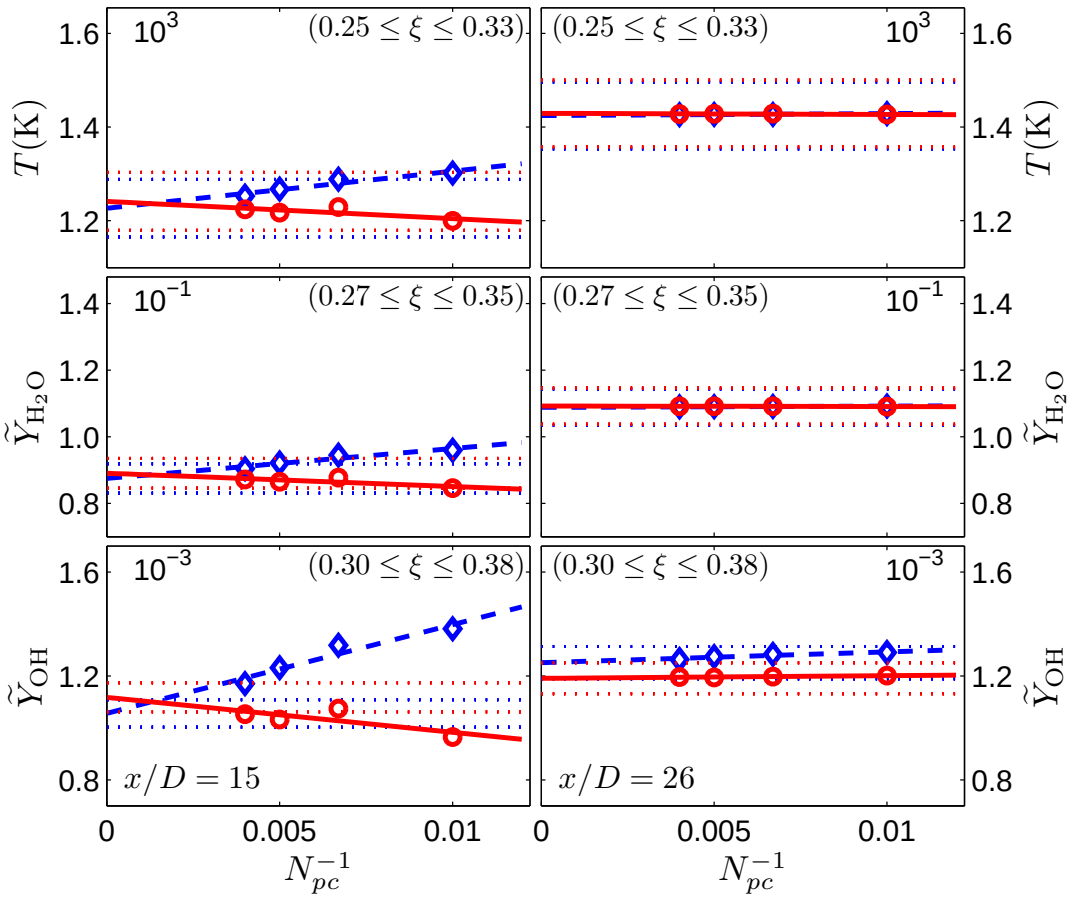

Figure 2.2: The conditional means of the temperature and mass fractions of H_2O and OH against N_{pc}^{-1} at the location of x/D = 15 (left) and 26 (right) in the Cabra lifted H_2/N_2 jet flame. (Circle: TAu; Diamond: NoTAu; Solid or dashed lines: linear least square fit; Dotted lines: ±5% error)

in unconditional statistics. The influence of TAu on conditional means is now investigated. In Figure 2.2 are shown the conditional means of temperature, mass fractions of H_2O and OH against N_{pc}^{-1} at $x/D = 15$ and 26 in the Cabra H_2/N_2 lifted jet flame, where the means are conditional on the mixture fraction ξ being in the ranges $[\xi_l, \xi_u]$ indicated in the figure. The ranges of mixture fraction are particularly chosen to cover the peaks where most sensitivity is expected. In contrast to the unconditional statistics in Figure 2.1, the bias involved in the calculations of conditional means obtained with NoTAu (Figure 2.2) is small. The results at $x/D = 15$ exhibit a larger sensitivity because this location is close to the base of the flame. In summary, the conditional statistics are affected little by the time-averaging strategy, which is very different from the case of the unconditional statistics.

2.3.2 Sandia piloted flame E

The simulation results of flame E obtained using HYB2D are reported recently in [5, 6]. If not specially mentioned, the details of the current simulation are the same as in [5, 6]. The test cases here use the EMST model with $C_\phi = 1.5$, the skeletal mechanism [21], the value $C_{\omega 1} = 0.65$ and ignore radiation. Figure 2.3 shows the means of the axial velocity $\widetilde{U}$, turbulence frequency $\widetilde{\omega}$, the Reynolds stress $\widetilde{uu}$, $\widetilde{uv}$, and the means and rms of the mixture fraction and temperature against N_{pc}^{-1} at the location of $(45D, 1D)$. Similar observations to the case of the Cabra lifted flame can be made. The Reynolds stress $\langle uu \rangle$, however, increases with N_{pc}^{-1} at the axial location shown. At upstream locations (e.g., $x \leqslant 40$), $\langle uu \rangle$ decreases with N_{pc}^{-1} generally. Figure 2.4 shows the conditional means of the temperature and mass fractions of CO_2, H_2O, CO, H_2 and OH against N_{pc}^{-1} at the

location of $x/D = 45$. The bias involved in the conditional statistics in flame E obtained using TAu and NoTAu is very small (below 5%).

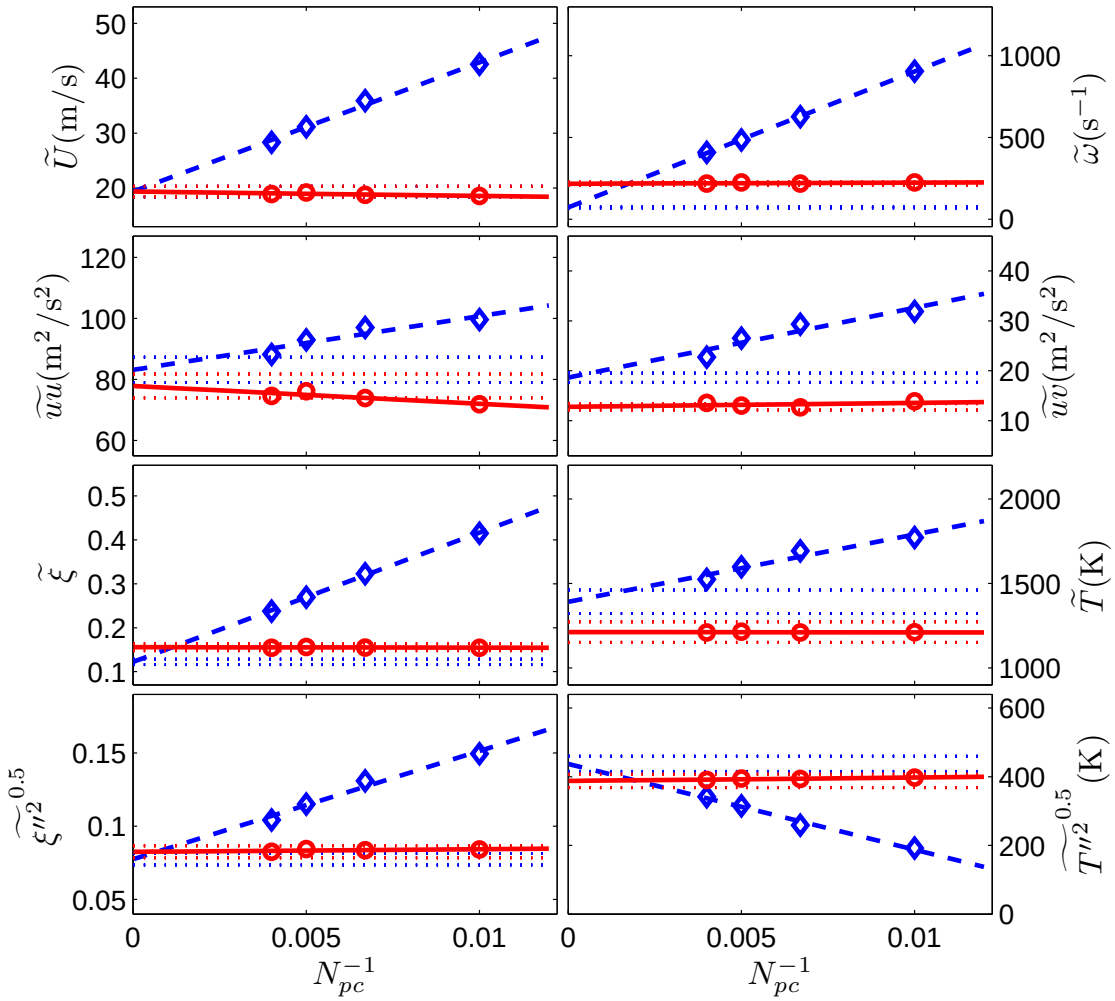

Figure 2.3: PDF calculations of the means of the axial velocity $\widetilde{U}$, turbulence frequency $\widetilde{\omega}$, the Reynolds stress $\widetilde{uu}$, $\widetilde{uv}$, and the means and rms of the mixture fraction and temperature against N_{pc}^{-1} at the location of $(45D, 1D)$ in the Sandia piloted flame E. (Circle: TAu; Diamond: NoTAu; Solid or dashed lines: linear least square fit; Dotted lines: ±5% error)

In the above discussion of both test cases, results are shown only at a few locations, but they are representative of all other locations of interest, i.e., two or three diameters downstream from the nozzle. The results near the nozzle are very sensitive to the imposed inlet boundary condition, so they are not appro-

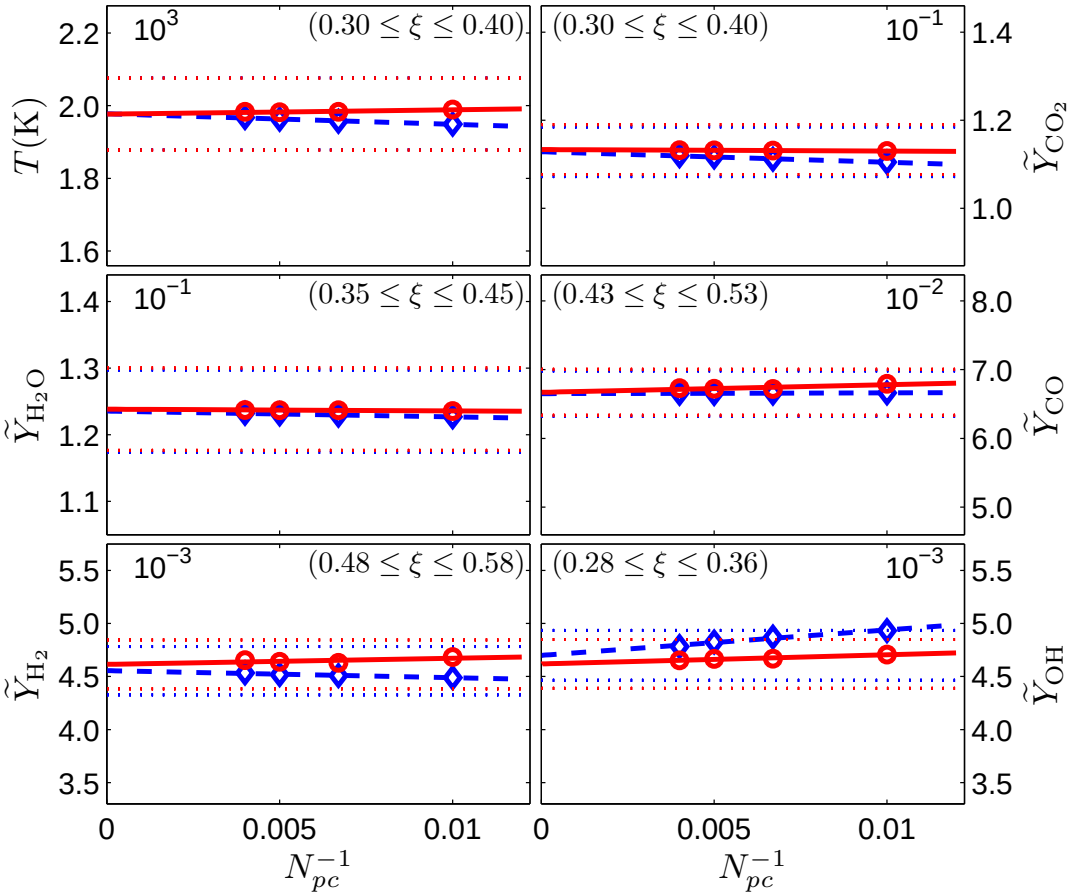

Figure 2.4: The means of the temperature and mass fractions of CO_2, H_2O, CO, H_2 and OH against N_{pc}^{-1} at the location of $x/D = 45$ in the Sandia piloted flame E. (Circle: TAu; Diamond: NoTAu; Solid or dashed lines: linear least square fit; Dotted lines: ±5% error)

priate for the current discussion.

2.3.3 Discussion

Based on the test cases of the Cabra lifted H_2/N_2 flame and the Sandia flame E by using TAu and NoTAu, it can be concluded that both TAu and NoTAu are legitimate, consistent methods in the sense that they converge to the same results as N_{pc} tends to infinity. For finite N_{pc} (e.g., 100), TAu reduces the bias involved in unconditional statistics of PDF calculations considerably. It confirms the correct design of the original velocity correction algorithm (Equation 2.7) [15]. The results of the Cabra lifted H_2/N_2 flame reported in [7] are reproduced by using the current version of the HYB2D with TAu. Compared to the early versions of the HYB2D used in [5, 7, 6], several minor corrections and modifications have been made, and a new version of the ISAT library [22] is used. The influence of these changes has been evaluated carefully and are found to be negligible. The current bias convergence tests and the consistency of the Cabra lifted flame results with the early version and the current updated version of the HYB2D enhance our confidence in the correctness of the implementation of the PDF method. The current results of flame E with NoTAu and $N_{pc} = 100$ are consistent with those reported in [5, 6]. Thus, large bias is involved in the unconditional statistics reported in [5, 6] due to the disabled time-averaging of the particle-to-particle quantities. However, this bias does affect the conclusions drawn in those papers. First, the inaccuracy of the results do not affect the qualitative conclusions of the relative performance of different reaction mechanisms drawn in [6] and of the relative performance of different mixing models drawn in [5]. Second, TAu affects the velocity field and the mixing field directly. Once

the velocity field and the mixing field are somehow calculated reasonably compared to the experimental data as in [5, 6], the mixing process and the chemical reaction process are not expected to be altered dramatically no matter the time-averaging strategy, as indicated by the conditional statistics in Figure 2.2 and Figure 2.4. This is discussed further in the next section.

2.4 Influence of the model constant $C_{\omega 1}$

We have seen that bias, to some extent, corresponds to additional dissipation of TKE. In the stochastic turbulence frequency model [8], increasing the model constant $C_{\omega 1}$ also leads to increased dissipation rate of TKE. In the numerical simulation, it is the total dissipation rate (physical plus numerical, Equation 2.21) which affects the TKE. Hypothetically, a decrease in $C_{\omega 1}$ can compensate for the bias error. This is an important issue for the following reason. The studies of these flames (e.g., the Cabra flame and flame E) over the past decade have focused on the details of the turbulence-chemistry interactions. In order to minimize the effects of shortcomings in the turbulence models, the general practice is to adjust $C_{\omega 1}$ (or $C_{\varepsilon 1}$) as needed to achieve the observed jet spreading rates (as revealed by the radial profiles of mean mixture fraction, for example), and different values for $C_{\omega 1}$ have been used, e.g., 0.56 in [3], and 0.65 in [5, 7, 6]. According to the above hypothesis, calculations involving substantial bias require lower values of $C_{\omega 1}$ (compared to bias-free calculations) in order to match the observed jet spreading rates.

To test this hypothesis, PDF calculations with TAu or NoTAu (involving different amounts of bias) and with different values of $C_{\omega 1}$ are performed for the

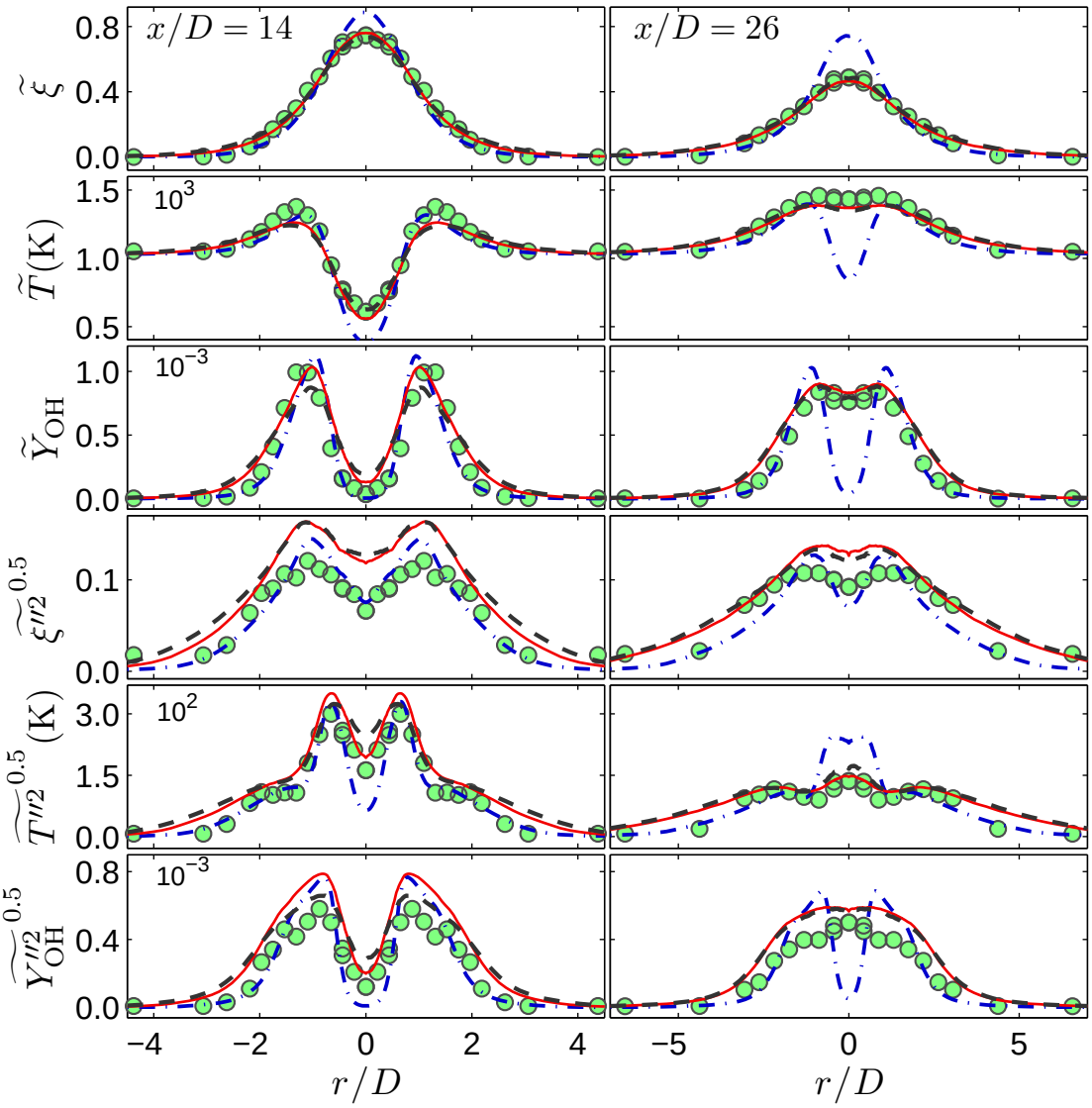

Figure 2.5: Radial profiles of the means and rms of the mixture fraction, temperature and OH mass fraction at the axial locations of x/D = 14 and 26 in the Cabra lifted H_2/N_2 jet flame. (Circles: experimental data; Curves: PDF calculations using TAu with $C_{\omega 1}$ = 0.65(solid), using NoTAu with $C_{\omega 1}$ = 0.56 (dashed), and using NoTAu with $C_{\omega 1}$ = 0.65 (dash-dotted))

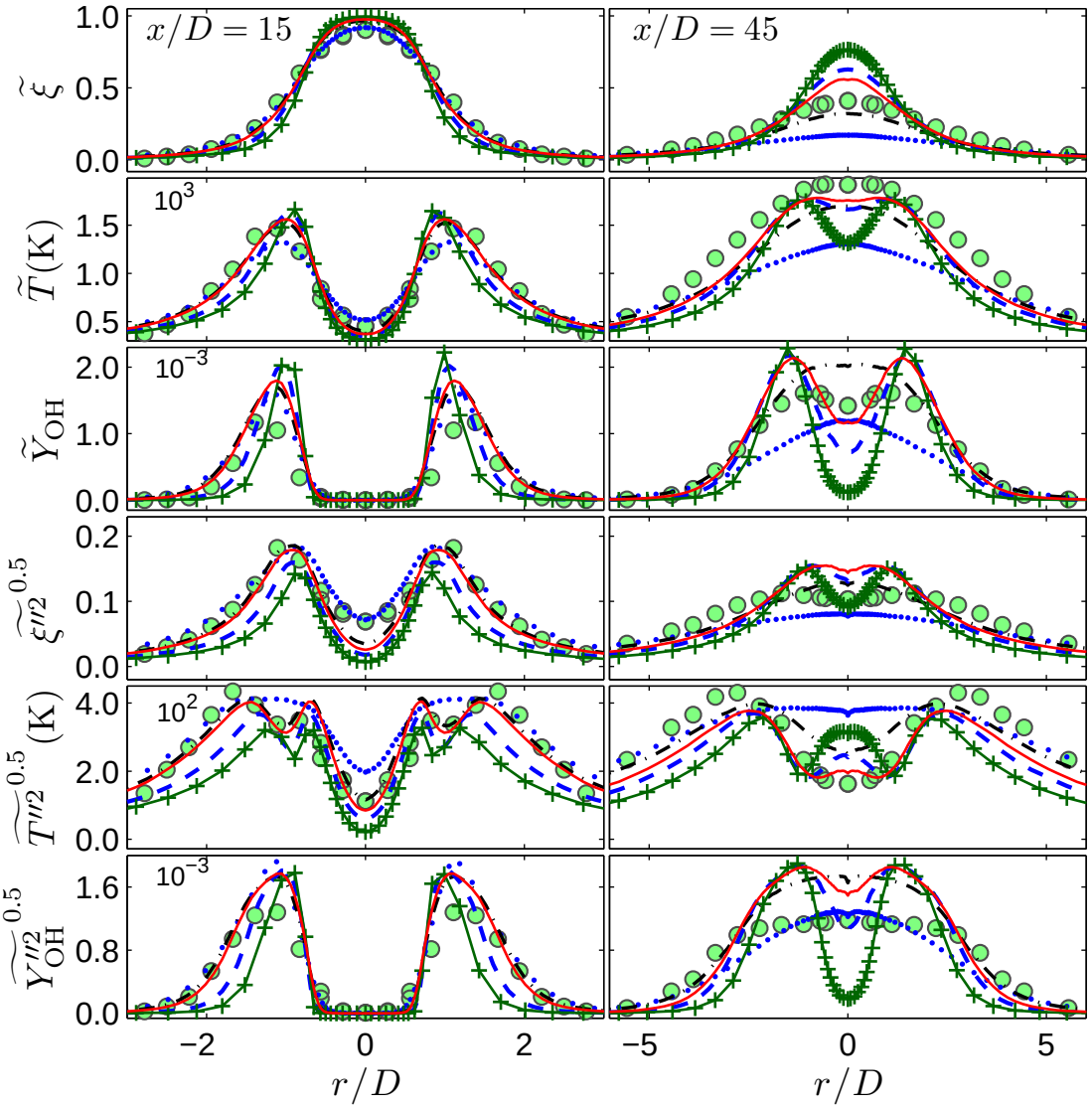

Figure 2.6: Radial profiles of the means and rms of the mixture fraction, temperature and OH mass fraction at the axial locations of x/D = 15 and 45 in the Sandia flame E. (Circles: experimental data; Curves: PDF calculations using NoTAu with $C_{\omega 1}$ = 0.65 (solid line), using TAu with $C_{\omega 1}$ = 0.85 (solid line with plus), using TAu with $C_{\omega 1}$ = 0.75 (dashed line), using TAu with $C_{\omega 1}$ = 0.70 (dash-dotted line), and using TAu with $C_{\omega 1}$ = 0.65 (dotted line))

Cabra lifted flame and for Sandia flame E. Figure 2.5 and Figure 2.6 show the radial profiles of the means and rms of the mixture fraction, temperature and OH mass fraction at different axial locations in the Cabra lifted H_2/N_2 jet flame and in the Sandia flame E. The same numerical settings as in Figure 2.1 are used with $N_{pc} = 100$, $C_{\omega 1} = 0.56$ or 0.65, and TAu or NoTAu for the Cabra flame. For the results with the different values of $C_{\omega 1}$ using NoTAu in Figure 2.5, we can see that increasing $C_{\omega 1}$ decreases the jet spreading rate and rms of the mixture fraction, so we confirm that the higher the value of $C_{\omega 1}$, the more dissipative is the turbulence model. For the same value of $C_{\omega 1}(= 0.65)$, NoTAu gives an under-prediction of the jet spreading rate and of the rms mixture fraction because of the numerical dissipation ε_n involved in NoTAu which weakens the turbulent transport. Comparing the results with TAu and $C_{\omega 1} = 0.65$ and the results with NoTAu and $C_{\omega 1} = 0.56$ in Figure 2.5, we can see that both cases give very similar predictions of the radial mean and rms profiles of the mixture fraction, temperature, and OH mass fraction.

For flame E in Figure 2.6, the numerical settings are the same as in Figure 2.3 with $N_{pc} = 100$, TAu or NoTAu, and different values for $C_{\omega 1}$. The results with NoTAu and $C_{\omega 1} = 0.65$ (solid lines in Figure 2.6) agree with the experimental data very well (equivalent to the results presented in [5, 6]), even though considerable bias is involved in the results. If TAu is used with $C_{\omega 1} = 0.65$ (dotted lines in Figure 2.6), the jet spreading rate is over-predicted as expected (because numerical dissipation is removed by TAu). To achieve the same jet spreading rate using TAu as using NoTAu with $C_{\omega 1} = 0.65$, it is necessary to increase $C_{\omega 1}$. The results with different values of $C_{\omega 1}$ (=0.70 (dash-dotted lines), 0.75 (dashed lines), and 0.85 (solid lines with plus)) for flame E are compared in Figure 2.6. To match the mean and rms profiles of the mixture fraction with the experimental

data, we can see that $C_{\omega 1} = 0.70$ is a reasonable choice. The results by TAu and $C_{\omega 1} = 0.70$ (dashed line) and by NoTAu and $C_{\omega 1} = 0.65$ (points) in Figure 2.6 are still different, but their overall agreement with the experimental data is similar. Thus, in some sense, the effect of the bias error in the PDF calculations is similar to the effect of increasing the value of $C_{\omega 1}$.

In the previous PDF calculations, different values for $C_{\omega 1}$ are used, e.g., 0.56 in [3], and 0.65 in [5, 7, 6]. In the calculations of the Sandia piloted flames by using the stand-alone particle method [3], the good agreement between the numerical results and the experimental data is achieved by using $C_{\omega 1} = 0.56$. The stand-alone particle method is expected to involve bias [18]. In the later calculations of the same flames by using the hybrid FV/particle method [5, 6], very similar results are obtained by using $C_{\omega 1} = 0.65$. The bias in [5, 6] is not small due to the disabled time-averaging. However, the bias involved in the results in [5, 6] should still be less than that in the results in [3] because the smooth FV fields are used in the particle method. By using TAu, we use a higher value $C_{\omega 1} = 0.7$ by using the hybrid method to produce the similar results to those in [5, 6]. Evidently, the increases in the value of $C_{\omega 1}$ used is a result of the decreasing bias error during the development of the solution algorithm of the PDF method.

The burning index (BI) is often used to quantify the amount of local extinction in the Sandia piloted flames. To evaluate the sensitivity of the BIs to the values of $C_{\omega 1}$ and to the time-averaging, the relative difference of the BIs are presented in Figure 2.7 by TAu and different values of $C_{\omega 1}$ relative to the BIs by NoTAu and $C_{\omega 1} = 0.65$ (equivalent to the results in [5, 6]). The BIs are calculated in the identical way to those in [3, 6]. The relative difference of BIs based

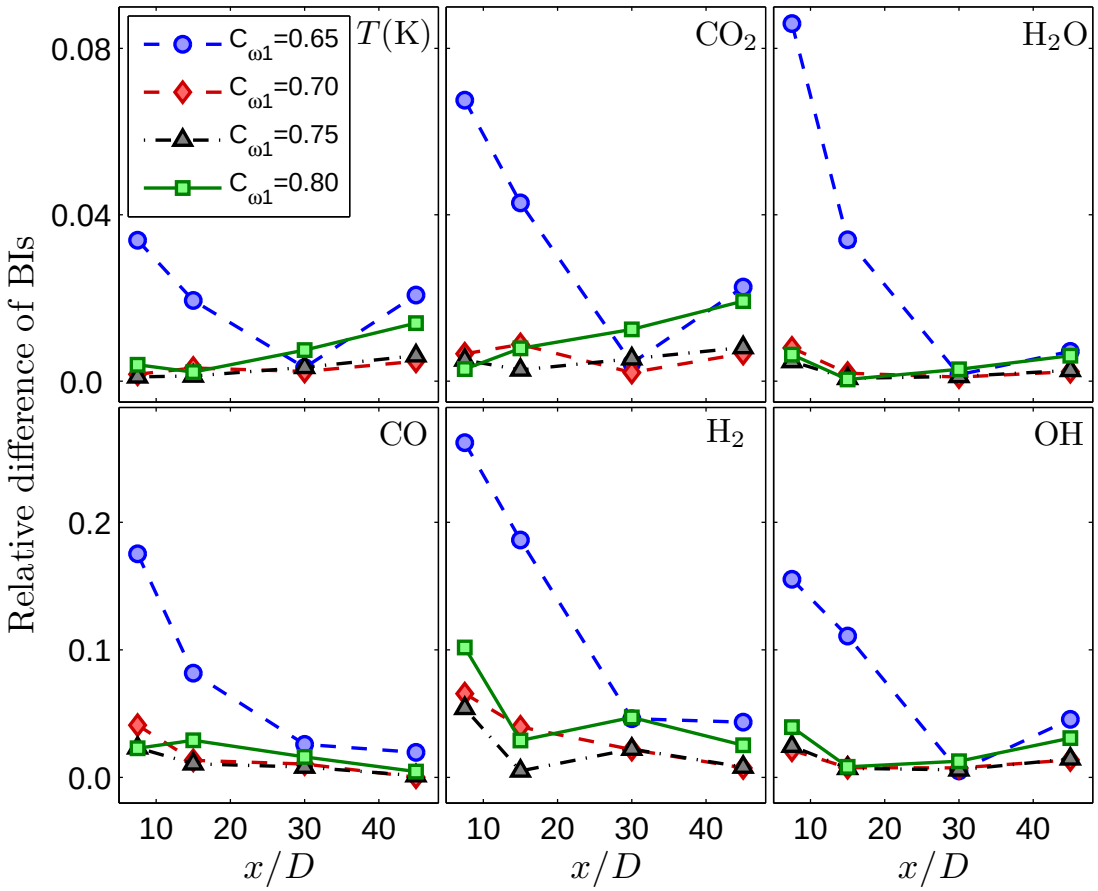

Figure 2.7: The difference in the BIs by TAu and different values of $C_{\omega 1}$ relative to the BI by NoTAu and $C_{\omega 1}$ = 0.65

on the temperature and the species mass fractions with $C_{\omega 1} = 0.65$ is evident (up to 25% for H_2 mass fraction at $x/D = 7.5$). The relative difference of BIs with $C_{\omega 1} > 0.65$ for all the test cases is within 5% except for H_2 mass fraction at $x/D = 7.5$ whose relative difference is within 11%. The small relative difference of the current updated results by using different values of $C_{\omega 1}$ (>0.65) and TAu relative to the results presented in [5, 6] for flame E demonstrates that the qualitative conclusions drawn in [5, 6] are not affected by the bias involved in those results.

The results presented in [3, 5, 6] and in this paper are quite similar, all in good agreement with the experimental data. This reminds us that good agreement between numerical results and experimental data does not necessarily indicate the numerical accuracy of numerical methods. The numerical errors can be compensated for somehow by adjusting model constants. A comprehensive exploration of numerical properties (such as numerical accuracy and convergence) of numerical methods is crucial for today's numerical simulations.

2.5 Conclusion

The time-averaging strategies in the hybrid solution method of the joint PDF method are investigated. The time-averaging of the mean fluctuating velocity (TAu) leads to the same variances of the fluctuating velocity before and after the velocity correction for a fixed number of particles per cell over a long time-averaging scale. Without TAu, the variances of the fluctuating velocity before and after the velocity correction are different, and an additional numerical dissipation is introduced for the turbulent kinetic energy. TAu reduces dramatically

the bias involved in the unconditional statistics of the tested turbulent flames, the Cabra H_2/N_2 lifted flame and the Sandia flame E. The conditional statistics in these flame, however, are hardly affected by TAu. The effect of the bias involved in the unconditional statistics is similar to the effect of increasing the value of the model constant $C_{\omega 1}$. The value of 0.7 for $C_{\omega 1}$ is suggested to yield the similar results of flame E with TAu to those without TAu and with 0.65 in [6, 5] (also in good agreement with the experimental data).

Acknowledgements

This work is supported by the Air Force Office of Scientific Research, Grant FA9550-06-1-0048. We are grateful to Steven R. Lantz and Daniel I. Sverdlik for their help on the parallel computations, and to Renfeng Cao for help on the HYB2D code. Various suggestions from David A. Caughey and Zhuyin Ren are appreciated. This research was conducted using the resources of the Cornell Theory Center, which receives funding from Cornell University, New York State, federal agencies, foundations, and corporate partners.

REFERENCES

[1] S.B. Pope, PDF methods for turbulent reactive flows, *Prog. Energy Combust. Sci.* 11(1985) 119-192.

[2] S.B. Pope, Turbulent Flows, Cambridge University Press, Cambridge, 2000.

[3] J. Xu, S.B. Pope, PDF calculations of turbulent nonpremixed flames with local extinction, *Combust. Flame* 123 (2000) 281-307.

[4] R.P. Lindstedt, S.A. Louloudi, E.M. Vaos, Joint scalar probability density function modeling of pollutant formation in piloted turbulent jet diffusion flames with comprehensive chemistry, *Proc. Combust. Inst.* 28 (2000) 149-156.

[5] R.R. Cao, H. Wang, S.B. Pope, The effect of mixing models in PDF calculations of piloted jet flames, *Proc. Combust. Inst.* 31 (2007) 1543-1550.

[6] R.R. Cao, S.B. Pope, The influence of chemical mechanisms on PDF calculations of nonpremixed piloted jet flames, *Combust. Flame* 143 (2005) 450-470.

[7] R.R. Cao, S.B. Pope, A.R. Masri, Turbulent lifted flames in a vitiated coflow investigated using joint PDF calculations, *Combust. Flame* 142 (2005) 438-453.

[8] P.R. Van Slooten, Jayesh, S.B. Pope, Advances in PDF modeling for inhomogeneous turbulent flows, *Phys. Fluids* 10 (1998) 246-265.

[9] S.B. Pope, A stochastic Lagrangian model for acceleration in turbulent flows, *Phys. Fluids* 14 (2002) 2360-2375.

[10] S. Subramaniam, S.B. Pope, A mixing model for turbulent reactive flows based on Euclidean minimum spanning trees, *Combust. Flame* 115 (1998) 487-514.

[11] S.B. Pope, A Monte Carlo method for the PDF equations of turbulent reactive flow, *Combust. Sci. Technol.* 25 (1981) 159-174.

[12] S.B. Pope, Particle method for turbulent flows: integration of stochastic model equations, *J. Comput. Phys.* 117 (1995) 332-349.

[13] M. Muradoglu, P. Jenny, S.B. Pope, D.A. Caughey, A consistent hybrid finite-volume/particle method for the PDF equations of turbulent reactive flows, *J Comput. Phys.* 154 (1999) 342-371.

[14] P. Jenny, S.B. Pope, M. Muradoglu, D.A. Caughey, A hybrid algorithm for the joint PDF equation for turbulent reactive flows, *J Comput. Phys.* 166 (2001) 218-252.

[15] M. Muradoglu, S.B. Pope, D.A. Caughey, The hybrid method for the PDF equations of turbulent reactive flows: consistency conditions and correction algorithms, *J Comput. Phys.* 172 (2001) 841-878.

[16] Y.Z. Zhang, D.C. Haworth, A general mass consistency algorithm for hybrid particle/finite-volume PDF methods, *J Comput. Phys.* 194 (2004) 156-193.

[17] K. Liu, Joint velocity-turbulence frequency-composition probability density function (PDF) calculations of bluff body stabilized flames. Ph.D. Dissertation, Cornell University, NY, 2004.

[18] J. Xu, S.B. Pope, Assessment of numerical accuracy of PDF/Monte carlo methods for turbulent reactive flows, *J Comput. Phys.* 152 (1999) 192-230.

[19] R. Cabra, T. Myhrvold, J.-Y. Chen, R.W. Dibble, A.N. Karpetis, R.W. Barlow, Simultaneous laser Raman-Rayleigh-Lif measurements and numerical modeling results of a lifted turbulent H-2/N-2 jet flame in a vitiated coflow, *Proc. Combust. Inst.* 29 (2002) 1881-1888.

[20] R.S. Barlow, J.H. Frank, Effects of turbulence on species mass fractions in methane-air jet flames, *Proc. Combust. Inst.* 27 (1998) 1087-1095.

[21] S. James, M.S. Anand, M.K. Razdan, S.B. Pope, In situ detailed chemistry calculations in combustor flow analysis, *ASME J. Engng. Gas Turbines Power* 123 (2001) 747-756.

[22] S.B. Pope, Computationally efficient implementation of combustion chemistry using in situ adaptive tabulation, *Combust. Theory Model.* 1 (1997) 41-63.

[23] M. Muradoglu, K. Liu, S.B. Pope, PDF modeling of a bluff-body stabilized turbulent flame, *Combust. Flame* 132 (2003) 115-137.

CHAPTER 3

LAGRANGIAN INVESTIGATION OF LOCAL EXTINCTION, RE-IGNITION AND AUTO-IGNITION IN TURBULENT FLAMES*

Abstract

Lagrangian PDF investigations are performed of the Sandia piloted flame E and the Cabra H_2/N_2 lifted flame to help develop a deeper understanding of local extinction, re-ignition and auto-ignition in these flames, and of the PDF models' abilities to represent these phenomena. Lagrangian particle time series are extracted from the PDF model calculations and are analyzed. In the analysis of the results for flame E, the particle trajectories are divided into two groups: continuous burning and local extinction. For each group, the trajectories are further sub-divided based on the particles' origin: the fuel stream, the oxidizer stream, the pilot stream, and the intermediate region. The PDF calculations are performed using each of three commonly used models of molecular mixing, namely the EMST, IEM and modified Curl mixing models. The calculations with different mixing models reproduce the local extinction and re-ignition processes observed in flame E reasonably well. The particle behavior produced by the IEM and modified Curl models is different from that produced by the EMST model, i.e., the temperature drops prior to (and sometimes during) re-ignition. Two different re-ignition mechanisms are identified for flame E: auto-ignition and mixing-reaction. In the Cabra H_2/N_2 lifted flame, the particle trajectories are divided into different categories based on the particles' origin: the fuel stream, the oxidizer stream, and the intermediate region. The calculations reproduce the

*Haifeng Wang, Stephen B. Pope, Lagrangian investigation of local extinction, re-ignition and auto-ignition in turbulent flames, *Combustion Theory and Modelling* 12(5) (2008) 857-882.

whole auto-ignition process reasonably well for the Cabra flame. Four stages of combustion in the Cabra flame are identified in the calculations by the different mixing models, i.e., pure mixing, auto-ignition, mixing-ignition, and fully burnt, although the individual particle behavior by the IEM and modified Curl models is different from that by the EMST model. The relative importance of mixing and reaction during re-ignition and auto-ignition are quantified for the IEM model.

3.1 Introduction

Flame extinction and ignition are fundamental phenomena in combustion problems. The occurrence of extinction and ignition in turbulent reactive flows, due to intensive non-linear turbulence-chemistry interactions, is a challenge to modern turbulent combustion models. The probability density function (PDF) transport equation method [1, 2, 3] is increasingly found to be able to account accurately for the turbulence-chemistry interactions, e.g., local extinction and re-ignition [4, 5]. In engineering practice, the statistics of the turbulent velocity and composition fields are of primary concern in the context of Reynolds averaged Navier-Stokes (RANS) simulations. In PDF methods, the modeled PDF transport equation is usually solved numerically by a Lagrangian particle method, and much more information can be extracted from the particle properties. Particle scatter plots (or joint PDFs) contain the most detailed information about the distribution of properties at a given position and time. All previous PDF calculations of turbulent flames have focused on Eulerian statistics and their comparison with experimental data, e.g., conditional or unconditional statistics of compositions, particle scatter plots and conditional PDFs of compositions.

Scatter plots of particle properties are able to illustrate qualitatively different kinds of complicated turbulent combustion phenomena such as local extinction and re-ignition. To explore the PDF calculation results comprehensively, and to understand the turbulence-chemistry interactions more deeply, here we extract and analyze Lagrangian time series of particle properties from the PDF calculations. The particle trajectories are presented to illustrate the dynamic evolution of complicated turbulent combustion processes, i.e., local extinction and re-ignition in the turbulent non-premixed piloted jet flame, and auto-ignition in the turbulent lifted jet flame.

Lagrangian properties are important physical properties relevant not only to the PDF method, but also to real turbulence and combustion problems. Many Lagrangian investigations have been performed of turbulence using direct numerical simulations (DNS). Yeung [6, 7] studied the Lagrangian characteristics of turbulence and passive scalar transport in stationary isotropic turbulence with uniform mean scalar gradients. The Lagrangian properties of the scalars investigated are important to molecular mixing models. Mitarai et al. [8] performed DNS of an idealized non-premixed flame in decaying isotropic turbulence for conditions where flame extinction and re-ignition occur. In that work, the fluid particles are tracked to investigate flame extinction and re-ignition. Different categories of particles are identified, e.g., continuous burning and local extinction. Also investigated are Lagrangian properties of the conditional scalar diffusion, which appears as an unclosed term in the PDF transport equation. The same methodology is used to investigate the performance of flamelet models [9] and the performance of different mixing models [10]. Sripakagorn et al. [11] performed Lagrangian flame element tracking along the stoichiometric surface in decaying isotropic turbulence to investigate flame extinction and

re-ignition. Three major scenarios of re-ignition in non-premixed combustion are identified, i.e., the independent flamelet scenario, re-ignition via edge flame propagation, and re-ignition through engulfment by hot neighbouring fluid. These Lagrangian investigations are helpful to provide insights into the dynamic evolution of turbulent combustion processes. Because of the formidable practical difficulties there are no experimental data on Lagrangian quantities in turbulent reactive flows. Experimental data are, however, becoming available on Lagrangian velocity and acceleration statistics in non-reactive flows [12, 13, 14].

The Lagrangian PDF method [2] represents the turbulent flow, transport and reaction processes via the time evolution of nominal Monte Carlo particles representing the joint PDF of velocity, turbulence frequency and compositions. Eulerian statistics obtained from PDF calculations have been explored extensively before, and are generally found to be in good agreement with the experimental data. It would be valuable to extract the Lagrangian time series which contains the whole history of the particle evolution in the multi-dimensional sample space. This work is dedicated, as a first effort, to explore the Lagrangian properties of the Monte Carlo particles in the PDF simulations of turbulent flames containing local extinction and re-ignition, and auto-ignition. The two flames studied are the Sandia non-premixed piloted jet flame E [15], and the lifted H_2/N_2 jet flame in a vitiated coflow [16], referred to as the Cabra flame.

In PDF methods, the closed form of the chemical reaction source term facilitates the exact treatment of detailed combustion chemistry. The modeling of the unclosed molecular mixing term in the PDF equation remains one of the major efforts of model development. Three mixing models are extensively used,

i.e. the Euclidean minimum spanning tree (EMST) model [21], the interaction by exchange with the mean (IEM) model [18] (or the least-mean-square estimator (LMSE) model [19]), and the modified Curl model [20, 22]. All the mixing models can represent local extinction and re-ignition to some extent [4, 5, 23], although the EMST model is usually thought to be superior in this respect. The simplicity of the IEM and modified Curl models makes them quite popular. In spite of the complexity of the EMST model, the public availability of a FORTRAN implementation [24] makes it easy to use. A desirable property of mixing models is "localness" [21]. All the models are local in physical space; only the EMST model is local in composition space; and none is local in velocity space. There is some recent progress in the development of more sophisticated mixing models, e.g., the multiple mapping conditioning (MMC) model [25], and the interaction by exchange with the conditional mean (IECM) mixing model [26, 27, 28, 29], which is local in velocity space. The present work focuses on the three traditional mixing models (EMST, IEM and modified Curl) and evaluates their relative performance from the Lagrangian viewpoint.

The primary aim of PDF methods is to calculate accurately one-point, one-time Eulerian quantities. It is well understood [1] that this objective can be achieved using stochastic Lagrangian models, even if the multi-time properties of the models are not physically accurate. While the multi-time behavior of the stochastic models for position and velocity are physically realistic, those of the mixing models are not. For example Curl's model involves jumps in compositions; and (for the simplest homogeneous turbulence) the IEM model yields a deterministic relaxation to the mean, with no fluctuations along Lagrangian trajectories. Hence, while this study is valuable in shedding light on the models' behavior and performance, a close correspondence between the models' La-

grangian trajectories and those in the flame (could they be measured!) should not be expected.

The remaining sections of this paper are organized as follows. In Section 3.2, Eulerian scatter plots of particle properties are presented for the Sandia piloted flame E [15] and for the Cabra H_2/N_2 lifted jet flame [16]. The illustrations of local extinction and re-ignition, and of auto-ignition are reviewed by reference to the Eulerian particle data. The limitations of the Eulerian data are discussed. In Section 3.3, the particle tracking and particle sampling procedures are presented. In Sections 3.4 and 3.5 (for the Sandia flame E and the Cabra lifted flame, respectively), the Lagrangian time series obtained from the PDF calculation using the different mixing models are analyzed to study the models' representation of extinction, re-ignition and auto-ignition. The relative roles of mixing and reaction during re-ignition and auto-ignition are quantified for the IEM model in Section 3.6. Conclusions are drawn in the final section.

3.2 Particle calculations and Eulerian scatter plots

Comprehensive PDF model investigations of the Sandia piloted flames and the Cabra H_2/N_2 lifted jet flame have been described elsewhere [4, 5, 16, 23, 30, 31, 32]. In this section, PDF calculations of the Sandia flame E and the Cabra lifted jet flame are repeated to review the Eulerian particle scatter plots. As in [23, 30], a PDF code called HYB2D is used, in which a hybrid finite volume (FV)/particle algorithm is implemented for solving the joint PDF transport equation of the velocity, turbulence frequency and compositions [34]. The details of the simulations for the Sandia flame E and the Cabra lifted jet flame are identical to those

in [35] and in [31], respectively, and are simply summarized in Table 3.1. (Quantities not listed in Table 3.1 can be found in [31] and [35].) Different values of the mixing model constant C_ϕ are specified for the different mixing models in the calculation of the Sandia flame E in order to achieve a stable burning flame with roughly the same amount of local extinction [23, 35] as observed experimentally. Similarly, different coflow temperatures are used in the calculation of the Cabra lifted flame with different mixing models in order to produce approximately the same flame lift-off height as observed experimentally [31].

Table 3.1: Details of the simulations for the Sandia flame E and the Cabra lifted H_2/N_2 jet flame

Model parameters	Sandia flame E			Cabra lifted flame		
Turbulence frequency model constant [17], $C_{\omega 1}$	0.7			0.65		
Number of particles per cell, N_{pc}	100			100		
Chemistry	GRI-Mech 3.0 [37]			H_2-O_2 mechanism [38]		
ISAT error tolerance [36], ε_{tol}	5.0×10^{-5}			6.25×10^{-6}		
Grid size	96×96			96×96		
	EMST	IEM	modified Curl	EMST	IEM	modified Curl
Mixing model constant, C_ϕ	1.5	2.7	3.3	1.5	1.5	1.5
Coflow temperature in Cabra lifted flame, T_c(K)	—	—	—	1033	1036	1036

Conventionally, the output from PDF calculations is Eulerian data for analysis at a fixed time (when the statistically stationary state has been reached) and at different locations. The conditional and unconditional statistics of the Eulerian data have been discussed extensively elsewhere [4, 5, 23, 30, 31] and will not

be repeated here. In this section, we review the scatter plots of the particle temperature versus the mixture fraction in the Sandia flame E and the Cabra lifted flame. As previously discussed [4], it is difficult to make a rigorous quantitative comparison between scatter plots from experiment and model calculations, because of differences in the sampling and weighting of particles. Nevertheless, this comparison is useful in assessing, at least qualitatively, the ability of the models to represent the phenomena observed experimentally.

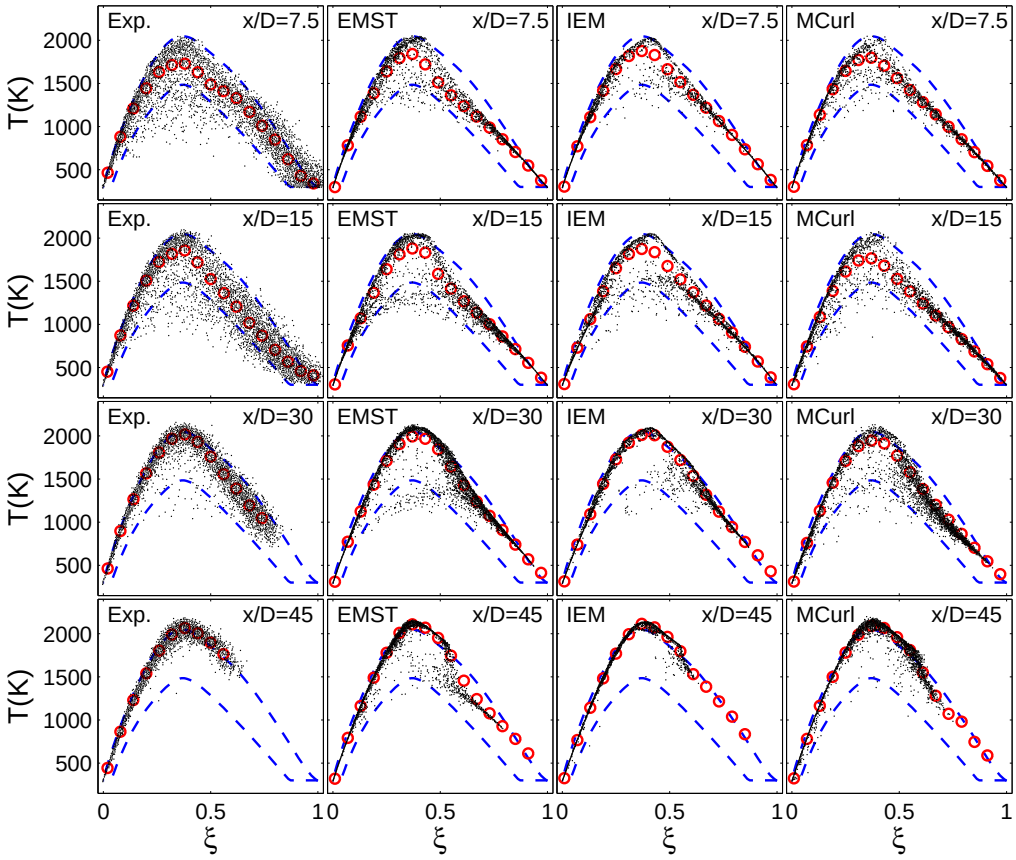

Figure 3.1: Scatter plots of temperature against the mixture fraction at the axial locations x/D =7.5, 15, 30, and 45 in the Sandia piloted flame E from experimental data and from PDF calculations using three different mixing models (Open circles: conditional mean temperature; Dashed lines: temperature profiles in the opposed-jet laminar flame with strain rate $a = 10\text{s}^{-1}$ (upper lines); and with strain rate $a = 310\text{s}^{-1}$ (lower lines), shifted down by 300K.)

Figure 3.1 shows the scatter plots of the particle temperature against the mixture fraction at different axial locations in the Sandia flame E from measurements [15], and from the PDF simulations with different mixing models. The axial distance x is shown as x/D, where D is the diameter of the fuel jet. Two laminar flame temperature profiles (dashed lines in Figure 3.1) are also shown for reference. The laminar calculations are conducted by using OPPDIF [39] with two strain rates, a=10s^{-1} and 310s^{-1}, and in the latter case, the temperature profile is shifted down by 300K. Following [8], we use this shifted temperature profiles with a=310s^{-1} as a simple criterion to distinguish between burning particles (above the line) and extinguished particles (below the line). For simplicity, we call this line the "extinction line", and the region above the "burning region", and the region below the "extinction region". There is of course an extinction limit of strain rate a_e ($a_e \approx$376s^{-1} for the current case) and its corresponding temperature profile in steady opposed laminar non-premixed jet flames, but we prefer not to use this extinction limit as our criterion. The extinction limit a_e applies only to steady laminar flames. In the unsteady case (e.g., laminar flames subject to the oscillation of strain rate), however, the instantaneous strain rate can exceed the extinction limit, without the flame being extinguished [40, 41]. Using the extinction limit of the steady laminar flame will somewhat over-estimate the amount of local extinction in this turbulent flame. Hence, as in [8], we use the shifted temperature profiles as a more conservative extinction limit. This criterion is somewhat arbitrary, but it is helpful for the qualitative analysis of the local extinction and re-ignition reported below.

From the experimental scatter plots in Figure 3.1, it may be seen that the number of the particles below the extinction lines decreases with increasing the axial distance from x/D = 7.5 to 45, indicating the evolution from local extinction

to re-ignition. The PDF calculations with the three mixing models qualitatively reproduce this process to some extent. The scatter plots of the Eulerian particle data visually illustrate the level of local extinction at different locations. However, the Lagrangian evolution of the particle properties is not evident. Where do the locally extinguished particles come from? How do they return to the burning region (in composition space)? How do different mixing models cause the particles to move in the composition space? The current Eulerian data cannot answer these questions.

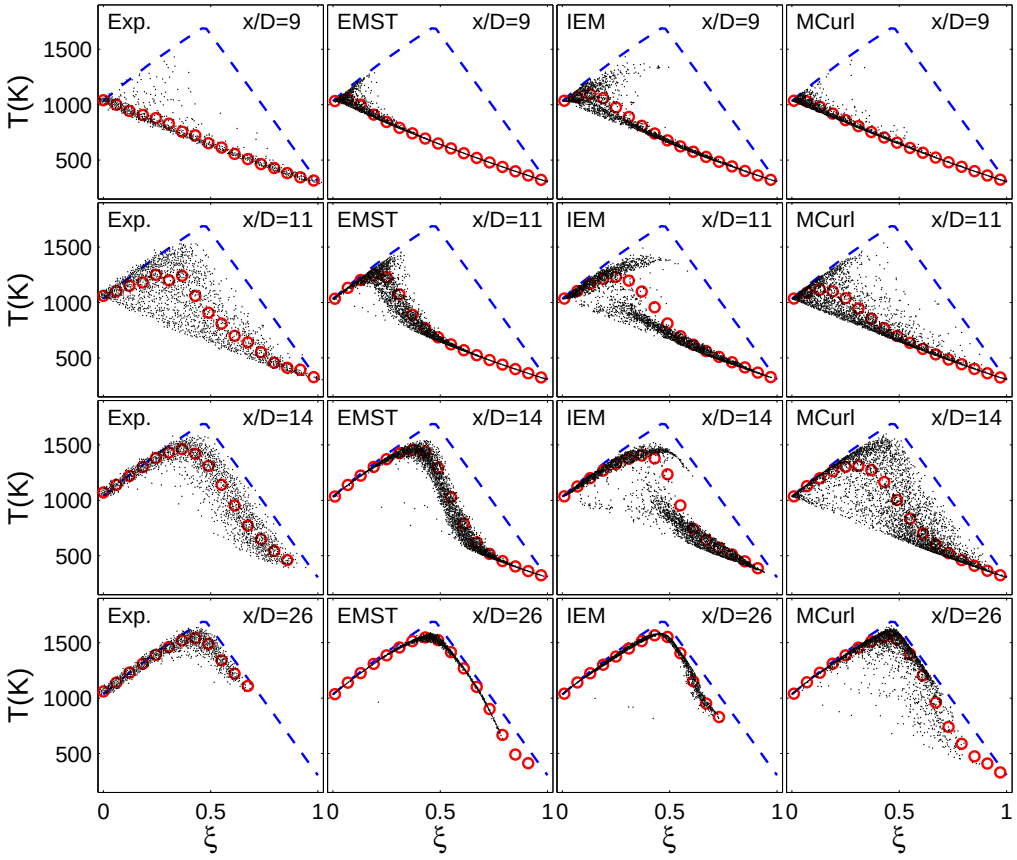

Figure 3.2: Scatter plots of particle temperature against mixture fraction at the axial locations x/D =9, 11, 14, and 26 in the Cabra H_2/N_2 lifted flame from experimental data and from PDF calculations using three different mixing models (Open circles: conditional mean temperature; Dashed lines: equilibrium state.)

We now turn our attention to the Cabra H_2/N_2 lifted jet flame. Figure 3.2

shows the scatter plots of temperature versus mixture fraction at different axial locations in the flame. The equilibrium state calculated by using EQUIL [42] is also shown in the plots for reference. The initial enthalpy h and the species mass fractions $\mathbf{Y}$ for the equilibrium calculation are taken to be linear in the mixture fraction ξ space, i.e.

$$h(\xi) = h_{\text{ox}} - (h_{\text{ox}} - h_{\text{fu}}) \cdot \xi \tag{3.1}$$

$$\mathbf{Y}(\xi) = \mathbf{Y}_{\text{ox}} - (\mathbf{Y}_{\text{ox}} - \mathbf{Y}_{\text{fu}}) \cdot \xi \tag{3.2}$$

where the subscript "fu" and "ox" denote the fuel stream and the oxidizer stream, respectively.

From the experimental data at $x/D = 9$ shown in Figure 3.2, it may be seen that the particles lie dominantly on the mixing line, with just a few rare particles with higher temperature. This combustion stage ($x/D \leqslant 9$) is called pure mixing. For $x/D \geqslant 11$, the particles leave the mixing line gradually, indicating an ignition process. By $x/D = 26$, almost all the particles have reached the fully burnt state, close to the equilibrium line. The PDF calculations using the three mixing models predict the mixing-ignition processes reasonably well. However, the scatter plots of temperature are different for the different mixing models. Similar questions arise, e.g., how do the different mixing models cause the particles to evolve through the mixing stage to the burning state? The Eulerian data cannot answer such questions.

3.3 Lagrangian particle tracking

The limitations of the Eulerian data from PDF calculations are evident. In this section, we discuss the extraction of Lagrangian time series from the PDF calcu-

lations, and these are analyzed for the Sandia flame E and the Cabra lifted flame in the following two sections.

In the Lagrangian PDF method [2], the modeled transport equation for the joint PDF of the velocity $\mathbf{U}$, turbulence frequency ω, and the compositions $\boldsymbol{\phi}$ is solved by a Monte Carlo particle method. A large number of Monte Carlo particles are released into the computational domain according to the Eulerian PDF initially. Each particle carries a full set of the fluid properties, i.e., $\mathbf{U}^*$, ω^*, mass m^*, locations $\mathbf{x}^*$ and $\boldsymbol{\phi}^*$ etc. The evolution of the joint PDF is represented by the movement of the particles in the multi-dimensional space governed by the following stochastic differential equations [1, 2, 3]

$$dx_i^* = U_i^* dt, \tag{3.3}$$

$$dU_i^* = -\frac{1}{\langle\rho\rangle}\frac{\partial\langle p\rangle}{\partial x_i}dt - \left(\frac{1}{2}+\frac{3}{4}C_0\right)\Omega\left(U_i^* - \widetilde{U}_i\right)dt + \left(C_0\widetilde{k}\Omega\right)^{1/2} dW_i, \tag{3.4}$$

$$d\omega^* = -C_{\omega 3}\Omega\left(\omega^* - \widetilde{\omega}\right)dt - S_\omega\Omega\omega^* dt + \left(2C_{\omega 3}C_{\omega 4}\tilde{\omega}\Omega\omega^*\right)^{1/2} dW, \tag{3.5}$$

$$\frac{d\phi_\alpha^*}{dt} = \mathcal{M}_\alpha(t) + S_\alpha\left(\phi^*(t)\right), \tag{3.6}$$

where ρ and p are the fluid density and pressure, respectively; "$\langle\ \rangle$" denotes the conventional mean; "$\widetilde{\ }$" denotes the Favre mean; C_0, $C_{\omega 3}$ and $C_{\omega 4}$ are model constants; $\mathbf{W}$ is an isotropic vector-valued Wiener process; W is another independent Wiener process; $\widetilde{k}$ is the turbulent kinetic energy; S_ω and S_α are the source term for ω and the reaction source term for ϕ_α, respectively; $\mathcal{M}_\alpha(t)$ denotes the mixing model; Ω is the conditional mean turbulence frequency defined as

$$\Omega \equiv C_\Omega \frac{\langle\rho^*\omega^*|\omega^* \geqslant \widetilde{\omega}\rangle}{\langle\rho\rangle}, \tag{3.7}$$

where the constant C_Ω is chosen so that Ω equals $\widetilde{\omega}$ in a fully turbulent region [17].

The correspondence between the statistics of the Monte Carlo particles and those of the underlying turbulent reactive flow needs careful consideration [1, 3]. A primary aim of the modeling is for the one-point, one-time joint PDF of the particles to accurately represent the same joint PDF of the fluid in the reactive flow. On the other hand, two-point, one-time statistics are radically different: in the particle system the properties at two points are statistically independent (in the infinite particle limit), and indeed two particles may have the same location $\mathbf{x}^*$ but completely different properties. Of particular relevance in the present study, is the question of correspondence of Lagrangian statistics. The Langevin equation model for velocity (Equation 3.4) has been constructed to be consistent with the Lagrangian velocity autocorrelation. However, the mixing models have been developed based solely on one-time Eulerian statistics, and the extent to which they represent Lagrangian statistics has not been evaluated even in simple non-reactive flows.

The solution procedure for the above equations is implemented in the code HYB2D which implements the consistent FV/particle algorithm [34]. The HYB2D code has been fully tested and validated in various papers, e.g. [23, 31, 34, 35]. This work slightly extends the HYB2D code to output the Lagrangian data.

A non-uniform mesh is used for both the FV solver and the particle tracking. The quantities at the mesh level are interpolated onto particles as needed. The statistics of particle properties on the mesh are formed from particles associated with the cell. The mixing between particles is performed within each grid cell.

The flames we are interested in are statistically stationary. The solution procedure implemented in HYB2D is a pseudo-time marching procedure. (A local

time-stepping algorithm [43] is used for the marching procedure.) Starting from a "reasonable" initial condition, we march in time steps until a statistically stationary state is achieved. We continue the calculation for further time steps in order to output quantities of interest. At any time after the statistically stationary state is reached, the joint PDF is represented by a set of particles which (to some extent) model fluid particles.

Conventionally, in the PDF calculations only Eulerian data are output for postprocessing, i.e., the data at a particular time step after the statistically stationary state has been reached. Due to the Lagrangian nature of the numerical method, it is a simple matter to explore the Lagrangian data by simply exporting the particle data for many time steps after the stationary state has been reached, so that the Lagrangian particle trajectories can be formed.

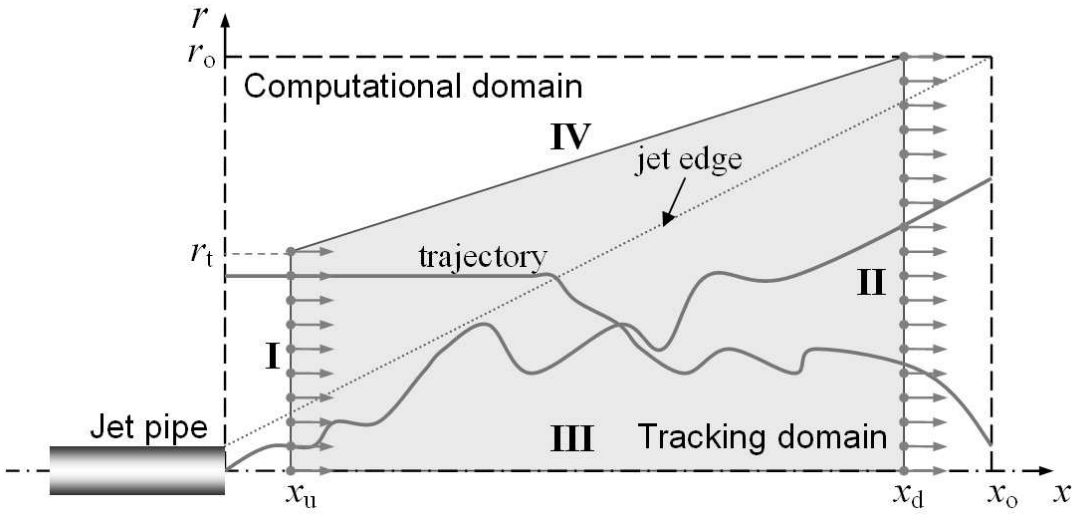

Figure 3.3: The computational domain and the tracking domain (consisting of four sides: **I**, **II**, **III**, and **IV**) for the jet flames.

Once the statistically stationary state is reached, we track a representative number N_t of particles through the active part of the flame defined as the tracking domain as shown in Figure 3.3. The geometry of the computational domain

Table 3.2: Geometry of the computational domain and the tracking domain, and the number of tracked particles N_t for the Sandia flame E and the Cabra lifted H_2/N_2 jet flame. See Figure 3.3 for definition of locations.

	x_u/D	x_d/D	x_o/D	r_t/D	r_o/D	N_t
Sandia flame E	3.0	45	80	10	20	2000
Cabra lifted flame	3.0	30	50	10	15	2000

and the tracking domain, and the values of N_t are shown in Table 3.2 for the Sandia flame E and the Cabra lifted H_2/N_2 jet flame.

In the particle method, there is a particle cloning and clustering algorithm designed to maintain an approximately uniform number of particles per cell. This algorithm creates some complications for particle tracking. When a tracked particle is cloned, it splits into two or more (initially) identical particles of less weight. We arbitrarily select just one of the clones to continue the particle trajectory. When several light particles are clustered to form one heavier particle, the initial identities are lost. To prevent this problem, we suppress clustering of tracked particles (at a small cost in computational accuracy and efficiency).

Examination of the particle trajectories in physical space revealed some problems with the velocity-frequency model and its numerical implementation. These are discussed in the Appendix A where a method of alleviating the problem is described.

3.4 Particle trajectories in Sandia flame E

PDF calculations of the Sandia flame E are performed by using the three mixing models, EMST, IEM and modified Curl. The Lagrangian tracking of particles is

conducted to investigate the roles of reaction and mixing in the regions of local extinction and re-ignition. We focus on the particle behavior based on the evolution of the particle temperature in the mixture fraction space. As in the scatter plots of particles in Figures 3.1 and 3.2, and similar to the DNS analysis in [8], we divide the particle trajectories into two groups: continuous burning and local extinction. For continuous burning, the whole particle trajectory remains within the burning region (i.e., above the "extinction line"). For local extinction, some segment of the particle trajectory lies in the extinction region (below the "extinction line"). Physically, continuous burning corresponds to a stretched and distorted yet still continuous non-premixed laminar flame front, and the local extinction produces holes in the flame front [44, 45]. It should be appreciated, however, that in PDF methods there is no representation of the instantaneous flame structure. For ease of analysis, in each group, we further sub-divide the particles into different categories based upon their mixture fraction at the trajectory's initial position x_{u} (see Figure 3.3 and Table 3.2 for details), i.e., fuel region ($\xi < 0.1$), oxidizer region ($\xi > 0.9$), pilot stream region ($0.22 < \xi < 0.55$), and the intermediate region (all other values of ξ).

In the flames considered here, the particle axial distance $x^*(t)$ is an increasing function of time t. To some extent, the axial distance can be viewed as a time-like variable since the particles do not flow backwards in the axial direction. Since we are more interested in local extinction and re-ignition at different axial locations, it is more revealing to explore the particle time series with respect to the axial distance x/D rather than with respect to time.

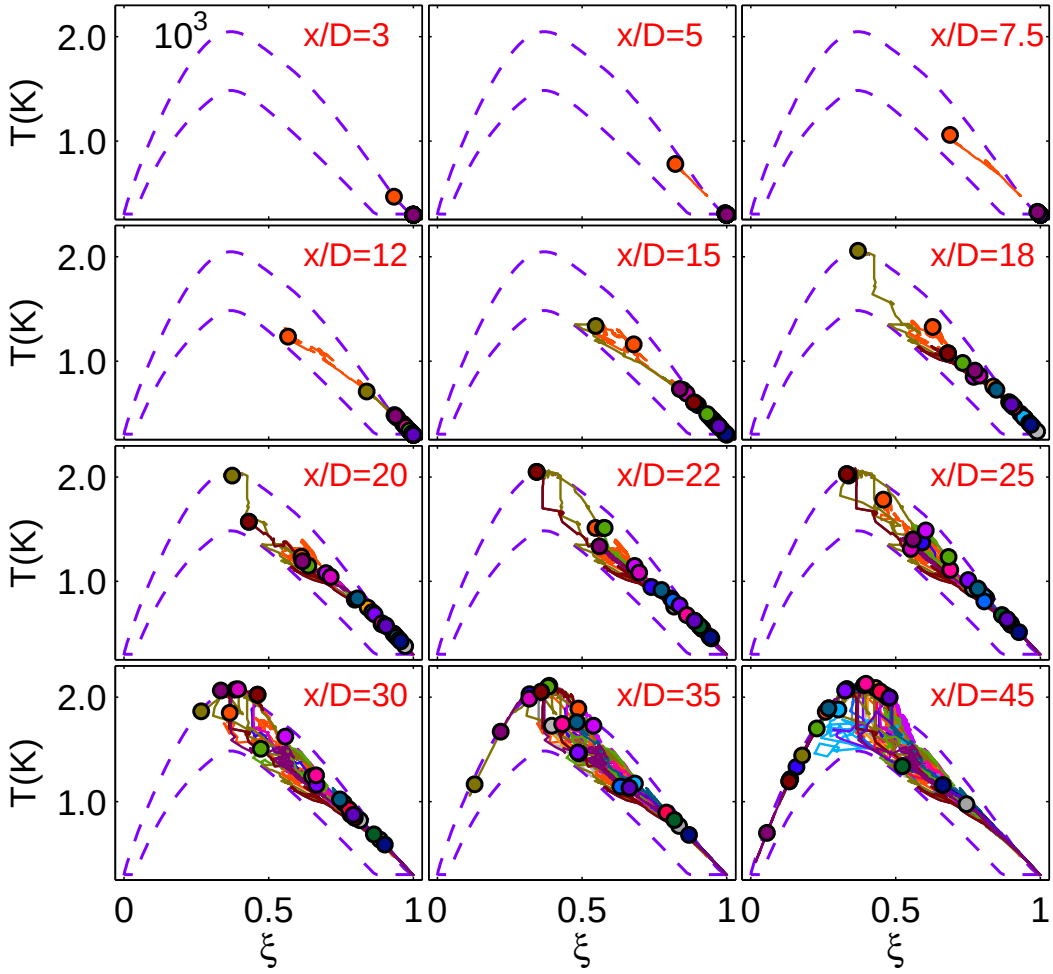

Figure 3.4: The continuous burning particle trajectories from the fuel region in flame E by the EMST model. (An animation of these particle trajectories is available at http://www.informaworld.com/mpp/uploads/fig04_pilot_emst_cb_fuel.mpg.)

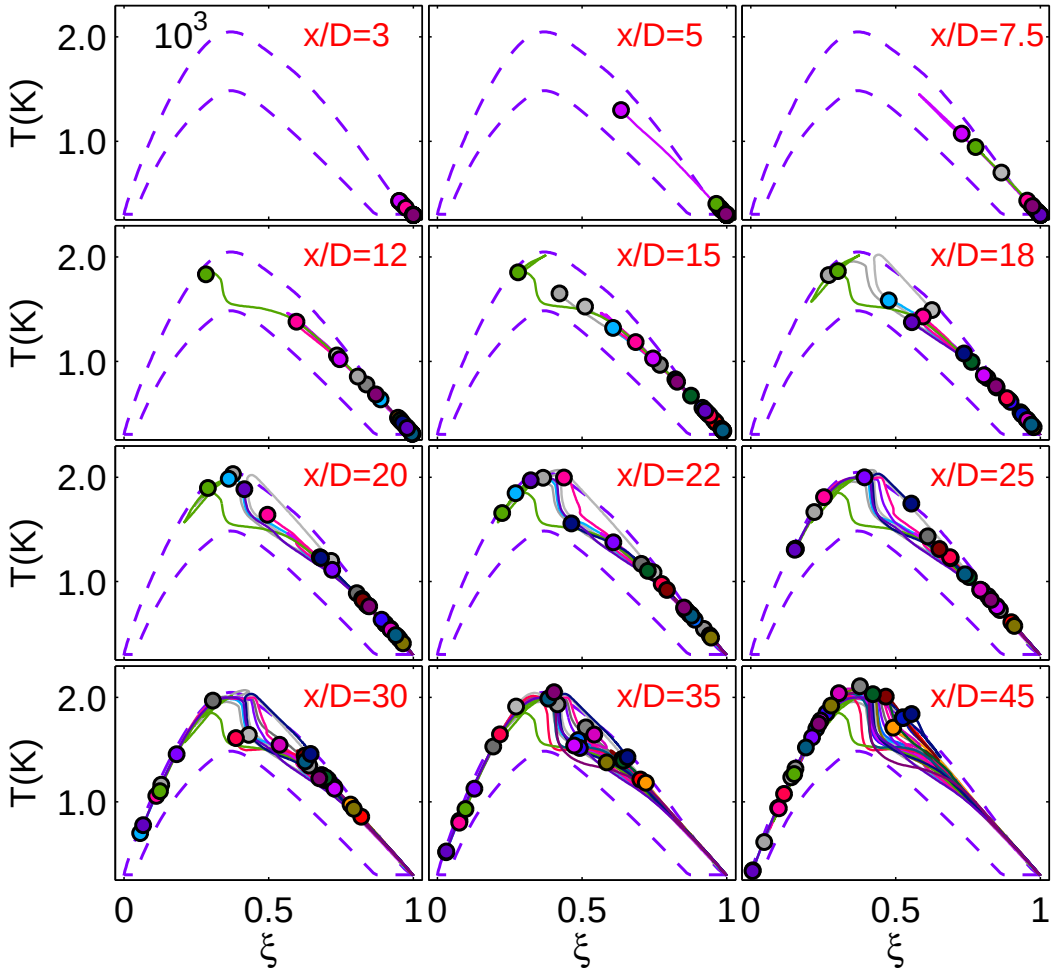

Figure 3.5: The continuous burning particle trajectories from the fuel region in flame E by the IEM model. (An animation of these particle trajectories is available at http://www.informaworld.com/mpp/uploads/fig05_pilot_iem_cb_fuel.mpg.)

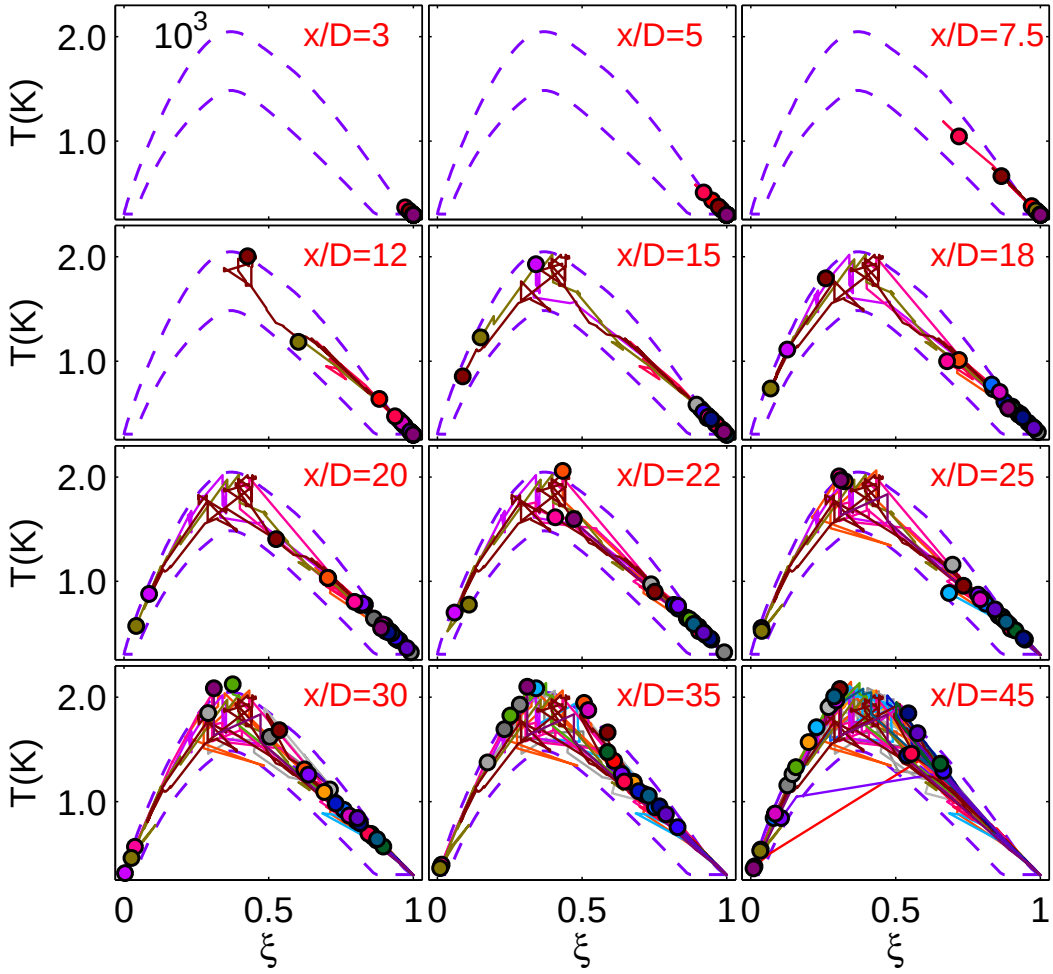

Figure 3.6: The continuous burning particle trajectories from the fuel region in flame E by the modified Curl model. (An animation of these particle trajectories is available at http://www.informaworld.com/mpp/uploads/tctm-2007-04-19-file004.mpg.)

3.4.1 Trajectories of continuously burning particles

The trajectories of continuously burning particles from the fuel region in flame E are shown in Figures 3.4-3.6 for PDF calculations using the different mixing models. Only 25 particles randomly chosen from the tracking dataset are shown for each category. The circles in the plots show the current compositions of particles, and the lines connect their past compositions. For each figure of particle trajectories (such as Figures 3.4-3.6), the supplementary material includes a corresponding animation. These animations show the evolution with axial distance of all tracked particles' compositions. In the temperature-mixture fraction 2-D plane in Figures 3.4-3.6, chemistry can only change the particle positions vertically due to element conservation during reaction (conservation of mixture fraction ξ), while mixing can move the particles both vertically and horizontally.

The general observations on the trajectories of the continuously burning particles calculated using the different mixing models are the following. First, the mixture fraction of particles can vary in the whole mixture fraction range, e.g., initially ξ^* is greater than 0.9 for all particles, while later ξ^* is less than 0.1 for some particles in Figures 3.4-3.6. As discussed before, this change is solely caused by mixing, indicating the important role of mixing in turbulent combustion. Second, different particles have completely different trajectories as expected in a turbulent flow. Third, at different stages of the particle evolution, the roles of reaction and mixing are different. In Figures 3.4-3.6, the particles from the fuel region tend to come close to the extinction line when first approaching the stoichiometric condition (ξ = 0.351).

At around the stoichiometric condition in Figures 3.4-3.6, we can observe that some particles suddenly shoot upward (e.g., at x/D=18, some particle tra-

jectories become nearly vertical). Apparently, in this stage, the reaction time scale is much less than the mixing time scale, and reaction becomes dominant. A quantitative presentation of the relative roles of mixing and reaction is discussed in Section 3.6

The particle behavior simulated by the different mixing models is qualitatively different. The particle trajectories produced by the EMST model are continuous but non-differentiable [21]. These trajectories are not smooth in Figure 3.4. The trajectories by the IEM model are continuous and differentiable, and the simulated trajectories are smooth and are clear in Figure 3.5. It is easy to follow each particle from the plot, making the observation and analysis much easier. The trajectories arising from the modified Curl model are discontinuous. The particles jump in composition space, possibly resulting in the direct mixing of a cold fuel particle and a cold oxidizer particle. This can be observed at $x/D = 45$ in Figure 3.6. Two particles with very lean and very rich mixtures are connected, indicating the jumping of the particle from the one side to the other side instantaneously. (For continuously burning particles, by definition, their compositions at no time lie in the extinction region, which means the straight lines across the extinction region at $x/D = 45$ in Figure 3.6 correspond to an instantaneous jump in particle composition.) This jump behavior by the modified Curl makes the particle trajectories difficult to follow.

Similar observations can be made from the trajectories of continuously burning particles from other categories (oxidizer region, pilot stream region and the intermediate region). Due to space limitations, these trajectories are not shown here.

3.4.2 Trajectories of locally extinguished particles

3.4.2.1 Particle trajectories from the EMST model

The locally extinguished particle trajectories originating from different regions in calculations using the EMST mixing model are shown in Figures 3.7-3.9.

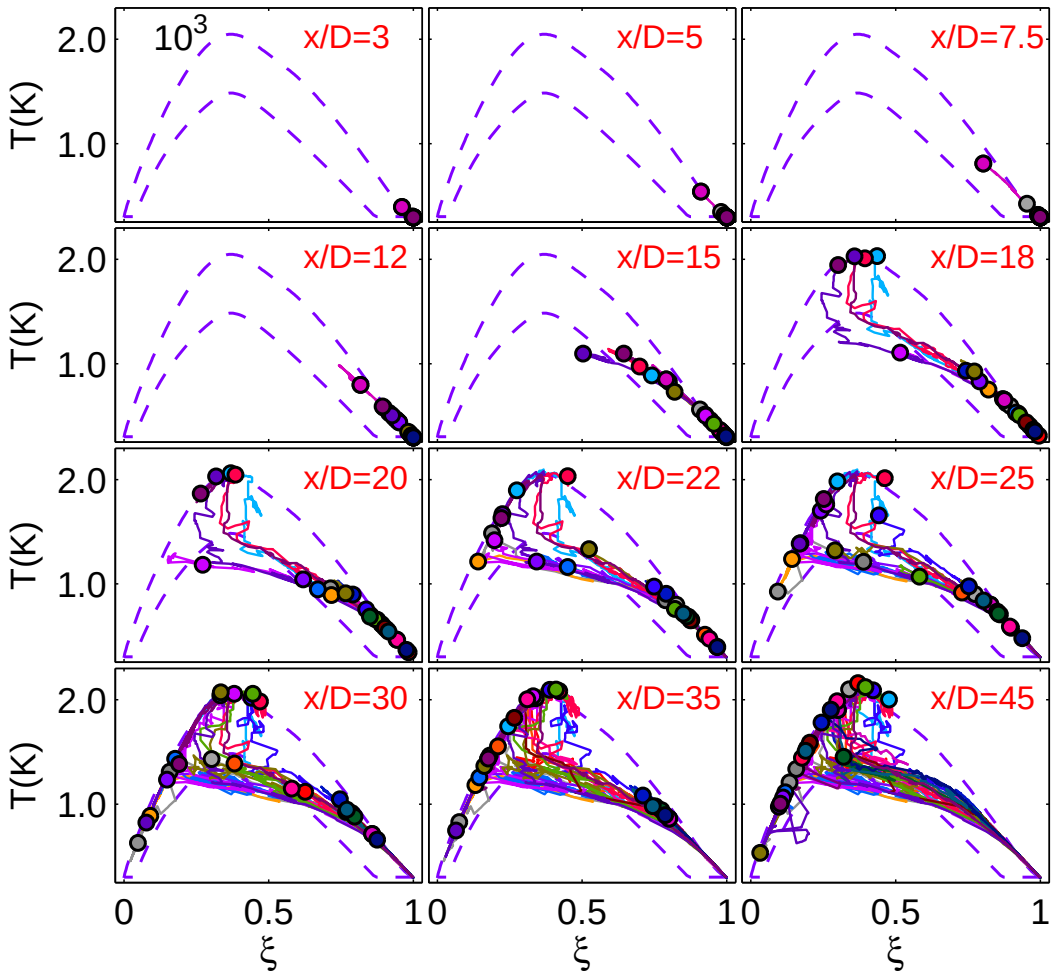

Figure 3.7: Trajectories of locally extinguished particles from the fuel region in flame E by the EMST model. (An animation of these particle trajectories is available at http://www.informaworld.com/mpp/uploads/tctm-2007-04-19-file005.mpg.)

Figure 3.7 shows the trajectories of particles initially from the fuel region. In

the temperature-mixture fraction space, the mixture fraction of particles first decreases, and the particles come close to the extinction line. Around $\xi = 0.6$, the particles enter the extinction region, and become locally extinguished according to our criterion for extinction. The particle trajectories inside the extinction region become nearly horizontal (little temperature rise), implying that mixing is at least as rapid as reaction. The return of the particles to the burning region corresponds to re-ignition. From Figure 3.7, two different re-ignition processes can be observed. First, at around the stoichiometric condition, some trajectories of extinguished particles turn and move upward to return to the burning state, e.g., at $x/D = 18$ in Figure 3.7 we can observe four trajectories of extinguished particles moving dominantly upward to return to the burning state. During this re-ignition process, the mixture fraction of the particles changes slightly while the temperature rises by more than 600 K. Although re-ignition is the result of mixing and reaction, reaction seems dominant in this re-ignition process, which is similar to auto-ignition. The local extinction induced by the mixing causes the coexistence of fuel and oxidizer in the same particle, and the temperature of these particles is greater than 1000 K, e.g., one particle in the extinction region at $x/D = 15$ in Figure 3.7. Given appropriate conditions (e.g., induction period and a relatively long mixing time scale), the auto-ignition brings the particles back to the burning state. We refer to this re-ignition mechanism as an auto-ignition mechanism. Second, instead of auto-ignition, the other extinguished particles keep moving in the same direction (nearly horizontally to the left) and re-enter the burning state on the lean side of stoichiometric, e.g., from $x/D = 20$ to 45. During this process, mixing is at least as rapid as reaction. We call this mechanism the mixing-reaction mechanism. It is worth mentioning that the above two re-ignition mechanisms are identified in the DNS study [11]. The particles

from the oxidizer region (not shown) behave similarly to the particles from the fuel region. The two different re-ignition processes are also observed there.

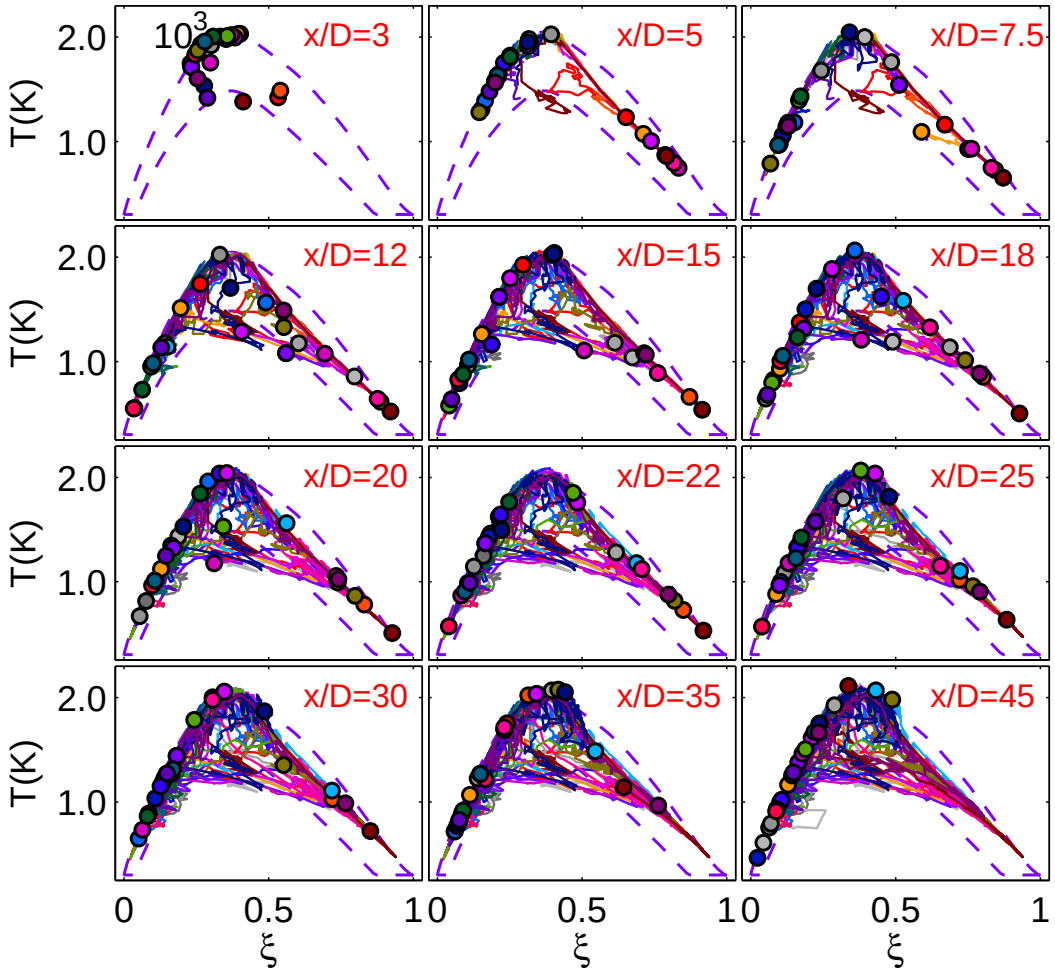

Figure 3.8: Trajectories of locally extinguished particles from the pilot stream region in flame E by the EMST model. (An animation of these particle trajectories is available at http://www.informaworld.com/mpp/uploads/tctm-2007-04-19-file006.mpg.)

Figure 3.8 shows the trajectories of the particles from the pilot stream region in flame E when using the EMST model. The pilot stream is used to stabilize the flame. From Figure 3.8, for this subset of particles (all of which enter the extinction region at some time), they dominantly enter the extinction region from the lean and rich sides, after there has been mixing essentially along the

fully burnt line. Only one or two particles enter the extinction region from above around stoichiometric.

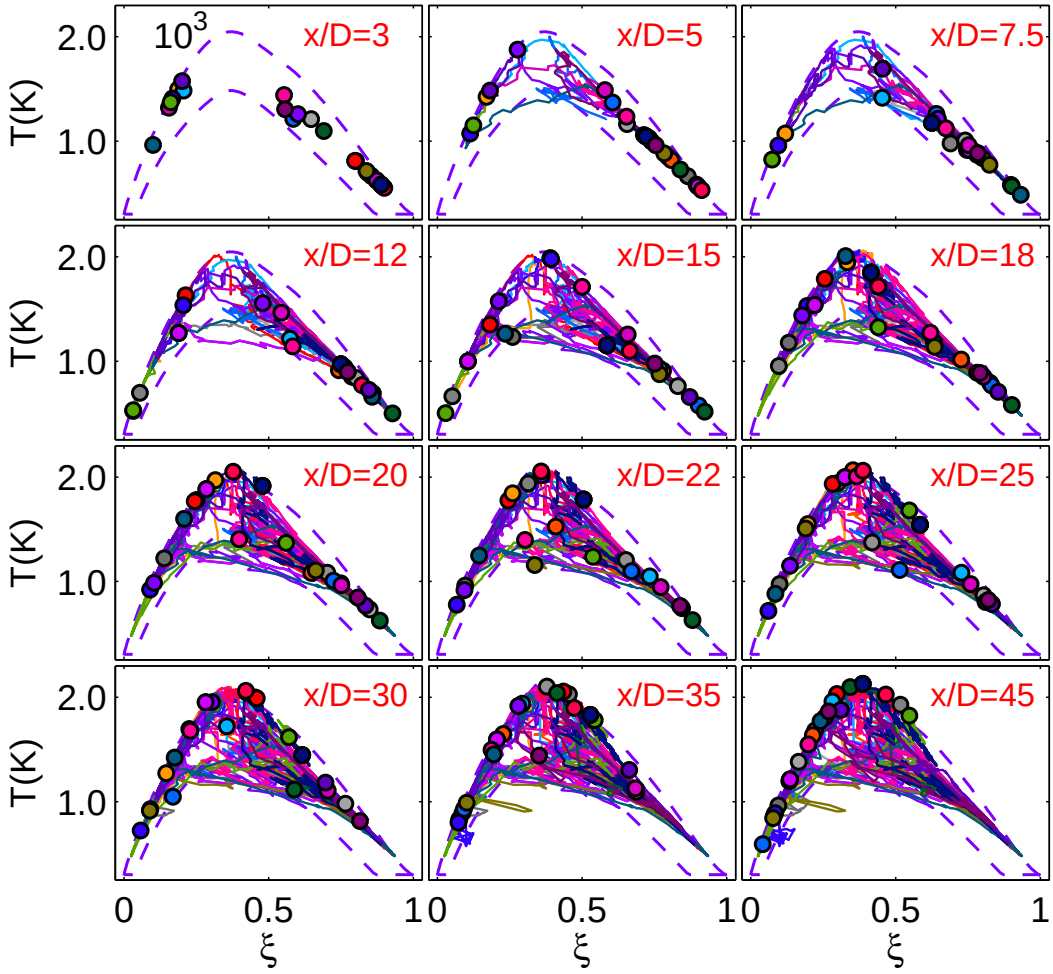

Figure 3.9: Trajectories of locally extinguished particles from the intermediate region in flame E by the EMST model. (An animation of these particle trajectories is available at http://www.informaworld.com/mpp/uploads/tctm-2007-04-19-file007.mpg.)

In Figure 3.9 are shown the trajectories of the particles from the intermediate region in flame E using the EMST model. Initially ($x/D \leqslant 7.5$) the particle composition changes due to mixing and reaction and remains, predominantly, in the burning region. The local extinction observable for $12 \leqslant x/D \leqslant 25$ occurs dominantly by mixing drawing rich and lean particles nearly horizontally into

the extinction region.

In summary, the local extinction and re-ignition processes in the Sandia flame E are illustrated by tracking particles using the EMST model. Two different re-ignition mechanisms are observed in the flame by using the EMST model, i.e. auto-ignition and mixing-reaction. The investigation of the mixing models in conjunction with the large eddy simulations using the DNS data by Mitarai et al. [10] demonstrates the very good performance of the EMST mixing model in predicting the particle behavior in the regions of local extinction and re-ignition. The above observed particle behavior by the EMST is expected to represent the actual situation qualitatively.

3.4.2.2 Particle trajectories using the IEM and modified Curl models

The trajectories of the particles from the fuel region in flame E using the IEM model are shown in Figure 3.10. Following each particle trajectory, we can observe the similar local extinction and re-ignition processes as in the case of the EMST model (shown in Figure 3.7). The two re-ignition mechanisms can also be identified: auto-ignition and mixing-reaction. The re-ignition process for the IEM model, however, is somewhat different from that for the EMST model in Figure 3.7. In Figure 3.7, the re-igniting particles for the EMST model tend to move almost horizontally first with a slight temperature rise, and then either move upward due to the auto-ignition mechanism or keep moving horizontally due to the mixing-reaction mechanism without an obvious temperature drop before entering the burning region. In Figure 3.10, however, some of the re-igniting particles induced by the auto-ignition mechanism experience a temperature drop before ignition. Almost all the re-igniting particles induced by

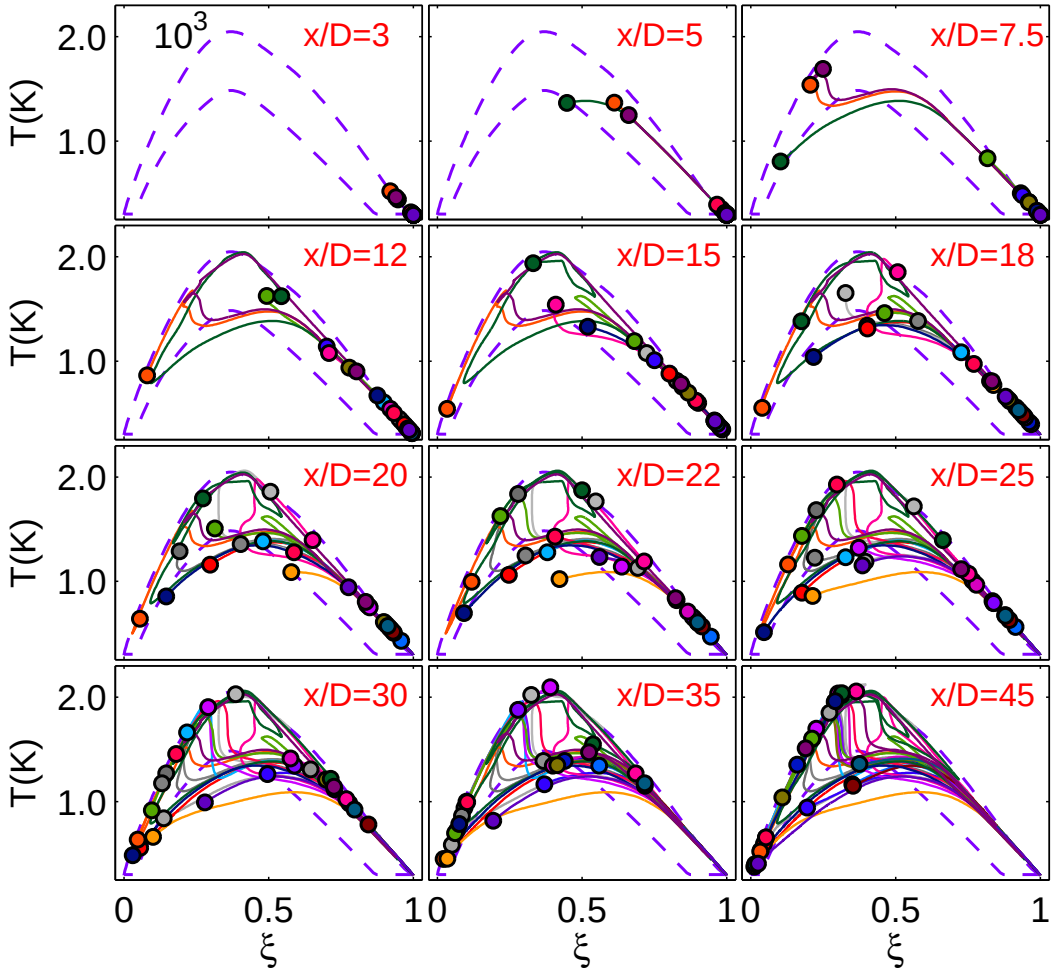

Figure 3.10: Trajectories of locally extinguished particles from the fuel region in flame E using the IEM model. (An animation of these particle trajectories is available at http://www.informaworld.com/mpp/uploads/tctm-2007-04-19-file008.mpg.)

the mixing-reaction mechanism tend to decrease their temperature significantly before entering the burning region. For the IEM model at the early stages of re-ignition, this behavior is explained by the fact that the mean temperature (to which the particle temperature relaxes) is lower than that of the particles, which are about to re-ignite, since these are the hottest particles in the ensemble. To some extent this reflects the physics of the problem in that conduction cools fluid at a local temperature maximum. The trajectories of the particles from the other regions in flame E using the IEM model (not shown) show similar behavior to those from the fuel region in Figure 3.10.

Figure 3.11 shows the particle trajectories from the fuel region using the modified Curl model. The jumps in the particle properties make the understanding of particle behavior more difficult. The particle evolution is generally quite similar to the IEM model. Local extinction and re-ignition are predicted, and the two re-ignition mechanisms can be observed. However, similar to the IEM model, the re-igniting particles tend to have some temperature drop before or during the re-ignition, which is not observed in the EMST results. The trajectories of the particles from the other regions in flame E using the modified Curl model (not shown) show similar behavior to those from the fuel region in Figure 3.11.

In this sub-section, the local extinction and re-ignition processes in the Sandia flame E are illustrated by tracking particles using the IEM and modified Curl models. The two re-ignition mechanisms (auto-ignition and mixing-reaction) identified by using the EMST model in Figure 3.7 are also observed here by using these two mixing models. However, the re-igniting particles by these two mixing models have somewhat different behavior from those by the EMST

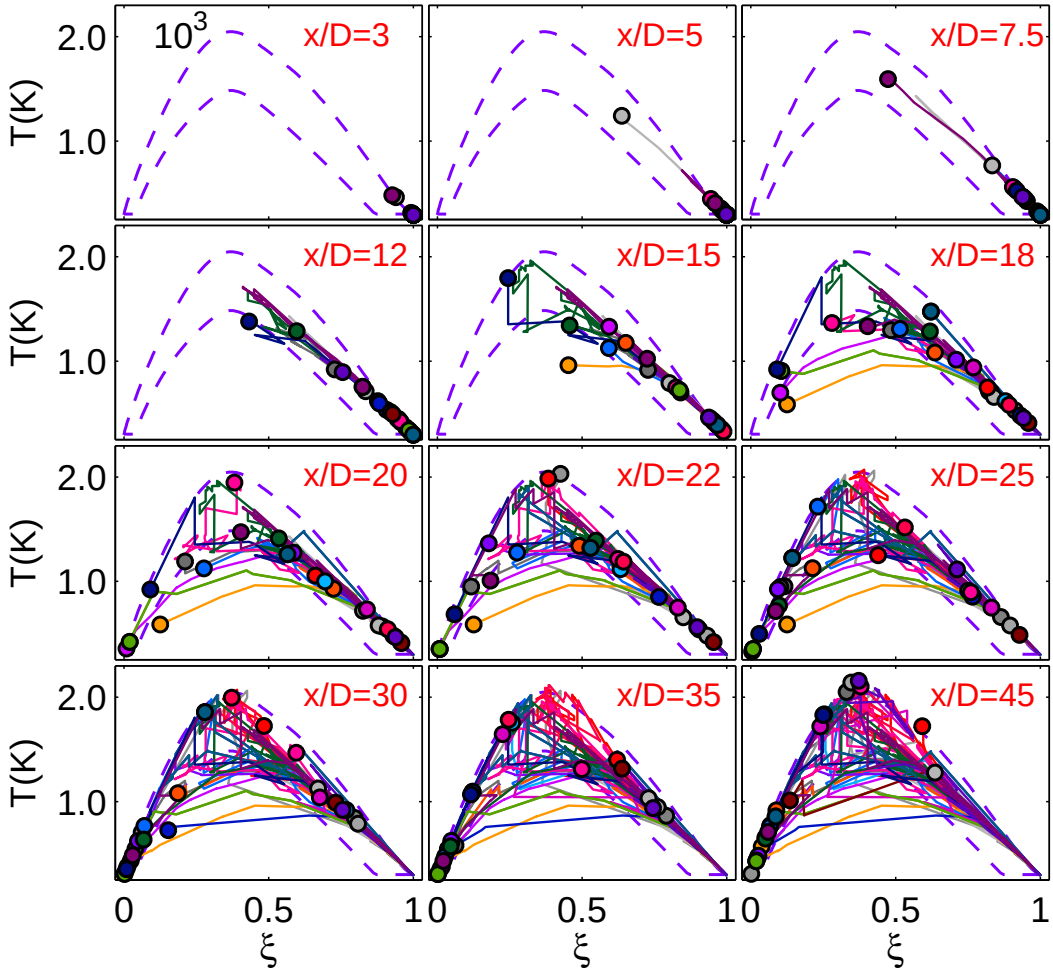

Figure 3.11: Trajectories of locally extinguished particles from the fuel region in flame E using the modified Curl model. (An animation of these particle trajectories is available at http://www.informaworld.com/mpp/uploads/tctm-2007-04-19-file009.mpg.)

model, i.e., a temperature drop before or during the re-ignition. This difference in re-ignition by the different mixing models is not clear yet because there is no experimental data on Lagrangian trajectories in the flame. Nevertheless, the two identified re-ignition mechanisms and the different particle behavior during the re-ignition by the different mixing models cannot be observed with the Eulerian particle data, and the observations contribute to our understanding of the performance of the models.

3.5 Particle trajectories in Cabra H_2/N_2 lifted flame

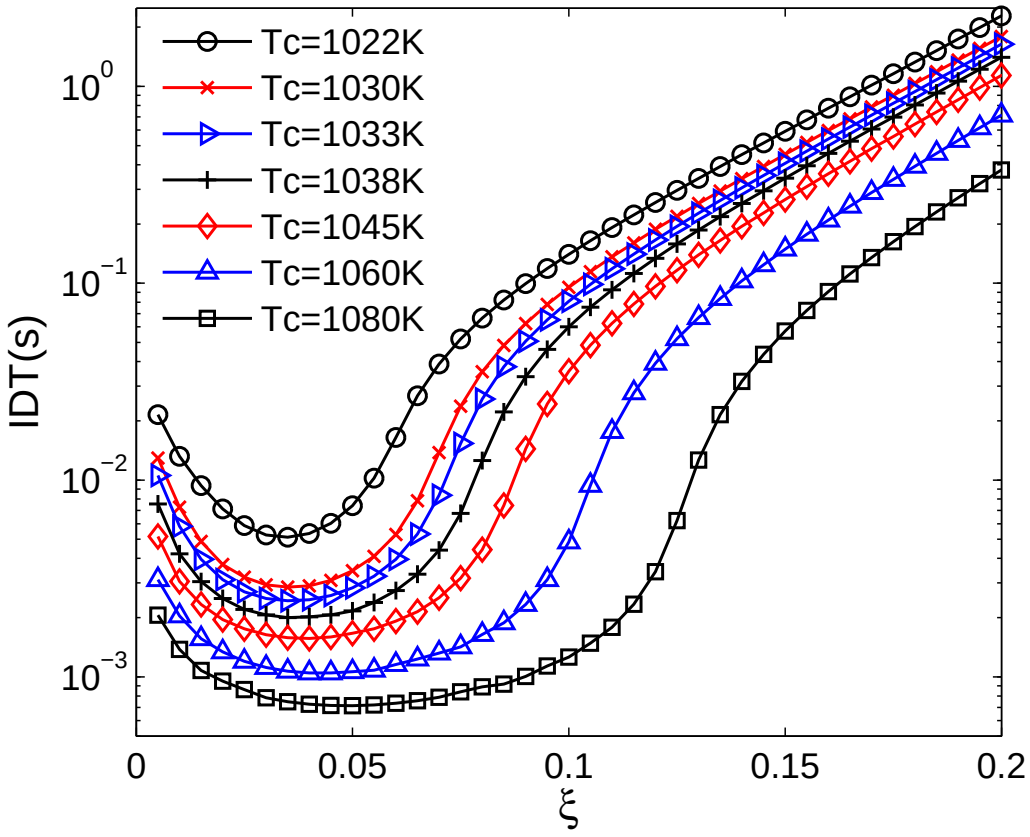

Figure 3.12: The ignition delay time (IDT) of $H_2/N_2/O_2$ mixture for different coflow temperature T_c.

Previous studies [31, 32] suggest that auto-ignition is a dominant mechanism in the stabilization of the Cabra H_2/N_2 lifted flame. In addition, both experimentally [33] and in modeling studies [31], it is found that the flames are extremely sensitive to the temperature of the vitiated coflow. To further understand and characterize these processes, we first perform auto-ignition tests in which the ignition delay time (IDT) is calculated as a function of mixture fraction and coflow temperature. The initial condition of the tests satisfies Equations (3.1)-(3.2). The fuel stream and the oxidizer stream in the tests are the same as those in the Cabra lifted flame. The coflow (oxidizer) temperature varies from T_c =1022 K to 1080K. Figure 3.12 shows the IDTs of the mixture for different coflow temperatures. The IDT is defined here as the time when the mixture temperature reaches the mid-point between the initial temperature and the equilibrium temperature. The strong sensitivity of the IDTs to the coflow temperature is evident from the plot, which is consistent with the findings in [31]. The shortest IDTs occur at the very fuel-lean region, around ξ =0.04. The stoichiometric condition is ξ =0.47 in the flame. The IDTs varies by three orders of magnitude over the range of mixture fraction shown.

The PDF calculations of the Cabra H_2/N_2 lifted flame are performed by using the three mixing models, EMST, IEM and modified Curl. The Lagrangian tracking of particles is conducted to investigate the roles of reaction and mixing in the flame. The tracking details are shown in Table 3.2. As in the analysis of flame E in Section 3.4, we focus on the particle behavior based on the evolution of the particle temperature in mixture fraction space. The particle trajectories are divided into different categories based upon their mixture fraction at the trajectory initial position x_u, i.e., fuel region ($\xi < 0.1$), oxidizer region ($\xi > 0.9$), and the intermediate region between the fuel and the oxidizer region. For each cate-

gory, 100 particles randomly chosen from the tracking dataset are shown in the following figures, whereas all tracked particles are shown in the corresponding animations in the supplementary material.

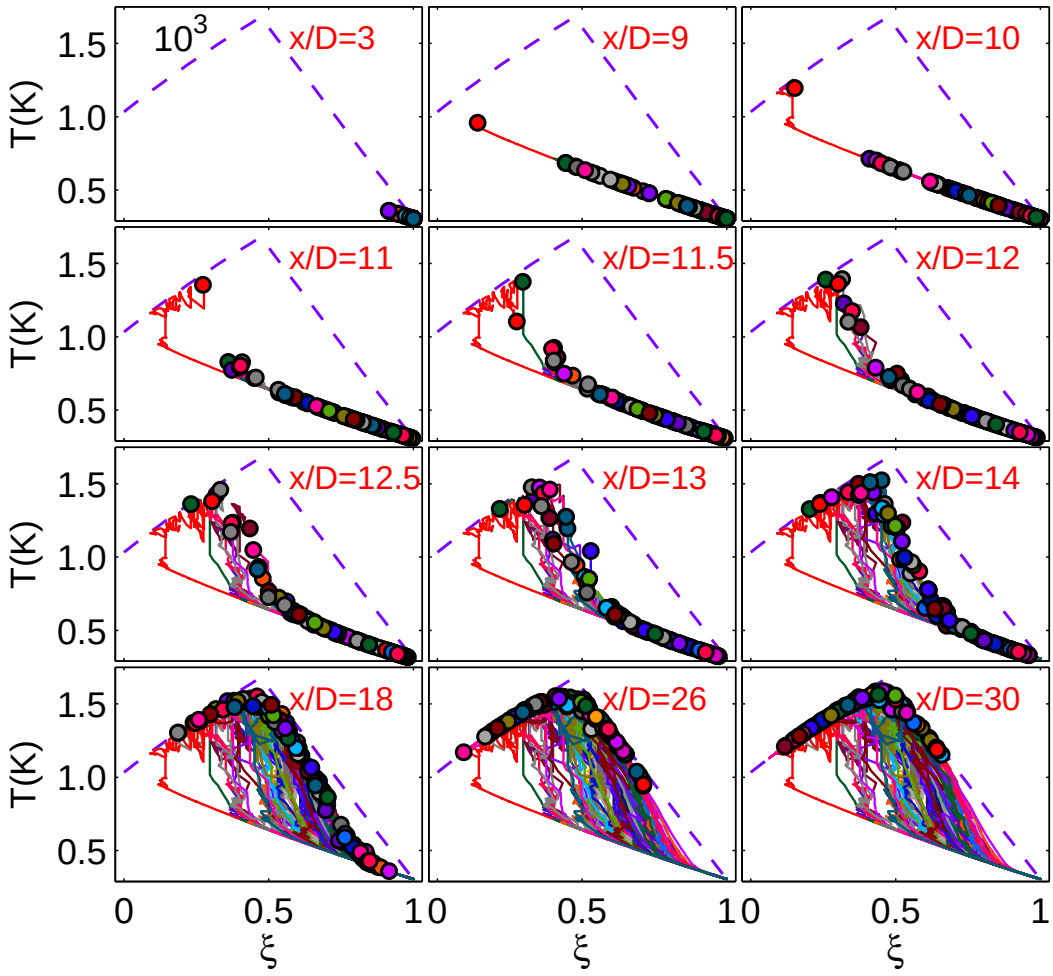

Figure 3.13: Particle trajectories from the fuel region in the Cabra lifted flame using the EMST model. (An animation of these particle trajectories is available at http://www.informaworld.com/mpp/uploads/tctm-2007-04-19-file010.mpg.)

Figure 3.13 shows the trajectories of the particles from the fuel region in the Cabra lifted flame using the EMST model. Initially, ($x/D \leqslant 9$) the particles move in the plane exclusively by mixing. A particle trajectory due to pure mixing is a nearly straight line between the cold fuel temperature and the hot coflow temperature. Pure mixing yields a partially premixed mixture of fuel and oxidizer

at different mixture fractions. At about $x/D = 10$, some particles near the oxidizer side start to ignite first due to their short IDTs as shown in Figure 3.12. The ignition mechanism of the first few particles is expected to be auto-ignition, similar to the auto-ignition of the homogeneous mixture in Figure 3.12.

After the rapid auto-ignition of the first few particles, these relatively hot burnt particles at $x/D > 11$ in Figure 3.13 mix with adjacent particles in composition space, thus raising their temperature (and radical concentration) and hence promoting their auto-ignition. Therefore the ignition progressively moves to richer mixtures. This burning process is not exclusively the auto-ignition of the particles. Both reaction and mixing play important roles. A plausible physical picture of the processes involved in the Cabra flame is that some regions under the fuel-lean condition ignite first after the induction period given an appropriate mixing condition. These ignition spots are distributed in the physical space separately. After the high temperature ignition spots are formed, they propagate toward each other and merge into a connected premixed flame front. This picture is supported by the DNS study of the auto-ignition of mixing layers between cold fuel and hot oxidizer in an isotropic and homogeneous turbulence flow [46]. The evolution of the particles using EMST in Figure 3.13 is consistent with this picture, even though the spatial structure of the instantaneous flame is not explicitly represented. We simply name this ignition process as mixing-ignition. By $x/D = 30$ in Figure 3.13, all the particles shown reach the full burnt state close to the equilibrium line. From the particle trajectories in the Cabra lifted jet flame using the EMST model, we can observe the whole mixing-reaction process. Four stages of combustion can be identified, i.e. pure mixing, auto-ignition, mixing-ignition, and fully burnt. Apparently, this combustion detail cannot be observed from the Eulerian data like the scatter plot in Figure 3.2.

The particles from the other regions in the Cabra lifted flame by using EMST model (not shown) show the similar ignition dynamics.

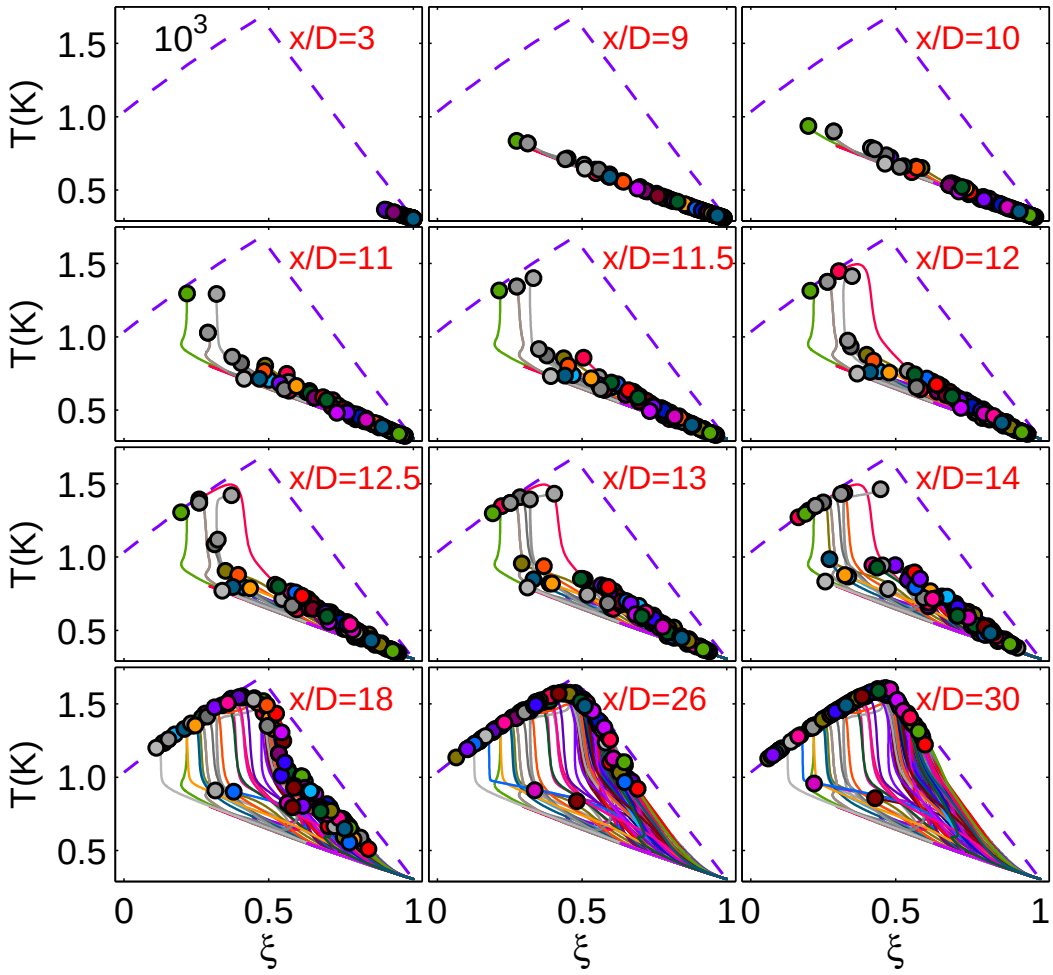

Figure 3.14: Particle trajectories from the fuel region in the Cabra lifted flame using the IEM model. (An animation of these particle trajectories is available at http://www.informaworld.com/mpp/uploads/tctm-2007-04-19-file011.mpg.)

In Figure 3.14 are shown the trajectories of the particles from the fuel region in the Cabra lifted flame using the IEM model. Pure mixing occurs for $x/D < 10$. At the locations between $x/D = 10$ and 11, a few particles near the oxidizer side (brought there by mixing) start to auto-ignite. After the auto-ignition of the first few particles, the temperature of other particles in the rich region is raised through their mixing with the elevated mean, and the ignition of these particles

is promoted. Mixing and reaction play important roles in this ignition process. As in the EMST model, this ignition process can be named as mixing-ignition. The particle behavior in this ignition process for the IEM model is slightly different from that for the EMST model in Figure 3.13. The EMST model is local in composition space. Hence the burnt particles at given ξ^* mix with particles around the same value of ξ^*. While in the IEM model all particles mix towards the mean. In spite of the different particle behavior, four stages of combustion can be identified for the IEM as those in the EMST model. The trajectories of the particles from the other regions (not shown) show similar particle behavior for IEM model as in Figure 3.14.

In Figure 3.15 are shown the particle trajectories from the fuel region in the Cabra lifted flame using the modified Curl model. The modified Curl model can reproduce the same four combustion stages in the flame identified by the previous two mixing models. As in the IEM model, the particle behavior in the mixing-ignition stage by the modified Curl model is also different from that by the EMST model due to the non-localness of the model in the composition space. The particle trajectories from the other regions in the Cabra lifted flame using the modified Curl model (not shown) show the same behavior.

In this section, the particle trajectories using the different mixing models are investigated in the Cabra H_2/N_2 lifted flame. The particle behavior by the IEM and modified Curl models is different from that by the EMST model, because of the non-localness of the IEM and modified Curl models compared to the localness property of the EMST model. In spite of the different individual particle behavior, the overall combustion processes revealed by the different mixing models are similar, and four stages of combustion in the flame can be identified,

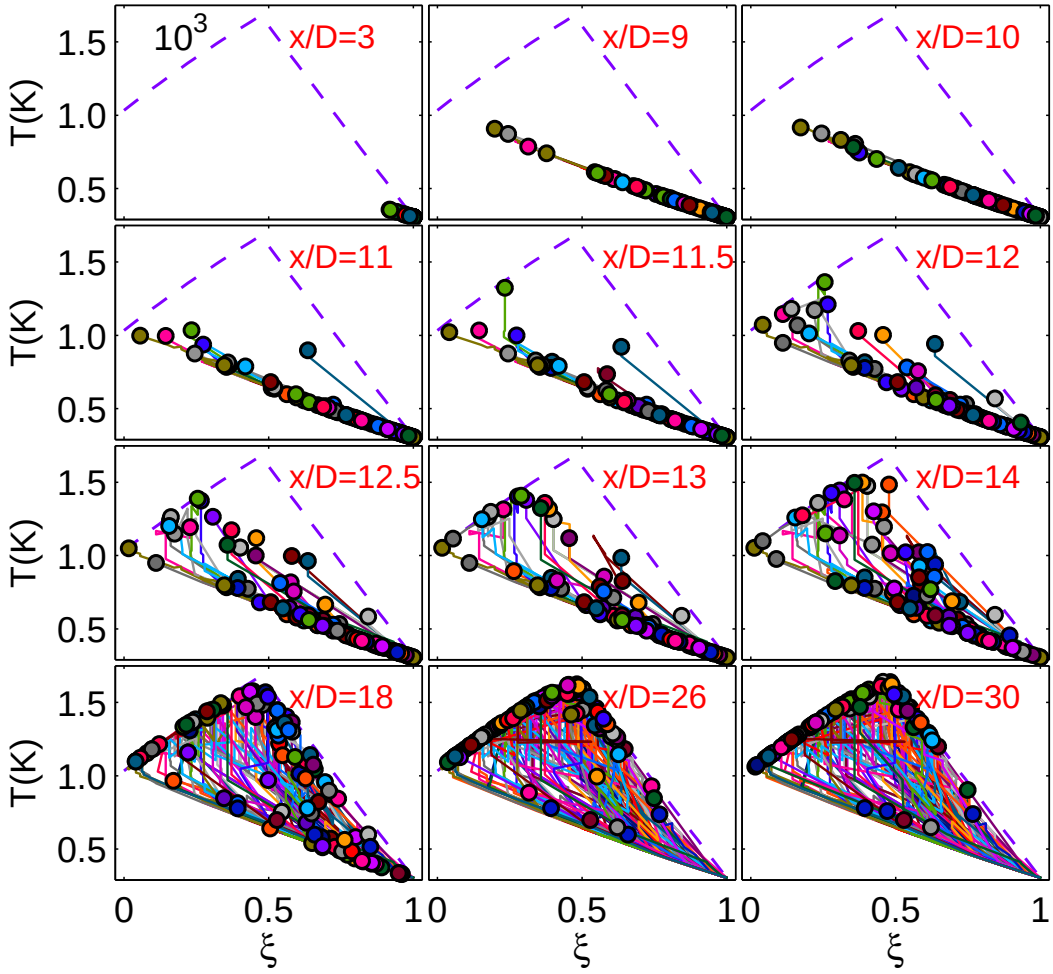

Figure 3.15: The particle trajectories from the fuel region in the Cabra lifted flame by the modified Curl model. (An animation of these particle trajectories is available at http://www.informaworld.com/mpp/uploads/tctm-2007-04-19-file012.mpg.)

i.e. pure mixing, auto-ignition, mixing-ignition, and fully burnt. In some sense, this finding is consistent with the DNS study of an auto-ignition problem in homogeneous isotropic turbulence [46], even though the particles do not provide a direct representation of spatial structure. This contributes to our understanding of the model performance in the turbulent lifted jet flames.

3.6 Roles of mixing and reaction during re-ignition and auto-ignition

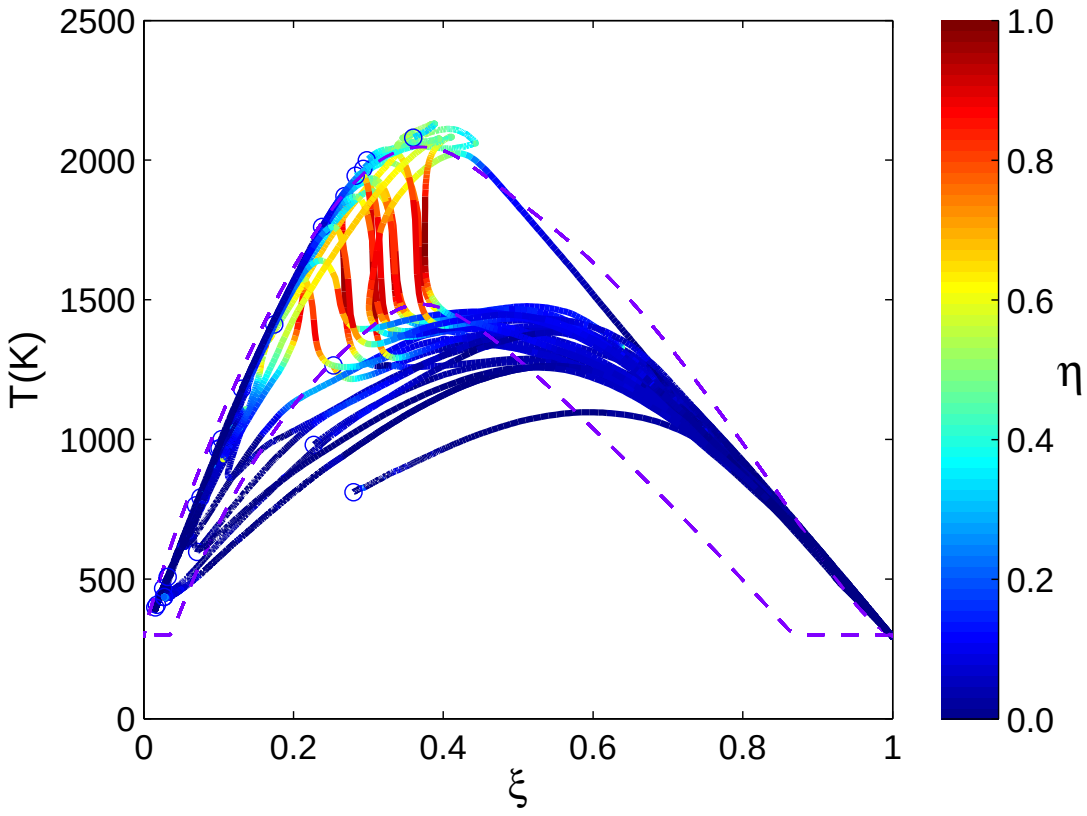

Figure 3.16: Trajectories (up to $x/D = 45$) color-coded by parameter η (Equation 3.10) of locally extinguished particles from the fuel region in flame E using the IEM model.

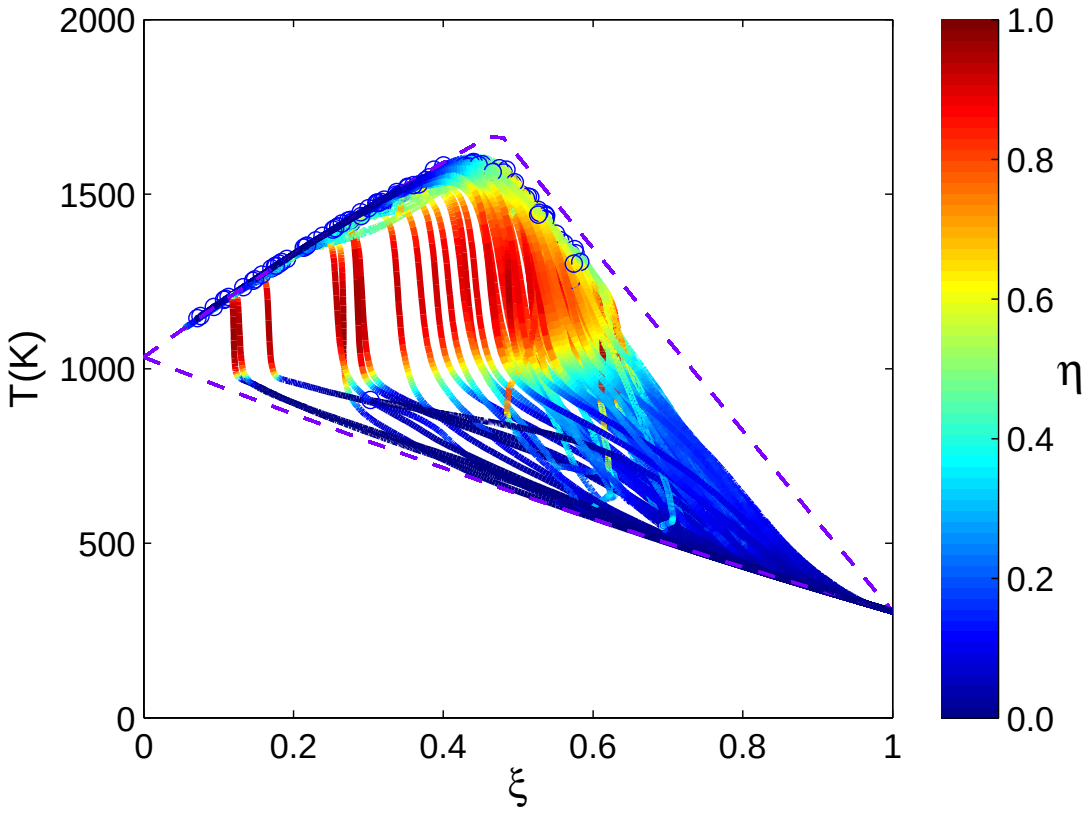

Figure 3.17: Particle trajectories (up to $x/D = 30$) color-coded by parameter η (Equation 3.10) from the fuel region in the Cabra lifted flame using the IEM model

In the previous sections, the roles of mixing and reaction during the particle evolution are discussed qualitatively. The relative importance of mixing and reaction for each particle as it evolves can be quantified by examining the mixing rate given by the mixing models relative to the reaction rate. For this purpose we define the mixing rate $\dot{\mathcal{M}}$ and reaction rate $\dot{S}$ for each particle as,

$$\dot{\mathcal{M}} = \left. \sqrt{\left(\frac{d\xi}{dt}\right)^2 + \left(\frac{1}{T_{ref}}\frac{dT}{dt}\right)^2} \right|_{\text{mix}}, \tag{3.8}$$

and

$$\dot{S} = \left| \frac{1}{T_{ref}}\frac{dT}{dt} \right|_{\text{react}}, \tag{3.9}$$

where $T_{ref} = 2000$ K, and in Equations (3.8) and (3.9) the rates of change pertain solely to the effects of mixing and reaction, respectively. (In the computations, these quantities are readily evaluated based on the particle properties before and after the mixing and reaction fractional steps.)

The relative importance of mixing and reaction can be quantified by the parameter

$$\eta = \frac{S}{S + \mathcal{M}}, \tag{3.10}$$

which varies between zero (corresponding to no reaction) and one (corresponding to no mixing).

We focus our investigation on the IEM mixing model. For the modified Curl model, the composition changes discontinuously, and so $d\xi/dt|_{\text{mix}}$ is not well defined. For the EMST mixing model, $d\xi/dt|_{\text{mix}}$ exhibits large fluctuations of small time scale which obscure the picture.

Figure 3.16 shows, for flame E, trajectories color-coded by the parameter η of locally extinguished particles initially from the fuel region. From the figure, we can clearly see the relative importance of mixing and reaction during

re-ignition. For the particles re-igniting due to auto-ignition mechanism, the reaction is dominant ($\eta \approx 1.0$) when the particles shoot upward at around stoichiometric condition. For those particles which re-ignite due to mixing-reaction, either both mixing and reaction are important (e.g., $\eta \approx 0.3$ for one particle entering the burning region at about $T = 1100$ K), or mixing is dominant due to the low temperature.

In Figure 3.17, the particle trajectories originating from fuel stream in the Cabra flame are shown. In the current simulation of the Cabra flame, the initial ignition process occurs when particles leave the pure mixing line between cold fuel and hot coflow. From the figure, it may be seen that the particle starting to ignite at fuel-lean side leave the pure mixing line dominantly by reaction, corresponding to the auto-ignition identified before. The particles leaving the pure mixing line on the fuel-rich side experience two stages: a mixing-dominant stage to raise the particle temperature to about 1000K, and reaction-dominant stage to raise the particle temperature close to the equilibrium. Both mixing and reaction are important for the ignition of these particles, and they correspond to the previously identified mixing-ignition process. The particle trajectories along with the rates of mixing and reaction provide insights on the roles of mixing and reaction during re-ignition and auto-ignition.

3.7 Conclusion

Lagrangian PDF investigations of the Sandia piloted flame E and the Cabra H_2/N_2 lifted flame are performed to help obtain a deeper understanding of the modeling of local extinction, re-ignition and auto-ignition in these flames. Eu-

lerian scatter plots (shown in Figures 3.1-3.2) of the two flames from the PDF calculations are reviewed to show the limitations of one-time statistics. A Lagrangian particle tracking procedure is implemented in the code HYB2D. Lagrangian particle data are extracted from the PDF calculations after the statistically stationary state is reached, in order to explore the PDF result more comprehensively.

Lagrangian particle tracking in the PDF calculations of Sandia flame E is performed for the different mixing models, EMST, IEM and modified Curl. The particle trajectories are divided into two groups, continuous burning and local extinction. For each group, the trajectories are further sub-divided into different categories based on the original particle locations: the fuel steam, the oxidizer stream, the pilot stream, and the intermediate region. The particle trajectories given by the different mixing models are different, i.e., continuous but non-differentiable by EMST, continuous and differentiable by IEM, and discontinuous by modified Curl. All three mixing models reproduce the local extinction and re-ignition processes reasonably. Two different re-ignition mechanisms are identified, the auto-ignition mechanism and the mixing-reaction mechanism.

Homogeneous auto-ignition tests for the same condition as in the Cabra H_2/N_2 lifted flame are conducted. The lowest ignition delay time (IDT) occurs at a very fuel-lean condition for a range of coflow (oxidizer) temperatures. The strong sensitivity of the IDTs to the coflow temperature is observed, which is also reported in previous PDF calculations of the Cabra lifted flame [31].

Lagrangian particle tracking in the PDF calculations of the Cabra H_2/N_2 lifted is also performed for the different mixing models. The particle trajectories are divided into different categories based on the original particle locations: the

fuel stream, the oxidizer stream, and the intermediate region. The models reproduce the whole auto-ignition process reasonably. Four stages of combustion in the Cabra flame are identified in the calculations, i.e., pure mixing, auto-ignition, mixing-ignition, and fully burnt.

The roles of mixing and reaction during re-ignition and auto-ignition are investigated by using IEM. The relative importance of mixing and reaction is quantified for particles during re-ignition and auto-ignition.

Acknowledgements

This work is supported by the Air Force Office of Scientific Research, Grant FA9550-06-1-0048 and by Department of Energy, Grant DE-FG02-90ER. Various suggestions from David A. Caughey, Zhuyin Ren and Steven R. Lantz are appreciated. This research was conducted using the resources of the Cornell Theory Center, which receives funding from Cornell University, New York State, federal agencies, foundations, and corporate partners.

REFERENCES

[1] S.B. Pope, PDF methods for turbulent reactive flows, *Prog. Energy Combust. Sci.* 11(1985) 119-192.

[2] S.B. Pope, Stochastic Lagrangian models for turbulence, *Annu. Rev. Fluid Mech.* 26 (1994) 23-63.

[3] S.B. Pope, Turbulent Flows, Cambridge University Press, Cambridge, 2000.

[4] J. Xu, S.B. Pope, PDF calculations of turbulent nonpremixed flames with local extinction, *Combust. Flame* 123 (2000) 281-307.

[5] R.P. Lindstedt, S.A. Louloudi, E.M. Vaos, Joint scalar probability density function modeling of pollutant formation in piloted turbulent jet diffusion flames with comprehensive chemistry, *Proc. Combust. Inst.* 28 (2000) 149-156.

[6] P.K. Yeung, Lagrangian characteristics of turbulence and scalar transport in direct numerical simulations, *J. Fluid Mech.* 427 (2001) 241-274.

[7] P.K. Yeung, Lagrangian investigations of turbulence, *Annu. Rev. Fluid Mech.* 34 (2002) 115-142.

[8] S. Mitarai, J.J. Riley, G. Kosaly, A Lagrangian study of scalar diffusion in isotropic turbulence with chemical reaction, *Phy. Fluids* 15 (2003) 3856-3866.

[9] S. Mitarai, G. Kosaly, J.J. Riley, A new Lagrangian flamelet model for local flame extinction and reignition, *Combust. Flame* 137 (2004) 306-319.

[10] S. Mitarai, J.J. Riley, G. Kosaly, Testing of mixing models for Monte Carlo probability density function simulations, *Phys. Fluids* 17 (2005) 047101.

[11] P. Sripakagorn, S. Mitarai, G. Kosaly, H. Pitsch, Extinction and reignition in a diffusion flame: a direct numerical simulation study, *J. Fluid Mech.* 518 (2004) 231-259.

[12] G.A. Voth, K. Satyanarayan, E. Bodenschatz, Lagrangian acceleration measurements at large Reynolds numbers, *Phys. Fluids* 10 (1998) 2268-2280.

[13] A. La Porta, G.A. Voth, A.M. Crawford, J. Alexander, E. Bodenschatz, Fluid particle accelerations in fully developed turbulence, *Nature* 409 (2001) 1017-1019.

[14] N. Mordant, E. Leveque, J.-F. Pinton, Experimental and numerical study of the Lagrangian dynamics of high Reynolds turbulence, *New J. Phys.* 6 (2004) 116-159.

[15] R.S. Barlow, J.H. Frank, Effects of turbulence on species mass fractions in methane-air jet flames, *Proc. Combust. Inst.* 27 (1998) 1087-1095.

[16] R. Cabra, T. Myhrvold, J.-Y. Chen, R.W. Dibble, A.N. Karpetis, R.W. Barlow, Simultaneous laser Raman-Rayleigh-Lif measurements and numerical modeling results of a lifted turbulent H-2/N-2 jet flame in a vitiated coflow, *Proc. Combust. Inst.* 29 (2002) 1881-1888.

[17] P.R. Van Slooten, Jayesh, S.B. Pope, Advances in PDF modeling for inhomogeneous turbulent flows, *Phys. Fluids* 10 (1998) 246-265.

[18] J. Villermaux, J.C. Devillon, Reprsentation de la coalescence et de la redispersion des domaines de sgrgation dans un fluide per modle dinteraction phnomnologique. In: *Proceedings of the Second International Symposia on Chemical Reaction,* Elsevier, New York, 1972.

[19] C. Dopazo, E.E. O'Brien, An approach to the autoignition of a turbulent mixture, *Acta Astronautica* 1 (1974) 1239-1266.

[20] J. Janicka, W. Kolbe, W. Kollmann, Closure of the transport-equation for the probability density function of turbulent scalar fields, *J. Non-Equil. Thermodynamics* 4 (1979) 47-66.

[21] S. Subramaniam, S.B. Pope, A mixing model for turbulent reactive flows based on Euclidean minimum spanning trees, *Combust. Flame* 115 (1998) 487-514.

[22] P.A. Nooren, H.A. Wouters, T.W.J. Peeters, D. Roekaerts, U. Maas, D. Schmidt, Monte Carlo PDF modelling of a turbulent natural-gas diffusion flame, *Combust. Theory Modelling* 1 (1997) 79-96.

[23] R.R. Cao, H. Wang, S.B. Pope, The effect of mixing models in PDF calculations of piloted jet flames, *Proc. Combust. Inst.* 31 (2007) 1543-1550.

[24] Z. Ren, S. Subramaniam, S.B. Pope, Implementation of the EMST mixing model, http://eccentric.mae.cornell.edu/~tcg/emst, 2004.

[25] A.Y. Klimenko, S.B. Pope, A model for turbulent reactive flows based on multiple mapping conditioning, *Phys. Fluids* 15 (2003) 1907-1925.

[26] S.B. Pope, On the relationship between stochastic Lagrangian models of turbulence and second-moment closures, *Phys. Fluids* 6 (1994) 973-985.

[27] R.O. Fox, On velocity conditioned scalar mixing in homogeneous turbulence, *Phys. Fluids* 8 (1996) 2678-2691.

[28] S.B. Pope, The vanishing effect of molecular diffusivity on turbulent dispersion: implications for turbulent mixing and the scalar flux, *J. Fluid Mech.* 359 (1998) 299-312.

[29] B.L. Sawford, Micro-Mixing Modelling of Scalar Fluctuations for Plumes in Homogeneous Turbulence, *Flow, Turb. Combust.* 72 (2004) 133-160.

[30] R.R. Cao, S.B. Pope, The influence of chemical mechanisms on PDF calculations of nonpremixed piloted jet flames, *Combust. Flame* 143 (2005) 450-470.

[31] R.R. Cao, S.B. Pope, Masri, A.R., Turbulent lifted flames in a vitiated coflow investigated using joint PDF calculations, *Combust. Flame* 142 (2005) 438-453.

[32] A.R. Masri, R. Cao, S.B. Pope, G.M. Goldin, PDF Calculations of Turbulent Lifted Flames of H2/N2 issuing into a vitiated co-flow, *Combust. Theory Modelling* 8 (2004) 1-22.

[33] Z. Wu, S.H. Starner, R.W. Bilger, Lift-off heights of turbulent H2/N2 jet flames in a vitiated co-flow. in: D.R. Honnery (Ed.), *Proceedings of the 2003 Australian Symposium on Combustion and the Eighth Australian Flame Days,* The Combustion Institute, 2003.

[34] M. Muradoglu, S.B. Pope, D.A. Caughey, The hybrid method for the PDF equations of turbulent reactive flows: consistency conditions and correction algorithms, *J. Comp. Phys.* 172 (2001) 841-878.

[35] H. Wang, S.B. Pope, Time averaging strategies in the finite-volume/particle hybrid algorithm for the joint PDF equation of turbulent reactive flows, *Combust. Theory Modelling* 12(3) (2008) 529-544.

[36] S.B. Pope, Computationally efficient implementation of combustion chemistry using in situ adaptive tabulation, *Combust. Theory Modelling* 1 (1997) 41-63.

[37] G.P. Smith, D.M. Golden, M. Frenklach, N.W. Moriarty, B. Eiteneer, M. Goldenberg, C.T. Bowman, R.K. Hanson, S. Song, W.C. Gardiner Jr., V.V. Lissianski, Z. Qin, http://www.me.berkeley.edu/gri_mech/.

[38] J. Li, Z. Zhao, A. Kazakov, F.L. Dryer, An updated comprehensive kinetic model for H_2 combustion. in: *Fall Technical Meeting of the Eastern States Section of the Combustion Institute,* Penn. State University, University Park, PA, 2003.

[39] A.E. Lutz, R.J. Kee, J.F. Grcar, F.M. Rupley, OPPDIF: A Fortran Program for Computing Opposed-flow Diffusion Flames, Report No. SAND96-8243, Sandia National Laboratories, 1997.

[40] C.J. Sung, C.K. Law, Structural sensitivity, response, and extinction of diffusion and premixed flames in oscillating counterflow, *Combust. Flame* 123 (2000) 375-388.

[41] F.N. Egolfopoulos, Structure and extinction of unsteady, counterflowing, strained, non-premixed flames, *Int. J. Energy Research* 24 (2000) 989-1010.

[42] A.E. Lutz, F.M. Rupley, R.J. Kee, EQUIL: A CHEMKIN Implementation of STANJAN, for Computing Chemical Equilibria, Report No. SAND96-xxxx, Sandia National Laboratories, 1996.

[43] M. Muradoglu, S.B. Pope, Local time-stepping algorithm for solving the probability density function turbulence model equations, *AIAA J.* 40 (2002) 1755-1763.

[44] C. Pantano, Direct simulation of non-premixed flame extinction in a methane-air jet with reduced chemistry, *J. Fluid Mech.* 514 (2004) 231-270.

[45] J. Hult, U. Meier, W. Meier, A. Harvey, C.F. Kaminski, Experimental analysis of local flame extinction in a turbulent jet diffusion flame by high repetition 2-D laser techniques and multi-scalar measurements, *Proc. Combust. Inst.* 30 (2005) 701-709.

[46] E. Mastorakos, T.A. Baritaud, T.J. Poinsot, Numerical simulations of autoignition in turbulent mixing flows, *Combust. Flame* 109 (1997) 198-223.

CHAPTER 4

WEAK SECOND-ORDER SPLITTING SCHEMES FOR LAGRANGIAN MONTE CARLO PARTICLE METHODS FOR THE COMPOSITION PDF/FDF TRANSPORT EQUATIONS*

Abstract

We study a class of methods for the numerical solution of the system of stochastic differential equations (SDEs) that arises in the modeling of turbulent combustion, specifically in the Monte Carlo particle method for the solution of the model equations for the composition probability density function (PDF) and the filtered density function (FDF). This system consists of an SDE for particle position and a random differential equation for particle composition. The numerical methods considered advance the solution in time with (weak) second-order accuracy with respect to the time step size. The four primary contributions of the paper are: (i) establishing that the coefficients in the particle equations can be frozen at the mid-time (while preserving second-order accuracy), (ii) examining the performance of three existing schemes for integrating the SDEs, (iii) developing and evaluating different splitting schemes (which treat particle motion, reaction and mixing on different sub-steps), and (iv) developing the method of manufactured solutions (MMS) to assess the convergence of Monte Carlo particle methods. Tests using MMS confirm the second-order accuracy of the schemes. In general, the use of frozen coefficients reduces the numerical errors. Otherwise no significant differences are observed in the performance of the dif-

*Haifeng Wang, Pavel P. Popov, Stephen B. Pope, Weak Second Order Splitting Schemes for Lagrangian Monte Carlo Particle Methods for the Composition PDF/FDF Transport Equations, *Journal of Computational Physics* 229 (2010) 1852-1878.

ferent SDE schemes and splitting schemes.

4.1 Introduction

Due to the global concern on energy and environmental issues, developing efficient and accurate numerical combustion tools is highly valuable for increasing our understanding of turbulent reactive systems and hence improving the design of combustion devices with high efficiency and low emissions. During the past several decades, different turbulent combustion models have been devised to represent finite-rate chemistry effects and turbulence-chemistry interactions, e.g., probability density function (PDF) methods [1, 2, 3] , flamelet models [4, 5], and the conditional moment closure (CMC) [6, 7]. PDF methods have proved to be very successful in modeling turbulent combustion (e.g., [8, 9, 10, 11, 12, 13]). PDF methods were originally developed in the context of Reynolds Averaged Navier-Stokes Simulations (RANS). Pope [2] introduced the concept of filtered density function (FDF) in the context of large-eddy simulation (LES) [3]. The FDF methods were further developed subsequently by Gao and O'Brien [14], Colucci et al. [15], Jaberi et al. [16] etc. Examples of recent FDF applications can be found in [17, 18, 19, 20, 21, 22]. The common practice in FDF methods is to combine the LES solutions for the velocity fields with the composition FDF method. In this work, we only discuss the composition FDF method, while some of the ideas such as designing the second-order splitting schemes are applicable to the joint PDF/FDF of the velocity, composition and additional variables (e.g., the dissipation rate). The FDF in the LES is analogous to the PDF in the RANS. In terms of applications, there is no essential difference between the PDF and the FDF, and almost all the methodologies developed for PDF meth-

ods are applicable to FDF methods. Hence, in this discussion, for convenience, we use the PDF to represent both the PDF and the FDF methods when there is no confusion.

Lagrangian Monte Carlo particle methods [1, 23] have been widely used to solve the PDF transport equations. In these methods, the continuous PDF is discretized by a finite number of nominal particles, and each particle is governed by a system of stochastic differential equations (SDE) [24] (including an Ito SDE for particle position and a scalar random equation) describing the underlying physical and chemical processes. The numerical solution of SDEs is a much harder problem than that of ordinary differential equations (ODEs). All the well developed high-order ODE schemes degrade to low order of accuracy when applied in Ito SDEs; and, even worse, they can lead to inconsistent schemes because (most) ODE schemes violate the non-anticipatory property of Ito SDEs. Cao and Pope [25] developed a second-order integration scheme for the Ito SDE of particle position arising from the composition PDF transport equations, which considers only position and velocity, not scalars. In this work, we consider the SDE system describing particle transport, molecular mixing and chemical reaction, and develop different weak second-order splitting schemes for the coupled system. To the authors' knowledge, no second-order splitting schemes have previously been developed for the Monte Carlo solution of the coupled SDE system, and have been applied in the RANS/PDF or LES/FDF practice.

Contrary to the supposition of Cao and Pope [25], the weak second-order mid-point Ito SDE scheme turns out to be only first-order accurate when simply coupled with the scalar equations. This is caused by the fact that the predicted

mid-point and the final point of the scheme are treated independently and hence the mid-point is not a first-order prediction with the correct conditional probability distribution given the initial and final particle positions. This and other considerations discussed below motivate us to consider other kinds of Ito SDE schemes available in the literature, e.g., predictor-corrector schemes [24, 26, 27], and Runge-Kutta schemes [24, 28, 29, 30, 31].

The numerical solution of SDEs is a broad research area. The SDEs can be interpreted in two ways, Ito SDEs and Stratonovich SDEs, and different integration schemes are developed for them, e.g., the Ito SDE schemes [24, 26, 28, 29, 30, 31, 32, 33, 34, 35] and the Stratonovich SDE schemes [27, 35, 36, 37]. (The Ito SDEs and the Stratonovich SDEs can be readily transformed to each other, so the schemes developed for one type of SDEs are applicable to the other.) In PDF methods, the SDEs are usually interpreted in the Ito view, and this work follows this convention.

Two different types of solutions to SDEs can be sought, the path-wise approximation (strong sense) and the approximation to the probability distribution (weak sense) [24]. In the application of PDF methods, we are more interested in the statistics of the flow fields, so it makes more sense to consider accurate weak solutions for the Monte Carlo particles. Many schemes are developed for this purpose, e.g. [24, 26, 28, 29, 30, 31, 32, 34, 35, 37]. Explicit SDE schemes are usually used for simplicity and efficiency, while implicit schemes can achieve better stability. In this stage of the PDF methods, we only consider the explicit SDE schemes. Implicit SDE schemes may be worthwhile to consider in the future to take advantage of larger time step size. However, with explicit methods we have not experienced any stability problems given that the

time step is determined by other factors, e.g., the CFL condition imposed on the solution of the velocity fields by the finite-volume method. The examples of explicit and implicit SDE schemes can be found in [24]. Second-order accuracy is a good compromise between accuracy and efficiency for PDF methods. First-order accuracy is too crude to eliminate numerical uncertainties arising from the modeling of turbulent combustion. The statistical error of the Monte Carlo method scales as $N^{-1/2}$, where N is the number of particles. Due to the slow convergence of the Monte Carlo particle method, most likely the statistical error dominates other numerical errors including the time-stepping error. (In practice, only a small number of particles per cell – on the order of 100 – are used in a RANS/PDF or LES/FDF calculation to make the computation affordable.) Hence using high-order accurate SDE schemes (third-order or higher) in the PDF methods only increases the complexity of the schemes without helping reduce the overall numerical errors.

Many SDE schemes involve derivatives of the coefficients (e.g. [24, 25, 32]), which increases the difficulty of using them. This makes the derivative-free SDE schemes more attractive, and in fact many derivative-free SDE schemes have been developed (see [24, 26, 27, 28, 29, 30, 31, 34, 35, 36, 37]). In this work, we consider three weak second-order SDE schemes, the mid-point scheme of Cao and Pope [25], the predictor-corrector scheme of Kloeden and Platen (pp. 504-506 of [24], also in [26]), and the Runge-Kutta scheme of Tocino and Vigo-Aguiar [30]. The latter two are derivative free. The derivative here refers to the derivative of the drift term, which already includes the derivative of the diffusivity in this work (see Section 4.2). Hence the Cao and Pope scheme requires the second-order derivative of the diffusivity, and the Kloeden and Platen scheme and the Tocino and Vigo-Aguiar scheme require the first-order derivative of the

diffusivity.

In the RANS/PDF simulations, many problems are statistically stationary, and the corresponding Ito SDEs are autonomous, i.e., the drift and diffusion coefficient of the SDEs do not depend on time. Some SDEs schemes are developed only for autonomous SDEs (e.g. [24, 26, 28, 32, 34, 36]). The LES/FDF simulations are always non-stationary, so the autonomous SDE schemes are generally not applicable[1], and the non-autonomous SDE schemes [29, 30, 31, 32, 35, 37] are desired. However, it can be verified that solving the non-autonomous SDE system is equivalent up to second-order to solving the SDE system with all the coefficients evaluated at the mid-point of the time step. That is, as far as the weak second-order SDE schemes are concerned, solving the non-autonomous SDE system is equivalent to solving the SDE system with the coefficients frozen at the mid-point using the weak second-order autonomous SDE schemes. Thus, all the weak second-order Ito SDE schemes, no matter whether developed for the autonomous or for the non-autonomous SDEs, are applicable to all the RANS/PDF and LES/FDF applications. Freezing the coefficients in the SDEs at the mid-point is also a big advantage for the staggered arrangement of different fields in the time advancement of the RANS or LES discretization, e.g., in the LES application [38], the velocity fields are staggered in time with the scalars. If the particles are also staggered with the velocity fields (and the turbulent diffusivity) as sketched in Fig. 4.1, the above freezing the coefficients facilitates the use of the staggered velocity and diffusivity for particle position advancement without interpolation of these quantities in time. (The non-autonomous SDE schemes usually require the evaluation of the drift and diffusion coefficients at

[1] Adding time as a new variable can make the autonomous SDE schemes applicable. However this procedure is not favorable because it leads to more evaluations of coefficients in some SDE schemes and hence increases the computational cost.

different times other than the mid-time [29, 30, 31, 32, 35, 37].) Hence, the complexity of the interface between the RANS or LES solver and the particle solver can be greatly reduced.

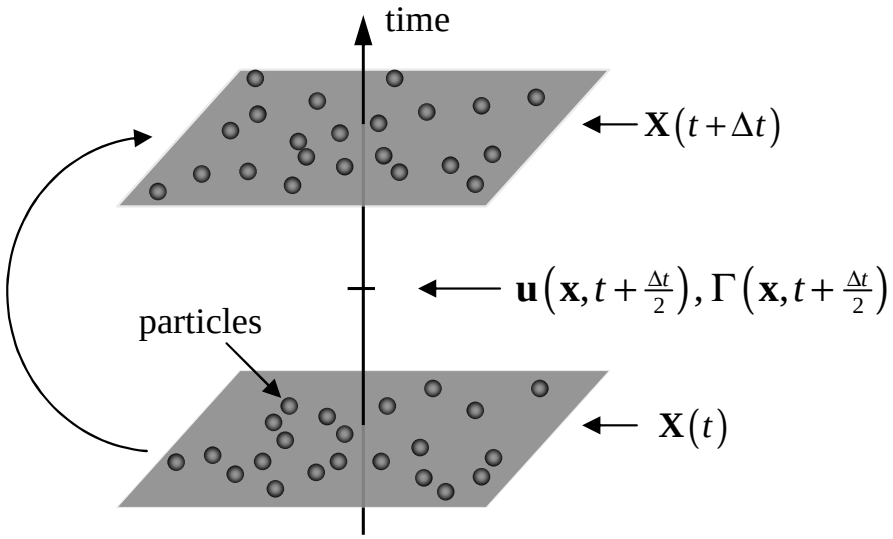

Figure 4.1: Sketch of the particle advancement with staggered velocity and diffusivity in time, showing the particle locations $\mathbf{X}$ at times t and $t + \Delta t$, and the velocity field $\mathbf{u}$ and the turbulent diffusivity field Γ at the half time, $t + \frac{\Delta t}{2}$.

To demonstrate the formal order of accuracy and convergence of different numerical schemes, the exact solution of the studied problem, or an accurate estimate of it, is required to provide reference for evaluating the numerical error. For some rare cases, the exact solution to the problem may be obtained with simplification of the problem. This simplification reduces the complexity of the problem, and hence may not be able to represent realistic problems. Given an arbitrary initial condition and other parameters, an accurate numerical solution to a realistic problem is generally available from numerical methods. This accurate numerical solution can be used for error estimation, and has been used in previous studies (e.g., [25]). The method of manufactured solutions (MMS) [39, 40] provides a general method for designing test cases with known exact solutions. The test cases can be designed to have the same level of complexity as the real

problem. Meanwhile, for the purpose of verification, the manufactured solution need not be related to a physically realistic problem. The idea of MMS is to specify the mathematical solutions *a priori* so that they satisfy a set of augmented governing equations with extra source terms. The augmented governing equations rather than the original ones are solved numerically, and the numerical error is readily evaluated given the (manufactured) exact solutions. The MMS has been used in the verification of different flow solvers [41, 42, 43, 44]. In this work, we develop the method of manufactured solutions for the Monte Carlo particle method. The augmented PDF transport equation and the corresponding SDE system are derived. This method is suitable for the verification of the weak convergence of Monte Carlo particle methods.

The developed MMS makes the verification of the Monte Carlo particle method possible. However in practice, this procedure is computationally demanding. A large number of particles are required in the Monte Carlo simulation to make the statistical error negligible compared to the other numerical errors, e.g., the temporal or spatial discretization error. In order to demonstrate the convergence of the weak second-order SDE schemes with respect to time, the computational cost is found to scale as Δt^{-5} (see Section 4.4.3), where Δt is the time step size. Halving the time step increases the computational cost up to 2^5 times. In this work, in order to make this verification procedure computationally tractable, we perform the simulations in parallel via MPI. In addition, we have to make some simplifications to the test case, which is one-dimensional, constant density, and single scalar. The representativity of the test case and its extension to the full three-dimensional, variable-density and multi-scalar case are discussed at the end of the paper.

The main contributions of the present work are

1. The introduction of an SDE system with frozen coefficients (Section 4.3.2)
2. The comparison of different Ito SDE schemes (Sections 4.3.3 and 4.6)
3. The development and assessment of different second-order splitting schemes (Sections 4.5 and 4.6)
4. The development of MMS for the Monte Carlo particle method (Section 4.4)

The rest of the paper is organized as follows. In Section 4.2, the composition PDF method and its Monte Carlo solution method are briefly described. In Section 4.3, the frozen-coefficient SDE system is presented, and several Ito SDE schemes from the literature are discussed. In Section 4.4, the MMS for the Monte Carlo particle method is developed, and the numerical error and computational cost are briefly discussed. The sub-stepping of the particle scalar equation and the different splitting schemes for the coupled SDE system are discussed in Section 4.5. The convergence test results of the different splitting schemes and their comparison are shown in Section 4.6. Further discussion is presented in Section 4.7, and the conclusions are drawn in Section 4.8.

4.2 PDF methods

In this work, only the PDF $f(\psi; \mathbf{x}, t)$ of a single scalar $\phi(\mathbf{x}, t)$ is considered, where ψ is the sample space variable corresponding to ϕ, and $\mathbf{x}$ and t denote space and time. The modeled transport equation of $f(\psi; \mathbf{x}, t)$ takes the following form [1]

$$\frac{\partial f(\psi; \mathbf{x}, t)}{\partial t} + \frac{\partial \overline{u}_i(\mathbf{x}, t) f(\psi; \mathbf{x}, t)}{\partial x_i} = \frac{\partial}{\partial x_i}\left(\Gamma(\mathbf{x}, t)\frac{\partial f(\psi; \mathbf{x}, t)}{\partial x_i}\right)$$

$$+ \quad \frac{\partial}{\partial \psi}\left(\Omega(\mathbf{x},t)(\psi-\overline{\phi}(\mathbf{x},t))f(\psi;\mathbf{x},t)\right)$$
$$- \quad \frac{\partial}{\partial \psi}\left(S(\psi)f(\psi;\mathbf{x},t)\right), \tag{4.1}$$

where $\mathbf{u} = (u_1, u_2, u_3)$ is the velocity field (satisfying $\nabla \cdot \mathbf{u} = 0$), $\Gamma(\mathbf{x}, t)$ is the effective scalar diffusivity (the sum of the molecular diffusivity and the turbulent diffusivity), $\Omega(\mathbf{x}, t)$ is the scalar mixing frequency, and $S(\phi)$ is the scalar source term (due to reaction). The overline operation "$\overline{\ }$" is the first moment, e.g., $\overline{\phi}$ is the first moment of ϕ. In (4.1), two models are used for the closure, the gradient-diffusion model [3] for the scalar flux (the first term on the right-hand side), and the interaction by exchange with the mean (IEM) mixing model [45] for the conditional dissipation term (the second term on the right-hand side). The IEM model is chosen for simplicity: other mixing models (e.g., modified Curl model [46], EMST model [47]) can be used for the discussion and do not affect the conclusions drawn in this work.

Given $f(\psi; \mathbf{x}, t)$, the qth raw moment of the scalar ϕ can be readily obtained as

$$\overline{\phi^q}(\mathbf{x}, t) = \int_{-\infty}^{+\infty} \psi^q f(\psi; \mathbf{x}, t)\, d\psi. \tag{4.2}$$

From (4.1) and (4.2), we can derive the transport equations for the first moment $\overline{\phi}(\mathbf{x}, t)$ and second moment $\overline{\phi^2}(\mathbf{x}, t)$

$$\frac{\partial \overline{\phi}(\mathbf{x},t)}{\partial t} + \frac{\partial \overline{u}_i(\mathbf{x},t)\overline{\phi}(\mathbf{x},t)}{\partial x_i} = \frac{\partial}{\partial x_i}\left(\Gamma(\mathbf{x},t)\frac{\partial \overline{\phi}(\mathbf{x},t)}{\partial x_i}\right) + \overline{S}(\mathbf{x},t), \tag{4.3}$$

$$\begin{aligned}\frac{\partial \overline{\phi^2}(\mathbf{x},t)}{\partial t} + \frac{\partial \overline{u}_i(\mathbf{x},t)\overline{\phi^2}(\mathbf{x},t)}{\partial x_i} &= \frac{\partial}{\partial x_i}\left(\Gamma(\mathbf{x},t)\frac{\partial \overline{\phi^2}(\mathbf{x},t)}{\partial x_i}\right) \\ &- 2\Omega(\mathbf{x},t)\left(\overline{\phi^2}(\mathbf{x},t) - \overline{\phi}^{\,2}(\mathbf{x},t)\right) + 2\overline{S\,\phi}(\mathbf{x},t),\end{aligned} \tag{4.4}$$

where $\overline{S}(\mathbf{x}, t)$ denotes the mean of $S(\phi(\mathbf{x}, t)$. With the definition of $\overline{\phi'^2}(\mathbf{x}, t) =$

$\overline{\phi^2}(\mathbf{x},t) - \overline{\phi}^{\,2}(\mathbf{x},t)$, the transport equation for $\overline{\phi'^2}(\mathbf{x},t)$ is

$$\begin{aligned}\frac{\partial \overline{\phi'^2}(\mathbf{x},t)}{\partial t} + \frac{\partial \overline{u}_i(\mathbf{x},t)\overline{\phi'^2}(\mathbf{x},t)}{\partial x_i} &= \frac{\partial}{\partial x_i}\left(\Gamma(\mathbf{x},t)\frac{\partial \overline{\phi'^2}(\mathbf{x},t)}{\partial x_i}\right) \\ &+ 2\Gamma(\mathbf{x},t)\frac{\partial \overline{\phi}(\mathbf{x},t)}{\partial x_i}\frac{\partial \overline{\phi}(\mathbf{x},t)}{\partial x_i} - 2\Omega(\mathbf{x},t)\overline{\phi'^2}(\mathbf{x},t) \\ &+ 2\left(\overline{S\,\phi}(\mathbf{x},t) - \overline{S}(\mathbf{x},t)\overline{\phi}(\mathbf{x},t)\right). \end{aligned} \tag{4.5}$$

These moment equations are useful for the verification of weak convergence. For convenience, we refer to $\overline{\phi}(\mathbf{x},t)$ and $\overline{\phi'^2}(\mathbf{x},t)$ as the scalar mean and scalar variance. (In the LES, it is appropriate to call them filtered scalar and sub-filter scalar variance.) Since the first two moments are of most interest in practical applications, we consider only these two moments in the development of MMS for the particle methods in Section 4.4, and in most discussions of the convergence tests in Section 4.6. For completeness, for one type of splitting schemes we show the results of weak second-order convergence for the third and fourth moments in Section 4.6.3.

The PDF equation (4.1) can be efficiently solved by the Lagrangian Monte Carlo particle method [1]. A number of nominal particles are introduced to represent the PDF, and each particle carries the properties of the physical position $\mathbf{X}(t)$ and scalar value $\phi(t)$. These properties evolve according to the following set of SDEs [1]

$$d\mathbf{X}(t) = (\overline{\mathbf{u}}(\mathbf{X}(t),t) + \nabla\Gamma(\mathbf{X}(t),t))\,dt + (2\Gamma(\mathbf{X}(t),t))^{\frac{1}{2}}\,d\,\mathbf{W}(t), \tag{4.6}$$

$$\frac{d\phi(t)}{dt} = -\Omega(\mathbf{X}(t),t)(\phi(t) - \overline{\phi}(\mathbf{X}(t),t)) + S\,(\phi(t))\,, \tag{4.7}$$

where $\mathbf{W}(t)$ is a standard isotropic Wiener process.

The aim of this work is to design weak second-order numerical schemes for the coupled SDE system (4.6) and (4.7), and to develop the verification procedure to demonstrate the accuracy and convergence of the schemes.

4.3 Numerical solutions of SDEs

4.3.1 Ito SDEs and weak convergence

The Ito SDE (4.6) arising from the Monte Carlo particle method has the following general form

$$d\mathbf{X}(t) \quad = \quad \mathbf{D}(\mathbf{X}(t), t)d\,t + b(\mathbf{X}(t), t)d\,\mathbf{W}(t), \tag{4.8}$$

for $t \in [0, T]$, where $\mathbf{D}(\mathbf{X}(t), t)$ and $b(\mathbf{X}(t), t)$ are the vector drift and scalar diffusion coefficients, respectively. We assume that the SDE coefficients $\mathbf{D}(\mathbf{X}(t), t)$ and $b(\mathbf{X}(t), t)$ are smooth and measurable functions satisfying a global Lipschitz and a linear growth condition, and all the initial moments of $\mathbf{X}(0)$ exist, so that (4.8) admits the existence and uniqueness of a solution $\mathbf{X}(T)$ (see, e.g., [24]).

Many Ito SDE schemes (e.g. [24, 26, 28, 32, 34, 36]) have been developed for the autonomous SDEs having the form

$$d\mathbf{X}(t) \quad = \quad \mathbf{D}(\mathbf{X}(t))d\,t + b(\mathbf{X}(t))d\,\mathbf{W}(t), \tag{4.9}$$

where the SDE coefficients do not depend directly on time. To take advantage of the autonomous SDE schemes, we will consider an SDE system with frozen coefficients in Section 4.3.2 which can use the autonomous SDE schemes for our problem (4.8).

We write the particle scalar equation (4.7) in the general form

$$\frac{d\phi(t)}{dt} \quad = \quad A(\mathbf{X}(t), \phi(t), t). \tag{4.10}$$

This is a random differential equation due to the randomness of the forcing term $A(\mathbf{X}(t), \phi(t), t)$ (see [24]). Regular ODE schemes can be applied to solve (4.10). Let

$\mathbf{Y}(T)$ and $\varphi(T)$ be numerical approximations of the Ito process $\mathbf{X}$(T) and scalar $\phi(T)$, respectively, where T is the specified stopping time. The weak pth order convergence of the numerical solutions $\mathbf{Y}(T)$ and $\varphi(T)$ to the SDE system (4.6) and (4.7) can be measured by the asymptotic behavior of the numerical error e

$$e = |E\left(g(\mathbf{Y}(T), \varphi(T), T)\right) - E\left(g(\mathbf{X}(T), \phi(T), T)\right)| \leqslant C\Delta t^p, \tag{4.11}$$

where g is a function (chosen to be $\overline{\phi}$ and $\overline{\phi^2}$ in this study), $E(\cdot)$ denotes mathematical expectation, and C is a constant independent of Δt. That is, the largest value of p for which (4.11) holds indicates the order of the scheme.

4.3.2 SDE system with frozen coefficients

Consider a single step numerical integration $[t_0, t_0 + \Delta t]$ of (4.8) and (4.10), where t_0 is the initial time and Δt is the time step size. It is verified in Appendix B that integrating (4.8) and (4.10) with weak second-order accuracy is equivalent to integrating the following system over the time interval

$$d\mathbf{X}'(t) = \mathbf{D}(\mathbf{X}'(t), t_{\frac{1}{2}})d\,t + b(\mathbf{X}'(t), t_{\frac{1}{2}})d\,\mathbf{W}(t), \tag{4.12}$$

$$\frac{d\phi'(t)}{dt} = A(\mathbf{X}'(t), \phi'(t), t_{\frac{1}{2}}), \tag{4.13}$$

where $t_\alpha = t_0 + \alpha\Delta t$ $(0 \leqslant \alpha \leqslant 1)$. Over one time step, (4.12) is an autonomous Ito SDE (similar to (4.9)), so any autonomous Ito SDE scheme can be used.

The advantages of this frozen-coefficient SDE system have been discussed in Section 4.1.

4.3.3 Weak second-order Ito SDE schemes

In this work, three weak second-order Ito SDE schemes for (4.8) and (4.9) are considered: the mid-point scheme of Cao and Pope [25]; the predictor-corrector scheme of Kloeden and Platen (pp. 504-506 of [24], also in [26]); and, the Runge-Kutta scheme of Tocino and Vigo-Aguiar [30].

In the following discussion, we use $\mathbb{T}$ to denote the transport step (step of the solution to the Ito SDE), and $\mathcal{T}$ to denote the results of the step. We consider the general step from time t_0 to $t_0 + \Delta t$ with initial condition $\mathbf{X}(t_0) = \mathbf{X}_0$.

4.3.3.1 Scheme of Cao and Pope (CP)

The CP scheme [25] consists of two sub-steps $\mathbb{T}^{\text{cp}} = \mathbb{T}_1^{\text{cp}}\mathbb{T}_2^{\text{cp}}$, where $\mathbb{T}_1^{\text{cp}}$ is the prediction of the mid-point and $\mathbb{T}_2^{\text{cp}}$ is the final solution.

First CP sub-step $\mathbb{T}_1^{\text{cp}}$:

$$\mathbf{Y}(t_{\frac{1}{2}}) = \mathbf{X}_0 + \mathcal{T}_1^{\text{cp}}(\mathbf{X}_0, t_0, \Delta t, \boldsymbol{\zeta}) \tag{4.14}$$

with $\mathcal{T}_1^{\text{cp}}(\mathbf{X}, s, \Delta t, \boldsymbol{\zeta}) = \frac{\Delta t}{2} \cdot \mathbf{D}(\mathbf{X}, s) + \left(\frac{1}{2}\Delta t\right)^{\frac{1}{2}} b(\mathbf{X}, s)\boldsymbol{\zeta}$, where $\boldsymbol{\zeta}$ is a standardized Gaussian random vector (each component of $\boldsymbol{\zeta}$ is an independent Gaussian random number with zero mean and unit variance).

Second CP sub-step $\mathbb{T}_2^{\text{cp}}$:

$$\mathbf{Y}(t_1) = \mathbf{Y}(t_{\frac{1}{2}}) + \mathcal{T}_2^{\text{cp}}(\mathbf{X}_0, \mathbf{Y}(t_{\frac{1}{2}}), t_{\frac{1}{2}}, \Delta t, \boldsymbol{\xi}, \boldsymbol{\eta}) \tag{4.15}$$

with $\mathcal{T}_2^{\text{cp}}(\mathbf{X}, \mathbf{Y}, s, \Delta t, \boldsymbol{\xi}, \boldsymbol{\eta}) = (\mathcal{T}_{2,1}^{\text{cp}}, \mathcal{T}_{2,2}^{\text{cp}}, \mathcal{T}_{2,3}^{\text{cp}})$, and

$$\mathcal{T}_{2,i}^{\text{cp}}(\mathbf{X}, \mathbf{Y}, s, \Delta t, \boldsymbol{\xi}, \boldsymbol{\eta}) \quad = \quad \Delta t D_i(\mathbf{Y}, s) + \left(\frac{1}{2}\Delta t\right)^{\frac{1}{2}} b(\mathbf{Y}, s)(\xi_i + \eta_i)$$

$$
\begin{aligned}
&+ \quad \Delta t b(\mathbf{Y}, s) \frac{\partial b(\mathbf{Y}, s)}{\partial X_j} (\eta_i \eta_j - \delta_{ij}) \\
&- \quad \left(\frac{1}{2}\Delta t\right)^{\frac{3}{2}} \left[b(\mathbf{Y}, s) \left(\frac{\partial b(\mathbf{Y}, s)}{\partial X_i} \frac{\partial b(\mathbf{Y}, s)}{\partial X_j} + \frac{\partial b(\mathbf{Y}, s)}{\partial X_k} \frac{\partial b(\mathbf{Y}, s)}{\partial X_k} \delta_{ij} \right) \right. \\
&- \quad \left. b(\mathbf{Y}, s) \left(\frac{\partial D_i(\mathbf{Y}, s)}{\partial X_j} + \frac{\partial D_j(\mathbf{Y}, s)}{\partial X_i} \right) \right] (\xi_j + \eta_j) \\
&+ \quad X_i - Y_i, \qquad (4.16)
\end{aligned}
$$

where $\boldsymbol{\xi}$ and $\boldsymbol{\eta}$ are two independent standardized Gaussian random vectors, and δ_{ij} is the Kronecker delta.

The overall CP step can be re-expressed as

$$\mathbf{Y}(t_1) = \mathbf{X}_0 + \mathcal{T}^{\text{cp}}(\mathbf{X}_0, t_0, t_{\frac{1}{2}}, \Delta t, \boldsymbol{\zeta}, \boldsymbol{\xi}, \boldsymbol{\eta}), \qquad (4.17)$$

where

$$\mathcal{T}^{\text{cp}}(\mathbf{X}, s_1, s_2, \Delta t, \boldsymbol{\zeta}, \boldsymbol{\xi}, \boldsymbol{\eta}) = \mathcal{T}_2^{\text{cp}}(\mathbf{X}, \mathbf{Y}_{\frac{1}{2}}, s_2, \Delta t, \boldsymbol{\xi}, \boldsymbol{\eta}) - \mathbf{X} + \mathbf{Y}_{\frac{1}{2}} \qquad (4.18)$$

with $\mathbf{Y}_{\frac{1}{2}} = \mathbf{X} + \mathcal{T}_1^{\text{cp}}(\mathbf{X}, s_1, \Delta t, \boldsymbol{\zeta})$.

The application of CP to the frozen-coefficient system is given by (4.17) and (4.18), but with s_1 and s_2 set to $t_{\frac{1}{2}}$ in (4.18).

4.3.3.2 Scheme of Kloeden and Platen (KP)

The KP scheme $\mathbb{T}^{\text{kp}}$ [24, 26] is a scheme of predictor-corrector type for autonomous Ito SDEs. The one-dimensional KP scheme is the following (the multi-dimensional KP scheme can be found in the same reference)

$$Y(t_1) \quad = \quad X_0 + \mathcal{T}^{\text{kp}}(X_0, \Delta t, \xi) \qquad (4.19)$$

with $\mathcal{T}^{\text{kp}}(X, \Delta t, \xi) = \frac{1}{2}\left(D(Y_a) + D(X)\right)\Delta t + Y_b$, and

$$Y^{\pm} \quad = \quad X_0 + D(X_0)\Delta t \pm b(X_0)\Delta t^{\frac{1}{2}},$$

$$
\begin{aligned}
Y_c &= X_0 + D(X_0)\Delta t + b(X_0)\Delta t^{\frac{1}{2}}\xi, \\
Y_b &= \frac{1}{4}\left[b(Y^+) + b(Y^-) + 2b(X_0)\right]\Delta t^{\frac{1}{2}}\xi + \frac{1}{4}\left[b(Y^+) - b(Y^-)\right]\Delta t^{\frac{1}{2}}\left(\xi^2 - 1\right), \\
Y_a &= X_0 + \frac{1}{2}\left(D(Y_c) + D(X_0)\right)\Delta t + Y_b,
\end{aligned}
$$

and ξ is either a standardized Gaussian random number or a three-point distributed random number with probability

$$
\text{Prob}\left(\xi = \pm\sqrt{3}\right) = \frac{1}{6}, \quad \text{Prob}\left(\xi = 0\right) = \frac{2}{3}. \tag{4.20}
$$

This autonomous Ito SDE scheme is applicable only to the frozen-coefficient SDE (4.12).

4.3.3.3 Scheme of Tocino and Vigo-Aguiar (TV)

Tocino and Vigo-Aguiar [30] proposed a family of weak second-order Runge-Kutta Ito SDE schemes. The one-dimensional version of TV scheme $\mathbb{T}^{\text{tv}}$ for non-autonomous SDEs is shown in the following (the multi-dimensional version can be found in the same reference)

$$
Y(t_1) = X_0 + \mathcal{T}^{\text{tv}}(X_0, \Delta t, t_0, \mu_0, \bar{\mu}_0, \xi), \tag{4.21}
$$

where ξ is a standardized Gaussian random number and

$$
\begin{aligned}
\mathcal{T}^{\text{tv}}(X, \Delta t, s, \mu_0, \bar{\mu}_0, \xi) &= \left(\alpha_1 k_0 + \alpha_2 k_1\right)\Delta t + \left(\gamma_1\xi + \gamma_2 + \gamma_3\xi^2\right)\Delta t^{1/2} s_0 \\
&+ \left(\lambda_1\xi + \lambda_2 + \lambda_3\xi^2\right)\Delta t^{1/2} s_1 \\
&+ \left(\mu_1\xi + \mu_2 + \mu_3\xi^2\right)\Delta t^{1/2} s_2,
\end{aligned} \tag{4.22}
$$

where

$$
k_0 = D(X, s),
$$

$$
\begin{aligned}
s_0 &= b(X, s), \\
k_1 &= D\left(X + \lambda_0 k_0 \Delta t + \left(\nu_1 \xi + \nu_2 \xi^3\right) \Delta t^{1/2} s_0,\ s + \mu_0 \Delta t\right), \\
s_1 &= b\left(X + \bar{\lambda}_0 k_0 \Delta t + \left(\beta_1 \xi + \beta_2 + \beta_3 \xi^2\right) \Delta t^{1/2} s_0,\ s + \bar{\mu}_0 \Delta t\right), \\
s_2 &= b\left(X + \bar{\lambda}_0 k_0 \Delta t + \left(\delta_1 \xi + \delta_2 + \delta_3 \xi^2\right) \Delta t^{1/2} s_0,\ s + \bar{\mu}_0 \Delta t\right).
\end{aligned}
$$

The example of the two-parameter (α_2 and μ_3) families of the TV scheme are

$$
\alpha_1 = 1 - \alpha_2,\ \ \mu_0 = \lambda_0 = \frac{1}{2\alpha_2},\ \ \nu_2 = \pm \frac{\sqrt{2\alpha_2 - 1}}{2\sqrt{6}\alpha_2},\ \ \nu_1 = \frac{1}{2\alpha_2} - 3\nu_2
$$

with $\alpha_2 \geqslant 1/2$, and either

$$
\begin{aligned}
&\beta_3 = \delta_3 = 0,\ \ \bar{\mu}_0 = \bar{\lambda}_0 = 1,\ \ \gamma_1 = \frac{1}{2},\ \ \gamma_2 = \gamma_3 = 0,\ \ \mu_1 = \lambda_1 = \frac{1}{4}, \\
&\mu_2 = -\lambda_2 = \frac{1 - 48\mu_3^2}{32\mu_3},\ \ \lambda_3 = -\mu_3,\ \ \beta_2 = -\delta_2 = \frac{8\mu_3}{1 - 48\mu_3^2},\ \ \beta_1 = \delta_1 = 1 + \frac{32\mu_3^2}{1 - 48\mu_3^2}
\end{aligned} \tag{4.23}
$$

with $\mu_3 \neq 0$ and $\mu_3 \neq \frac{1}{4\sqrt{3}}$, or

$$
\begin{aligned}
&\beta_1 = \beta_2 = \delta_1 = \delta_2 = 0,\ \ \gamma_2 = \gamma_3 = 0,\ \ \gamma_1 = 1 - \frac{24\mu_3^2}{5},\ \ \mu_1 = \lambda_1 = \frac{12\mu_3^2}{5}, \\
&\bar{\mu}_0 = \bar{\lambda}_0 = \frac{5}{48\mu_3^2},\ \ \delta_3 = -\beta_3 = \frac{1}{12\mu_3},\ \ \lambda_2 = -\mu_2 = 3\mu_3,\ \ \lambda_3 = -\mu_3,
\end{aligned} \tag{4.24}
$$

with $\mu_3 \neq 0$. In the results presented in Section 4.6, the values of $\alpha_2 = 1.0$ and $\mu_3 = 0.5$ and (4.24) are used. The effect of choosing the different constants and different families of the parameters is discussed in Section 4.7.

When $s = t_{\frac{1}{2}}$ and $\mu_0 = \bar{\mu}_0 = 0$ in (4.22), this scheme is applicable to the frozen-coefficient Ito SDE (4.12).

The CP scheme (4.17) involves the spatial derivatives of coefficients, while KP scheme (4.19) and TV scheme (4.21) are derivative-free.

In this section, the numerical solution to the Ito SDEs (4.8) and (4.12) is discussed. Below (in Section 4.5), we discuss the numerical solution to the scalar

equation (4.7) and the splitting schemes of the coupled system (4.6) and (4.7). Before discussing the solution of the scalar equation, in the next section we first develop the method of manufactured solutions (MMS) for the particle method, and derive the augmented particle scalar equation for the purpose of verification.

4.4 Method of manufactured solutions (MMS) for Monte Carlo particle methods

A numerical test case with known exact solutions (or with highly accurate numerical solutions via other methods) is often required for validating models and algorithms and for verifying the computer programming. MMS [39, 40] provides a general procedure for generating an analytical solution for this purpose. MMS was primarily used in the verification of the numerical solution of partial differential equations (PDEs) with finite-difference, finite-volume, and finite-element based numerical methods in the past [41, 42, 43, 44]. In that practice, the analytical solutions to the equations to be solved were manufactured. In the current Monte Carlo particle method, however, we need the analytical solutions to the quantities which are not directly solved, i.e., the SDE system (4.6) and (4.7) is solved numerically, while the moments of the scalar $\overline{\phi^q}$ are used for examining the weak convergence. In the following, we first obtain the augmented PDEs admitting the manufactured solutions of scalar moments, then derive the augmented SDE system consistent with the augmented PDEs. In principle, any order of scalar moment should be tested for convergence. However, this is technically impractical. In this work, we consider mostly the first

and second moments of the scalar, which are the primary interest of PDF applications. For one case, we present the convergence results for the third and fourth moments (Section 4.6.3). The analysis of the schemes discussed in this paper indicates that they are all convergent (with first or second-order accuracy) for the PDF and hence for all moments. This convergence has been verified for the first four moments, and there is no reason to doubt that higher moments converge similarly.

4.4.1 Augmented SDE system for MMS

In this work, we consider the manufactured solutions only for the scalar mean and variance. In the transport equations for the scalar mean $\overline{\phi}$ (4.3) and variance $\overline{\phi'^2}$ (4.5), the terms containing the reaction source term $S(\phi)$ are generally unclosed because of the non-linearity of the reaction term. Closing these equations requires that $\overline{S\phi}(\mathbf{x}, t)$ and $\overline{S}(\mathbf{x}, t)$ be known in terms of $\overline{\phi}$ and $\overline{\phi^2}$, which in turn requires $S(\phi)$ to be linear in ϕ. Hence, for verification purposes, we specify the following linear relation

$$S(\phi) = R_a(\phi(\mathbf{x}, t) - R_b), \tag{4.25}$$

in which R_a and R_b are specified constants. Substituting the above equation into (4.3) and (4.5), we see that those equations become closed.

We need analytical solutions for $\overline{\phi}$ and $\overline{\phi'^2}$ to (4.3) and (4.5) for the error estimate in the convergence study. In general, these analytical solutions cannot be obtained. The idea of the MMS is to specify analytical functions of $\overline{\phi}_m$ and $\overline{\phi'^2}_m$ in advance, where the subscript "m" denotes manufactured solution. These functions certainly do not satisfy (4.3) and (4.5) in general. They satisfy the fol-

lowing augmented equations with extra source terms (S_m and S_v) compared to the original ones

$$\begin{aligned}\frac{\partial\overline{\phi}_m(\mathbf{x},t)}{\partial t}+\frac{\partial\overline{u}_i(\mathbf{x},t)\overline{\phi}_m(\mathbf{x},t)}{\partial x_i} &= \frac{\partial}{\partial x_i}\left(\Gamma(\mathbf{x},t)\frac{\partial\overline{\phi}_m(\mathbf{x},t)}{\partial x_i}\right)\\ &+ R_a\left(\overline{\phi}_m(\mathbf{x},t)-R_b\right)+S_m(\mathbf{x},t), \qquad (4.26)\end{aligned}$$

$$\begin{aligned}\frac{\partial\overline{\phi'^2}_m(\mathbf{x},t)}{\partial t}+\frac{\partial\overline{u}_i(\mathbf{x},t)\overline{\phi'^2}_m(\mathbf{x},t)}{\partial x_i} &= \frac{\partial}{\partial x_i}\left(\Gamma(\mathbf{x},t)\frac{\partial\overline{\phi'^2}_m(\mathbf{x},t)}{\partial x_i}\right)\\ &+ 2\Gamma(\mathbf{x},t)\frac{\partial\overline{\phi}_m(\mathbf{x},t)}{\partial x_i}\frac{\partial\overline{\phi}_m(\mathbf{x},t)}{\partial x_i}-2\Omega(\mathbf{x},t)\overline{\phi'^2}_m(\mathbf{x},t)\\ &+ 2R_a\overline{\phi'^2}_m(\mathbf{x},t)+S_v(\mathbf{x},t). \qquad (4.27)\end{aligned}$$

The forcing terms S_m and S_v are determined from the above equations, given the specifications for all the other functions in the equations. We now turn our attention to a problem satisfying the above equations (4.26) and (4.27).

Due to the extra source terms, the above equations (4.26) and (4.27) are no longer consistent with the PDF equation (4.1) and the particle equations (4.6) and (4.7). A consistent PDF equation can be obtained in the following

$$\begin{aligned}\frac{\partial f(\psi;\mathbf{x},t)}{\partial t}+\frac{\partial\overline{u}_i(\mathbf{x},t)f(\psi;\mathbf{x},t)}{\partial x_i} &= \frac{\partial}{\partial x_i}\left(\Gamma(\mathbf{x},t)\frac{\partial f(\psi;\mathbf{x},t)}{\partial x_i}\right)\\ &+ \frac{\partial}{\partial\psi}\left(\Omega(\mathbf{x},t)(\psi-\overline{\phi}_m(\mathbf{x},t))f(\psi;\mathbf{x},t)\right)\\ &- \frac{\partial}{\partial\psi}\left(R_a(\psi-R_b)f(\psi;\mathbf{x},t)\right)\\ &- S_m(\mathbf{x},t)\frac{\partial f(\psi;\mathbf{x},t)}{\partial\psi}\\ &+ \frac{\partial}{\partial\psi}\left(\Omega_v(\mathbf{x},t)(\psi-\overline{\phi}_m(\mathbf{x},t))f(\psi;\mathbf{x},t)\right) \qquad (4.28)\end{aligned}$$

where $\Omega_v(\mathbf{x},t)=-S_v(\mathbf{x},t)/\left(2\overline{\phi'^2}_m(\mathbf{x},t)\right)$ is a scalar-frequency-like quantity due to the source term S_v. (Notice that $\Omega_v(\mathbf{x},t)$ can be negative.) The implementation of the IEM model is adapted to account for the effect of Ω_v to obtain the correct variation rate of scalar variance. Other mixing models (e.g. modified Curl or

EMST) are not appropriate for this term when $\Omega_v(\mathbf{x}, t)$ becomes negative. The corresponding (augmented) particle scalar equation is then

$$\begin{aligned}\frac{d\phi(t)}{dt} = & - \Omega(\mathbf{X}(t), t)(\phi(t) - \overline{\phi}_m(\mathbf{X}(t), t)) + R_a(\phi(t) - R_b) + S_m(\mathbf{X}(t), t) \\ & - \Omega_v(\mathbf{X}(t), t)(\phi(t) - \overline{\phi}_m(\mathbf{X}(t), t)). \end{aligned} \tag{4.29}$$

The four terms on the right-hand side represent the molecular mixing process $\mathbb{M}$, reaction process $\mathbb{R}$, scalar mean forcing process $\mathbb{S}$, and scalar variance forcing process $\mathbb{V}$, respectively. This equation can be simplified, e.g., by combining $\mathbb{M}$ and $\mathbb{V}$, but we generally do not combine them due to the physical difference of each process and due to the flexibility of implementing different sub-models for each process (e.g., using other mixing models for $\mathbb{M}$).

The particle position equation (4.6) deals with the convection and diffusion of the PDF which are not changed in (4.28), so (4.6) remains the same after using the MMS. The particle equations to be considered now become (4.6) and (4.29).

A particular MMS test case requires the specification of $\overline{\phi}_m(\mathbf{x}, t)$, $\overline{\phi^2}_m(\mathbf{x}, t)$, $\overline{u}(\mathbf{x}, t)$, $\Gamma(\mathbf{x}, t)$, $S_m(\mathbf{x}, t)$, $S_v(\mathbf{x}, t)$, and $\Omega(\mathbf{x}, t)$. In Appendix D, these specifications are given for the tests used in this study.

4.4.2 Error analysis for weak convergence

The manufactured solutions to the first two moments of the scalar are discussed in the previous sub-section. Here, we discuss how to use these solutions to measure the numerical error.

We consider a one-dimensional problem, and the computational domain $[0, L_0]$ is partitioned into I cells $[x_i - \frac{\Delta x_i}{2}, x_i + \frac{\Delta x_i}{2}]$, $i = 1, \cdots, I$, where x_i is the

center of the ith grid cell and Δx_i is the cell size. The grid used for the error analysis is often the same as the grid used in the finite-volume method of the flow fields which is generally non-uniform. The volume average $\left\langle \overline{\phi^q} \right\rangle_i$ of the qth scalar moment in the ith cell is

$$\left\langle \overline{\phi^q} \right\rangle_i = \frac{1}{\Delta x_i} \int_{x_i - \frac{\Delta x_i}{2}}^{x_i + \frac{\Delta x_i}{2}} \overline{\phi^q}_m(x, T) dx, \tag{4.30}$$

where $\langle \cdot \rangle$ denotes volume average and $\overline{\phi^q}_m(x, t)$ is the manufactured solution. The volume average $\left\langle \overline{\phi^q} \right\rangle$ is used as the exact solution in (4.11) to evaluate the numerical error of the particle method.

The Monte Carlo particle method involves the tracking of many particles governed by (4.6) and (4.29). To obtain accurate estimates of scalar moments, a very large number of particles is required (e.g., up to the order of 10^{10}) for the currently considered test case (with a small time step). The exact required number of particles is not known in advance. We perform the convergence tests with an adaptive number of particles, i.e., we perform the simulation with a fixed number of particles (e.g., 10^4) and repeat the trials independently many times as needed (e.g., repeat 10^6 times to achieve 10^{10} particles for the above case).

The numerical approximation to $\left\langle \overline{\phi^q} \right\rangle_i$ can be estimated from the ensemble average of the particles in the cell

$$\left\langle \overline{\phi^q} \right\rangle_{i,k}^* = \frac{1}{N_{i,k}} \sum_{n=1}^{N_{i,k}} \phi_{n,i,k}^q(T), \tag{4.31}$$

where $\phi_{n,i,k}$ is the scalar value of the nth particle in the ith cell for the kth trial, $N_{i,k}$ is the number of particles in the cell for the kth trial, and $\langle \cdot \rangle^*$ denotes an ensemble average.

The numerical error in predicting the qth scalar moment for the ith cell on

the kth trial is then measured as

$$e_{q,i,k} = \left\langle \overline{\phi^q} \right\rangle_{i,k}^{*} - \left\langle \overline{\phi^q} \right\rangle_{i}. \tag{4.32}$$

For the finite number of particles in the simulation, the numerical error $e_{q,i,k}$ is a random variable with an approximately Gaussian distribution, and can be decomposed as

$$e_{q,i,k} = \mu_{q,i} + \sigma_{q,i}\xi_{q,i,k}, \tag{4.33}$$

(with no implied summation), where $\mu_{q,i} \equiv E\left(e_{q,i,k}\right)$, $\sigma_{q,i}^2 \equiv \mathrm{var}\left(e_{q,i,k}\right)$, and $\xi_{q,i,k}$ is a standardized Gaussian random variable ($\left\langle \xi_{q,i,k} \right\rangle = 0$, $\mathrm{var}(\xi_{q,i,k}) = 1$), which is independent on each trial ($\left\langle \xi_{q,i,k}\xi_{q,i,l} \right\rangle = 0$, $k \neq l$), but not necessarily from cell to cell ($\left\langle \xi_{q,i,k}\xi_{q,l,k} \right\rangle \neq 0$). The deterministic error $\mu_{q,i}$ consists of two possible sources: the time-stepping error (which scales as Δt^2 for second-order schemes), and the bias error (which scales as N_{trial}^{-1} [23], N_{trial} being the number of particles per trial). In this study, the number of particles is on the order of 10^4, and the results reported in Section 4.6 support the supposition that the bias error is small compared to the time-stepping error (for the smallest time step $\Delta t/T = \frac{1}{40}$). The statistical error $\sigma_{q,i}$ scales as $N^{-1/2}$ in which N is the total number of particles used in a convergence test.

We define a global error $\mathcal{E}_{\overline{\phi^q}}$,

$$E\left(\mathcal{E}_{\overline{\phi^q}}\right) \equiv \left[\frac{1}{I}\sum_{i=1}^{I}\mu_{q,i}^2\right]^{1/2}, \tag{4.34}$$

which, in the case of an infinite number of trials, is the two-norm (over the cells) of the expectation of $e_{q,i,k}$. In Appendix C we describe the construction of an un-biased estimate of $\mathcal{E}_{\overline{\phi^q}}$ based on a finite number of trials.

We use the global measure of error $\mathcal{E}_{\overline{\phi^q}}$ to investigate the numerical accuracy and convergence. The global error uses all the particles from the simulation, so it presumably involves less statistical error than the local error which uses a small portion of particles from the simulations, although the cell-to-cell estimates of the local error are not independent. Due to the random nature of the global error, multiple sets of trials are performed to estimate the mean and variance of $\mathcal{E}_{\overline{\phi^q}}$, and hence to estimate the confidence interval of the error.

4.4.3 Computational cost of a Monte Carlo convergence study

In this sub-section, we give an estimate of the computational requirement for verifying the convergence of the Monte Carlo method. In this work, we are primarily interested in the time-stepping error. The computational cost of the Monte Carlo simulation is proportional to the number of particles multiplied by the time steps taken. From the previous discussion, we know that the mean and standard deviation of the error scale as $\mu_{q,i} \approx C_\mu \Delta t^p$ and $\sigma_{q,i} \approx C_\sigma N^{-1/2}$, so (4.33) becomes

$$e_{q,i,k}\left(\overline{\phi^q}\right) \approx C_\mu \Delta t^p + C_\sigma \frac{1}{N^{1/2}} \xi_{q,i,k}, \tag{4.35}$$

where C_μ and C_σ are constants.

To show the numerical convergence of $e_{q,i,k}$ with respect to the time step Δt, we require that the time-stepping error dominates the statistical error in (4.35), i.e., $C_\mu \Delta t^p \gg C_\sigma N^{-1/2}$. The ratio between the statistical error and the time-stepping error is

$$C_r = C_\sigma N^{-1/2} / C_\mu \Delta t^p \ll 1, \tag{4.36}$$

where C_r is a constant, then

$$N = C_\sigma^2 C_\mu^{-2} C_r^{-2} \Delta t^{-2p}. \tag{4.37}$$

The total number of time steps taken is $N_t = T/\Delta t$, so then the computational cost F for verifying Monte Carlo convergence scales as

$$F = N \cdot N_t = C_\sigma^2 T C_\mu^{-2} C_r^{-2} \Delta t^{-2p-1} \propto \Delta t^{-2p-1}. \tag{4.38}$$

For weak second-order numerical schemes ($p = 2$), the computational cost F scales as Δt^{-5}. Hence to make the computation affordable, simplification is made on the test case as discussed in Section 4.1, i.e., one-dimensional, constant density, and single scalar.

In this section, the MMS for the Monte Carlo particle method is developed. The error analysis and the computational cost are discussed. The manufactured analytical solutions to the one-dimensional problem for convergence test is designed and shown in Appendix D.

4.5 Weak second-order splitting schemes

In this section, we develop the weak second-order splitting schemes for the coupled SDE system (4.8) and (4.10) (and the frozen-coefficient system (4.12) and (4.13)). To construct second-order splitting schemes for the coupled system, a necessary condition is to have the SDE and the scalar equation each integrated with at least second-order accuracy. The (weak) second-order schemes to the SDE have been discussed in Section 4.3.3. In the following, different second-order splitting schemes for the scalar equation are first discussed, and then the splitting schemes for the coupled SDE system.

4.5.1 Sub-stepping of scalar evolution

The augmented particle scalar equation (4.29) can be solved by ODE schemes. As discussed in Section 4.4.1, this equation describes four processes (mixing $\mathbb{M}$, reaction $\mathbb{R}$, scalar mean forcing $\mathbb{S}$, and scalar variance forcing $\mathbb{V}$), and sub-stepping is often used to solve this kind of equation, i.e., splitting (4.29) into the following four equations to solve separately with each describing one process,

$$\mathbb{M}: \frac{d\phi(t)}{dt} = -\Omega(\mathbf{X}(t),t)(\phi(t)-\overline{\phi}(\mathbf{X}(t),t)), \tag{4.39}$$

$$\mathbb{R}: \frac{d\phi(t)}{dt} = +R_a\left(\phi(t)-R_b\right), \tag{4.40}$$

$$\mathbb{S}: \frac{d\phi(t)}{dt} = +S_m(\mathbf{X}(t),t), \tag{4.41}$$

$$\mathbb{V}: \frac{d\phi(t)}{dt} = -\Omega_v(\mathbf{X}(t),t)(\phi(t)-\overline{\phi}(\mathbf{X}(t),t)). \tag{4.42}$$

Consider one step of integration over the time interval $[t_0, t_0+\Delta t]$ from the initial condition $\phi_0 = \phi(t_0)$. The numerical solution $\varphi(t)$ to the above four equations can be obtained as following.

Mixing sub-step $\mathbb{M}$: In (4.39), if Ω and $\overline{\phi}$ are frozen at some particle position $\mathbf{X}(r)$ and time s ($r, s \in [t_0, t_0+\Delta t]$), then the analytical solution to the mixing sub-step is

$$\begin{aligned}\varphi(t_1) &= \mathcal{M}(\phi_0, \mathbf{X}(r), s, \Delta t)\\ &= \overline{\phi}(\mathbf{X}(r),s) + \left(\phi_0 - \overline{\phi}(\mathbf{X}(r),s)\right)\exp\left(-\Omega(\mathbf{X}(r),s)\Delta t\right).\end{aligned} \tag{4.43}$$

For the splitting schemes of the SDE system (4.8) and (4.10), we require that the time r to be equal to s to evaluate the coefficients Ω and $\overline{\phi}$, and the time (r and s) can be specified for different schemes, e.g., $r = s = t_0$ for explicit schemes, $t_0 < r = s \leqslant t_1$ for implicit schemes, where $t_\alpha = t_0 + \alpha\Delta t$ ($0 \leqslant \alpha \leqslant 1$). Second-order accuracy can be achieved by choosing $r = s = t_{\frac{1}{2}}$. When used in solving

the frozen-coefficient scalar equation (4.13), the time in (4.43) is $s = t_{\frac{1}{2}}$, while the time r can be different from s. The particle position $\mathbf{X}(r)$ at time r for the evaluation of the scalar coefficients is the result of the previous transport sub-step, and is available only at three times $r = t_0$, $t_{\frac{1}{2}}$ and t_1 in a second-order splitting scheme (with the exceptions of $\mathbb{T}^{\text{cp}}\mathbb{C}\mathbb{R}\mathbb{C}'\mathbb{T}^{\text{cp}}$ and $\mathbb{T}^{\text{cp}}\mathbb{C}\mathbb{R}\mathbb{C}'\mathbb{T}^{\text{cp}}$-F in Section 4.5.2 in which $\mathbf{X}$ is available also at $r = t_{\frac{1}{4}}$ and $t_{\frac{3}{4}}$). The meaning of r and s is the same for the other sub-steps.

The scalar mean $\overline{\phi}(\mathbf{X}, s)$ can be approximated by the cell mean of particles at time s. During the mixing sub-step (and the scalar variance forcing sub-step), the scalar mean is preserved, and so the scalar mean is the same at different times within the sub-step, e.g., $\overline{\phi}(\mathbf{X}, s) = \overline{\phi}(\mathbf{X}, t_0)$. Hence the scalar mean at t_0 approximated by the initial particle scalar can be used in (4.43) to construct different splitting schemes including second-order accurate schemes. For the nth particle in the ith cell, the scalar mean is approximated as

$$\overline{\phi}^{(n)}(\mathbf{X}_n, s) = \overline{\phi}^{(n)}(\mathbf{X}_n, t_0) \approx \frac{1}{N_i - 1} \sum_{j=1, j\neq n}^{N_i} \phi_j(t_0)\big|_{\mathbf{X}_j \in \left[\mathbf{x}_i - \frac{\Delta \mathbf{x}_i}{2}, \mathbf{x}_i + \frac{\Delta \mathbf{x}_i}{2}\right]}, \tag{4.44}$$

where the particle itself is removed from the cell mean in order to remove the correlation between the particle and the cell mean. This is a first-order approximation in space to $\overline{\phi}^{(n)}(\mathbf{X}_n, t_0)$. A second-order approximation can be constructed by interpolating the cell mean to the particle position. We consider only the time-stepping error in this work, so the simplest approximation method is used to obtain $\overline{\phi}^{(n)}(\mathbf{X}_n, t_0)$. The grid size is specified to be sufficiently small that the spatial discretization error is small compared to the time-stepping error. All the results in Section 4.6 show the consistent asymptotical behavior of the numerical errors against the time step for the time steps considered, confirming that the spatial discretization error in the test is significantly smaller than the

time-stepping error.

Reaction sub-step $\mathbb{R}$**:** The linear reaction sub-step (4.40) is integrated analytically

$$\begin{aligned} \varphi(t_1) &= \mathcal{R}(\phi_0, \Delta t) \\ &= R_b + (\phi_0 - R_b) \exp(R_a \Delta t). \end{aligned} \tag{4.45}$$

Scalar mean forcing sub-step $\mathbb{S}$**:** The scalar mean forcing sub-step (4.41) is integrated as

$$\begin{aligned} \varphi(t_1) &= \mathcal{S}(\phi_0, \mathbf{X}(r), s, \Delta t) \\ &= \phi_0 + S_m(\mathbf{X}(r), s)\Delta t. \end{aligned} \tag{4.46}$$

Scalar variance forcing sub-step $\mathbb{V}$**:** In (4.42), if Ω_v and $\overline{\phi}$ are frozen at some particle position $\mathbf{X}(r)$ and time s, then the analytical solution to the scalar variance forcing sub-step is

$$\begin{aligned} \varphi(t_1) &= \mathcal{V}(\phi_0, \mathbf{X}(r), s, \Delta t) \\ &= \overline{\phi}(\mathbf{X}(r), s) + \left(\phi_0 - \overline{\phi}(\mathbf{X}(r), s)\right) \exp(\Omega_v(\mathbf{X}(r), s)\Delta t). \end{aligned} \tag{4.47}$$

For designing different second-order splitting schemes for the scalar equation only, we consider the limit of no particle movement $\mathbf{X}(r) = \mathbf{X}(0)$ (e.g., $\mathbf{D} = 0$ and $b = 0$ in the SDE), and then the scalar equation is an ODE. If the four scalar sub-steps (4.43), (4.45), (4.46) and (4.47) are advanced in order (e.g., $\mathbb{MRSV}$) with each one taking one full time step once, the result is first-order accurate (provided that each sub-step is integrated with at least first-order accuracy). Symmetric splitting schemes can be constructed which potentially have second-order accuracy, for example, the scheme denoted $\mathbb{SVMRMVS}$. By this notation,

we mean that the processes $\mathbb{S}$, $\mathbb{V}$, $\mathbb{M}$, $\mathbb{R}$, $\mathbb{M}$, $\mathbb{V}$, $\mathbb{S}$ are performed (in that order) with the initial condition for each process being the result of its predecessor. If a process is performed just once (like $\mathbb{R}$ in this example), then it is performed for a time interval Δt. On the other hand, if the process is performed twice (like $\mathbb{S}$, $\mathbb{V}$, and $\mathbb{M}$ in this example) then it is for a time interval of $\Delta t/2$ each time.

If each sub-step of $\mathbb{SVMRMVS}$ is integrated with second-order accuracy (e.g., by evaluating coefficients at the mid-time of the sub-step), this splitting is called Strang splitting [48] which has overall second-order accuracy. We denote the Strang splitting scheme as $\mathbb{SVMRMVS}$-I, and write down the scheme in Table 4.1. The Strang splitting needs to evaluate coefficients at $t_{\frac{1}{4}}$ and $t_{\frac{3}{4}}$, and $\mathbf{X}(t_{\frac{1}{4}})$ and $\mathbf{X}(t_{\frac{3}{4}})$. These particle locations are not computed in the transport sub-step of the most of the splitting schemes discussed in this work. For most schemes, only $\mathbf{X}(t_0)$, and approximations to $\mathbf{X}(t_{\frac{1}{2}})$ and $\mathbf{X}(t_1)$ are available for the construction of the second-order splitting schemes. It is not necessary, however, to have each sub-step of $\mathbb{SVMRMVS}$ integrated with second-order accuracy to construct a second-order splitting scheme. We consider two splitting schemes $\mathbb{SVMRMVS}$-II and $\mathbb{SVMRMVS}$-III (as shown in Table 4.1) which involve only first-order integration of some sub-steps, e.g., the first half time step of $\mathcal{S}$, $\mathcal{V}$ and $\mathcal{M}$. The second-order accuracy of the two splitting schemes $\mathbb{SVMRMVS}$-II and $\mathbb{SVMRMVS}$-III can be easily shown for ODEs (by freezing particle position and by showing that the results from $\mathbb{SVMRMVS}$-II and $\mathbb{SVMRMVS}$-III are consistent with those from $\mathbb{SVMRMVS}$-I up to order Δt^2, using Taylor series expansions). The three schemes in Table 4.1 can be generalized to a class of second-order splitting schemes by evaluating the scalar coefficients at $t = t_{\frac{1}{2}\pm h}$ ($h \in [0, \frac{1}{2}]$), i.e., evaluating coefficients at $t = t_{\frac{1}{2}-h}$ for the first half steps of $\mathcal{S}$, $\mathcal{V}$ and $\mathcal{M}$ and at $t = t_{\frac{1}{2}+h}$ for their second half steps. In this work, we only use the splitting

$\mathbb{SVMRMVS}$-II and $\mathbb{SVMRMVS}$-III for the construction of the second-order splitting schemes for the coupled SDE system.

Table 4.1: Second-order splitting schemes for the particle scalar equation (4.29)

$\mathbb{SVMRMVS}$-I	$\mathbb{SVMRMVS}$-II	$\mathbb{SVMRMVS}$-III
$\varphi_1 = \mathcal{S}(\phi_0, \mathbf{X}(t_{\frac{1}{4}}), t_{\frac{1}{4}}, \frac{\Delta t}{2})$	$\varphi_1 = \mathcal{S}(\phi_0, \mathbf{X}(t_{\frac{1}{2}}), t_{\frac{1}{2}}, \frac{\Delta t}{2})$	$\varphi_1 = \mathcal{S}(\phi_0, \mathbf{X}(t_0), t_0, \frac{\Delta t}{2})$
$\varphi_2 = \mathcal{V}(\varphi_1, \mathbf{X}(t_{\frac{1}{4}}), t_{\frac{1}{4}}, \frac{\Delta t}{2})$	$\varphi_2 = \mathcal{V}(\varphi_1, \mathbf{X}(t_{\frac{1}{2}}), t_{\frac{1}{2}}, \frac{\Delta t}{2})$	$\varphi_2 = \mathcal{V}(\varphi_1, \mathbf{X}(t_0), t_0, \frac{\Delta t}{2})$
$\varphi_3 = \mathcal{M}(\varphi_2, \mathbf{X}(t_{\frac{1}{4}}), t_{\frac{1}{4}}, \frac{\Delta t}{2})$	$\varphi_3 = \mathcal{M}(\varphi_2, \mathbf{X}(t_{\frac{1}{2}}), t_{\frac{1}{2}}, \frac{\Delta t}{2})$	$\varphi_3 = \mathcal{M}(\varphi_2, \mathbf{X}(t_0), t_0, \frac{\Delta t}{2})$
$\varphi_4 = \mathcal{R}(\varphi_3, \Delta t)$	$\varphi_4 = \mathcal{R}(\varphi_3, \Delta t)$	$\varphi_4 = \mathcal{R}(\varphi_3, \Delta t)$
$\varphi_5 = \mathcal{M}(\varphi_4, \mathbf{X}(t_{\frac{3}{4}}), t_{\frac{3}{4}}, \frac{\Delta t}{2})$	$\varphi_5 = \mathcal{M}(\varphi_4, \mathbf{X}(t_{\frac{1}{2}}), t_{\frac{1}{2}}, \frac{\Delta t}{2})$	$\varphi_5 = \mathcal{M}(\varphi_4, \mathbf{X}(t_1), t_1, \frac{\Delta t}{2})$
$\varphi_6 = \mathcal{V}(\varphi_5, \mathbf{X}(t_{\frac{3}{4}}), t_{\frac{3}{4}}, \frac{\Delta t}{2})$	$\varphi_6 = \mathcal{V}(\varphi_5, \mathbf{X}(t_{\frac{1}{2}}), t_{\frac{1}{2}}, \frac{\Delta t}{2})$	$\varphi_6 = \mathcal{V}(\varphi_5, \mathbf{X}(t_1), t_1, \frac{\Delta t}{2})$
$\varphi(t_1) = \mathcal{S}(\varphi_6, \mathbf{X}(t_{\frac{3}{4}}), t_{\frac{3}{4}}, \frac{\Delta t}{2})$	$\varphi(t_1) = \mathcal{S}(\varphi_6, \mathbf{X}(t_{\frac{1}{2}}), t_{\frac{1}{2}}, \frac{\Delta t}{2})$	$\varphi(t_1) = \mathcal{S}(\varphi_6, \mathbf{X}(t_1), t_1, \frac{\Delta t}{2})$

The splitting schemes discussed above are applicable to the original scalar equation (4.10). They are also applicable to the frozen-coefficient scalar equation (4.13) by specifying $s = t_{\frac{1}{2}}$ in function $\mathcal{S}, \mathcal{V}, \mathcal{M}$ (retaining the time r in $\mathbf{X}(r)$ in the schemes).

We can construct different symmetric splitting schemes with potential second-order accuracy, e.g., $\mathbb{SVRMRVS}$, $\mathbb{MRSVSRM}$. We will not discuss the difference of these different splittings for the scalar equation. In practice, performing one step of reaction $\mathbb{R}$ (like $\mathbb{SVMRMVS}$) in the middle is preferable. Usually, the reaction computation in combustion is dominant, so reducing the number of sub-steps of reactions in the computation reduces the overall computational cost linearly. In order to reduce the reaction computational cost significantly, the *in situ* adaptive tabulation (ISAT) method [49] is often used. Taking a longer time step in ISAT reduces the table size and hence speeds up ISAT. Therefore, performing one step of reaction in the splitting is advantageous.

In the following discussion, we will consider only the splitting $\mathbb{SVMRMVS}$. For simplicity, we denote $\mathbb{SVM}$ as $\mathbb{C}$ and $\mathbb{MVS}$ as $\mathbb{C}'$, and so the splitting simply becomes $\mathbb{CRC}'$.

4.5.2 Splitting schemes of the coupled SDE system

The numerical schemes for the Ito SDE (4.8) and (4.12) and for the augmented particle scalar equation (4.29) have been discussed in Sections 4.3.3 and 4.5.1, respectively. Second-order accuracy is achieved for solving the individual equation. In this part, we combine these numerical schemes and develop the weak second-order splitting schemes for the coupled SDE system.

4.5.2.1 Splitting schemes based on the CP scheme

The splitting schemes in this part (4.5.2.1) are only appropriate for the mid-point SDE schemes (e.g., the CP scheme (4.14) and (4.15)). The splitting scheme first suggested by Cao and Pope [25] is denoted by $\mathbb{T}_1^{\text{cp}}\mathbb{CRC}'\mathbb{T}_2^{\text{cp}}$ in Table 4.2, where the functions $\mathcal{T}_1^{\text{cp}}$ and $\mathcal{T}_2^{\text{cp}}$ are defined in (4.14) and (4.15), and the splitting scheme $\mathbb{SVMRMVS}$-II in Table 4.1 is used for the scalar equation. Note that this scheme is not symmetrical, in that the final process $\mathcal{T}_2^{\text{cp}}$ is different from the first process $\mathcal{T}_1^{\text{cp}}$.

From the previous discussions, if the equations for $\mathbf{X}(t)$ and $\phi(t)$ are integrated separately, $\mathbf{Y}(t_1)$ and $\varphi(t_1)$ from $\mathbb{T}_1^{\text{cp}}\mathbb{CRC}'\mathbb{T}_2^{\text{cp}}$ are (weak) second-order approximations to $\mathbf{X}(t_1)$ and $\phi(t_1)$, respectively. When coupled, in order to achieve overall weak second-order accuracy, $\mathbf{Y}(t_{\frac{1}{2}})$ must be a weak first-order approxi-

Table 4.2: Splitting schemes for the coupled SDE system (4.8) (or (4.12)) and (4.29) based on the CP scheme (4.14) and (4.15)

$\mathbb{T}_1^{\text{cp}}\mathbb{C}\mathbb{R}\mathbb{C}'\mathbb{T}_2^{\text{cp}}$	$\mathbb{T}_1^{\text{cp}}\hat{\mathbb{T}}_1^{\text{cp}}\mathbb{C}\mathbb{R}\mathbb{C}'\mathbb{T}_2^{\text{cp}}$	$\mathbb{T}_1^{\text{cp}}\hat{\mathbb{T}}_1^{\text{cp}}\mathbb{C}\mathbb{R}\mathbb{C}'\mathbb{T}_2^{\text{cp}}$-F
$\mathbf{Y}(t_{\frac{1}{2}}) = \mathbf{X}_0 +$ $\mathcal{T}_1^{\text{cp}}(\mathbf{X}_0, t_0, \Delta t, \boldsymbol{\zeta})$	$\mathbf{Y}(t_{\frac{1}{2}}) = \mathbf{X}_0 +$ $\mathcal{T}_1^{\text{cp}}(\mathbf{X}_0, t_0, \Delta t, \frac{\boldsymbol{\xi}+\boldsymbol{\eta}}{2} + \frac{\boldsymbol{\vartheta}}{\sqrt{2}})$ $\hat{\mathbf{Y}}(t_{\frac{1}{2}}) = \mathbf{X}_0 +$ $\mathcal{T}_1^{\text{cp}}(\mathbf{X}_0, t_0, \Delta t, \boldsymbol{\zeta})$	$\mathbf{Y}(t_{\frac{1}{2}}) = \mathbf{X}_0 +$ $\mathcal{T}_1^{\text{cp}}(\mathbf{X}_0, t_{\frac{1}{2}}, \Delta t, \frac{\boldsymbol{\xi}+\boldsymbol{\eta}}{2} + \frac{\boldsymbol{\vartheta}}{\sqrt{2}})$ $\hat{\mathbf{Y}}(t_{\frac{1}{2}}) = \mathbf{X}_0 +$ $\mathcal{T}_1^{\text{cp}}(\mathbf{X}_0, t_{\frac{1}{2}}, \Delta t, \boldsymbol{\zeta})$
$\varphi_1 = \mathcal{S}(\phi_0, \mathbf{Y}(t_{\frac{1}{2}}), t_{\frac{1}{2}}, \frac{\Delta t}{2}),\quad \varphi_2 = \mathcal{V}(\varphi_1, \mathbf{Y}(t_{\frac{1}{2}}), t_{\frac{1}{2}}, \frac{\Delta t}{2}),\quad \varphi_3 = \mathcal{M}(\varphi_2, \mathbf{Y}(t_{\frac{1}{2}}), t_{\frac{1}{2}}, \frac{\Delta t}{2})$ $\varphi_4 = \mathcal{R}(\varphi_3, \Delta t)$ $\varphi_5 = \mathcal{M}(\varphi_4, \mathbf{Y}(t_{\frac{1}{2}}), t_{\frac{1}{2}}, \frac{\Delta t}{2}),\quad \varphi_6 = \mathcal{V}(\varphi_5, \mathbf{Y}(t_{\frac{1}{2}}), t_{\frac{1}{2}}, \frac{\Delta t}{2}),\quad \varphi(t_1) = \mathcal{S}(\varphi_6, \mathbf{Y}(t_{\frac{1}{2}}), t_{\frac{1}{2}}, \frac{\Delta t}{2})$		
$\mathbf{Y}(t_1) = \mathbf{Y}(t_{\frac{1}{2}}) +$ $\mathcal{T}_2^{\text{cp}}(\mathbf{X}_0, \mathbf{Y}(t_{\frac{1}{2}}), t_{\frac{1}{2}}, \Delta t, \boldsymbol{\xi}, \boldsymbol{\eta})$	$\mathbf{Y}(t_1) = \hat{\mathbf{Y}}(t_{\frac{1}{2}}) +\quad \mathcal{T}_2^{\text{cp}}(\mathbf{X}_0, \hat{\mathbf{Y}}(t_{\frac{1}{2}}), t_{\frac{1}{2}}, \Delta t, \boldsymbol{\xi}, \boldsymbol{\eta})$	

mation to the mid-point $\mathbf{X}(t_{\frac{1}{2}})$ given the initial and final positions $\mathbf{X}_0$ and $\mathbf{Y}(t_1)$. However, the sub-steps of the CP scheme (4.14) and (4.15) use independent Gaussian random vectors, which makes the mid-point approximation $\mathbf{Y}(t_{\frac{1}{2}})$ impossible to represent the correct distribution given the initial and final positions. Hence the splitting scheme $\mathbb{T}_1^{\text{cp}}\mathbb{C}\mathbb{R}\mathbb{C}'\mathbb{T}_2^{\text{cp}}$ degrades to overall first-order accuracy despite of the second-order accuracy achieved by each equation.

Introducing another mid-point $\mathbf{Y}(t_{\frac{1}{2}})$ (the original one is $\hat{\mathbf{Y}}(t_{\frac{1}{2}})$) which is correlated to the increment of the second-step of the CP scheme achieves overall second-order accuracy. The new splitting scheme is shown as $\mathbb{T}_1^{\text{cp}}\hat{\mathbb{T}}_1^{\text{cp}}\mathbb{C}\mathbb{R}\mathbb{C}'\mathbb{T}_2^{\text{cp}}$ in Table 4.2 in which the $\hat{\mathbf{Y}}(t_{\frac{1}{2}})$ step is denoted by $\hat{\mathbb{T}}_1^{\text{cp}}$, and $\boldsymbol{\vartheta}$ is another independent Gaussian random vector. The step $\mathbb{T}_1^{\text{cp}}$ is exactly the same as $\hat{\mathbb{T}}_1^{\text{cp}}$ except using a different random vector for the Wiener process. The second-step (4.15) of the CP scheme can be simply viewed as a Wiener process $\mathbf{W}(t)$. If we consider $\mathbf{W}(t_1) = \boldsymbol{\xi} + \boldsymbol{\eta}$ at $t_1 = 2$ starting from $\mathbf{W}(t_0) = 0$, then $\mathbf{W}(t_{\frac{1}{2}})$ has the same distribution as $\frac{\boldsymbol{\xi}+\boldsymbol{\eta}}{2} + \frac{\boldsymbol{\vartheta}}{\sqrt{2}}$. Therefore, $\mathbf{Y}(t_{\frac{1}{2}})$ represents the distribution of $\mathbf{X}(t_{\frac{1}{2}})$ cor-

rectly, and this splitting scheme $\mathbb{T}_1^{\text{cp}}\hat{\mathbb{T}}_1^{\text{cp}}\mathbb{CRC}'\mathbb{T}_2^{\text{cp}}$ is expected to be overall second-order accurate. The results below confirm this expectation. We can apply the second-order splitting $\mathbb{T}_1^{\text{cp}}\hat{\mathbb{T}}_1^{\text{cp}}\mathbb{CRC}'\mathbb{T}_2^{\text{cp}}$ to the frozen-coefficient SDE system (4.12) and (4.13), and obtain the scheme $\mathbb{T}_1^{\text{cp}}\hat{\mathbb{T}}_1^{\text{cp}}\mathbb{CRC}'\mathbb{T}_2^{\text{cp}}$-F in Table 4.2 where "F" denotes the frozen-coefficient system.

The schemes in Table 4.2 (in standard form) are not symmetric, whereas those below are.

4.5.2.2 Splitting schemes of type $\mathbb{TCRC}'\mathbb{T}$

Table 4.3: Splitting schemes of the type $\mathbb{TCRC}'\mathbb{T}$ for the coupled SDE system (4.8) and (4.29)

$\mathbb{T}^{\text{cp}}\mathbb{CRC}'\mathbb{T}^{\text{cp}}$	$\mathbb{T}^{\text{tv}}\mathbb{CRC}'\mathbb{T}^{\text{tv}}$
$\mathbf{Y}(t_{\frac{1}{2}}) = \mathbf{X}_0 +$ $\mathcal{T}^{\text{cp}}(\mathbf{X}_0, t_0, t_{\frac{1}{4}}, \frac{\Delta t}{2}, \boldsymbol{\zeta}, \boldsymbol{\xi}, \boldsymbol{\eta})$	$Y(t_{\frac{1}{2}}) = X_0 +$ $\mathcal{T}^{\text{tv}}(X_0, \frac{\Delta t}{2}, t_0, \mu_0, \bar{\mu}_0, \xi)$
$\varphi_1 = \mathcal{S}(\phi_0, \mathbf{Y}(t_{\frac{1}{2}}), t_{\frac{1}{2}}, \frac{\Delta t}{2}),\quad \varphi_2 = \mathcal{V}(\varphi_1, \mathbf{Y}(t_{\frac{1}{2}}), t_{\frac{1}{2}}, \frac{\Delta t}{2}),\quad \varphi_3 = \mathcal{M}(\varphi_2, \mathbf{Y}(t_{\frac{1}{2}}), t_{\frac{1}{2}}, \frac{\Delta t}{2})$ $\varphi_4 = \mathcal{R}(\varphi_3, \Delta t)$ $\varphi_5 = \mathcal{M}(\varphi_4, \mathbf{Y}(t_{\frac{1}{2}}), t_{\frac{1}{2}}, \frac{\Delta t}{2}),\quad \varphi_6 = \mathcal{V}(\varphi_5, \mathbf{Y}(t_{\frac{1}{2}}), t_{\frac{1}{2}}, \frac{\Delta t}{2}),\quad \varphi(t_1) = \mathcal{S}(\varphi_6, \mathbf{Y}(t_{\frac{1}{2}}), t_{\frac{1}{2}}, \frac{\Delta t}{2})$	
$\mathbf{Y}(t_1) = \mathbf{Y}(t_{\frac{1}{2}}) +$ $\mathcal{T}^{\text{cp}}(\mathbf{Y}(t_{\frac{1}{2}}), t_{\frac{1}{2}}, t_{\frac{3}{4}}, \frac{\Delta t}{2}, \boldsymbol{\zeta}', \boldsymbol{\xi}', \boldsymbol{\eta}')$	$Y(t_1) = Y(t_{\frac{1}{2}}) +$ $\mathcal{T}^{\text{tv}}(Y(t_{\frac{1}{2}}), \frac{\Delta t}{2}, t_{\frac{1}{2}}, \mu_0, \bar{\mu}_0, \xi')$

Second-order splitting schemes can be constructed based on any Ito SDE schemes (e.g., the KP scheme and the TV scheme in Section 4.3.3). We can construct the scheme of the type $\mathbb{TCRC}'\mathbb{T}$. The splitting with the CP scheme is written as $\mathbb{T}^{\text{cp}}\mathbb{CRC}'\mathbb{T}^{\text{cp}}$ in Table 4.3 where $\mathcal{T}^{\text{cp}}$ is defined in (4.17). In contrast to the CP schemes described in previous sub-sections, this scheme performs a complete CP step (of duration $\Delta t/2$) on each of the first and last sub-steps. Similarly, we can construct the splitting schemes with the TV scheme $\mathbb{T}^{\text{tv}}\mathbb{CRC}'\mathbb{T}^{\text{tv}}$ in

Table 4.4: Splitting schemes of the type $\mathbb{TCRC'T}$ for the coupled SDE system (4.12) and (4.29)

$\mathbb{T}^{\text{cp}}\mathbb{CRC'}\mathbb{T}^{\text{cp}}$-F	$\mathbb{T}^{\text{tv}}\mathbb{CRC'}\mathbb{T}^{\text{tv}}$-F	$\mathbb{T}^{\text{kp}}\mathbb{CRC'}\mathbb{T}^{\text{kp}}$-F
$\mathbf{Y}(t_{\frac{1}{2}}) = \mathbf{X}_0 +$ $\mathcal{T}^{\text{cp}}(\mathbf{X}_0, t_{\frac{1}{2}}, t_{\frac{1}{2}}, \frac{\Delta t}{2}, \boldsymbol{\zeta}, \boldsymbol{\xi}, \boldsymbol{\eta})$	$Y(t_{\frac{1}{2}}) = X_0 +$ $\mathcal{T}^{\text{tv}}(X_0, \frac{\Delta t}{2}, t_{\frac{1}{2}}, 0, 0, \xi)$	$Y(t_{\frac{1}{2}}) = X_0 +$ $\mathcal{T}^{\text{kp}}(X_0, \frac{\Delta t}{2}, \xi)$
$\varphi_1 = \mathcal{S}(\phi_0, \mathbf{Y}(t_{\frac{1}{2}}), t_{\frac{1}{2}}, \frac{\Delta t}{2})$, $\varphi_2 = \mathcal{V}(\varphi_1, \mathbf{Y}(t_{\frac{1}{2}}), t_{\frac{1}{2}}, \frac{\Delta t}{2})$, $\varphi_3 = \mathcal{M}(\varphi_2, \mathbf{Y}(t_{\frac{1}{2}}), t_{\frac{1}{2}}, \frac{\Delta t}{2})$ $\varphi_4 = \mathcal{R}(\varphi_3, \Delta t)$ $\varphi_5 = \mathcal{M}(\varphi_4, \mathbf{Y}(t_{\frac{1}{2}}), t_{\frac{1}{2}}, \frac{\Delta t}{2})$, $\varphi_6 = \mathcal{V}(\varphi_5, \mathbf{Y}(t_{\frac{1}{2}}), t_{\frac{1}{2}}, \frac{\Delta t}{2})$, $\varphi(t_1) = \mathcal{S}(\varphi_6, \mathbf{Y}(t_{\frac{1}{2}}), t_{\frac{1}{2}}, \frac{\Delta t}{2})$		
$\mathbf{Y}(t_1) = \mathbf{Y}(t_{\frac{1}{2}}) +$ $\mathcal{T}^{\text{cp}}(\mathbf{Y}(t_{\frac{1}{2}}), t_{\frac{1}{2}}, t_{\frac{1}{2}}, \frac{\Delta t}{2}, \boldsymbol{\zeta}', \boldsymbol{\xi}', \boldsymbol{\eta}')$	$Y(t_1) = Y(t_{\frac{1}{2}}) +$ $\mathcal{T}^{\text{tv}}(Y(t_{\frac{1}{2}}), \frac{\Delta t}{2}, t_{\frac{1}{2}}, 0, 0, \xi')$	$Y(t_1) = Y(t_{\frac{1}{2}}) +$ $\mathcal{T}^{\text{kp}}(Y(t_{\frac{1}{2}}), \frac{\Delta t}{2}, \xi')$

Table 4.3 with $\mathcal{T}^{\text{tv}}$ defined in (4.21).

Applying the splitting scheme to the frozen-coefficient SDE system with CP and TV schemes, we have the $\mathbb{T}^{\text{cp}}\mathbb{CRC'}\mathbb{T}^{\text{cp}}$-F scheme and the $\mathbb{T}^{\text{tv}}\mathbb{CRC'}\mathbb{T}^{\text{tv}}$-F scheme as shown in Table 4.4. The KP scheme is only applicable to the frozen-coefficient system, so the splitting scheme combining the KP scheme is $\mathbb{T}^{\text{kp}}\mathbb{CRC'}\mathbb{T}^{\text{kp}}$-F in Table 4.4 with $\mathcal{T}^{\text{kp}}$ defined in (4.19).

We discussed five splitting schemes of the type of $\mathbb{TCRC'T}$, which are all confirmed to be second-order accurate by the results below.

4.5.2.3 Splitting schemes of type $\mathbb{CTRTC'}$

We can design other second-order splitting schemes using different combinations of the transport sub-step and scalar sub-step. One example is $\mathbb{CTRTC'}$, which takes one step of reaction with half steps of transport right before and after the reaction sub-step. As expected, this splitting scheme is second-order accurate. This splitting combined with the CP and TV schemes are denoted by

Table 4.5: Splitting schemes of the type $\mathbb{CTRTC}'$ for the coupled SDE system (4.8) and (4.29)

$\mathbb{CT}^{\mathrm{cp}}\mathbb{RT}^{\mathrm{cp}}\mathbb{C}'$	$\mathbb{CT}^{\mathrm{tv}}\mathbb{RT}^{\mathrm{tv}}\mathbb{C}'$
$\varphi_1 = \mathcal{S}(\phi_0, \mathbf{X}_0, t_0, \frac{\Delta t}{2}),\quad \varphi_2 = \mathcal{V}(\varphi_1, \mathbf{X}_0, t_0, \frac{\Delta t}{2}),\quad \varphi_3 = \mathcal{M}(\varphi_2, \mathbf{X}_0, t_0, \frac{\Delta t}{2})$	
$\mathbf{Y}(t_{\frac{1}{2}}) = \mathbf{X}_0 +$ $\mathcal{T}^{\mathrm{cp}}(\mathbf{X}_0, t_0, t_{\frac{1}{4}}, \frac{\Delta t}{2}, \boldsymbol{\zeta}, \boldsymbol{\xi}, \boldsymbol{\eta})$	$Y(t_{\frac{1}{2}}) = X_0 +$ $\mathcal{T}^{\mathrm{tv}}(X_0, \frac{\Delta t}{2}, t_0, \mu_0, \bar{\mu}_0, \xi)$
$\varphi_4 = \mathcal{R}(\varphi_3, \Delta t)$	
$\mathbf{Y}(t_1) = \mathbf{Y}(t_{\frac{1}{2}}) +$ $\mathcal{T}^{\mathrm{cp}}(\mathbf{Y}(t_{\frac{1}{2}}), t_{\frac{1}{2}}, t_{\frac{3}{4}}, \frac{\Delta t}{2}, \boldsymbol{\zeta}', \boldsymbol{\xi}', \boldsymbol{\eta}')$	$Y(t_1) = Y(t_{\frac{1}{2}}) +$ $\mathcal{T}^{\mathrm{tv}}(Y(t_{\frac{1}{2}}), \frac{\Delta t}{2}, t_{\frac{1}{2}}, \mu_0, \bar{\mu}_0, \xi')$
$\varphi_5 = \mathcal{M}(\varphi_4, \mathbf{Y}(t_1), t_1, \frac{\Delta t}{2}),\quad \varphi_6 = \mathcal{V}(\varphi_5, \mathbf{Y}(t_1), t_1, \frac{\Delta t}{2}),\quad \varphi(t_1) = \mathcal{S}(\varphi_6, \mathbf{Y}(t_1), t_1, \frac{\Delta t}{2})$	

Table 4.6: Splitting schemes of the type $\mathbb{CTRTC}'$ for the coupled SDE system (4.12) and (4.29)

$\mathbb{CT}^{\mathrm{cp}}\mathbb{RT}^{\mathrm{cp}}\mathbb{C}'$-F	$\mathbb{CT}^{\mathrm{tv}}\mathbb{RT}^{\mathrm{tv}}\mathbb{C}'$-F	$\mathbb{CT}^{\mathrm{kp}}\mathbb{RT}^{\mathrm{kp}}\mathbb{C}'$-F
$\varphi_1 = \mathcal{S}(\phi_0, \mathbf{X}_0, t_{\frac{1}{2}}, \frac{\Delta t}{2}),\quad \varphi_2 = \mathcal{V}(\varphi_1, \mathbf{X}_0, t_{\frac{1}{2}}, \frac{\Delta t}{2}),\quad \varphi_3 = \mathcal{M}(\varphi_2, \mathbf{X}_0, t_{\frac{1}{2}}, \frac{\Delta t}{2})$		
$\mathbf{Y}(t_{\frac{1}{2}}) = \mathbf{X}_0 +$ $\mathcal{T}^{\mathrm{cp}}(\mathbf{X}_0, t_{\frac{1}{2}}, t_{\frac{1}{2}}, \frac{\Delta t}{2}, \boldsymbol{\zeta}, \boldsymbol{\xi}, \boldsymbol{\eta})$	$Y(t_{\frac{1}{2}}) = X_0 +$ $\mathcal{T}^{\mathrm{tv}}(X_0, \frac{\Delta t}{2}, t_{\frac{1}{2}}, 0, 0, \xi)$	$Y(t_{\frac{1}{2}}) = X_0 +$ $\mathcal{T}^{\mathrm{kp}}(X_0, \frac{\Delta t}{2}, \xi)$
$\varphi_4 = \mathcal{R}(\varphi_3, \Delta t)$		
$\mathbf{Y}(t_1) = \mathbf{Y}(t_{\frac{1}{2}}) +$ $\mathcal{T}^{\mathrm{cp}}(\mathbf{Y}(t_{\frac{1}{2}}), t_{\frac{1}{2}}, t_{\frac{1}{2}}, \frac{\Delta t}{2}, \boldsymbol{\zeta}', \boldsymbol{\xi}', \boldsymbol{\eta}')$	$Y(t_1) = Y(t_{\frac{1}{2}}) +$ $\mathcal{T}^{\mathrm{tv}}(Y(t_{\frac{1}{2}}), \frac{\Delta t}{2}, t_{\frac{1}{2}}, 0, 0, \xi')$	$Y(t_1) = Y(t_{\frac{1}{2}}) +$ $\mathcal{T}^{\mathrm{kp}}(Y(t_{\frac{1}{2}}), \frac{\Delta t}{2}, \xi')$
$\varphi_5 = \mathcal{M}(\varphi_4, \mathbf{Y}(t_1), t_{\frac{1}{2}}, \frac{\Delta t}{2}),\quad \varphi_6 = \mathcal{V}(\varphi_5, \mathbf{Y}(t_1), t_{\frac{1}{2}}, \frac{\Delta t}{2}),\quad \varphi(t_1) = \mathcal{S}(\varphi_6, \mathbf{Y}(t_1), t_{\frac{1}{2}}, \frac{\Delta t}{2})$		

$\mathbb{CT}^{\mathrm{cp}}\mathbb{RT}^{\mathrm{cp}}\mathbb{C}'$ and $\mathbb{CT}^{\mathrm{tv}}\mathbb{RT}^{\mathrm{tv}}\mathbb{C}'$, respectively, in Table 4.5 where the splitting scheme $\mathbb{SVMRMVS}$-III in Table 4.1 for the scalar equation is used. The splitting $\mathbb{CTRTC}'$ combined with the CP, TV and KP schemes for the frozen-coefficient system (4.12) and (4.13) are denoted by $\mathbb{CT}^{\mathrm{cp}}\mathbb{RT}^{\mathrm{cp}}\mathbb{C}'$-F, $\mathbb{CT}^{\mathrm{tv}}\mathbb{RT}^{\mathrm{tv}}\mathbb{C}'$-F and $\mathbb{CT}^{\mathrm{kp}}\mathbb{RT}^{\mathrm{kp}}\mathbb{C}'$-F in Table 4.6.

Five second-order splitting schemes of the type of $\mathbb{CTRTC}'$ are discussed in this part 4.5.2.3. Second-order accuracy of these schemes are confirmed by the results below.

4.5.2.4 Splitting schemes of type $\mathbb{CRTC}'$

Table 4.7: Splitting schemes of the type $\mathbb{CRTC}'$ for the coupled SDE system (4.8) and (4.29)

$\mathbb{CRT}^{\mathrm{cp}}\mathbb{C}'$	$\mathbb{CRT}^{\mathrm{tv}}\mathbb{C}'$
$\varphi_1 = \mathcal{S}(\phi_0, \mathbf{X}_0, t_0, \frac{\Delta t}{2})$, $\varphi_2 = \mathcal{V}(\varphi_1, \mathbf{X}_0, t_0, \frac{\Delta t}{2})$, $\varphi_3 = \mathcal{M}(\varphi_2, \mathbf{X}_0, t_0, \frac{\Delta t}{2})$	
$\varphi_4 = \mathcal{R}(\varphi_3, \Delta t)$	
$\mathbf{Y}(t_1) = \mathbf{X}_0 +$ $\mathcal{T}^{\mathrm{cp}}(\mathbf{X}_0, t_0, t_{\frac{1}{2}}, \Delta t, \boldsymbol{\zeta}, \boldsymbol{\xi}, \boldsymbol{\eta})$	$Y(t_1) = X_0 +$ $\mathcal{T}^{\mathrm{tv}}(X_0, \Delta t, t_0, \mu_0, \bar{\mu}_0, \xi)$
$\varphi_5 = \mathcal{M}(\varphi_4, \mathbf{Y}(t_1), t_1, \frac{\Delta t}{2})$, $\varphi_6 = \mathcal{V}(\varphi_5, \mathbf{Y}(t_1), t_1, \frac{\Delta t}{2})$, $\varphi(t_1) = \mathcal{S}(\varphi_6, \mathbf{Y}(t_1), t_1, \frac{\Delta t}{2})$	

Table 4.8: Splitting schemes of the type $\mathbb{CRTC}'$ for the coupled SDE system (4.12) and (4.29)

$\mathbb{CRT}^{\mathrm{cp}}\mathbb{C}'$-F	$\mathbb{CRT}^{\mathrm{tv}}\mathbb{C}'$-F	$\mathbb{CRT}^{\mathrm{kp}}\mathbb{C}'$-F
$\varphi_1 = \mathcal{S}(\phi_0, \mathbf{X}_0, t_{\frac{1}{2}}, \frac{\Delta t}{2})$, $\varphi_2 = \mathcal{V}(\varphi_1, \mathbf{X}_0, t_{\frac{1}{2}}, \frac{\Delta t}{2})$, $\varphi_3 = \mathcal{M}(\varphi_2, \mathbf{X}_0, t_{\frac{1}{2}}, \frac{\Delta t}{2})$		
$\varphi_4 = \mathcal{R}(\varphi_3, \Delta t)$		
$\mathbf{Y}(t_1) = \mathbf{X}_0 +$ $\mathcal{T}^{\mathrm{cp}}(\mathbf{X}_0, t_{\frac{1}{2}}, t_{\frac{1}{2}}, \Delta t, \boldsymbol{\zeta}, \boldsymbol{\xi}, \boldsymbol{\eta})$	$Y(t_1) = X_0 +$ $\mathcal{T}^{\mathrm{tv}}(X_0, \Delta t, t_{\frac{1}{2}}, 0, 0, \xi)$	$Y(t_1) = X_0 +$ $\mathcal{T}^{\mathrm{kp}}(X_0, \Delta t, \xi)$
$\varphi_5 = \mathcal{M}(\varphi_4, \mathbf{Y}(t_1), t_{\frac{1}{2}}, \frac{\Delta t}{2})$, $\varphi_6 = \mathcal{V}(\varphi_5, \mathbf{Y}(t_1), t_{\frac{1}{2}}, \frac{\Delta t}{2})$, $\varphi(t_1) = \mathcal{S}(\varphi_6, \mathbf{Y}(t_1), t_{\frac{1}{2}}, \frac{\Delta t}{2})$		

In this work, the restriction of constant density has been made for the discussion, which makes the transport sub-step independent of the reaction sub-step, so that the transport sub-step $\mathbb{T}$ and the reaction sub-step $\mathbb{R}$ can be commuted if they are adjacent to each other in a splitting scheme. The previous splitting $\mathbb{CTRTC}'$ is the same as $\mathbb{CRTTC}'$ (i.e., with $\mathbb{T}$ and $\mathbb{R}$ commuted). The two $\mathbb{T}$ sub-steps can be combined to yield $\mathbb{CRTC}'$. (It should be noticed that $\mathbb{CTRTC}'$ is identical to $\mathbb{CRTTC}'$, but that $\mathbb{T}$ is not identical to $\mathbb{TT}$: they both do a second-order step of size Δt, but with different truncation error.) This scheme $\mathbb{CRTC}'$ requires only one step of reaction and one step of transport, and it is second-order accurate for constant-density problems. This splitting combined with the CP scheme and TV schemes are denoted by $\mathbb{CRT}^{\mathrm{cp}}\mathbb{C}'$ and $\mathbb{CRT}^{\mathrm{tv}}\mathbb{C}'$ in Table 4.7. When used on the frozen-coefficient system (4.12) and (4.13), the splitting yields $\mathbb{CRT}^{\mathrm{cp}}\mathbb{C}'$-F, $\mathbb{CRT}^{\mathrm{tv}}\mathbb{C}'$-F and $\mathbb{CRT}^{\mathrm{kp}}\mathbb{C}'$-F as shown in Table 4.8 when combined with the CP, TV and KP schemes.

Five second-order splitting schemes of the type $\mathbb{CRTC}'$ are discussed in this part 4.5.2.4, and their second-order accuracy is confirmed in Section 4.6.

In summary, in this section, we developed the sub-stepping scheme of the scalar evolution (4.29) and different splitting schemes for the stochastic particle equations. There are certainly many other second-order splitting schemes not discussed above. We limit our discussion on the above proposed splitting schemes. In the next section, we report convergence tests which confirm the order of accuracy of the proposed splitting schemes. The testing and discussion can be applied to other splitting schemes not discussed in this paper (such as $\mathbb{TSVRMRVST}$ or $\mathbb{SVTMRMTVS}$).

4.6 Convergence tests

The convergence tests are performed for a one-dimensional periodic turbulent reactive flow system with constant density ($\nabla \cdot \overline{\mathbf{u}} = 0$). The manufactured solutions to the scalar mean and variance are shown in Appendix D together with the velocity, diffusivity, scalar frequency and forcing terms. For the convergence test of third and fourth moments, we estimate the exact solution of the moments required for evaluating the numerical error from a high-resolution finite-difference solution of the transport equations of these moments (Section 4.6.3).

The domain $[0, L_0]$ is partitioned into $N_g = 50$ uniform grid cells. The grid is used to calculate the ensemble average of particles for the error estimate (4.32) and to compute the scalar mean (4.44) used in the mixing sub-step (4.43) and in the scalar variance forcing sub-step (4.47). The test case is integrated on $t \in [0, T]$, and $N_t = [1, 2, 4, 6, 8, 10, 12, 16, 20, 24, 32, 40]$ equal time steps (of size $\Delta t = T/N_t$) are taken to the same stopping time T, in order to show the asymptotic convergence with respect to the time step, Δt. In total $N = 50000$ particles are used for each simulation trial. Independent trails are performed to compute the global error $\mathcal{E}_{\overline{\phi^q}}$ in (C.9). A total of 30 sets of trails are performed to estimate the mean and variance of $\mathcal{E}_{\overline{\phi^q}}$, and hence to construct the 95% confidence interval of the estimated global error. The 95% confidence interval of the global error is $[E(\mathcal{E}_{\overline{\phi^q}}) - 1.96 \times \text{std}(\mathcal{E}_{\overline{\phi^q}}), E(\mathcal{E}_{\overline{\phi^q}}) + 1.96 \times \text{std}(\mathcal{E}_{\overline{\phi^q}})]$, where "std" is the standard deviation. The confidence interval needs to be small for us to draw confident conclusions. The size of the confidence interval depends on the number of independent trials performed. We require that

$$\frac{1.96 \times \text{std}(\mathcal{E}_{\overline{\phi^q}})}{E(\mathcal{E}_{\overline{\phi^q}})} \leqslant \varepsilon, \tag{4.48}$$

for the moments of the scalar to control the size of the confidence interval, where

the threshold ε is increased from 0.1 to 0.95 gradually with decreasing Δt. This requirement is used as a stopping criterion for the simulations. More and more trials are performed and added into the ensemble of trials to estimate the global error until the criterion (4.48) is fulfilled. In the tests, depending on different splitting schemes, up to 1.4×10^6 trials may be required to fulfill the criterion (4.48), resulting effectively in 7×10^{10} particles in total. This kind of simulation can be perfectly performed via parallel computers with little message communication. The simulations are done using 32-processes per case on an HPC cluster of 36 Dell servers featuring dual, dual-core Intel Xeon "Woodcrest" processors, tied together using a QLogic 4X SDR InfiniBand interconnect. The total cost of the convergence test for one splitting scheme is up to 600 CPU-hours for the most expensive case.

The particle positions are initialized to be uniformly distributed in the domain $[0, L_0]$. For the divergence-free flow considered, this uniform spatial distribution remains uniform for all later times (in expectation and absent numerical errors) [1], which guarantees approximately the same number of particles to evaluate the volume average of the scalar moments in (4.31). The periodic boundary condition is applied to the particle position so that all the particles remain in the computational domain at all time. The particle scalar is specified to be Gaussian randomly distributed initially, and is initialized according to the scalar mean $\overline{\phi}_m$ and variance $\overline{\phi'^2}_m$, i.e., $\phi = \overline{\phi}_m + \left(\overline{\phi'^2}_m\right)^{\frac{1}{2}} \xi$, where ξ is a standardized Gaussian random number and $\overline{\phi}_m$ and $\overline{\phi'^2}_m$ are evaluated at the particle initial position according to (D.1) and (D.2).

4.6.1 Order of weak convergence of different splitting schemes

For various CP schemes, Fig. 4.2 shows the global errors $\mathcal{E}_{\overline{\phi^q}}$ (C.9) of the first moment $\overline{\phi}$ and second moment $\overline{\phi^2}$ against the time step Δt. On these log-log plots, lines of slope one and two indicate first and second-order convergence, respectively. The global errors of all simulations show asymptotic convergence given the 95% confidence interval when Δt decreases to zero.

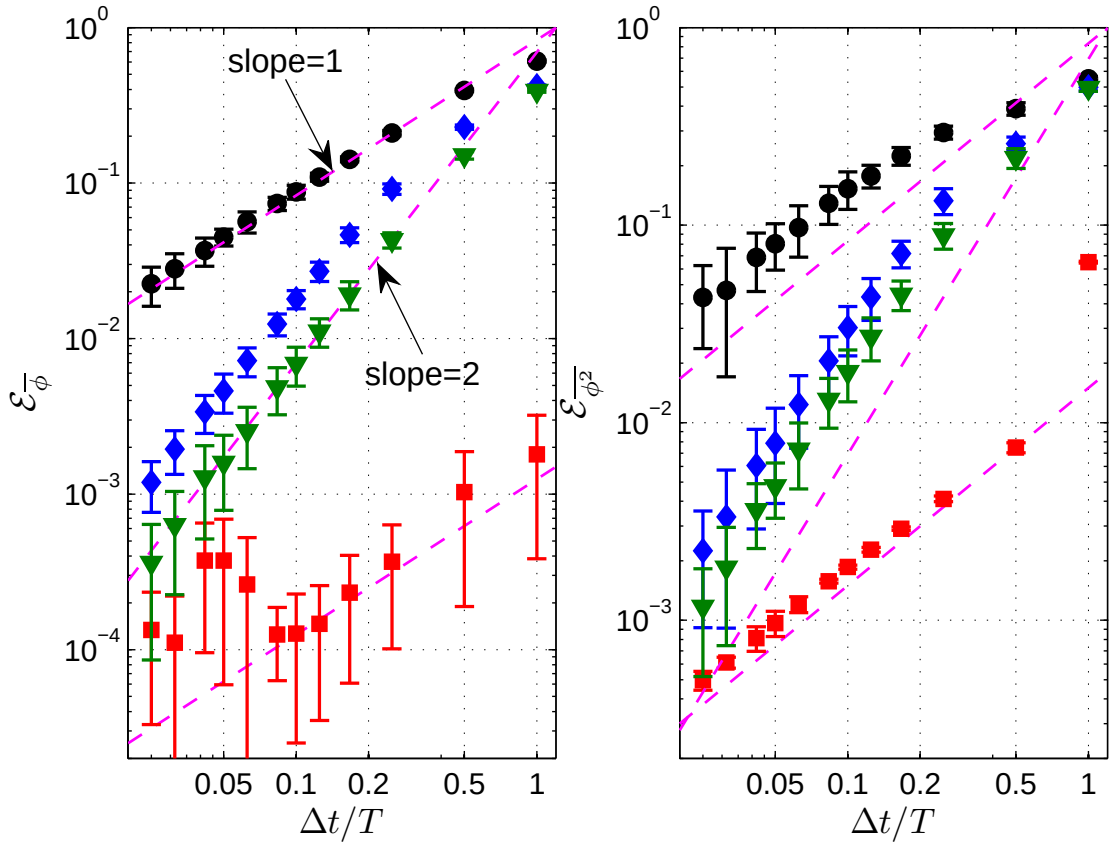

Figure 4.2: The convergence of the global error of $\overline{\phi}$ and $\overline{\phi^2}$ against the time step Δt with $\mathbb{T}_1^{\mathrm{cp}}\mathbb{C}\mathbb{R}\mathbb{C}'\mathbb{T}_2^{\mathrm{cp}}$ in Table 4.2 (circle), with $\mathbb{T}_1^{\mathrm{cp}}\hat{\mathbb{T}}_1^{\mathrm{cp}}\mathbb{C}\mathbb{R}\mathbb{C}'\mathbb{T}_2^{\mathrm{cp}}$ in Table 4.2 (diamond), with $\mathbb{T}_1^{\mathrm{cp}}\hat{\mathbb{T}}_1^{\mathrm{cp}}\mathbb{C}\mathbb{R}\mathbb{C}'\mathbb{T}_2^{\mathrm{cp}}$-F in Table 4.2 (down triangle), and with $\mathbb{T}_1^{\mathrm{cp}}\mathbb{C}\mathbb{R}\mathbb{C}'\mathbb{T}_2^{\mathrm{cp}}$ in Table 4.2 without MMS forcing terms (square). (The error bars indicate 95% confidence intervals.)

In Fig. 4.2, the results of the $\mathbb{T}_1^{\mathrm{cp}}\mathbb{C}\mathbb{R}\mathbb{C}'\mathbb{T}_2^{\mathrm{cp}}$ scheme (in Table 4.2) (circles in the figure) show first-order asymptotic behavior in comparison with the reference

dash-lines of slope one and two. So this scheme is only first-order accurate for the reason explained in Section 4.5.2.1. Notice that these results (circles) are obtained using the MMS solutions and forcing terms. These forcing terms do not appear in a realistic problem. To show the effect of these forcing terms, we perform the computations of the same problem (e.g., the same configuration, the same initial and boundary conditions) without the forcing terms. The "exact" solution required for the error measurement (4.32) is obtained from a high-resolution finite-difference simulation. The results (shown as squares in Fig. 4.2) show first-order convergence, which confirms the first-order accuracy of the $\mathbb{T}_1^{cp}\mathbb{CRC}'\mathbb{T}_2^{cp}$ scheme. The numerical errors with MMS terms are about two orders of magnitude larger than without in Fig. 4.2. This significant difference is caused by the different solutions of the first and second moments at the stopping time with and without MMS terms. As shown in Fig. 4.3, given the same initial condition and other functions, the profiles of the first and second moments of the scalar with MMS terms are over one order of magnitude larger than those without.

Although the accurate numerical solutions can be obtained for the current verification test case without MMS terms, the MMS is preferable to the accurate numerical solutions in general for the Monte Carlo method. The MMS introduces more processes (forcing terms), which incur more numerical error in the numerical solutions, and hence makes the verification easier in terms of computational cost. Without the MMS terms, the existing test cases indicate that the computational cost may be two orders of magnitude greater than those with MMS terms. In designing the MMS solutions, we need to make sure that none of the terms in the transport equations of scalar mean and variance dominate over the other terms. The magnitudes of the terms for the current test case are

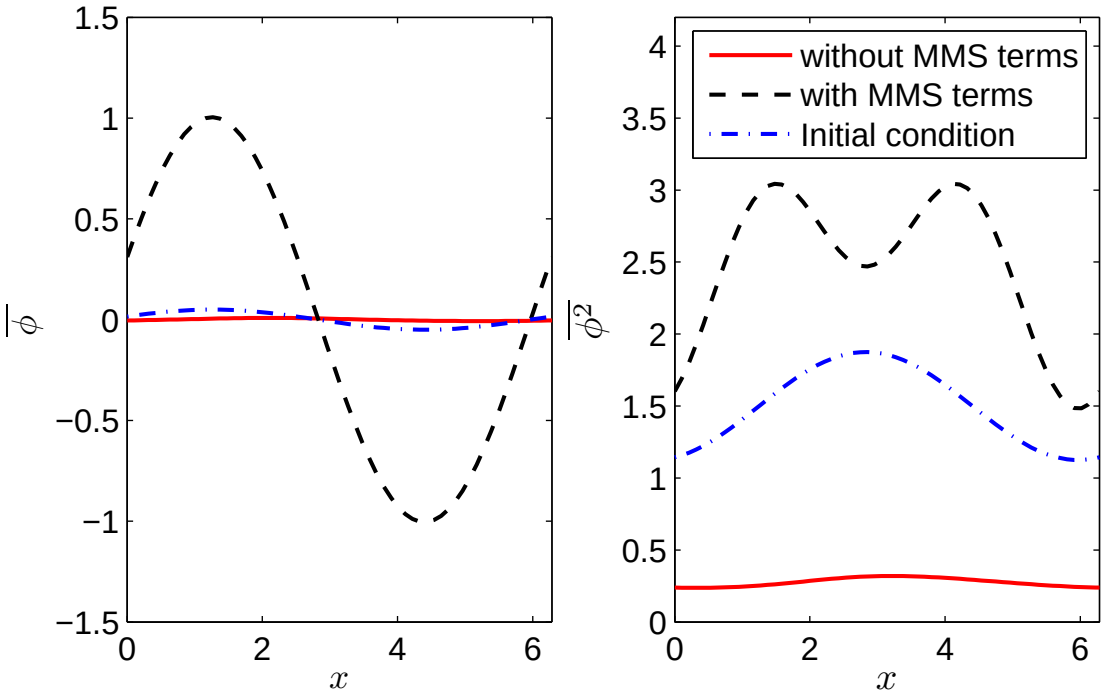

Figure 4.3: The initial profiles of the first and second scalar moments and their profiles at the stopping time with and without MMS terms.

examined in Appendix D.

The modified mid-point scheme $\mathbb{T}_1^{cp}\hat{\mathbb{T}}_1^{cp}\mathbb{CRC}'\mathbb{T}_2^{cp}$ in Table 4.2 improves the convergence rate to second-order as shown by the diamonds in Fig. 4.2. When the frozen-coefficient SDE system (4.12)and (4.13) is used, the scheme $\mathbb{T}_1^{cp}\hat{\mathbb{T}}_1^{cp}\mathbb{CRC}'\mathbb{T}_2^{cp}$-F retains the same order of accuracy (shown by the down triangles in the figure). Meanwhile, for the test case, it suggests that the absolute error from $\mathbb{T}_1^{cp}\hat{\mathbb{T}}_1^{cp}\mathbb{CRC}'\mathbb{T}_2^{cp}$-F is lower than that from $\mathbb{T}_1^{cp}\hat{\mathbb{T}}_1^{cp}\mathbb{CRC}'\mathbb{T}_2^{cp}$. For schemes $\mathbb{T}_1^{cp}\hat{\mathbb{T}}_1^{cp}\mathbb{CRC}'\mathbb{T}_2^{cp}$ and $\mathbb{T}_1^{cp}\hat{\mathbb{T}}_1^{cp}\mathbb{CRC}'\mathbb{T}_2^{cp}$-F, the required time steps are in the ratio of 1:1.6 for 1% accuracy of the first scalar moment, and in the ratio of 1:1.3 for 1% accuracy of the second scalar moment.

Fig. 4.4 shows the convergence test results of the five splitting schemes of the type $\mathbb{TCRC}'\mathbb{T}$ described in Section 4.5.2.2. The convergence results verify the

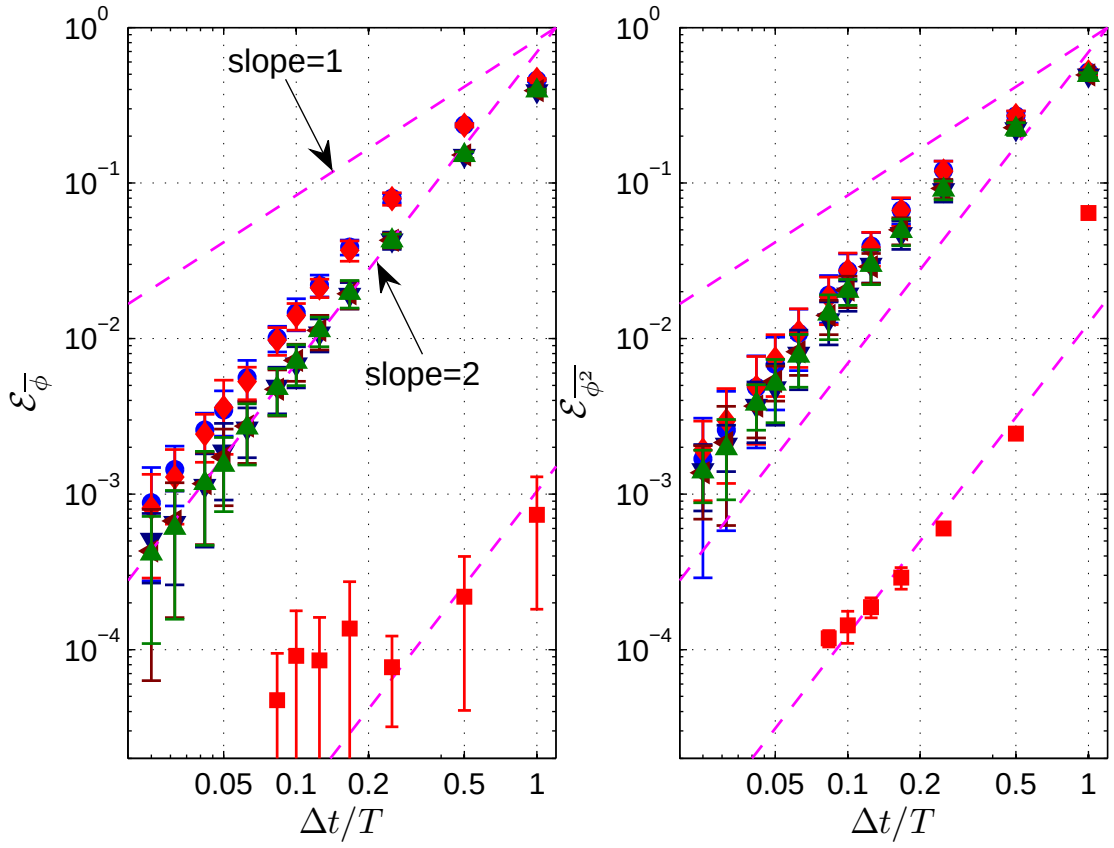

Figure 4.4: The convergence of the global error of $\overline{\phi}$ and $\overline{\phi^2}$ against the time step Δt with $\mathbb{T}^{\text{cp}}\mathbb{CRC}'\mathbb{T}^{\text{cp}}$ in Table 4.3 (circle), with $\mathbb{T}^{\text{tv}}\mathbb{CRC}'\mathbb{T}^{\text{tv}}$ in Table 4.3 (diamond), with $\mathbb{T}^{\text{cp}}\mathbb{CRC}'\mathbb{T}^{\text{cp}}$-F in Table 4.4 (down triangle), with $\mathbb{T}^{\text{tv}}\mathbb{CRC}'\mathbb{T}^{\text{tv}}$-F in Table 4.4 (left triangle), with $\mathbb{T}^{\text{kp}}\mathbb{CRC}'\mathbb{T}^{\text{kp}}$-F in Table 4.4 (up triangle), and with $\mathbb{T}^{\text{cp}}\mathbb{CRC}'\mathbb{T}^{\text{cp}}$ in Table 4.3 without MMS forcing terms (square). (The error bars indicate 95% confidence intervals.)

second-order accuracy of the splitting schemes ($\mathbb{T}^{cp}\mathbb{C}\mathbb{R}\mathbb{C}'\mathbb{T}^{cp}$ in Table 4.3 (circles in Fig. 4.4), $\mathbb{T}^{tv}\mathbb{C}\mathbb{R}\mathbb{C}'\mathbb{T}^{tv}$ in Table 4.3 (diamonds in Fig. 4.4), $\mathbb{T}^{cp}\mathbb{C}\mathbb{R}\mathbb{C}'\mathbb{T}^{cp}$-F in Table 4.4 (down triangles in Fig. 4.4), $\mathbb{T}^{tv}\mathbb{C}\mathbb{R}\mathbb{C}'\mathbb{T}^{tv}$-F in Table 4.4 (left triangles in Fig. 4.4), $\mathbb{T}^{kp}\mathbb{C}\mathbb{R}\mathbb{C}'\mathbb{T}^{kp}$-F in Table 4.4 (up triangles in Fig. 4.4)), and the weak second-order accuracy of the two derivative-free Ito SDE schemes, the KP scheme (4.19) and the TV scheme (4.21). One test of $\mathbb{T}^{cp}\mathbb{C}\mathbb{R}\mathbb{C}'\mathbb{T}^{cp}$ (in Table 4.3) without the MMS forcing terms is done and is shown as squares in Fig. 4.4. The test implies that the extra forcing terms introduced for the MMS do not interfere in the order of accuracy of the different splitting schemes. The numerical errors without MMS terms are significantly lower than those with MMS terms for the same reason given in relation to Fig. 4.2. The same splitting schemes on the SDE system (4.8) and (4.10) and on its frozen-coefficient counterpart (4.12) and (4.13) perform slightly differently, and the absolute error incurred by the splitting on the frozen-coefficient SDE system is a little lower than that incurred by the same splitting on the original SDE system, e.g., $\mathbb{T}^{cp}\mathbb{C}\mathbb{R}\mathbb{C}'\mathbb{T}^{cp}$ (circle) vs. $\mathbb{T}^{cp}\mathbb{C}\mathbb{R}\mathbb{C}'\mathbb{T}^{cp}$-F (down triangle) in Fig. 4.4. For schemes $\mathbb{T}^{cp}\mathbb{C}\mathbb{R}\mathbb{C}'\mathbb{T}^{cp}$ and $\mathbb{T}^{cp}\mathbb{C}\mathbb{R}\mathbb{C}'\mathbb{T}^{cp}$-F (and the same for schemes $\mathbb{T}^{tv}\mathbb{C}\mathbb{R}\mathbb{C}'\mathbb{T}^{tv}$ and $\mathbb{T}^{tv}\mathbb{C}\mathbb{R}\mathbb{C}'\mathbb{T}^{tv}$-F), the required time steps are in the ratio of 1:1.4 for 1% accuracy of the first scalar moment, and in the ratio of 1:1.1 for 1% accuracy of the second scalar moment approximately.

The test results of the splitting schemes of the type $\mathbb{C}\mathbb{T}\mathbb{R}\mathbb{T}\mathbb{C}'$ in Section 4.5.2.3 are shown in Fig. 4.5, $\mathbb{C}\mathbb{T}^{cp}\mathbb{R}\mathbb{T}^{cp}\mathbb{C}'$ in Table 4.5 (circles in Fig. 4.5), $\mathbb{C}\mathbb{T}^{tv}\mathbb{R}\mathbb{T}^{tv}\mathbb{C}'$ in Table 4.5 (squares in Fig. 4.5), $\mathbb{C}\mathbb{T}^{cp}\mathbb{R}\mathbb{T}^{cp}\mathbb{C}'$-F in Table 4.6 (diamonds in Fig. 4.5), $\mathbb{C}\mathbb{T}^{tv}\mathbb{R}\mathbb{T}^{tv}\mathbb{C}'$-F in Table 4.6 (down triangles in Fig. 4.5), and $\mathbb{C}\mathbb{T}^{kp}\mathbb{R}\mathbb{T}^{kp}\mathbb{C}'$-F in Table 4.6 (left triangles in Fig. 4.5). The second-order convergence of the splitting schemes is clearly indicated by the results. The difference in the performance of the different splitting schemes is not distinguishable from Fig. 4.5. The more

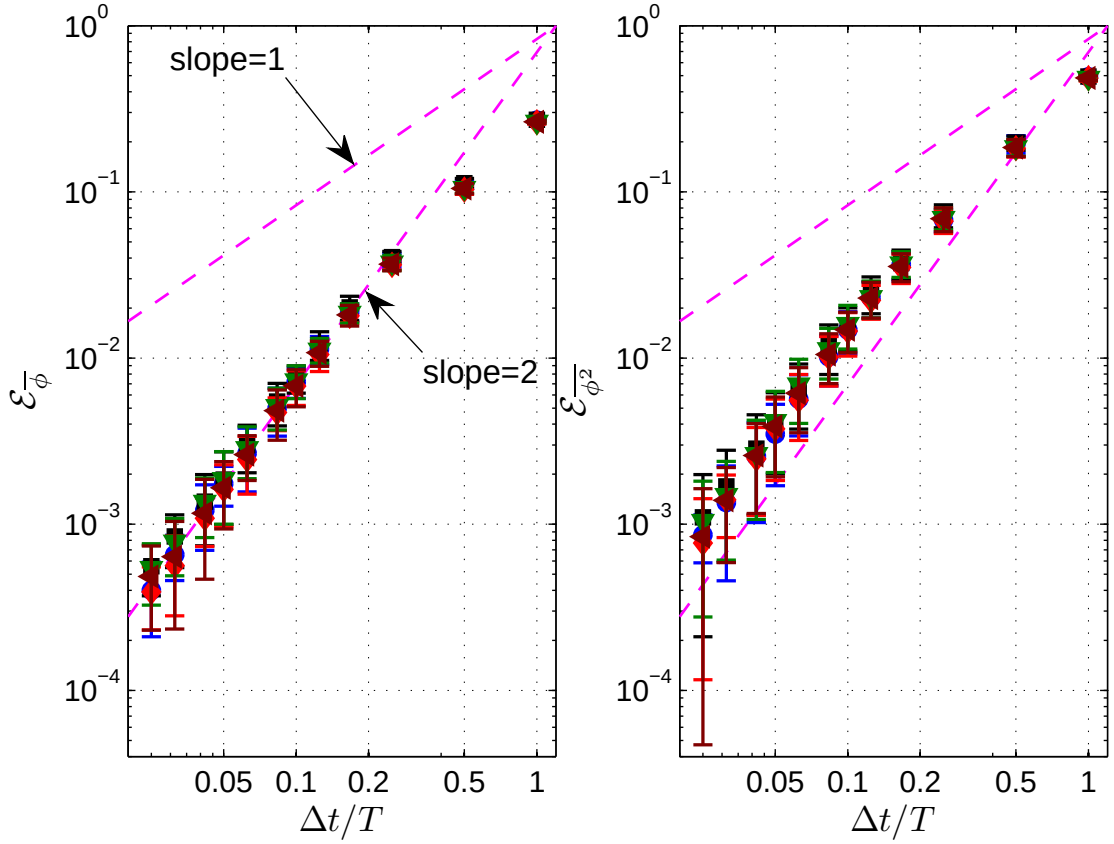

Figure 4.5: The convergence of the global error of $\overline{\phi}$ and $\overline{\phi^2}$ against the time step Δt with $\mathbb{CT}^{\text{cp}}\mathbb{RT}^{\text{cp}}\mathbb{C}'$ in Table 4.5 (circle), with $\mathbb{CT}^{\text{tv}}\mathbb{RT}^{\text{tv}}\mathbb{C}'$ in Table 4.5 (square), with $\mathbb{CT}^{\text{cp}}\mathbb{RT}^{\text{cp}}\mathbb{C}'$-F in Table 4.6 (diamond), with $\mathbb{CT}^{\text{tv}}\mathbb{RT}^{\text{tv}}\mathbb{C}'$-F in Table 4.6 (down triangle), and with $\mathbb{CT}^{\text{kp}}\mathbb{RT}^{\text{kp}}\mathbb{C}'$-F in Table 4.6 (left triangle). (The error bars indicate 95% confidence intervals.)

detailed comparison of the different splitting schemes is discussed in the next sub-section.

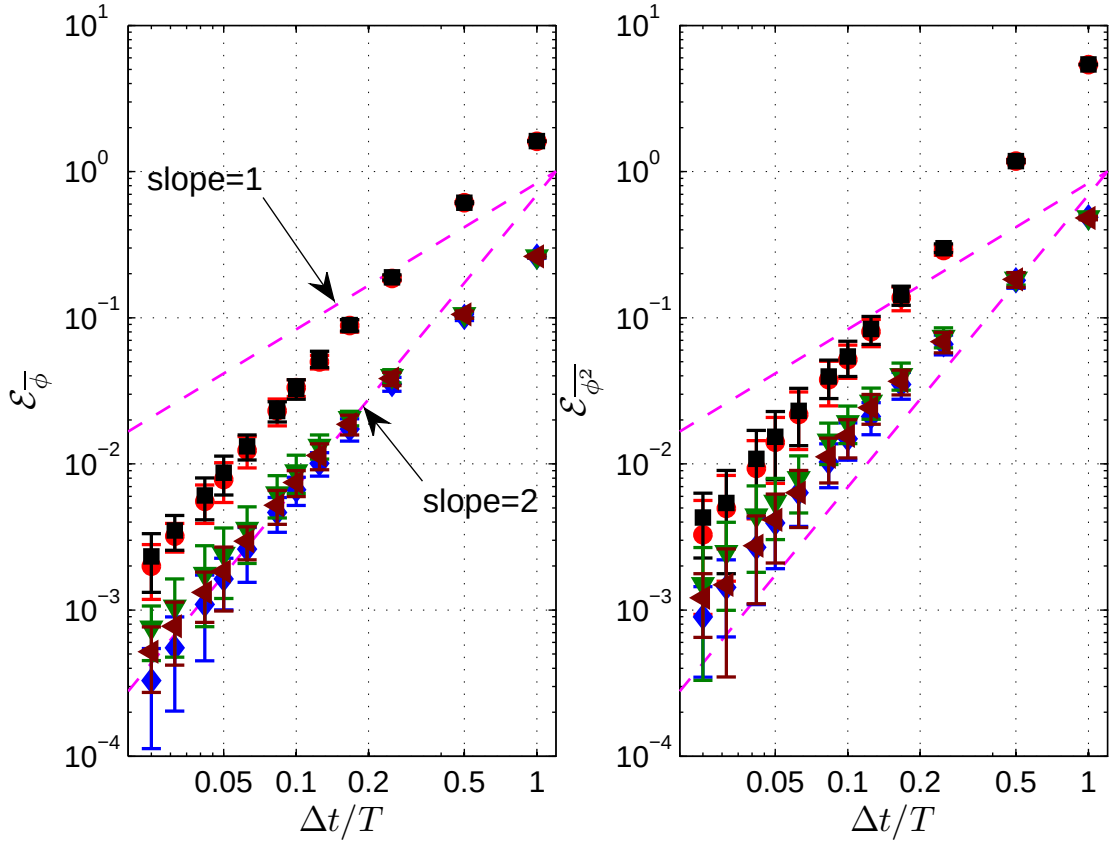

Figure 4.6: The convergence of the global error of $\overline{\phi}$ and $\overline{\phi^2}$ against the time step Δt with $\mathbb{CRT}^{\text{cp}}\mathbb{C}'$ in Table 4.7 (circle), with $\mathbb{CRT}^{\text{tv}}\mathbb{C}'$ in Table 4.7 (square), with $\mathbb{CRT}^{\text{cp}}\mathbb{C}'$-F in Table 4.8 (diamond), with $\mathbb{CRT}^{\text{tv}}\mathbb{C}'$-F in Table 4.8 (down triangle), and with $\mathbb{CRT}^{\text{kp}}\mathbb{C}'$-F in Table 4.8 (left triangle). (The error bars indicate 95% confidence intervals.)

Fig. 4.6 shows the test results of the splitting schemes of type $\mathbb{CRTC}'$ in Section 4.5.2.4 suitable for the current constant density test case, $\mathbb{CRT}^{\text{cp}}\mathbb{C}'$ in Table 4.7 (circles in Fig. 4.6), $\mathbb{CRT}^{\text{tv}}\mathbb{C}'$ in Table 4.7 (squares in Fig. 4.6), $\mathbb{CRT}^{\text{cp}}\mathbb{C}'$-F in Table 4.8 (diamonds in Fig. 4.6), $\mathbb{CRT}^{\text{tv}}\mathbb{C}'$-F in Table 4.8 (down triangles in Fig. 4.6), and $\mathbb{CRT}^{\text{kp}}\mathbb{C}'$-F in Table 4.8 (left triangles in Fig. 4.6). The second-order accuracy of the splitting scheme is clearly shown. The frozen-coefficient SDE system is helpful to reduce the error when the same splitting scheme is

used, e.g., $\mathbb{CRT}^{cp}\mathbb{C}'$ (circle) vs. $\mathbb{CRT}^{cp}\mathbb{C}'$-F (diamond), and $\mathbb{CRT}^{tv}\mathbb{C}'$ (square) vs. $\mathbb{CRT}^{tv}\mathbb{C}'$-F (down triangle) in Fig. 4.6. For schemes $\mathbb{CRT}^{cp}\mathbb{C}'$ and $\mathbb{CRT}^{cp}\mathbb{C}'$-F (and the same for schemes $\mathbb{CRT}^{tv}\mathbb{C}'$ and $\mathbb{CRT}^{tv}\mathbb{C}'$-F), the required time steps are in the ratio of 1:2.0 for 1% accuracy of the first scalar moment, and in the ratio of 1:1.8 for 1% accuracy of the second scalar moment approximately.

In this sub-section, we demonstrate the convergence of the different splitting schemes described in Section 4.5 in terms of the first and second moments. We show the convergence results of higher moments (third and fourth) for one type of splitting $\mathbb{CTRTC}'$ (Section 4.5.2.3) in Section 4.6.3. Before that, we compare the performance of different splitting schemes in the following sub-section.

4.6.2 Comparison of different splitting schemes

In the previous sub-section, the order of accuracy of the different splitting schemes is verified. Here, we compare the performance and efficiency of the different second-order splitting schemes.

The global errors of the different splitting schemes at $\Delta t = 0.05$ are compared in Table 4.9. Several observations can be made based on the comparison. First, the different Ito SDE schemes (CP, TV, KP) perform essentially the same when combined with the same splitting scheme according to the different columns of Table 4.9. The mean global errors obtained for each Ito SDE scheme are well inside of the others' 95% confidence interval. Second, comparing the same splitting schemes applied to the original SDE system (4.8) and (4.10) and to the frozen-coefficient SDE system (4.12) and (4.13), we can see that, for the most part, solving the frozen-coefficient SDE system helps to reduce the numerical er-

ror, e.g., $\mathbb{T}_1^{cp}\hat{\mathbb{T}}_1^{cp}\mathbb{CRC}'\mathbb{T}_2^{cp}$-F incurs an error about half of that of $\mathbb{T}_1^{cp}\hat{\mathbb{T}}_1^{cp}\mathbb{CRC}'\mathbb{T}_2^{cp}$, and the error of $\mathbb{CRTC}'$-F is about one-third of that of $\mathbb{CRTC}'$. The schemes $\mathbb{CTRTC}'$ and $\mathbb{CTRTC}'$-F are exceptions to this observation because the mean error of the scalar variance of $\mathbb{CT}^{cp}\mathbb{RT}^{cp}\mathbb{C}'$-F is slightly greater than that of $\mathbb{CT}^{cp}\mathbb{RT}^{cp}\mathbb{C}'$, and so are the mean errors of the scalar mean and variance for the TV scheme. But given the 95% confidence interval, there is no evidence that solving the frozen-coefficient SDE system incurs more error based on the existing test cases. This suggests that solving the frozen-coefficient SDE system is helpful to reduce the numerical error (or at least not to incur more numerical error than solving the original SDE system). Third, the different splitting schemes applied to the original SDE system (4.12) and (4.13) perform differently, e.g., the mean errors of $\mathbb{CRTC}'$ are about three times of those of $\mathbb{CTRTC}'$. However, when the splitting schemes are applied to the frozen-coefficient SDE system (4.12) and (4.13), the numerical errors of the different splitting schemes are indistinguishable from each other, i.e., the mean errors of one scheme are inside of others' 95% confidence intervals. This suggests that the difference in performance of the different splitting schemes on the original SDE system can be reduced by using them instead on the frozen-coefficient SDE system.

The computational cost of the different splitting schemes are compared in Table 4.10 in terms of micro-seconds (μs) per particle per time step. First, the computational cost of the different splitting schemes is slightly different, e.g., for the CP scheme, the least expensive scheme $\mathbb{CRTC}'$ is about 20% quicker than the most expensive scheme $\mathbb{TCRC}'\mathbb{T}$, and for the same splitting $\mathbb{TCRC}'\mathbb{T}$-F, the least expensive scheme TV is about 10% quicker than the most expensive scheme KP. Second, the overall computational cost of about 3μs per particle per time step of the test case is cheap. (The computational cost of the three-dimensional case

Table 4.9: Comparison of the different splitting schemes combined with different Ito SDE schemes (time step $\Delta t = 0.05$) (the ± intervals indicate 95% confidence intervals).

	the CP scheme		the TV scheme		the KP scheme	
	$\mathcal{E}_{\overline{\phi}} \times 10^3$	$\mathcal{E}_{\overline{\phi^2}} \times 10^3$	$\mathcal{E}_{\overline{\phi}} \times 10^3$	$\mathcal{E}_{\overline{\phi^2}} \times 10^3$	$\mathcal{E}_{\overline{\phi}} \times 10^3$	$\mathcal{E}_{\overline{\phi^2}} \times 10^3$
$\mathbb{T}_1^{cp}\hat{\mathbb{T}}_1^{cp}\mathbb{C}\mathbb{R}\mathbb{C}'\mathbb{T}_2^{cp}$	4.62 ± 1.30	7.87 ± 3.97	—	—	—	—
$\mathbb{T}_1^{cp}\hat{\mathbb{T}}_1^{cp}\mathbb{C}\mathbb{R}\mathbb{C}'\mathbb{T}_2^{cp}$-F	1.59 ± 0.80	4.77 ± 1.49	—	—	—	—
$\mathbb{T}\mathbb{C}\mathbb{R}\mathbb{C}'\mathbb{T}$	3.48 ± 1.12	6.83 ± 3.36	3.60 ± 1.80	7.42 ± 3.18	—	—
$\mathbb{T}\mathbb{C}\mathbb{R}\mathbb{C}'\mathbb{T}$-F	1.88 ± 0.97	4.80 ± 2.03	1.73 ± 0.89	5.31 ± 1.35	1.54 ± 0.77	5.11 ± 2.24
$\mathbb{C}\mathbb{T}\mathbb{R}\mathbb{T}\mathbb{C}'$	1.76 ± 0.47	3.48 ± 1.78	1.86 ± 0.86	4.10 ± 2.09	—	—
$\mathbb{C}\mathbb{T}\mathbb{R}\mathbb{T}\mathbb{C}'$-F	1.62 ± 0.66	3.75 ± 1.92	1.87 ± 0.87	4.18 ± 2.13	1.66 ± 0.72	3.88 ± 1.95
$\mathbb{C}\mathbb{R}\mathbb{T}\mathbb{C}'$	7.82 ± 2.38	14.08 ± 6.72	8.71 ± 2.58	15.31 ± 7.52	—	—
$\mathbb{C}\mathbb{R}\mathbb{T}\mathbb{C}'$-F	1.63 ± 0.63	3.94 ± 2.02	2.42 ± 1.22	5.50 ± 2.47	1.84 ± 0.86	4.15 ± 2.05

is certainly higher but will not increase in order of magnitude. And also the above cost includes the evaluation of the manufactured solutions in Appendix D which is estimated to be over 60% of the overall cost and is not needed in the real PDF simulations.) It is estimated that the computational cost of a PDF code featuring detailed chemistry using ISAT is about 10 to 100 μs per particle per time step. So the cost of the particle transport and mixing (with simple mixing models) is only a very small portion of the total cost, and choosing different Ito SDE schemes and the different splitting schemes does not change the total computational cost of the PDF applications significantly.

4.6.3 Convergence of high moments

The weak convergence of the SDE schemes and splitting schemes has been verified for the first and second moments in Section 4.6.1. For completeness, we also perform the convergence tests for the second-order splitting schemes discussed in this paper in terms of the third and fourth moments. The tests confirm the

Table 4.10: Computational cost of the different splitting schemes in terms of μs per particle per time step

	the CP scheme	the TV scheme	the KP scheme
$\mathbb{T}_1^{cp}\hat{\mathbb{T}}_1^{cp}\mathbb{C}\mathbb{R}\mathbb{C}'\mathbb{T}_2^{cp}$	2.63	—	—
$\mathbb{T}_1^{cp}\hat{\mathbb{T}}_1^{cp}\mathbb{C}\mathbb{R}\mathbb{C}'\mathbb{T}_2^{cp}$-F	2.66	—	—
$\mathbb{T}\mathbb{C}\mathbb{R}\mathbb{C}'\mathbb{T}$	3.23	3.01	—
$\mathbb{T}\mathbb{C}\mathbb{R}\mathbb{C}'\mathbb{T}$-F	3.22	3.03	3.34
$\mathbb{C}\mathbb{T}\mathbb{R}\mathbb{T}\mathbb{C}'$	3.18	3.02	—
$\mathbb{C}\mathbb{T}\mathbb{R}\mathbb{T}\mathbb{C}'$-F	3.20	3.07	3.33
$\mathbb{C}\mathbb{R}\mathbb{T}\mathbb{C}'$	2.46	2.39	—
$\mathbb{C}\mathbb{R}\mathbb{T}\mathbb{C}'$-F	2.49	2.38	2.54

second-order convergence of all the second-order splitting schemes discussed in Section 4.5. For brevity, here we present the convergence results for only one type of splitting $\mathbb{C}\mathbb{T}\mathbb{R}\mathbb{T}\mathbb{C}'$ in Section 4.5.2.3. The analytical solutions of the third and fourth moments are not known for the estimate of numerical error in the test. We perform a high resolution finite-difference simulation of the transport equations of the third and fourth moments to obtain an accurate estimate of the their exact solutions. The transport equations for the third and fourth scalar moments derived from the PDF transport equation (4.28) are

$$\begin{aligned}
\frac{\partial\overline{\phi^3}(\mathbf{x},t)}{\partial t}+\frac{\partial\overline{u}_i(\mathbf{x},t)\overline{\phi^3}(\mathbf{x},t)}{\partial x_i} &= \frac{\partial}{\partial x_i}\left(\Gamma(\mathbf{x},t)\frac{\partial\overline{\phi^3}(\mathbf{x},t)}{\partial x_i}\right)\\
&- 3\Omega(\mathbf{x},t)\left(\overline{\phi^3}(\mathbf{x},t)-\overline{\phi^2}_m(\mathbf{x},t)\overline{\phi}_m(\mathbf{x},t)\right)\\
&+ 3R_a\left(\overline{\phi^3}(\mathbf{x},t)-R_b\overline{\phi^2}_m(\mathbf{x},t)\right)\\
&+ 3S_m(\mathbf{x},t)\overline{\phi^2}_m(\mathbf{x},t)\\
&- 3\Omega_v(\mathbf{x},t)\left(\overline{\phi^3}(\mathbf{x},t)-\overline{\phi^2}_m(\mathbf{x},t)\overline{\phi}_m(\mathbf{x},t)\right), \qquad (4.49)\\
\frac{\partial\overline{\phi^4}(\mathbf{x},t)}{\partial t}+\frac{\partial\overline{u}_i(\mathbf{x},t)\overline{\phi^4}(\mathbf{x},t)}{\partial x_i} &= \frac{\partial}{\partial x_i}\left(\Gamma(\mathbf{x},t)\frac{\partial\overline{\phi^4}(\mathbf{x},t)}{\partial x_i}\right)\\
&- 4\Omega(\mathbf{x},t)\left(\overline{\phi^4}(\mathbf{x},t)-\overline{\phi^3}(\mathbf{x},t)\overline{\phi}_m(\mathbf{x},t)\right)
\end{aligned}$$

$$
\begin{aligned}
&+ \quad 4R_a\left(\overline{\phi^4}(\mathbf{x},t) - R_b\overline{\phi^3}(\mathbf{x},t)\right) \\
&+ \quad 4S_m(\mathbf{x},t)\overline{\phi^3}(\mathbf{x},t) \\
&- \quad 4\Omega_v(\mathbf{x},t)\left(\overline{\phi^4}(\mathbf{x},t) - \overline{\phi^3}(\mathbf{x},t)\overline{\phi}_m(\mathbf{x},t)\right). \qquad (4.50)
\end{aligned}
$$

The equations are in closed form and can be solved numerically. Given the initial Gaussian distribution which is used in the particle initialization and the manufactured solutions for the first and second moments, we obtain the initial conditions for the numerical solutions of Eqs. (4.49) and (4.50) as follows:

$$
\begin{aligned}
\overline{\phi^3}(\mathbf{x},0) &= 3\overline{\phi}_m(\mathbf{x},0)\overline{\phi^2}_m(\mathbf{x},0) - 2\overline{\phi}^3_m(\mathbf{x},0), \qquad (4.51) \\
\overline{\phi^4}(\mathbf{x},0) &= 3\overline{\phi^2}^2_m(\mathbf{x},0) - 2\overline{\phi}^4_m(\mathbf{x},0), \qquad (4.52)
\end{aligned}
$$

where $\overline{\phi}_m$ and $\overline{\phi^2}_m$ are from Eqs. (D.1) and (D.3).

We obtain an accurate numerical solution of Eqs. (4.49) and (4.50) using a finite-difference method. The equations are discretized by central-differences in space and Crank-Nicolson scheme in time, yielding second-order accuracy in space and time. A total of 7500 grid cells are used in the simulation, and the time step is controlled to have the CFL number less than one, resulting in about 6000 time steps in total. The obtained numerical solutions from Eqs. (4.49) and (4.50) are used for estimating global errors (4.34) of the third and fourth moments sampled from the particles. The results of the convergence test for schemes $\mathbb{CTRTC}'$ (Section 4.5.2.3) are shown in Fig. 4.7. The test cases in the figure are the same as those in Fig. 4.5. From the figure, clearly we can see that the splitting schemes are second-order convergent for the third and fourth moments. The convergence tests are performed for all the second-order splitting schemes discussed in Section 4.5, and the test results confirm the second-order convergence. (These test results are not shown.)

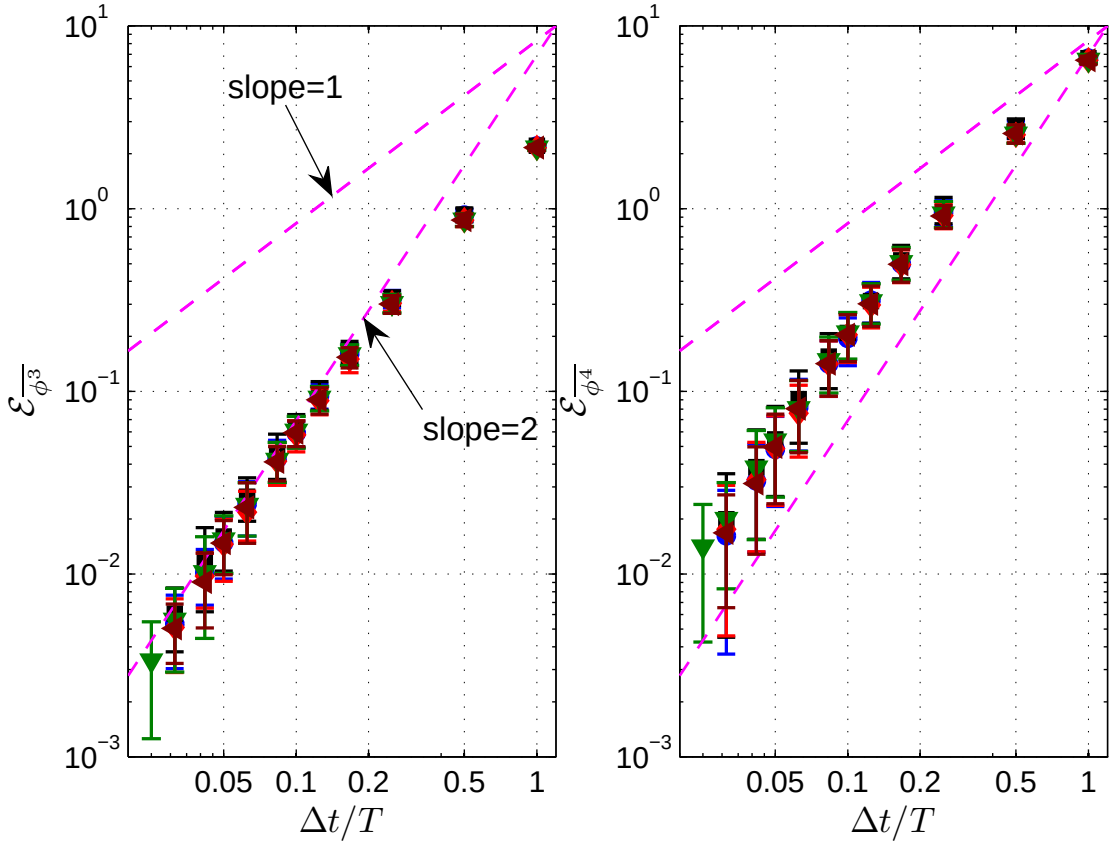

Figure 4.7: The convergence of the global error of $\overline{\phi^3}$ and $\overline{\phi^4}$ against the time step Δt with $\mathbb{C}\mathbb{T}^{\mathrm{cp}}\mathbb{R}\mathbb{T}^{\mathrm{cp}}\mathbb{C}'$ in Table 4.5 (circle), with $\mathbb{C}\mathbb{T}^{\mathrm{tv}}\mathbb{R}\mathbb{T}^{\mathrm{tv}}\mathbb{C}'$ in Table 4.5 (square), with $\mathbb{C}\mathbb{T}^{\mathrm{cp}}\mathbb{R}\mathbb{T}^{\mathrm{cp}}\mathbb{C}'$-F in Table 4.6 (diamond), with $\mathbb{C}\mathbb{T}^{\mathrm{tv}}\mathbb{R}\mathbb{T}^{\mathrm{tv}}\mathbb{C}'$-F in Table 4.6 (down triangle), and with $\mathbb{C}\mathbb{T}^{\mathrm{kp}}\mathbb{R}\mathbb{T}^{\mathrm{kp}}\mathbb{C}'$-F in Table 4.8 (left triangle). (The error bars indicate 95% confidence intervals.)

4.7 Discussion

In the convergence tests performed in Section 4.6, the simplifications of one dimension, single scalar and constant density have been made. The developed splitting schemes in Section 4.5.2.1-4.5.2.3 can be applied to all general three-dimensional, multi-scalar and variable-density problems. (The three-dimensional versions of the TV scheme and KP scheme in Section 4.3.3 must be used which can be found in the respective references. Any other weak second-order Ito SDE schemes can be used for the splitting. And the scalar equations are not limited to contain only the processes discussed.) The splitting scheme of the type $\mathbb{CRTC}'$ in Section 4.5.2.4 is designed for the non-coupled case between the reaction and the transport, e.g., constant density. It features only one step of reaction and one step of transport in the splitting. This splitting can also be used in the variable-density case without the feedback of density from the particle system to the flow solver, i.e., the reaction and the transport are independent, and the flow solver has its own estimate of density. This no-feedback configuration is a good study case for the development of PDF algorithms and code. It is also possible to apply the splitting $\mathbb{CRTC}'$ to the coupled variable-density problems. For example, if a second-order time extrapolation of the density is already obtained to perform the second sub-step of transport in $\mathbb{CTRTC}'$, then this splitting might be possibly reduced to $\mathbb{CRTC}'$ still with second-order accuracy. The formal order of accuracy of $\mathbb{CRTC}'$ in variable-density problems certainly needs further investigation in the future.

In the development of the MMS for the particle method, the linear reaction (4.25) is specified which is required for the closure of the moment equations (4.3) and (4.4) for weak convergence. This specification is introduced for verification

purposes only. Any complex (non-linear) reaction mechanism can be incorporated in the PDF methods without approximation. And the weak second-order accuracy of the splitting holds for the non-linear system. Due to sub-stepping, the reaction sub-step (4.40) is separated from the system and is independent from the particle position $\mathbf{X}(t)$. As far as the reaction sub-step is integrated stably with at least second-order accuracy, the splitting schemes (with second-order accuracy for the linear system) developed in this paper are still second-order accurate. The developed MMS for Monte Carlo particle methods can be applied to general problems with multi-dimension, multi-scalar and variable-density. In the design of the manufactured solutions, although the original PDF transport equation (4.1) is not satisfied by the manufactured solutions in general, the continuity equation is often chosen to be satisfied by the manufactured solutions due to the significance of mass conservation in our problem [44]. (Manufactured solutions without mass conservation are certainly possible for verification purposes, in which case a mass changing process is introduced.)

The convergence of the different splitting schemes discussed in this work is verified based on a one-dimensional test case. This test case is representative as far as non-trivial variations in the manufactured solutions are specified and proper initial and boundary conditions are imposed. In Appendix D, the manufactured solutions to the test case are specified which have non-trivial variations. Notice that the velocity component $\overline{u}$ (D.4) is uniform to satisfy the continuity equation. However, in the Ito SDE (4.6), the velocity always appears in the form of the drift velocity $D = \overline{u} + \nabla\Gamma$. As far as the diffusivity Γ (D.5) has a non-trivial gradient, the drift velocity D has non-trivial variation in space. The test case is periodic in space, so the periodic boundary condition is imposed on particles' positions. The test can be straightforwardly extended to three-

dimensional general test cases with other types of boundary conditions. The only concern with the extension is the computational cost which might be prohibitive when the test case is more complicated. Simple functions (e.g., a single sine or cosine mode with long wave length and time period) are suggested to design the manufactured solutions in order to take a relatively longer time step and larger grid size but still having the desired asymptotic convergent behavior.

In this work, only the time convergence of the Monte Carlo particle method is considered. In the Monte Carlo particle method it is not necessary to have a grid. However, in practice, the SDE coefficients are usually obtained from grid-based methods and are stored on a grid. The interpolation of these grid level SDE coefficients to the particles involves spatial error. The estimate of the particle scalar mean (4.44) for the IEM model often requires a grid to have sufficient particles inside a grid level, which involves a spatial smearing error. Hence the grid convergence of the Monte Carlo particle method also needs to be addressed. Some discussion has been made in a previous work [50]. The developed MMS for the particle method is applicable to the verification of the grid convergence of the particle method. Notice that, if a second-order spatial accurate method is used, in order to verify the grid convergence the computational cost scales as Δx^{-5}, where Δx is the grid size and Δt is fixed for different Δx in the estimate. Hence a simple test case is suggested to make the computational cost affordable.

The TV Ito SDE scheme (4.21) involves the specification of two free parameters α_2 and μ_3 and the choice between two families of parameters, (4.23) and (4.24). In all the results presented in Section 4.6, constants $\alpha_2 = 1.0$ and $\mu_3 = 0.5$ and parameters (4.24) are used. In addition, a set of tests is performed with

$\alpha_2 \in [0.5, 10]$ and $\mu_3 \in [-100, 10]$ for (4.24) and with $\alpha_2 = 1.0$ and $\mu_3 = 0.5$ for (4.23). No significant difference is found among all these tests in terms of accuracy and efficiency of the scheme. All choices of the constants result in the same number of coefficient evaluations for the one-dimensional version of the scheme, i.e., no simplification of the scheme. In the KP scheme (4.19), the random variable ξ can be specified as a three-point distributed random number (4.20) rather than a standardized Gaussian random number. The weak second-order accuracy of the scheme with this three-point distributed random number is confirmed by the test. No significant difference in the accuracy and efficiency is found when compared to the standardized Gaussian random number.

Among the splitting schemes discussed in this work, the splitting schemes for the frozen-coefficient SDE system are usually a little more accurate than those for the original SDE system. Other than that, no significant difference in accuracy and efficiency is found among the different splitting schemes. In RANS/PDF or LES/FDF applications, there might be additional considerations for choosing one scheme over others. The splitting schemes for the frozen-coefficient SDE system require only one time level of flow fields (at the mid-time in the particle step) for particle advancement, while those for the original SDE system require at least two time levels of flow fields, e.g., $\mathbb{T}_1^{\text{cp}}\hat{\mathbb{T}}_1^{\text{cp}}\mathbb{CRC}'\mathbb{T}_2^{\text{cp}}$ in Table 4.2 requires two levels of flow fields (at t_0 and $t_{\frac{1}{2}}$) and $\mathbb{T}^{\text{cp}}\mathbb{CRC}'\mathbb{T}^{\text{cp}}$ in Table 4.3 requires four levels of flow fields (at t_0, $t_{\frac{1}{4}}$, $t_{\frac{1}{2}}$, and $t_{\frac{3}{4}}$). To implement the splitting schemes for the original SDE system, at least two time levels of flow fields are needed in the particle solver to interpolate or extrapolate the required flow fields. The use of the frozen-coefficient splitting schemes simplifies the coupling between the flow solver and the particle solver, and reduces the storage requirement of the particle code because only one time level of flow fields is needed in

the particle solver. Another coupling issue between the flow solver and the particle solver is the time arrangement of the flow fields in the flow solver and the particles in the particle solver. There are usually two kinds of time arrangements of the flow fields and particles: staggered and collocated, as shown in Fig. 4.8. The splitting schemes for the frozen-coefficient SDE are applicable to both of them. In the staggered arrangement, the flow fields are stored at the mid-time of the particle step, so the flow fields are used naturally for the particle time advancement. In the collocated arrangement, the flow fields and particles are stored at the same time level, so the required mid-time flow fields for the particle time advancement need to be interpolated or extrapolated from the adjacent flow fields. There are some other issues in the coupling between the flow solver and particle solver, e.g., in a fully coupled variable-density LES/FDF code, iteration of the flow time step and particle time step may be needed. This is beyond the discussion of this work and will be addressed in the future work.

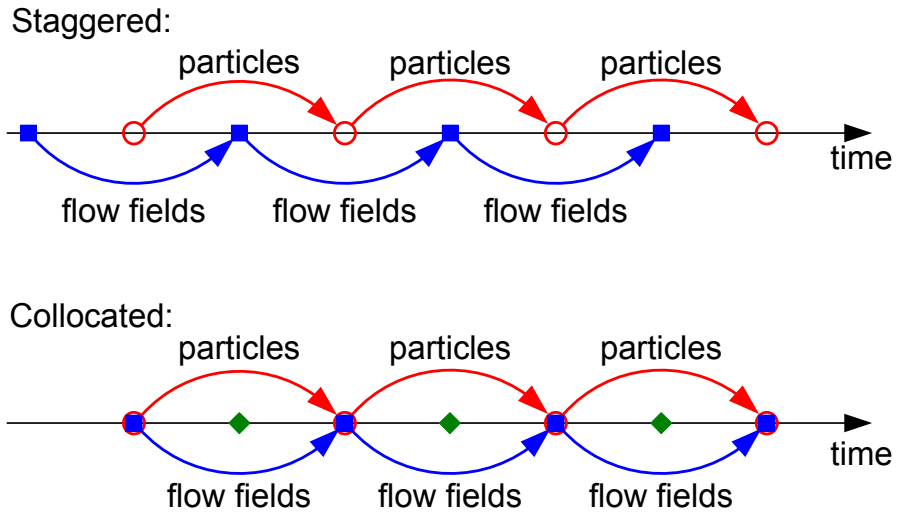

Figure 4.8: Staggered and collocated arrangement of flow fields and particles in time. (The circles are the time levels of particles, and the solid squares are the time levels to store flow fields (velocity and diffusivity etc.). The solid lines with arrows indicate the time advancement step for particles and flow fields. The solid diamonds indicate the flow fields at the mid-time interpolated from the neighbors.)

4.8 Conclusions

In this work, different weak second-order splitting schemes for solving the SDE system from the composition PDF methods are developed. Three Ito SDE schemes from the literature are chosen for investigation, the CP scheme (4.17), the KP scheme (4.19) and the TV scheme (4.21). A frozen-coefficient SDE system (4.12) and (4.13) is proposed as an alternative system to solve. The MMS for the Monte Carlo particle method is developed, in which the augmented scalar moment equations and the augmented particle scalar equation are derived. Different types of splitting schemes (on the original SDE system or on the frozen-coefficient SDE system) are discussed. The formal order of accuracy of the different splitting schemes is demonstrated by the particle MMS with a one-dimensional test case. The first-order accuracy of the CP scheme simply coupled with the scalar equation is shown, and it is shown that second-order accuracy is achieved by introducing a modified mid-point. The second-order accuracy of the other proposed splitting schemes is verified. The different second-order splitting schemes are compared in terms of accuracy and efficiency. The comparison suggests that solving the original SDE system with different splitting schemes yields somewhat different numerical errors, and that solving the frozen-coefficient SDE system helps to reduce the numerical error, and to reduce the difference of the numerical errors yielded by the different splitting schemes. No other significant difference is found in the comparison in terms of accuracy and efficiency of the different splitting schemes. This is a useful conclusion in that there is a considerable range of accurate and efficient schemes that can be implemented; and in practice there may be additional considerations and constraints which favor one scheme over others. The applicability and extensibility

of the developed methodologies to the general three-dimensional, multi-scalar and variable-density problems are briefly discussed.

Acknowledgements

This work is supported by Air Force Office of Scientific Research under Grant No. FA9550-09-1-0047. Helpful discussions with Steven R. Lantz are appreciated.

REFERENCES

[1] S.B. Pope, PDF methods for turbulent reactive flows, *Prog. Energy Combust. Sci.* 11 (1985) 119-192.

[2] S.B. Pope, Computations of turbulent combustion: progress and challenges, *Proc. Combust. Inst.* 23 (1990) 591-612.

[3] S.B. Pope, Turbulent Flows, Cambridge University Press, Cambridge, 2000.

[4] N. Peters, Laminar diffusion flamelet models in non-premixed turbulent combustion, *Prog. Energy Combust. Sci.* 10 (1984) 319-339.

[5] N. Peters, Turbulent Combustion, Cambridge University Press, Cambridge, 2000.

[6] R.W. Bilger, Conditional moment closure for turbulent reacting flow, *Phys. Fluids A* 5(2) (1993) 436-444.

[7] A.Y. Klimenko, R.W. Bilger, Conditional moment closure for turbulent combustion, *Prog. Energy Combust. Sci.* 25 (1999) 595-687.

[8] J. Xu, S.B. Pope, PDF calculations of turbulent nonpremixed flames with local extinction, *Combust. Flame* 123 (2000) 281-307.

[9] Q. Tang, J. Xu, S.B. Pope, PDF calculations of local extinction and NO production in piloted-jet turbulent methane/air flames, *Proc. Combust. Inst.* 28 (2000) 133-139.

[10] R.P. Lindstedt, S.A. Louloudi, E.M. Váos, Joint scalar probability density function modeling of pollutant formation in piloted turbulent jet diffusion flames with comprehensive chemistry, *Proc. Combust. Inst.* 28 (2000) 149-156.

[11] R.R. Cao, S.B. Pope, A.R. Masri, Turbulent lifted flames in a vitiated coflow investigated using joint PDF calculations, *Combust. Flame* 142 (2005) 438-453.

[12] R.P. Lindstedt, E.M. Váos, Transported PDF modeling of high-Reynolds-number premixed turbulent flames, *Combust. Flame* 145 (2006) 495-511.

[13] H. Wang, S.B. Pope, Lagrangian investigation of local extinction, re-ignition and auto-ignition in turbulent flames, *Combust. Theory and Model.* (2008) DOI: 10.1080/13647830802056137.

[14] F. Gao, E.E. O'Brien, A large-eddy simulation scheme for turbulent reacting flows, *Phys. Fluids A* 5 (1993) 1282-1284.

[15] P.J. Colucci, F.A. Jaberi, P. Givi, S.B. Pope, Filtered density function for large eddy simulation of turbulent reacting flows, *Phys. Fluids* 10(2) (1998) 499-515.

[16] F.A. Jaberi, P.J. Colucci, S. James, P. Givi, S.B. Pope, Filtered mass density function for large-eddy simulation of turbulent reacting flows, *J. Fluid Mech.* 401 (1999) 85-121.

[17] V. Raman, H. Pitsch, R.O. Fox, Hybrid large-eddy simulation/Lagrangian filtered-density-function approach for simulating turbulent combustion, *Combust. Flame* 143(1-2) (2005) 56-78.

[18] M.R.H. Sheikhi, T.G. Drozda, P. Givi, F.A. Jaberi, S.B. Pope, Large eddy simulation of a turbulent nonpremixed piloted methane jet flame (Sandia Flame D), *Proc. Combust. Inst.* 30 (2005) 549-556.

[19] C. Olbricht, F. Hahn, A. Sadiki, J. Janicka, Analysis of subgrid scale mixing using a hybrid LES-Monte-Carlo PDF method, *Int. J. Heat Fluid Flow* 28(6) (2007) 1215-1226.

[20] W.P. Jones, S. Navaffo-Martinez, Large eddy simulation of autoignition with a subgrid probability density function method, *Combust. Flame* 150 (3) (2007) 170-187.

[21] V. Raman, H. Pitsch, A consistent LES/filtered-density function formulation for the simulation of turbulent flames with detailed chemistry, *Proc. Combust. Inst.* 31 (2007) 1711-1719.

[22] S. James, J. Zhu, M.S. Anand, Large eddy simulations of turbulent flames using the filtered density function model, *Proc. Combust. Inst.* 31 (2007) 1737-1745.

[23] S.B. Pope, Particle method for turbulent flows: integration of stochastic model equations, *J. Comput. Phys.* 117 (1995) 332-349.

[24] P.E. Kloeden, E. Platen, Numerical Solution of Stochastic Differential Equations, Springer-Verlag, Berlin, 1992.

[25] R. Cao, S.B. Pope, Numerical integration of stochastic differential equations: weak second-order mid-point scheme for applications in the composition PDF method, *J. Comput. Phys.* 185 (2003) 194-212.

[26] E. Platen, On weak implicit and predictor-corrector methods, *Math. Comput. Simulat.* 38 (1995) 69-76.

[27] K. Burrage, T. Tian, Predictor-corrector methods of Runge-Kutta type for stochastic differential equations, *SIAM J. Numer. Anal.* 40(4) (2002) 1516-1537.

[28] J.R. Klauder, W.P. Petersen, Numerical integration of multiplicative-noise stochastic differential equations, *SIAM J. Numer. Anal.* 22(6) (1985) 1153-1166.

[29] M.I. Abukhaled, E. J. Allen, A class of second-order Runge-Kutta methods for numerical solution of stochastic differential equations, *Stochastic Anal. Appl.* 16(6) (1998) 977-991.

[30] A. Tocino, J. Vigo-Aguiar, weak second order conditions for stochastic Runge-Kutta methods, *SIAM J. Sci. Comput.* 24(2) (2002) 507-523.

[31] A. Rößler, Runge-Kutta methods for Itô stochastic differential equations with scalar noise, *BIT Numer. Math.* 46 (2006) 97-110.

[32] G.N. Milstein, A method of second-order accuracy integration of stochastic differential equations, *Theory Prob. Appl.* 23(2) (1978) 396-401.

[33] A. Greiner, W. Strittmatter, J. Honerkamp, Numerical integration of stochastic differential equations, *J. Stat. Phys.* 51(1-2) (1988) 95-108.

[34] V. Mackevičius, J. Navikas, Second order weak Runge-Kutta type methods for Itô equations, *Math. Comput. Simulat.* 57(1) (2001) 29-34.

[35] A. Rößler, Rooted tree analysis for order conditions of stochastic Runge-Kutta methods for the weak approximation of stochastic differential equations, *Stochastic Anal. Appl.* 24 (2006) 97-134.

[36] T.H. Tian, K. Burrage, Two-stage stochastic Runge-Kutta methods for stochastic differential equations, *BIT* 42(3) (2002) 625-643.

[37] A. Rößler, Second order Runge-Kutta methods for Stratonovich stochastic differential equations, *BIT Numer. Math.* 47 (2007) 657-680.

[38] C.D. Pierce, P. Moin, Progress-variable approach for large-eddy simulation of turbulent combustion, *J. Fluid Mech.* 504 (2004) 73-97.

[39] P.J. Roache, Code verification by the method of manufactured solutions, *J. Fluids Eng.* 124(1) (2002) 4-10.

[40] C.J. Roy, Review of code and solution verification procedures for computational simulation, *J. Comput. Phys.* 205 (2005) 131-156.

[41] C.J. Roy, C.C. Nelson, T.M. Smith, C.C. Ober, Verification of Euler/Navier-Stokes codes using the method of manufactured solutions, *Int. J. Numer. Method Fluids* 44 (2004) 599-620.

[42] L. Eça, M. Hoekstra, A. Hay, D. Pelletier, On the construction of manufactured solutions for one and two-equation eddy-viscosity models, *Int. J. Numer. Method Fluids* 54 (2007) 119-154.

[43] L. Eça, M. Hoekstra, A. Hay, D. Pelletier, Verification of RANS solvers with manufactured solutions, *Eng. Comput.* 23 (2007) 253-270.

[44] L. Shunn, F. Ham, Method of manufactured solutions applied to variable-density flow solvers, Annual Res. Briefs (2007) 155-168, Center for Turbulence Reseach, Stanford University.

[45] J. Villermaux, J.C. Devillon, Représentation de la coalescence et de la redispersion des domaines de ségrégation dans un fluide par un modèle d'interaction phénoménologique, Proceedings of the Second International Symposia on Chemical Reaction (1972) 1-13, Elsevier, New York.

[46] J. Janicka, W. Kolbe, W. Kollmann, Closure of the transport-equation for the probability density function of turbulent scalar fields, *J. Non-Equil. Thermodynam.* 4 (1979) 47-66.

[47] S. Subramaniam, S.B. Pope, A mixing model for turbulent reactive flows based on Euclidean minimum spanning trees, *Combust. Flame* 115 (1998) 487-514.

[48] G. Strang, On the construction and comparison of difference schemes, *SIAM J. Numer. Anal.* 5(3) (1968) 506-517.

[49] S.B. Pope, Computationally efficient implementation of combustion chemistry using in situ adaptive tabulation, *Combust. Theory and Model.* 1 (1997) 41-63.

[50] R. McDermott, S.B. Pope, The parabolic edge reconstruction method (PERM) for Lagrangian particle advection, *J. Comput. Phys.* 227 (2008) 5447-5491.

CHAPTER 5

LARGE EDDY SIMULATION/PROBABILITY DENSITY FUNCTION MODELING OF A TURBULENT $CH_4/H_2/N_2$ JET FLAME*

Abstract

In this work, we develop the large-eddy simulation (LES)/probability density function (PDF) simulation capability for turbulent combustion and apply it to a turbulent $CH_4/H_2/N_2$ jet flame (DLR Flame A). The PDF code is verified to be second-order accurate with respect to the time-step size and the grid size in a manufactured one-dimensional test case. Three grids ($64\times64\times16$, $192\times192\times48$, $320\times320\times80$) are used in the simulation of DLR Flame A to examine the effect of the grid resolution. The numerical solutions of the resolved mixture fraction and mixture fraction squared, and the density are duplicated in the LES code and the PDF code to explore the numerical consistency between them. A single laminar flamelet profile is used to reduce the computational cost of treating the chemical reactions of the particles. Both first and second-order time splitting schemes are used for integrating the stochastic differential equations for the particles, and these are compared in the jet flame simulation. The numerical results are found to be sensitive to the grid resolution, and the $192\times192\times48$ grid is adequate to capture the main flow fields of interest for this study. The numerical consistency between LES and PDF is confirmed by the small difference of their numerical predictions. Overall good agreement between the LES/PDF predictions and experimental data is observed for the resolved flow fields and

*Haifeng Wang, Stephen B. Pope, Large Eddy Simulation/Probability Density Function Modeling of a Turbulent CH4/H2/N2 Jet Flame, *Proceedings of the Combustion Institute*, 2010, (submitted).

the composition fields, including for the mass fractions of the minor species and NO. The first-order splitting scheme performs as well as the second-order splitting scheme in predicting the resolved mean and rms mixture fraction and the density for this flame.

5.1 Introduction

With the rapid development of modern high-performance computing technologies, numerical simulations of turbulent reactive flows have become a major approach to understanding fundamental phenomena of turbulence, combustion and their strong interactions. Three levels of numerical simulations exist for turbulent combustion: direct numerical simulation (DNS); large-eddy simulation (LES); and Reynolds averaged Navier-Stokes simulation (RANS). DNS resolves all scales, and hence requires the most computer resources that are currently prohibitive for a high-Reynolds number turbulent combustion problem. RANS models turbulence at all scales and has the least requirement of resolution and computer resources. LES resolves the large scales of turbulence, with the small scales being modeled, which poses an intermediate requirement for resolution and computer resources between DNS and RANS. Since the late 1990s, LES has become accessible to more and more studies and is likely to be a dominant methodology for the study of turbulence and turbulent combustion for a few decades to come.

In the LES of low-Mach number turbulent reactive flows, closure is required for chemical reactions due to their small scales compared to the turbulence resolution length scale, in additional to the closure requirements for the residual

stress and scalar flux. A few promising closure models for sub-grid scale (SGS) combustion have emerged over the last 20 years, mostly derived directly from the models used in the RANS context, e.g., the laminar flamelet models [1], the conditional moment closure (CMC) [2, 3], and the probability density function (PDF) methods [4, 5, 6]. PDF methods [7] have proved to be most successful in predicting turbulence-chemistry interactions in both RANS (e.g., [8, 9]) and LES (e.g., [10, 11]). The analogue of PDF in LES is often called filtered-density function (FDF) [4] defined based on the filtering operation normally used in LES. Different FDF approaches have been developed in the past, e.g., the composition FDF [6], the velocity-composition joint FDF [12] etc. The LES-FDF approaches have been employed in several previous studies of turbulent combustion, e.g., [10, 11]. There are different viewpoints of the PDF used in LES, in addition to FDF. Fox [13] defined it as a conditional PDF (conditioned on resolved quantities). Recently, Pope [14] developed an alternative foundation for LES of turbulent flows based on self-conditioned fields, rather than on filtering. In this framework, it is the self-conditioned PDF that is defined to describe the residual fluctuations. Several advantages are provided by this method over the traditional LES as illustrated in [14]. In this work, we follow this new framework and use the terminology PDF instead of FDF. Practically, different methods of LES and PDF do not lead to substantially different partial differential equations to be solved. Meanwhile, almost all models and algorithms for the PDF methods developed in the RANS context can be applied directly in LES.

An important task in advancing PDF methods in the LES context is to develop efficient and accurate algorithms and codes for practical applications. The Lagrangian Monte Carlo particle method [7] is widely used to solve the PDF transport equation. In this method, an equivalent particle system is designed

to represent the PDF, and the evolution of the particles to represent the evolution of the PDF. For each particle, a set of stochastic different equations (SDEs) is solved in the physical and composition spaces to account for particle transport, mixing and reaction. Particle tracking and the accurate solution of the SDEs are hence crucial for the success of the methods. In this work, we use the LES for the velocity, and the PDF for the chemical compositions. The numerical solution of the coupled SDEs arising from the composition PDF method is non-trivial and includes an SDE for particle position and a random ordinary differential equation for compositions. In all previous LES-PDF practice, only first-order accuracy is achieved in integrating the particle equations due to the lack of second-order splitting schemes for the coupled SDEs. Recently, Wang *et al.* [15] developed several second-order splitting schemes to solve the coupled SDEs more accurately.

In this work, we develop the LES/PDF capability for turbulent combustion. A new PDF code called HPDF has been developed with the following attributes: second-order accuracy in space and time; scalable up to 4096 cores; supporting Cartesian and polar cylindrical coordinate systems; parallelizable by domain decomposition in two dimensions; and it has a general interface to facilitate coupling to different existing LES (or RANS) codes etc. Here, we link HPDF to an existing LES code [18, 19, 10] to study a turbulent $CH_4/H_2/N_2$ jet flame (DLR Flame A) [16, 17]. In this first publication based on the new code, we address the following issues: the verification of the PDF code, the effect of the LES grid resolution, the consistency between LES and PDF, and the performance of different time-integration schemes (first-order and second-order) in HPDF. Comparison is also made with the experimental data [16, 17] to show the capability of the LES/PDF code. This study establishes the basis for our future work to con-

sider many species, differential-diffusion, advanced numerical models etc. in LES/PDF.

In this initial study, to address the above issues, we select a flame without strong turbulence/chemistry interactions so that it can be accurately described by a simple combustion model. Accordingly, we make the following simplifications. First, a single laminar flamelet profile is used in both LES and PDF to retrieve density and compositions as functions of mixture fraction. DLR Flame A (Re = 15200) exhibits very little local extinction. For this flame, the flamelet profile is expected to be capable of representing the turbulent non-premixed flame reasonably well. Second, no feedback (primarily density) from the PDF to the LES is taken into account. We refer to this as one-way coupling. In the LES, the transport equations for the mass, the momentum, and the resolved mixture fraction and mixture fraction squared are solved, and density is obtained from the flamelet profile by presuming a beta-PDF for the SGS fluctuations of the mixture fraction. The velocity, diffusivity, and density obtained from the LES is used in the particle transport. The density obtained from the PDF is computed for output only to address the consistency between LES and PDF. No feedback from the PDF to the LES takes place in this study. In contrast, two-way coupling would have feedback from the PDF to the LES in order to obtain density that can be used for the LES solution (and for the particle transport). This two-way coupling between the LES and the PDF is an important issue which will be addressed in our future work.

LES simulations of DLR Flame A have been performed by Ihme *et al.* [23] for the study of noise generation. In that study, a flamelet/progress variable combustion model is employed. The numerical results of the resolved mean and

rms of the axial velocity, the mixture fraction and the temperature were found to be in very good agreement with the measurement [16, 17] at the axial locations x/D=10, 20, and 40. PDF calculations of DLR Flame A in the RANS context have been performed by Lindstedt and Ozarovsky [24]. A reduced reaction mechanism containing 20 species is used in the PDF calculations. Generally, good agreement of the PDF results with the experimental data is observed for the velocity, temperature, and the species mass fractions. No work has been previously reported in the literature based on the LES/PDF approaches for this flame.

5.2 Computational details

5.2.1 LES solution

The LES code used in this work is based on [18, 19, 10]. The LES transport equations for mass, momentum and scalars are cast in a cylindrical-coordinate form for the simulation of the jet flame. The equations are solved using finite-differences in the cylindrical-coordinate system with a structured non-uniform grid and with second-order accuracy in space and time. The pressure projection (or fractional-step method) is used to enforce continuity. The Smagorinsky model with the dynamic procedure is employed to obtain the SGS eddy viscosity μ_{sgs} and diffusivity Γ_{sgs}. Details of the LES solution algorithms can be found in [18, 19, 10].

The transport equations for the resolved mixture fraction $\widetilde{\xi}$ and the resolved mixture fraction squared $\widetilde{\xi^2}$ are solved in LES. The dissipation rate $\widetilde{\chi}$ of the resid-

ual variance of mixture fraction is modeled as

$$\widetilde{\chi} = \Gamma \nabla \widetilde{\xi} \cdot \nabla \widetilde{\xi} + \left(\Gamma_{\text{sgs}} + 2\Gamma\right) \widetilde{\xi''^2} \Big/ \Delta^2, \tag{5.1}$$

where Γ is the molecular diffusivity, $\widetilde{\xi''^2}$ is the residual variance of mixture fraction ($\widetilde{\xi''^2} = \widetilde{\xi^2} - \widetilde{\xi}^2$), and Δ is the filter size. The tilde "$\widetilde{\ }$" denotes density-weighted filtering.

A single laminar flamelet profile $\boldsymbol{\phi} = \mathbf{F}(\xi)$ (where $\boldsymbol{\phi}$ is species mass fractions $\mathbf{Y}$, temperature T, density ρ, etc.) is used to obtain the compositions, which is obtained from an OPPDIF [20] calculation. The GRI 2.11 mechanism [21] is used to describe the chemical reactions in OPPDIF, and the mixture-averaged formula for diffusion velocities is used to treat molecular transport. A nominal strain rate of $a_n = 100\text{s}^{-1}$ is specified for the OPPDIF calculation.

A beta-function PDF is presumed for the SGS mixture fraction fluctuations, and a pre-computed 2D table $\widetilde{\boldsymbol{\phi}} = \mathbf{G}(\widetilde{\xi}, \widetilde{\xi''^2})$ is created based on the flamelet profile to retrieve resolved species mass fractions $\widetilde{\mathbf{Y}}$, temperature $\widetilde{T}$, and density $\overline{\rho}$ in the LES given the solutions of $\widetilde{\xi}$ and $\widetilde{\xi''^2}$. the overline "–" denotes the filtering operation.

The molecular transport properties used in the LES are approximated by the following relations, which are obtained from an empirical fit to the laminar flame calculations:

$$\mu/\overline{\rho} = \nu_0 (\widetilde{T}/T_0)^{1.66}, \tag{5.2}$$

$$\Gamma/\overline{\rho} = c_0 \nu_0 (\widetilde{T}/T_0)^{1.69}, \tag{5.3}$$

where $\nu_0 = 2.22 \times 10^{-5}\text{m}^2/\text{s}$, $T_0 = 300\text{K}$, $c_0 = 1.22$. Thus, $\mu/\overline{\rho}$ and $\Gamma/\overline{\rho}$ are taken to depend solely on $\widetilde{T}$.

5.2.2 PDF methods and particle methods

The composition PDF method accounts for the evolution of the PDF $f(\boldsymbol{\psi})$ of compositions $\boldsymbol{\phi}$ explicitly by solving the PDF transport equation. The PDF equation is solved numerically by integrating the following modeled SDEs for an ensemble of particles which represent the PDF,

$$\begin{aligned} d\mathbf{X}(t) &= \left[\widetilde{\mathbf{U}} + \frac{\nabla\left[\overline{\rho}\left(\Gamma_{\text{sgs}} + \Gamma\right)\right]}{\overline{\rho}}\right]^{*} dt \\ &+ \left[2\left(\Gamma^{*}_{\text{sgs}} + \Gamma^{*}\right)\right]^{\frac{1}{2}} d\mathbf{W}, \qquad (5.4) \\ d\boldsymbol{\phi}(t) &= -\Omega^{*}\left(\boldsymbol{\phi} - \widetilde{\boldsymbol{\phi}}^{*}\right) dt + \mathbf{S}(\boldsymbol{\phi})dt, \qquad (5.5) \end{aligned}$$

where $\mathbf{X}(t)$ is the particle position, $\widetilde{\mathbf{U}}$ is the resolved velocity field, Ω is the scalar mixing frequency, $\mathbf{S}$ is the reaction source term, and the superscript "*" denotes evaluating the quantity at $(\mathbf{X}(t), t)$. The IEM model is used to model the mixing in the scalar equation (5.5).

A simple splitting scheme can be constructed to integrate the SDEs (5.4) and (5.5), e.g., $\mathbb{T}^{\text{Euler}}\mathbb{MR}$ which denotes taking sub-steps of transport $\mathbb{T}$, mixing $\mathbb{M}$, and reaction $\mathbb{R}$ in this order each for a time-step Δt. The first-order Euler scheme is used to integrate (5.4) in this splitting, and overall first-order accuracy is observed for this scheme. Different types of second-order splitting schemes are developed in [15]. In this work, we consider the following type of second-order splitting, $\mathbb{T}^{\text{kp}}\mathbb{MRMT}^{\text{kp}}$, in which $\mathbb{T}$ and $\mathbb{M}$ appear twice to indicate that the transport and mixing are performed twice with time-step size $\Delta t/2$ within each time-step. A second-order SDE scheme KP [22] is used to integrate (5.4) in this splitting. Details about the second-order splitting for (5.4) and (5.5) are given in [15].

The coefficients needed for integrating (5.4) and (5.5) (e.g., $\widetilde{\mathbf{U}}^{*}$, Γ^{*}_{sgs}, Ω^{*}) are

obtained by interpolating the corresponding LES grid-based fields to the particle locations with simple tri-linear interpolation [1]. A mesh grid identical to the LES grid is used to track the particles and to form the statistics. Ghost cells with particles are used on the inflow/outflow boundary of the computational domain to have the desired particle mass flow rate through the boundary. Algorithms for particle cloning and annihilation are used to ensure an approximately constant number of particles in each cell after each particle transport sub-step, so that sufficient particles are available to form cell ensemble statistics, e.g., the density $\overline{\rho}_{\mathrm{p}}$ and the qth moment of the mixture fraction $\widetilde{\xi^q}_{\mathrm{p}}$ (where the subscript "p" denotes a quantity obtained from the particles to distinguish it from the same quantity obtained from the LES). In a given cell containing N particles, these quantities are determined as

$$\overline{\rho}_{\mathrm{p}} = \sum_{i=1}^{N} m_i^* \Big/ \sum_{i=1}^{N} m_i^* v_i^*, \tag{5.6}$$

$$\widetilde{\xi^q}_{\mathrm{p}} = \sum_{i=1}^{N} m_i^* \xi_i^{*q} \Big/ \sum_{i=1}^{N} m_i^*, \tag{5.7}$$

where m_i^*, v_i^*, and ξ_i^* are the mass, specific volume and mixture fraction of the ith particle in the cell.

In this work, only a single scalar (mixture fraction) is considered in the scalar equation (5.5). The first two moments $\widetilde{\xi^q}_{\mathrm{p}}$ ($q = 1, 2$) from the particles are consistent mathematically with $\widetilde{\xi^q}$ ($q = 1, 2$) from LES given that the mixing frequency Ω in Eq. (5.5) is modeled as $\Omega = \widetilde{\chi}/\widetilde{\xi''^2}$. The laminar flamelet profile $\boldsymbol{\phi} = \mathbf{F}(\xi)$ is used to obtain density, temperature and species mass fractions for particles.

[1] Tri-linear interpolation introduces a second-order spatial error $O(\Delta x^2)$. This causes a perturbation in the order $O(\Delta x^2 \Delta t)$ when integrating (5.4) and (5.5) for one time-step Δt. Due to the CFL restriction in the LES code, the ratio of $\Delta x/\Delta t$ is usually in the order of one. As a result, tri-linear interpolation causes a perturbation of order $O(\Delta t^3)$ when integrating (5.4) and (5.5) for one time-step, which is in the same order as the truncation error caused by second-order time integration schemes.

5.3 Verification of the HPDF code

The new HPDF code is verified for grid convergence and temporal convergence using the manufactured 1D test case described in [15] . Details about the testing are given in [15]. The grid convergence is shown in Fig. 5.1. The convergence error $\mathcal{E}$ [15] is measured in terms of $\widetilde{\xi}_{\mathrm{p}}$, $\widetilde{\xi^2}_{\mathrm{p}}$, and the particle mass density $\overline{\varrho}_{\mathrm{p}} = \sum_{i=1}^{N} m_i^* / V_{\mathrm{cell}}$, where V_{cell} is the volume of the corresponding grid cell. It is clear from Fig. 5.1 that (for small Δx) all of the errors are proportional to Δx^2, thus verifying the second-order spatial accuracy of the HPDF code.

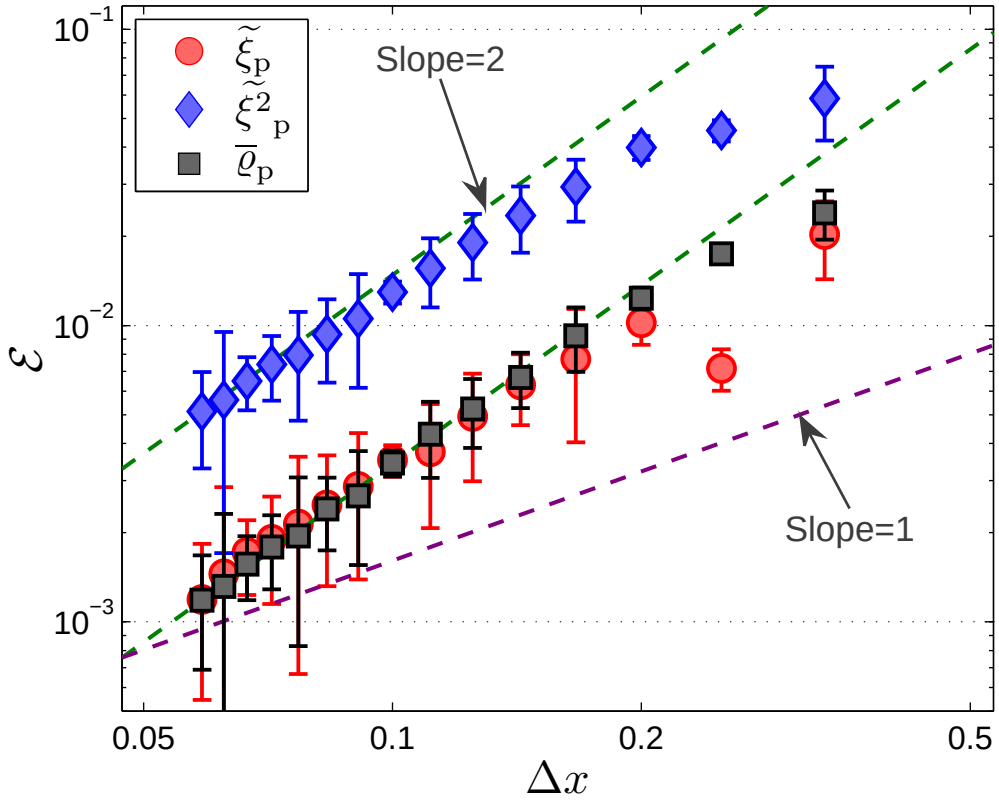

Figure 5.1: Numerical error $\mathcal{E}$ as a function of grid spacing Δx for the 1D test of the HPDF code. Circles: mean mixture fraction; Diamonds: mean mixture fraction squared; Squares: mean density; Error bars: 95% confidence intervals; Dashed lines: reference lines with slope one and two, corresponding to first and second-order spatial accuracy, respectively.

The temporal convergence is shown in Fig. 5.2 for both the first-order and second-order splitting schemes discussed in Section 5.2.2. For the first-order splitting scheme (the left sub-plot of Fig. 5.2), the errors for small Δt are proportional to Δt, which confirms the first-order temporal convergence of the scheme. For the second-order splitting scheme (the right sub-plot of Fig. 5.2), the errors for small Δt are proportional to Δt^2, thus verifying the second-order accuracy of the scheme.

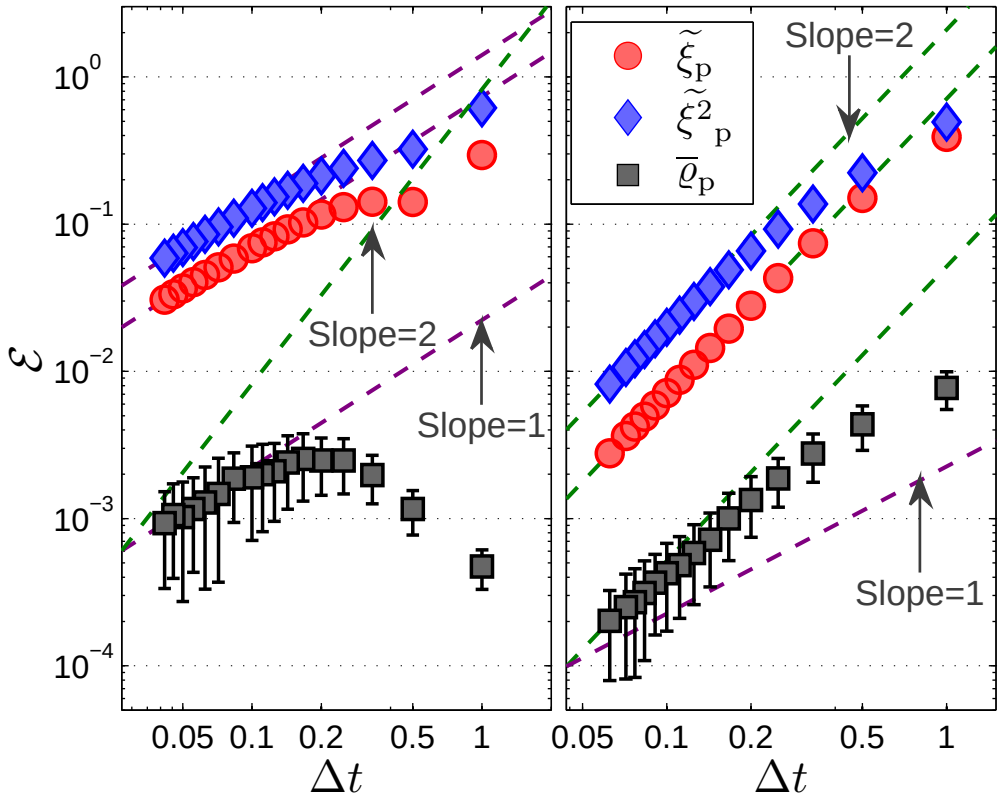

Figure 5.2: Numerical error $\mathcal{E}$ as a function of time-step size Δt for the 1D test of the HPDF code (left: first-order splitting scheme; right: second-order splitting scheme). Circles: mean mixture fraction; Diamonds: mean mixture fraction squared; Squares: mean density; Error bars: 95% confidence intervals; Dashed lines: reference lines with slope one and two, corresponding to first and second-order temporal accuracy, respectively.

Next we link HPDF with the LES code [18, 19, 10] and perform the LES/PDF simulations of DLR Flame A.

5.4 LES/PDF calculations of DLR Flame A

A simple turbulent jet flame of $CH_4/H_2/N_2$ [16, 17] at moderate Reynolds number (Re = 15200), DLR Flame A, is chosen for the study in this work. The jet nozzle has a diameter of D = 8mm (with bulk velocity U_0 = 42.2m/s) surrounded by a low-velocity air coflow (0.3m/s). The fuel consists of 22.1% CH_4, 33.2% H_2, and 44.7% N_2 by volume. The flame exhibits very little local extinction, and hence is suitable for this study using a single laminar flamelet profile to obtain the thermochemical properties.

The computational domain is specified to be $[0, 120D] \times [0, 30D] \times [0, 2\pi]$ in the axial (x), radial (r) and azimuthal (θ) directions. Three non-uniform grids are used in the simulations, of sizes $64 \times 64 \times 16$, $192 \times 192 \times 48$, and $320 \times 320 \times 80$ in axial, radial, and azimuthal directions. The grids are concentrated near the nozzle in the axial and radial directions. In HPDF, the same computational domain and grid size are used as in LES. The time-step size is determined by a fixed maximum CFL number (=0.2) based on the axial velocity only, and the same time-step size is used in both LES and PDF. The maximum CFL number occurs near the jet exit, where the axial velocity is large and the grid spacing is small. The resulting time step is relatively small, e.g., $\Delta t \approx 3.3\mu$s for the $192 \times 192 \times 48$ grid.

5.4.1 Effect of LES grid resolution

We first discuss the time-averaged LES calculations of the flow field in DLR Flame A and their comparison with the experimental data [16, 17]. Fig. 5.3

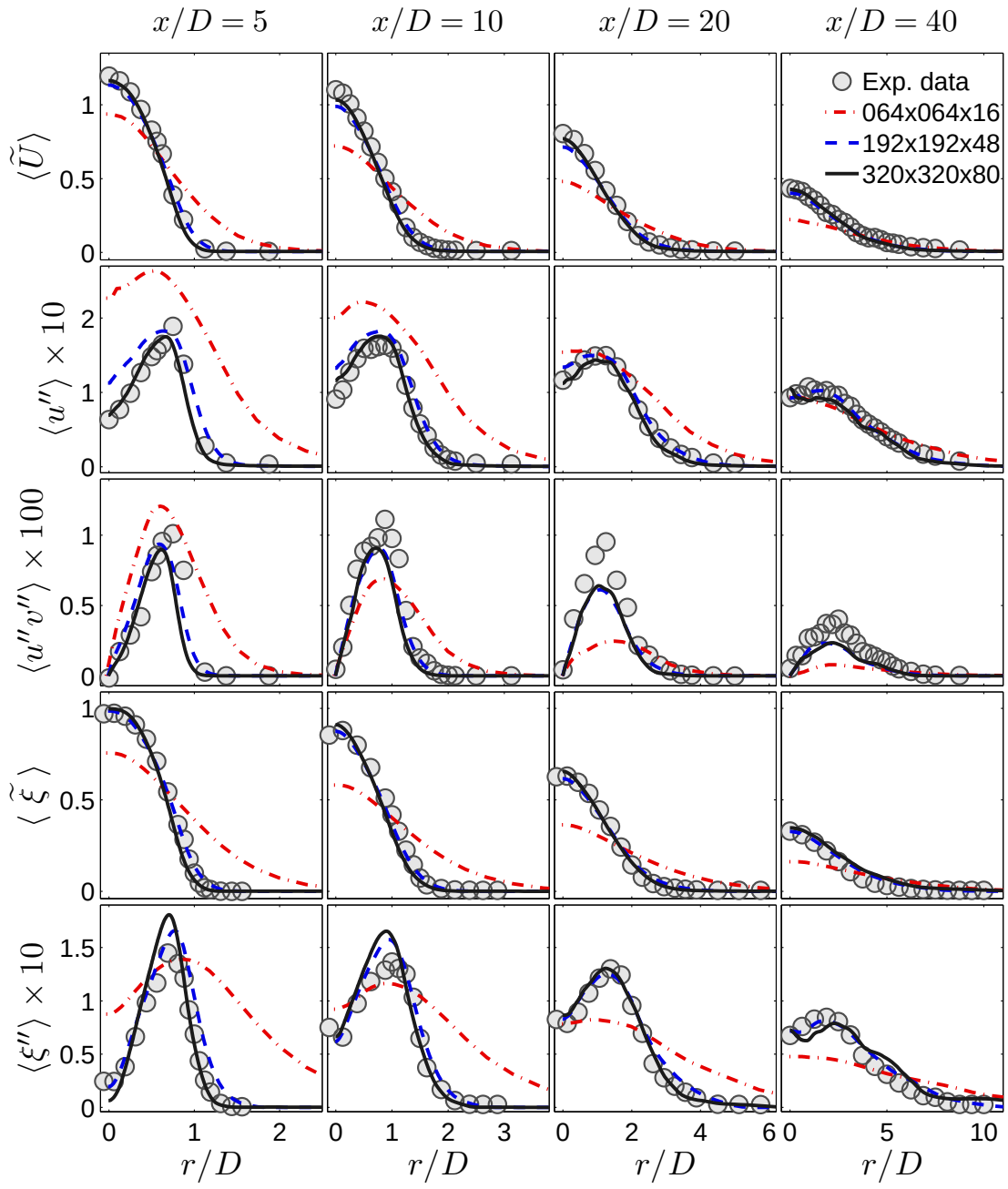

Figure 5.3: Radial profiles of the time-averaged axial velocity $\langle \widetilde{U} \rangle$, the axial turbulence intensity $\langle u'' \rangle$, the Reynolds shear stress $\langle u''v'' \rangle$, the resolved mean mixture fraction $\langle \widetilde{\xi} \rangle$, and the resolved rms $\langle \xi'' \rangle$ at the four axial locations x/D =5, 10, 20, and 40. Symbols: experimental data [16, 17]; Lines: LES calculations, dash-dotted — $64 \times 64 \times 16$ grid, dashed — $192 \times 192 \times 48$ grid, solid — $320 \times 320 \times 80$ grid.

compares the time-averaged radial profiles at the four axial locations x/D =5, 10, 20, and 40. Time-averaging is denoted by $\langle\cdot\rangle$. The quantities shown are the resolved axial velocity $\langle\widetilde{U}\rangle$, the resolved axial turbulence intensity $\langle u''\rangle = (\langle(\widetilde{U})^2\rangle - \langle\widetilde{U}\rangle^2)^{1/2}$, the resolved Reynolds shear stress $\langle u''v''\rangle = \langle\widetilde{U}\widetilde{V}\rangle - \langle\widetilde{U}\rangle\langle\widetilde{V}\rangle$, the resolved mean mixture fraction $\langle\widetilde{\xi}\rangle$, and the resolved root mean square (rms) $\langle\xi''\rangle = (\langle(\widetilde{\xi})^2\rangle - \langle\widetilde{\xi}\rangle^2)^{1/2}$. As may be seen from Fig. 5.3, the results from the two finest grids ($192 \times 192 \times 48$ and $320 \times 320 \times 80$) are almost coincident, with the largest differences being in $\langle u''\rangle$ at x/D=5. There is striking agreement between these results and the experimental data. In contrast, the results from the coarse grid ($64 \times 64 \times 16$) are significantly different (and in extremely poor agreement with the experimental data). The $192 \times 192 \times 48$ grid seems adequate to capture the flow fields of interest, and hence this grid is used to obtain all the results presented below.

5.4.2 Consistency between LES and PDF

In this work, the fields of mixture fraction ($\widetilde{\xi}$ and $\widetilde{\xi^2}$) and density $\overline{\rho}$ are duplicated in the LES and PDF codes. The evolution equations for the resolved mixture fraction $\widetilde{\xi}$ and mixture fraction squared $\widetilde{\xi^2}$ used in LES are consistent with those for the first two moments implied by the modeled PDF equation ($\widetilde{\xi^q}_{\rm p}$, $q = 1, 2$) given the proper modeling of the residual mixture fraction dissipation rate $\widetilde{\chi}$ (Eq. 5.1) and the mixing frequency Ω (modeled as $\Omega = \widetilde{\chi}/\widetilde{\xi''^2}$) in Eq. (5.5). Numerically, these results are not the same due to the different numerical errors involved in the LES and PDF codes. It is interesting to see how different these two sets of numerical results are from each other. The density field from LES $\overline{\rho}$, however, is not consistent with the density from PDF $\overline{\rho}_{\rm p}$ due to the different

probability distribution of SGS mixture fraction used in the LES code (presumed beta-PDF) and in the PDF code (explicitly solved from the PDF transport equation).

In HPDF, 50 particles per grid cell are used, resulting in about 88 million particles in total for the grid $192 \times 192 \times 48$. The code starts from existing LES fields in the statistically-stationary state, and initializes the particle properties from the LES fields, e.g., initializing the particle mixture fraction by interpolating the LES field $\widetilde{\xi}$ to the particle locations. About 50,000 time steps are marched for the particles to reach the statistically-stationary state. Then, another 50,000 time steps are executed to perform time averaging. The 50,000 time steps correspond to about seven flow through time estimated based on the centerline jet inlet velocity. The second-order time integration scheme $\mathbb{T}^{kp}\mathbb{M}\mathbb{R}\mathbb{M}\mathbb{T}^{kp}$ (Section 5.2.2) [15] for the particle equations (Eq. 5.4-5.5) is used in all the following simulations unless otherwise specified.

In Fig. 5.4, we compare the radial profiles of $\langle \widetilde{\xi} \rangle$, $\langle \xi'' \rangle$, the total rms $\langle \xi'' \rangle_{\text{Total}} = (\langle \widetilde{\xi^2} \rangle - \langle \widetilde{\xi} \rangle^2)^{1/2}$, and the density $\langle \overline{\rho} \rangle$ from LES and PDF at the four axial locations x/D =5, 10, 20, and 40. Note that the total variance $\langle \xi'' \rangle^2_{\text{Total}}$ consists of two parts: the resolved variance $\langle \xi'' \rangle^2 = \langle (\widetilde{\xi})^2 \rangle - \langle \widetilde{\xi} \rangle^2$ and the residual variance $\langle \xi'' \rangle^2_{\text{Residual}} = \langle \widetilde{\xi^2} \rangle - \langle (\widetilde{\xi})^2 \rangle$, i.e., $\langle \xi'' \rangle^2_{\text{Total}} = \langle \xi'' \rangle^2 + \langle \xi'' \rangle^2_{\text{Residual}}$. The calculations of $\langle \widetilde{\xi} \rangle$, $\langle \xi'' \rangle$, $\langle \xi'' \rangle_{\text{Total}}$ from LES (solid lines) and PDF (dashed lines) are slightly different, yet both agree with the experimental data reasonably well. The PDF calculations are in slightly better agreement than those by LES, e.g., $\langle \xi'' \rangle_{\text{Total}}$ near the jet edge and its peak values at x/D =5, 10 and 20, which is probably due to the lower spatial truncation errors in the particle method. The percentage of the resolved rms $\langle \xi'' \rangle$ of mixture fraction over the total predicted rms $\langle \xi'' \rangle_{\text{Total}}$ is about 80% near

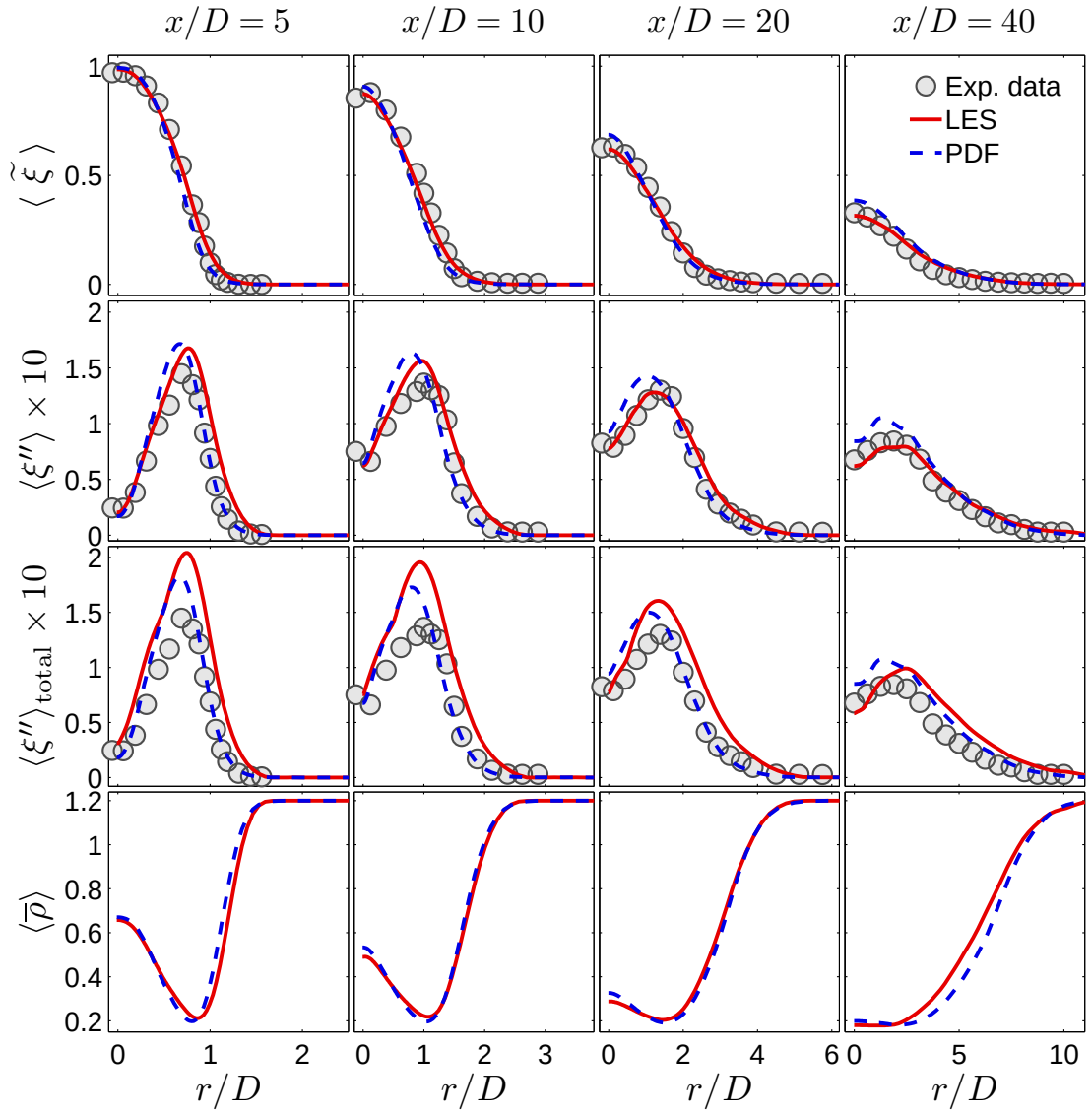

Figure 5.4: Radial profiles of the time-averaged mean $\langle \widetilde{\xi} \rangle$, the resolved rms $\langle \xi'' \rangle$, the total rms $\langle \xi'' \rangle_{\text{Total}}$, and the density $\langle \overline{\rho} \rangle$ at the four axial locations x/D =5, 10, 20, and 40. Symbols: experimental data [16]; Solid lines: LES calculations; Dashed lines: PDF calculations. (The calculations of $\langle \xi'' \rangle$and $\langle \xi'' \rangle_{\text{Total}}$ are both compared to the experimental data for $\langle \xi'' \rangle_{\text{Total}}$.)

the peak value for the LES results and 95% for the PDF results. This slightly better resolution of the PDF results is probably also due to the lower spatial truncation errors.

The density calculations from LES and PDF are in good agreement as shown in Fig. 5.4. The slight discrepancy can be explained by the different numerical errors involved in LES and PDF, and by the different probability distribution of SGS mixture fraction in LES and PDF. Recall that in this work, there is no feedback of density from the PDF code, i.e., the density used in the LES code and in the particle transport is from the LES code. The numerical consistency of the density from LES and PDF makes this one-way coupling strategy acceptable for this study.

5.4.3 Composition fields

In this sub-section, we examine in detail the calculations of the composition fields in DLR Flame A. Figure 5.5 shows the radial profiles of the time-averaged resolved temperature $\langle\widetilde{T}\rangle$, and the resolved mass fractions $\langle\widetilde{\mathbf{Y}}\rangle$ of CH_4, O_2, CO_2, H_2O, CO, H_2, OH, and NO at the four axial locations x/D =5, 10, 20, and 40. Figure 5.6 shows the time-averaged rms temperature ($(\langle\widetilde{T}^2\rangle - \langle\widetilde{T}\rangle^2)^{1/2}$) and the time-averaged r.m.s. species mass fractions $(\langle\widetilde{\mathbf{Y}}^2\rangle - \langle\widetilde{\mathbf{Y}}\rangle^2)^{1/2}$. These quantities are computed based on the 2D flame table $\widetilde{\boldsymbol{\phi}} = \mathbf{G}(\widetilde{\xi}, \widetilde{\xi''^2})$ in LES and based on the flamelet profile $\boldsymbol{\phi} = \mathbf{F}(\xi)$ in PDF (see Section 5.2.1). Overall good agreement of the calculations with the experimental data [16] is observed, including for the minor species and NO, largely due to the accurate calculation of the mixture fraction as shown in Fig. 5.4. The discrepancy between the calculations and the

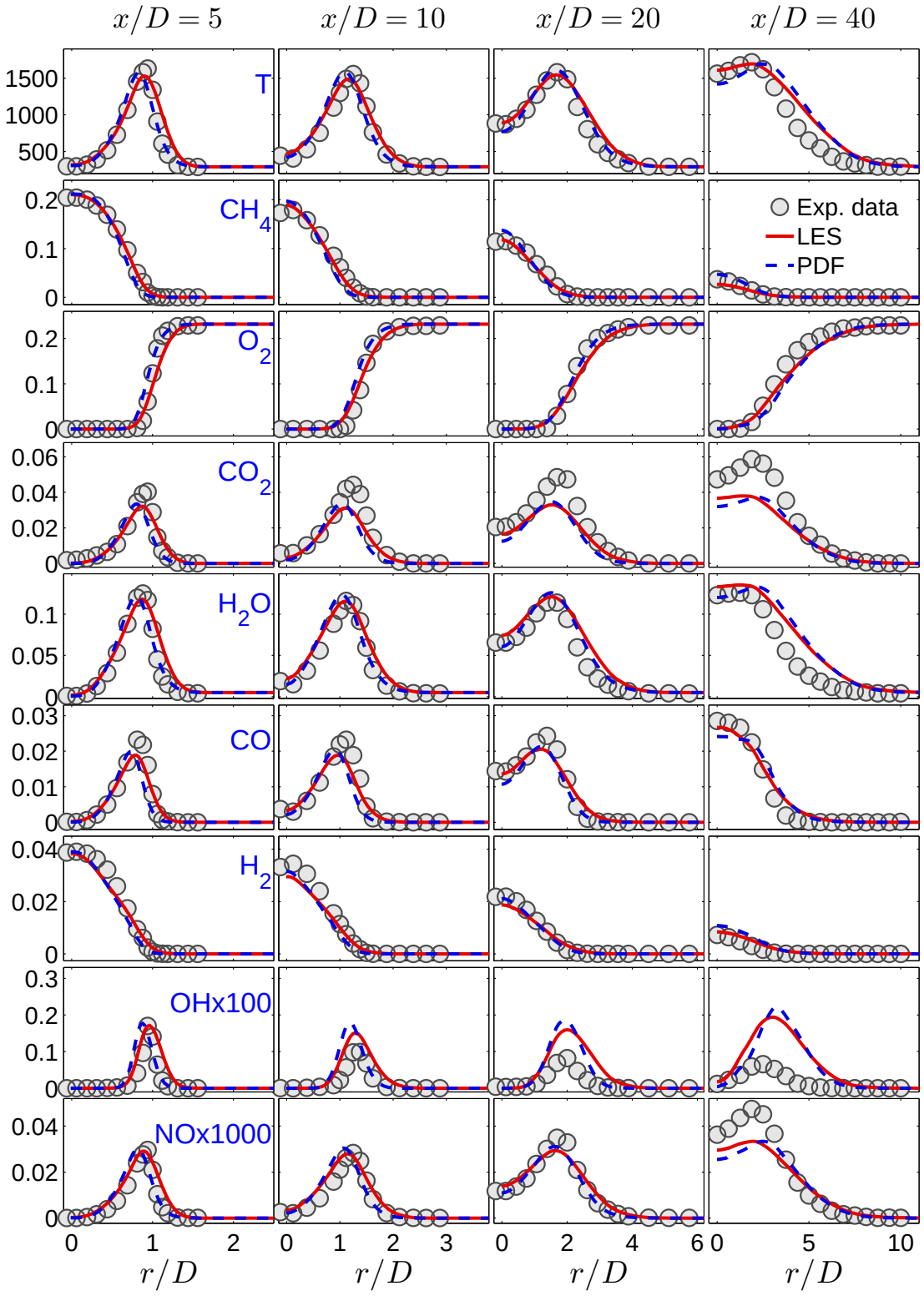

Figure 5.5: Radial profiles of the time-averaged mean temperature $\langle \widetilde{T} \rangle$, and mean mass fractions of CH_4, O_2, CO_2, H_2O, CO, H_2, OH, and NO at the four axial locations x/D =5, 10, 20, and 40. Symbols: experimental data [16]; Solid lines: LES calculations; Dashed lines: PDF calculations.

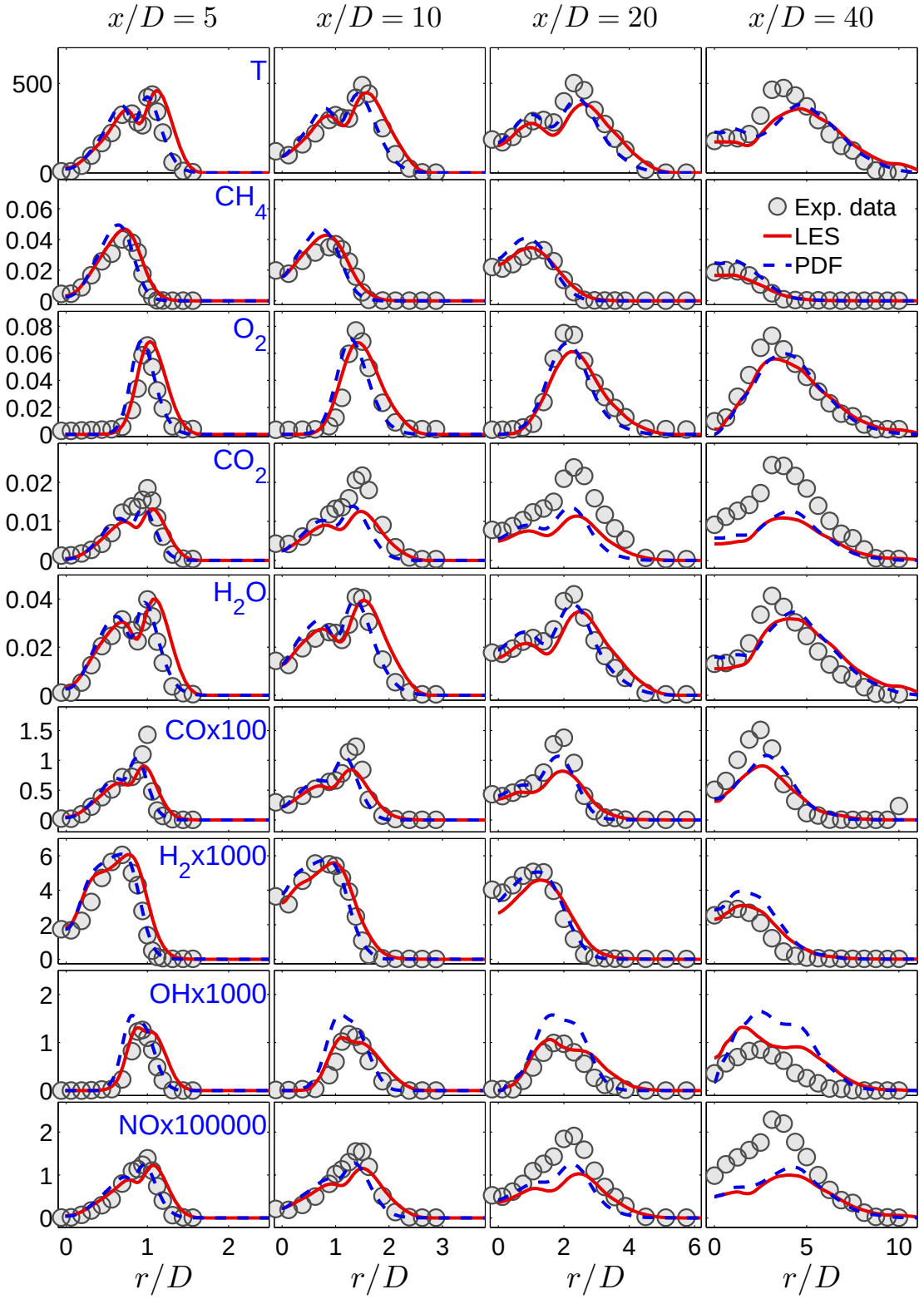

Figure 5.6: Radial profiles of the rms temperature, and rms mass fractions of CH_4, O_2, CO_2, H_2O, CO, H_2, OH, and NO at the four axial locations x/D =5, 10, 20, and 40. Symbols: experimental data [16]; Solid lines: LES calculations; Dashed lines: PDF calculations.

measurement may be explained by the single laminar flamelet model, which does not account for the effect of fluctuations of the scalar dissipation rate on the flame, and the effect of local extinction. The difference between the LES and PDF predictions is small as expected, given the similar predictions of mixture fraction in LES and PDF shown in Fig. 5.4.

5.4.4 Effect of time integration schemes

In all the previous LES/PDF practices with Lagrangian Monte Carlo particle methods, only first-order temporal accuracy is achieved in integrating the coupled SDEs for particles (Eq. 5.4-5.5) due to the lack of second-order splitting schemes for the SDEs. In this work, a second-order splitting scheme for the SDEs developed in [15] is applied in the simulation of the turbulent jet flame. The performance of the second-order scheme has been shown in [15] and in Fig. 5.2 for a manufactured 1D test case. In the simulation of DLR Flame A, the first-order splitting scheme is found to be as good as the second-order scheme in predicting the resolved mean $\langle \widetilde{\xi} \rangle$, the resolved rms $\langle \xi'' \rangle$, and the density $\langle \overline{\rho} \rangle$. The relative difference of the calculations from these two splitting schemes is within 5% (the results are not shown). This small difference is probably due to the relatively small time-step ($\Delta t \approx 3.3\mu$s) used in the simulation which is determined by the maximum CFL=0.2. The temporal truncation errors resulting from this small time-step size are probably lower than the other numerical errors, e.g., the statistical errors, the spatial truncation errors, etc., in most of the computational domain, especially downstream where the grid size is large and the velocity is small. The first-order splitting scheme seems adequate to evolve the particles accurately for this flame, which is a useful observation because the

first-order splitting scheme has only about half of the computational cost of the second-order splitting for the simulations in this work. This, however, does not suggest that the first-order splitting is adequate for the integration of the particle equations (Eq. 5.4-5.5) in all applications of PDF methods. For the simulations of turbulent flows with more uniform CFL number in the whole computational domain, the temporal truncation errors may be comparable to the other numerical errors, and hence the superiority of the second-order splitting schemes may be evident in those situations.

5.4.5 Computational cost

We estimate the computational cost of the LES/PDF code for the $192 \times 192 \times 48$ grid with the second-order splitting scheme. About 1.77 million grid cells are used in the LES and PDF. A number of 50 particles per cell is used in HPDF, resulting in about 88 million particles in total. The simulation is performed using 256 cores on the Linux cluster Ranger at the Texas Advanced Computing Center. A 2D domain-decomposition of 64×4 in axial and radial directions is specified in the LES code. A different domain-decomposition strategy is used in HPDF, which optimizes the domain-decomposition automatically by balancing the estimated overall workload (including field operations and particle operations) on each core. The resulting domain-decomposition in HPDF happens to be the same as in LES in this case. The computational cost of the LES/PDF code is about 1600μs per grid cell per time-step. The wall clock time for the code to run for 50000 time steps is about 6.4 days on 256 cores. The cost for the LES part is about 155μs per grid cell per time-step. The HPDF code costs about 26μs per particle per time step. The cost percentage of the HPDF code over the whole

code is 90%, i.e., the HPDF cost dominates the LES cost. The parallel scalability of the LES/PDF code depends primarily on the scalability of the HPDF code. We have profiled the HPDF code in a simple 3D manufactured test case. So far, it is found that HPDF scales well up to 4096 cores for a fixed size problem per core. It is expected that the LES/PDF code scales well up to the same number of cores. More scalability tests will be performed in the future work.

5.5 Conclusions

In this work, we perform LES/PDF simulations of a turbulent $CH_4/H_2/N_2$ jet flame (DLR Flame A). A manufactured 1D test case is used to verify the convergence of the PDF code, specifically to verify the second-order convergence in space, and the first-order and second-order convergence in time for the first-order and second-order splitting schemes, respectively. Three grids ($64\times64\times16$, $192 \times 192 \times 48$, $320 \times 320 \times 80$) are used in the simulations to examine the effect of the grid resolution. The numerical results are found to be sensitive to the grid-refinement. The moderate resolution of $192 \times 192 \times 48$ is found adequate to capture the flow fields of interest. The LES and PDF results for the mean and rms mixture fraction and mean density are compared to examine the numerical consistency between LES and PDF. Good agreement between them is observed, suggesting good numerical consistency. Both LES and PDF results are compared with the experimental data. Overall good agreement of the predictions with the experimental data is observed, showing the capability of the employed models to represent the flow and composition fields of this flame. The performance of the first and second-order splitting schemes for the particle equations is compared in the jet flame simulation. For this flame, the first-order splitting scheme

performs as well as the second-order splitting scheme in predicting the mean and rms mixture fraction and mean density. This work establishes the basis for our future work to consider two-way coupling, molecular diffusion, detailed chemsitry, other flames etc. in LES/PDF.

Acknowledgments

The authors thank Steven R. Lantz for help with high-performance computing. Helpful discussions with Sharadha Viswanathan, Pavel P. Popov, Konstantin A. Kemenov, David A. Caughey, Venkat Raman and Heinz Pitsch are appreciated. Large parts of the computational results presented in this paper are obtained using the Ranger cluster at the Texas Advanced Computing Center at The University of Texas at Austin. This work was supported in part by Air Force Office of Scientific Research under grant FA-9550-09-1-0047 and in part it is based upon work supported as part of the Combustion Energy Frontier Research Center funded by the U.S. Department of Energy, Office of Science, Office of Basic Energy Sciences under Award Number DE-SC0001198.

REFERENCES

[1] A. W. Cook, J.J. Riley, G. Kosály, A laminar flamelet approach to subgrid-scale chemistry in turbulent flows, *Combust. Flame* 109(3) (1997) 332-341.

[2] S. Navarro-Martinez, A. Kronenburg, F. Di Mare, Conditional moment closure for large eddy simulations, *Flow Turbulence Combust.* 75(1-4) (2005) 245-274.

[3] S.H. Kim, H. Pitsch, Conditional filtering method for large-eddy simulation of turbulent nonpremixed combustion, *Phys. Fluids* 17(10) (2005) 105103.

[4] S.B. Pope, Computations of turbulent combustion: progress and challenges, *Proc. Combust. Inst.* 23 (1990) 591-612.

[5] F. Gao, E.E. O'Brien, A large-eddy simulation scheme for turbulent reacting flows, *Phys. Fluids* A 5(6) (1993) 1282-1284.

[6] P.J. Colucci, F.A. Jaberi, P. Givi, S.B. Pope, Filtered density function for large eddy simulation of turbulent reacting flows, *Phys. Fluids* 10(2) (1998) 499-515.

[7] S.B. Pope, PDF methods for turbulent reactive flows, *Prog. Energy Combust. Sci.* 11 (1985) 119-192.

[8] J. Xu, S.B. Pope, PDF calculations of turbulent nonpremixed flames with local extinction, *Combust. Flame* 123 (2000) 281-307.

[9] H. Wang, S.B. Pope, Lagrangian investigation of local extinction, re-ignition and auto-ignition in turbulent flames, *Combust. Theory and Model.* 12(5) (2008) 857-882.

[10] V. Raman, H. Pitsch, A consistent LES/filtered-density function formulation for the simulation of turbulent flames with detailed chemistry, *Proc. Combust. Inst.* 31(2) (2007) 1711-1719.

[11] S. James, J. Zhu, M.S. Anand, Large eddy simulations of turbulent flames using the filtered density function model, *Proc. Combust. Inst.* 31(2) (2007) 1737-1745.

[12] M.R.H Sheikhi, T.G Drozda, P. Givi, S.B. Pope, Velocity-scalar filtered density function for large eddy simulation of turbulent flows, *phys. Fluids* 15(8) (2003) 2321-2337.

[13] R.O., Fox, Computational Models for Turbulent Reacting Flows, Cambridge University Press, 2003.

[14] S.B. Pope, Self-Conditioned Fields for Large-Eddy Simulations of Turbulent Flows, *J. Fluid Mech.* (2010), to be published.

[15] H. Wang, P. P. Popov, S. B. Pope, Weak Second Order Splitting Schemes for Lagrangian Monte Carlo Particle Methods for the Composition PDF/FDF Transport Equations, *J. Comput. Phys.* 229 (2010) 1852-1878.

[16] W. Meier, R.S. Barlow, Y.-L. Chen, and J.-Y. Chen, Raman/Rayleigh/LIF measurements in a turbulent CH4/H-2/N-2 jet diffusion flame: Experimental techniques and turbulence-chemistry interaction, *Combust. Flame* 123 (2000) 326-343.

[17] Ch. Schneider, A. Dreizler, J. Janicka, Flow Field Measurements of Stable and Locally Extinguishing Hydrocarbon-Fuelled Jet Flames, *Combust. Flame* 135 (2003) 185-190.

[18] C.D. Pierce, Progress-Variable Approach for Large-Eddy Simulation of Turbulent Combustion, PhD thesis, Stanford University, 2001.

[19] C.D. Pierce, P. Moin, Progress-variable approach for large-eddy simulation of non-premixed turbulent combustion, *J. Fluid Mech.* 504 (2004) 73-97.

[20] A.E. Lutz, R.J. Kee, J.F. Grcar, F.M. Rupley, OPPDIF: A Fortran Program for Computing Opposed-flow Diffusion Flames, Report No. SAND96-8243, Sandia National Laboratories, 1997.

[21] C.T. Bowman, R.K. Hanson, D.F. Davidson, W.C. Gardiner, Jr., V. Lissianski, G.P. Smith, D.M. Golden, M. Frenklach and M. Goldenberg, http://www.me.berkeley.edu/gri_mech/.

[22] P.E. Kloeden, E. Platen, Numerical Solution of Stochastic Differential Equations, Springer-Verlag, Berlin, 1992.

[23] M. Ihme, H. Pitsch, D. Bodony, Radiation of noise in turbulent non-premixed flames, *Proc. Combust. Inst.* 32 (2009) 1545-1553.

[24] R.P. Lindstedt, H.C. Ozarovsky, Joint scalar transported PDF modeling of nonpiloted turbulent diffusion flames, *Combust. Flame* 143 (2005) 471-490.

CHAPTER 6

CONCLUSIONS AND FUTURE WORK

This thesis work performs further studies of the PDF calculations in the RANS context using the existing HYB2D code following the previous studies, and then advances the PDF calculations to the next stage — LES. A next-generation high-performance PDF code called HPDF is developed which builds an accurate and efficient numerical platform for subsequent research on LES/PDF by the group over the next decade. The main conclusions drawn from the work are summarized in the following (Section 6.1), and then the future work on LES/PDF is discussed (Section 6.2).

6.1 Conclusions

Based on the work on the time-averaging strategies in Chapter 2, the following observations are made:

- Time-averaging is a powerful tool to reduce the statistical errors and hence the bias errors in the Monte Carlo particle method in the RANS context;
- Time-averaging does not change the order of convergence of the statistical errors and bias errors with respect to the number of particles per cell. But the reduced errors with time-averaging allow a much smaller number of particles per cell to achieve the same accuracy, and hence reduce the computational cost significantly;
- In the hybrid finite volume/particle method implemented in HYB2D, the feedback of the mean fluctuating velocity is the major source of the bias errors compared to all the other feedback quantities. The time-averaging

of this mean fluctuating velocity before feedback reduces the bias errors dramatically for the unconditional statistics in the Sandia flame E and in the Cabra flame. The conditional statistics in these flames, however, are hardly affected by time-averaging;

- The substantial bias errors involved in HYB2D without time-averaging can be compensated by adjusting the model constant $C_{\omega 1}$, and good agreement between the numerical results and experimental data may be observed in spite of the inaccurate numerical results (without time-averaging). This illustrates that it is usually dangerous to analyze the numerical results and to draw conclusions without quantifying the numerical errors involved in the numerical results;
- A value of $C_{\omega 1}$=0.7 different from the previous calculations ($C_{\omega 1}$=0.65) is suggested for the Sandia flame E to produce numerically accurate results which are still in good agreement with the measurement.

From the Lagrangian investigation of local extinction, re-ignition and auto-ignition in Chapter 3, we draw the following conclusions:

- The Eulerian one-time statistics of the PDF calculations are of main interest, and they can reveal many interesting combustion phenomena including the local extinction and re-ignition in the Sandia flame E and the auto-ignition in the Cabra flame. The one-time statistics do not contain the history information of the particle evolution and hence are limited for good understanding of unsteady combustion processes like extinction and ignition;
- Particle time-series provide deeper insight into the complicated extinction and ignition combustion phenomena and the model's capability to repre-

sent these phenomena. This work is the first study of the particle time-series in the PDF calculations of turbulent flames;

- The three different mixing models (EMST, IEM and MC) reproduce the local extinction and re-ignition processes in the Sandia flame E reasonably well in spite of the quantitatively different predictions of the different mixing models. Two different re-ignition mechanisms are identified: the auto-ignition mechanism and the mixing-reaction mechanism;
- The auto-ignition tests for the homogeneous mixture of the Cabra flame conditions are performed to study the lowest ignition delay time which is found to occur at a very fuel-lean condition for a range of coflow (oxidizer) temperatures;
- The three mixing models reproduce the whole auto-ignition process in the Cabra flame reasonably well. Four stages of combustion in the flame are identified from the calculations, i.e., pure mixing, auto-ignition, mixing-ignition, and fully burnt;
- The roles of mixing and reaction during re-ignition and auto-ignition are investigated by using IEM. The relative importance of the mixing and reaction is quantified for the particles during the re-ignition and auto-ignition.

From the development of the weak second-order splitting schemes for the composition PDF method in Chapter 4, we draw the following conclusions:

- Different kinds of weak second-order splitting schemes for solving the SDE system from the composition PDF methods are developed, which for the first time makes the particle method for the composition PDF second-order accurate in time, in contrast to the first-order accuracy in all the pre-

vious composition PDF calculations. The second-order convergence of the proposed splitting schemes is validated by a numerical test;

- The mid-point rule (freezing the coefficients at the mid-time step) which is usually used in designing second-order numerical schemes for ODEs and PDEs is found applicable to the SDE particle system;
- A general methodology for generating test cases is developed for the convergence study of the Monte Carlo particle method based on the method of manufactured solutions (MMS);
- The different splitting schemes are compared in terms of accuracy and efficiency. Solving the frozen-coefficient SDE system helps reduce the numerical errors, and reduce the difference of the numerical errors yielded by the different splitting schemes. No other significant difference is found in the comparison of the accuracy and efficiency. This is a useful conclusion in that there is a considerable range of accurate and efficient schemes that can be implemented; and in practice there may be additional considerations and constraints which favor one scheme over others. The applicability and extensibility of the developed methodologies to the general three-dimensional, multi-scalar and variable-density problems are briefly discussed.

The first LES/PDF calculations based on the existing LES code [1, 2, 3] and the new HPDF code are reported for a turbulent non-premixed flame DLR Flame A in Chapter 5. The following observations are made from the study:

- The numerical convergence of the HPDF code with respect to the grid size, the time-step size and the number of particles per cell is verified comprehensively with a wide range of manufactured test cases in one, two and

three dimensions, in both Cartesian and cylindrical coordinate systems, with different kinds of boundary conditions (periodic, inflow/outflow, wall, symmetric etc.), and with constant and variable density. The numerical test results for the one-dimensional constant density test case are shown in Chapter 5. Similar convergence is observed for all the other test cases (the results are not shown in this work);

- The LES results are found to be sensitive to the grid-refinement. The moderate resolution of $192 \times 192 \times 48$ is found adequate to capture the flow fields of interest among the three tested grids ($64 \times 64 \times 16$, $192 \times 192 \times 48$, $320 \times 320 \times 80$);
- Good numerical consistency between the LES and PDF results is achieved based on the good agreement between the LES and PDF predictions of the mean and rms mixture fraction and mean density;
- Overall good agreement of the numerical results with the experimental data is observed, demonstrating the capability of the employed models to represent the flow and composition fields of this flame, and the capability of the LES/PDF code;
- The superiority of the second-order splitting scheme over the first-order scheme is clearly shown in a 1D test case. In the jet flame calcualtions, the first-order splitting scheme performs as well as the second-order splitting scheme in predicting the mean and rms mixture fraction and mean density most likely due to the very small-step size used in the calculations;
- This work establishes the basis for our future work on LES/PDF that is discussed briefly in the following Section 6.2.

6.2 Future work on LES/PDF

The HPDF code has been developed with good extensibility, a general interface, easy user control and comprehensive benchmark testing. The combined LES/PDF code with basic capabilities has also been developed. Future extension of the code's capabilities and applicability is discussed in the following in these aspects: the LES code; the LES/PDF code; and its applications in future studies.

6.2.1 LES code

- The current LES code in our LES/PDF code is based on [1, 2, 3]. The LES part will soon be the bottleneck of the whole LES/PDF code due to the lack of the verification of the numerical convergence and the quantification of the numerical errors for this code. Comprehensive verification work of the LES code is needed to ensure numerically accurate standalone LES calculations and LES/PDF calculations;
- Thorough understanding of the LES code is needed for proper and efficient use of the code, such as the choices of optimal setting of parameters (grid size, grid stretching, CFL number etc.), parallel scalability and optimal domain-decompositions, numerical stability;
- Some improvements of the LES code may be made in the future, such as parallel efficiency (possibly in the pressure solver), relaxation of the CFL number restriction;
- Extension of the code capability may be made in using the TVD schemes to ensure the boundedness of the scalars, in separating the specifications

of the grid size and the filter size to investigate the LES convergence in terms of numerical errors and model errors, in implementing fully energy conservative schemes, and in implementing high-order (say, fourth-order) numerical schemes;

- The HPDF code has a general interface to enable the linking of the code to different LES codes easily. Alternative LES codes (preferably existing, high-order accurate and energy conservative) can be used in the future LES/PDF work.

6.2.2 LES/PDF code

- A general interface for multiple species is needed to handle the user-friendly input, controllable ouput, and the communications among the LES code, HPDF code, CHEMKIN code, ISAT code and x2f_mpi;
- The basic algorithms accounting for differential diffusion have been implemented (in collaboration with Sharadha Viswanathan). Rudimentary testing has been performed for the correctness of the implementation. Further testing is needed next, followed by the study of the effect of molecular diffusion and differential diffusion on the calculations of turbulent flames;
- The basic smoothing algorithms have been implemented and tested for correctness (in collaboration with Sharadha Viswanathan and Steven R. Lantz). A thorough understanding is needed of the influence of the smoothing and its interactions with the specifications of the amount of time-averaging for output and the number of particles per cell;
- More advanced interpolation schemes for the particle tracking (PERM, PPERM) have been implemented (in collaboration with Pavel P. Popov).

Basic testing has been done for correctness. More testing is needed. Then the comparison of the different interpolation schemes (e.g., tri-linear vs PERM) can be made in terms of accuracy, particle distribution, efficiency;

- The cell agglomeration algorithms have been implemented and tested. More work is needed to test cell agglomeration for efficiency and its interactions with smoothing, time-averaging, number of particles per cell;
- A second implementation of IEM has been integrated (in collaboration with Sharadha Viswanathan), which presumably has better numerical properties like conservation, boundedness etc. Further testing and comparison with the original simple IEM implementation are needed. More mixing models can be added straightforwardly, such as MC, EMST;
- Two-way coupling between the LES and PDF is needed, including the development of the coupling algorithms (e.g., direct feedback of density, hybrid method by solving energy equations in LES), implementation of the algorithms, modification of the LES iteration procedure to incorporate the coupling, testing and comparison of different coupling;
- The parallel performance of HPDF has been examined in simple test cases in weak scalability. More scalability testing is required to quantify the parallel efficiency of the LES/PDF code.

6.2.3 LES/PDF applications

- After the completion of the LES/PDF code, direct three-way comparisons of LES/PDF calculations, HYB2D (RANS/PDF) calculations, and experimental data (or DNS) can be made in order to investigate the performance of the models and codes in different contexts;

- A series of flame calculations can be performed by the LES/PDF code and HYB2D. A wide range of well-documented flame measurements is available for validation and comparison, such as premixed, partially premixed and non-premixed flames in piloted or non-piloted jet, bluff-body jet, swirling jet, attached or lifted jet flames, stratified flames, counterflow turbulent jet;
- LES/PDF provides an excellent opportunity to study complicated dynamics in turbulent flames, like flame local extinction, global extinction, reignition, auto-ignition. The analysis of the particle time-series developed in Chapter 3 may be incorporated for the studies of these problems in LES/PDF.

REFERENCES

[1] C.D. Pierce, Progress-Variable Approach for Large-Eddy Simulation of Turbulent Combustion, PhD thesis, Stanford University, 2001.

[2] C.D. Pierce, P. Moin, Progress-variable approach for large-eddy simulation of non-premixed turbulent combustion, *J. Fluid Mech.* 504 (2004) 73-97.

[3] V. Raman, H. Pitsch, A consistent LES/filtered-density function formulation for the simulation of turbulent flames with detailed chemistry, *Proc. Combust. Inst.* 31(2) (2007) 1711-1719.

APPENDIX A

PARTICLE TRAJECTORIES IN PHYSICAL SPACE

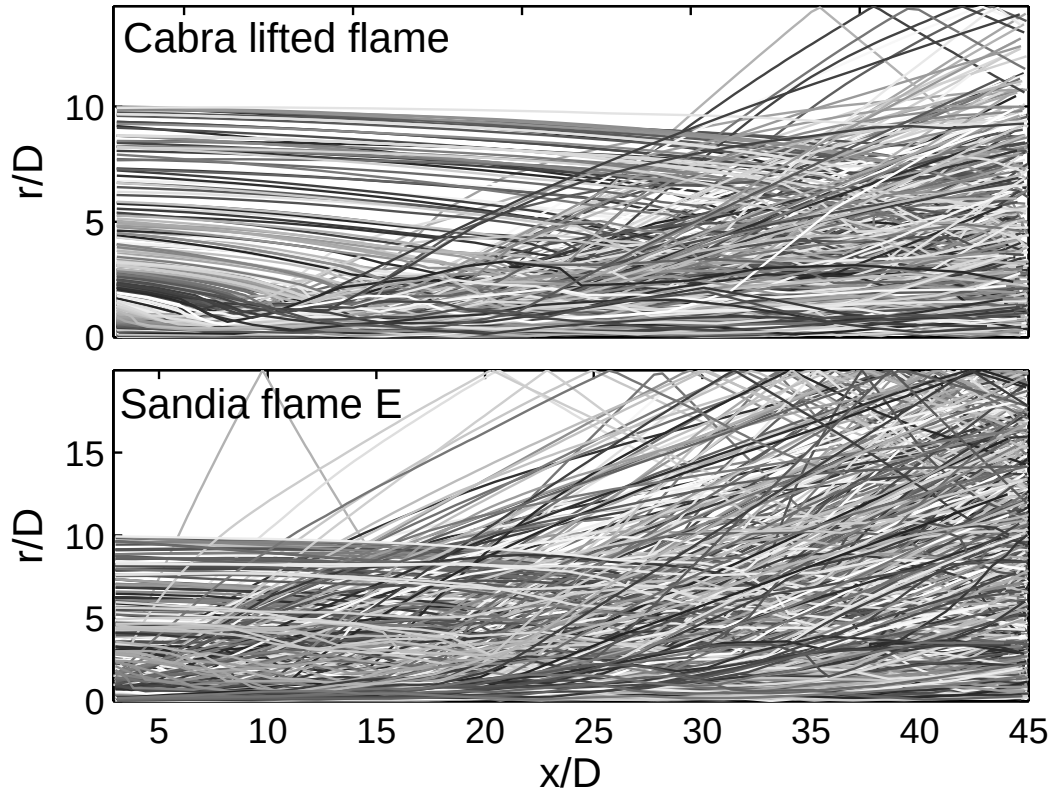

Figure A.1: Particle trajectories in physical space for the Cabra H_2/N_2 lifted jet flame and for the Sandia flame E from the original turbulence frequency model.

Figure A.1 shows the particle trajectories in physical space for the Cabra H_2/N_2 lifted flame and for the Sandia flame E, from calculations using the EMST mixing model. The top border of the plot is the free-stream boundary. When the particles from the turbulent jet approach the non-turbulent free stream, their velocity should relax rapidly towards the free stream velocity. However, from Figure A.1, it may be seen that some particles shoot into the free stream with little or no relaxation of velocity, and are then reflected off the free-stream boundary (according to the specified boundary condition). This non-physical behavior

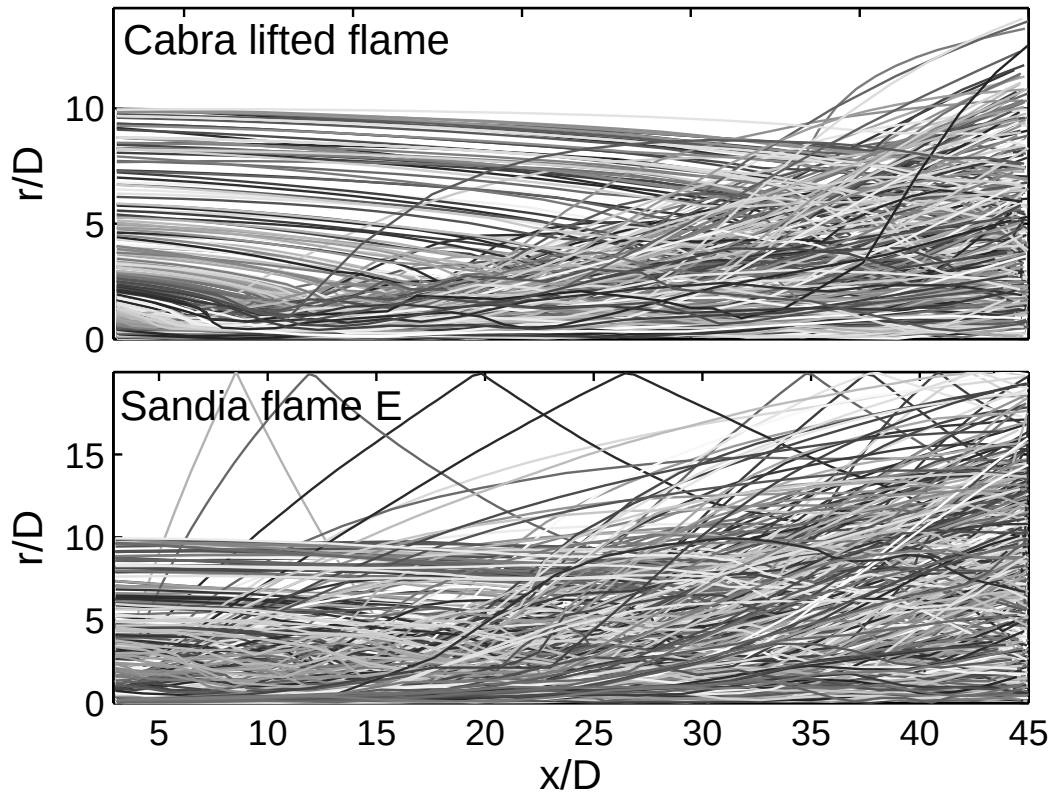

Figure A.2: Particle trajectories in the physical space for the Cabra H_2/N_2 lifted jet flame and for the Sandia flame E with an *ad hoc* revision to the turbulence frequency model.

of the particles is not expected to occur when the conditional mean frequency Ω (Equation (3.7)) is used to define the time-scale in the stochastic turbulence frequency model (Equation (3.5)) [1]. The turbulence frequency in the turbulent region is much greater than that in the non-turbulent free stream. Ideally, if one turbulent fluid particle $\mathcal{P}$ dives into one mesh cell C in the laminar free stream environment, the turbulence frequency of particle $\mathcal{P}$ will be the only frequency used to determine Ω (= $C_\Omega \cdot \omega^*_\mathcal{P}$, where $\omega^*_\mathcal{P}$ is the turbulence frequency of particle $\mathcal{P}$) in cell C according to Equation (3.7). From the Langevin model Equation (3.4), the velocity of particle $\mathcal{P}$ will decay rapidly at rate Ω toward the free stream velocity. However, under certain circumstances, the particle $\mathcal{P}$ is not the only particle chosen to determine the conditional mean frequency Ω. In the current situation (of a cylindrical coordinate system), the initial mass of a particle is linearly proportional to the particle's radial location. Compared to the particle mass in the free stream, the mass of the particle $\mathcal{P}$ originating closer to the axis is much less. In this case, the mass-weighted mean frequency $\widetilde{\omega}$ in cell C is close to the mean frequency in the free stream. On the other hand, numerically the turbulence frequency for the particles in the free stream is not exactly the same, i.e., there are small fluctuations in particle turbulence frequency in the free stream. These fluctuations are caused by the Wiener process in Equation (3.5) and by the disturbance caused by the turbulent fluid particle $\mathcal{P}$. Assume that the maximum of the turbulence frequency in cell C is ω^*_{m2} when particle $\mathcal{P}$ is excluded. It may happen that ω^*_{m2} is greater than $\widetilde{\omega}$, so that the possibly massive particle with frequency ω^*_{m2} is included in the calculation of Ω. Therefore the value of Ω is much less than the desired value $C_\Omega \cdot \omega^*_\mathcal{P}$. In another words, the value of Ω is greatly under-estimated, and so is the decaying rate of the velocity of the particle $\mathcal{P}$.

In spite of the non-physical behavior of the particles described above, it should be appreciated that this behavior occurs with low probability (less than 1% of the number of tracked particles in the Cabra lifted flame, and about 5% in the Sandia flame E). They do not influence the statistics significantly. Since the particle behavior is relatively more important in this work, we try to eliminate or reduce the non-physical behavior in the following *ad hoc* way. In the above discussed case, the particle $\mathcal{P}$ should be chosen as the only particle to determine Ω, in spite of the small fluctuations of the turbulence frequency in the free stream. If we can identify this particular case, we can avoid this problem by calculating Ω using particle $\mathcal{P}$ only. We use the following criteria to identify the case. If in one grid cell, the maximum turbulence frequency $\omega^*_{\mathcal{P}}$ of a particle $\mathcal{P}$ is much greater than the Favre mean frequency $\widetilde{\omega}$ ($\omega^*_{\mathcal{P}} > c_1 \cdot \widetilde{\omega}$), and also much greater than the frequency of all other particles in the cell ($\omega^*_{\mathcal{P}} > c_2 \cdot \omega^*_{m2}$), and the mass of the particle $m^*_{\mathcal{P}}$ is much less than the average mass of the particles $\langle m \rangle$ ($m^*_{\mathcal{P}} < c_3 \cdot \langle m \rangle$), we then use particle $\mathcal{P}$ exclusively to determine Ω. The constants are chosen as c_1=15, c_2=8, and c_3=0.2. The particle trajectories in physical space obtained with this special treatment of the frequency model are shown in Figure A.2. The non-physical particles disappear in the Cabra lifted flame, and the number of the non-physical particles is significantly reduced in Sandia flame E. The special treatment improves the practical performance of the turbulence frequency model to some extent. The remaining non-physical particles in the Sandia flame E shown in Figure A.2 are due to the limitation of the criteria. Using a different specification of c_1, c_2, and c_3, we can eliminate the non-physical particles completely, but it also then affects the turbulence region. In this work, we use this *ad hoc* revision to reduce the number of non-physical particles. Those particles not caught by the criteria are removed from the par-

ticle subset in the discussion. This *ad hoc* revision to the frequency model does not change the statistics of the velocity and composition fields. We appreciate that the criteria does not guarantee the convergence of the method when the number particles tends to infinity.

APPENDIX B

PROOF OF THE SDE SYSTEM WITH FROZEN COEFFICIENTS

We prove that the solutions of the SDEs with frozen coefficients (4.12) and (4.13) are consistent with those of the original SDEs (4.8) and (4.10) to order Δt^2 for one time step in the weak sense (i.e., the difference between the solutions is of order Δt^3). For weak second-order numerical schemes, the numerical solutions are consistent with the exact solutions to Δt^2 for one time step in the weak sense. Hence this proof guarantees the equivalence of solving (4.8) and (4.10), and (4.12) and (4.13) with second-order accuracy.

B.1 Proof of the frozen-coefficient Ito SDE[1]

We first prove that the solution of (4.12) is consistent with that of (4.8) to order Δt^2 for one time step in the weak sense. According to the sufficient conditions for weak second-order accuracy obtained in [2], we only need to verify the consistency of the first four moments of $\Delta\mathbf{X}$ from (4.8) and (4.12).

Following [2], we consider one integration step $[0, \Delta t]$ (i.e., $t_0 = 0$), from the deterministic initial condition $\mathbf{X}(0) = \mathbf{X}'(0) = 0$, then $\Delta\mathbf{X} = \mathbf{X}(\Delta t)$ and $\Delta\mathbf{X}' = \mathbf{X}'(\Delta t)$, where $\mathbf{X}$ and $\mathbf{X}'$ denote the numerical solutions to (4.8) and (4.12), respectively. The moments of $\mathbf{X}$ can be obtained from its PDF $f(\mathbf{x}; t)$ and the Fokker-Planck equation. The first four moments of $\Delta\mathbf{X}$ for (4.8) are [2]

$$E(\Delta X_p) = \Delta t D_p^0 + \Delta t^2 \left(\frac{1}{2} D_j^0 D_{p,j}^0 + \frac{1}{4} b^0 D_{p,jj}^0 + \frac{1}{2} \dot{D}_p^0 \right) + O(\Delta t^3), \tag{B.1}$$

[1] Using the corresponding Fokker-Planck equation seems a natural starting point for the proof, but we are not successful in that direction.

$$E(\Delta X_p \Delta X_q) = \Delta t b^0 \delta_{pq} + \Delta t^2 \left(D_p^0 D_q^0 + \frac{1}{2} b^0 \left(D_{p,q}^0 + D_{q,p}^0 \right) + \frac{1}{2} \delta_{pq} D_j^0 b_{,j}^0 + \frac{1}{4} b^0 b_{,jj}^0 \delta_{pq} + \frac{1}{2} \dot{b}^0 \delta_{pq} \right) + O(\Delta t^3), \tag{B.2}$$

$$E(\Delta X_p \Delta X_q \Delta X_r) = \Delta t^2 \left(b^0 \left(D_p^0 \delta_{qr} + D_q^0 \delta_{pr} + D_r^0 \delta_{pq} \right) + \frac{1}{2} b^0 \left(b_{,p}^0 \delta_{qr} + b_{,q}^0 \delta_{pr} + b_{,r}^0 \delta_{pq} \right) \right) + O(\Delta t^3), \tag{B.3}$$

$$E(\Delta X_p \Delta X_q \Delta X_r \Delta X_s) = \Delta t^2 (b^0)^2 \left(\delta_{pq} \delta_{rs} + \delta_{pr} \delta_{qs} + \delta_{ps} \delta_{qs} \right) + O(\Delta t^3), \tag{B.4}$$

where the superscript "0" denotes the evaluation at the initial position ($\mathbf{X}(0) = 0$) and initial time ($t = 0$), and other quantities appearing in these equations are defined as $D_{i,j} \equiv \partial D_i / \partial X_j$, $D_{i,jj} \equiv \partial^2 D_i / \partial X_j \partial X_j$, $\dot{D}_i \equiv \partial D_i / \partial t$, $b_{,j} \equiv \partial b / \partial X_j$, $b_{,jj} \equiv \partial^2 b / \partial X_j X_j$, and $\dot{b} \equiv \partial b / \partial t$.

The frozen-coefficient Ito SDE (4.12) is a special case of the SDE (4.8), i.e., eliminating the dependence of the coefficients D_i and b on time and freezing the coefficients at the mid-time ($t = t_{\frac{1}{2}} = \frac{1}{2}\Delta t$). From (B.1) to (B.4), we can readily obtain the first four moments of $\Delta \mathbf{X}'$ for (4.12)

$$E(\Delta X_p') = \Delta t D_p^* + \Delta t^2 \left(\frac{1}{2} D_j^* D_{p,j}^* + \frac{1}{4} b^* D_{p,jj}^* \right) + O(\Delta t^3), \tag{B.5}$$

$$E(\Delta X_p' \Delta X_q') = \Delta t b^* \delta_{pq} + \Delta t^2 \left(D_p^* D_q^* + \frac{1}{2} b^* \left(D_{p,q}^* + D_{q,p}^* \right) + \frac{1}{2} \delta_{pq} D_j^* b_{,j}^* + \frac{1}{4} b^* b_{,jj}^* \delta_{pq} \right) + O(\Delta t^3), \tag{B.6}$$

$$E(\Delta X_p' \Delta X_q' \Delta X_r') = \Delta t^2 \left(b^* \left(D_p^* \delta_{qr} + D_q^* \delta_{pr} + D_r^* \delta_{pq} \right) + \frac{1}{2} b^* \left(b_{,p}^* \delta_{qr} + b_{,q}^* \delta_{pr} + b_{,r}^* \delta_{pq} \right) \right) + O(\Delta t^3), \tag{B.7}$$

$$E(\Delta X_p' \Delta X_q' \Delta X_r' \Delta X_s') = \Delta t^2 (b^*)^2 \left(\delta_{pq} \delta_{rs} + \delta_{pr} \delta_{qs} + \delta_{ps} \delta_{qs} \right) + O(\Delta t^3), \tag{B.8}$$

where the superscript "*" denotes the evaluation at the initial position ($\mathbf{X}'(0) = 0$) and mid-time ($t = t_{\frac{1}{2}}$).

Expanding the coefficient (D_i^*, b^* and their spatial derivatives) at $t = 0$, we obtain

$$G^* = G^0 + \dot{G}^0 \frac{\Delta t}{2} + O(\Delta t^2), \tag{B.9}$$

where G is any one of the coefficients and their derivatives in (B.5)-(B.8).

Substituting the Taylor series expansions (B.9) into (B.5)-(B.8) and collecting all the leading order terms, we have

$$E(\Delta X'_p) = \Delta t D_p^0 + \Delta t^2 \left(\frac{1}{2} D_j^0 D_{p,j}^0 + \frac{1}{4} b^0 D_{p,jj}^0 + \frac{1}{2} \dot{D}_p^0 \right) + O(\Delta t^3), \tag{B.10}$$

$$\begin{aligned} E(\Delta X'_p \Delta X'_q) &= \Delta t b^0 \delta_{pq} + \Delta t^2 \left(D_p^0 D_q^0 + \frac{1}{2} b^0 \left(D_{p,q}^0 + D_{q,p}^0 \right) + \frac{1}{2} \delta_{pq} D_j^0 b_{,j}^0 \right. \\ &+ \left. \frac{1}{4} b^0 b_{,jj}^0 \delta_{pq} + \frac{1}{2} \dot{b}^0 \delta_{pq} \right) + O(\Delta t^3), \end{aligned} \tag{B.11}$$

$$\begin{aligned} E(\Delta X'_p \Delta X'_q \Delta X'_r) &= \Delta t^2 \left(b^0 \left(D_p^0 \delta_{qr} + D_q^0 \delta_{pr} + D_r^0 \delta_{pq} \right) + \frac{1}{2} b^0 \left(b_{,p}^0 \delta_{qr} + b_{,q}^0 \delta_{pr} + b_{,r}^0 \delta_{pq} \right) \right) \\ &+ O(\Delta t^3), \end{aligned} \tag{B.12}$$

$$E(\Delta X'_p \Delta X'_q \Delta X'_r \Delta X'_s) = \Delta t^2 (b^0)^2 \left(\delta_{pq} \delta_{rs} + \delta_{pr} \delta_{qs} + \delta_{ps} \delta_{qs} \right) + O(\Delta t^3). \tag{B.13}$$

Evidently, with the same initial condition $\mathbf{X}(0) = \mathbf{X}'(0)$, (B.10)-(B.13) are consistent with (B.1)-(B.4) to order Δt^2. Thus the SDEs (4.8) and (4.12) are equivalent when solved with weak second-order SDE schemes.

B.2 Proof of the frozen-coefficient scalar equation

We now prove the equivalence of solving scalar equations (4.10) and (4.13) to second-order accuracy. For simplicity, we consider one step integration $[0, \Delta t]$

with the same Ito process $\mathbf{X}(t)$ in (4.10) and (4.13) and with the initial condition $\phi(0) = \phi'(0) = \phi_0$.

Equation (4.10) is

$$\begin{aligned} \frac{d\phi(t)}{dt} &= A(\mathbf{X}(t), \phi(t), t) \\ &= A(\mathbf{X}(t), \phi_0 + \Delta\phi(t), t_{\frac{1}{2}} + (t - t_{\frac{1}{2}})) \\ &= A + A_\phi \Delta\phi(t) + \dot{A}(t - t_{\frac{1}{2}}) + O(\Delta t^2), \end{aligned} \tag{B.14}$$

for $t = O(\Delta t)$, A_ϕ and $\dot{A}$ denote derivatives of A with respect to the second and third arguments, and in the last line A, A_ϕ and $\dot{A}$ are evaluated at $(\mathbf{X}(t), \phi_0, t_{\frac{1}{2}})$.

Similarly, (4.13) is

$$\frac{d\phi'(t)}{dt} = A + A_\phi \Delta\phi'(t) + O(\Delta t^2), \tag{B.15}$$

where A and A_ϕ, being evaluated at $(\mathbf{X}(t), \phi_0, t_{\frac{1}{2}})$, are identical in the above two equations. Thus, the difference $\phi - \phi'$ evolve by

$$\frac{d(\phi(t) - \phi'(t))}{dt} = A_\phi(\phi(t) - \phi'(t)) + \dot{A}(t - t_{\frac{1}{2}}) + O(\Delta t^2). \tag{B.16}$$

Since $\phi'(t)$ is certainly at least a first-order approximation to $\phi(t)$, it follows that the difference $\phi(t) - \phi'(t)$ is of order Δt^2 (or higher), and the first term on the right-hand side of (B.16) when integrated over $[0, \Delta t]$ is of order Δt^3 (or higher). It is readily shown that the second term on the right-hand side of (B.16) when integrated over $[0, \Delta t]$ is also of order Δt^3. Thus the difference $\phi(t) - \phi'(t)$ is of order Δt^3, confirming the second-order accuracy of (4.13) with frozen coefficients.

APPENDIX C

MEASUREMENT OF THE GLOBAL ERROR FOR WEAK CONVERGENCE

The error $e_{q,i,k}$ (4.32) estimates the local deterministic error $\mu_{q,i}$ from the kth trial. If the number of particles used in the trial is small, this estimate involves large statistical error. Here, we derive an un-biased estimate of the global error $\mathcal{E}_{\overline{\phi^q}}$ (4.34) based on $e_{q,i,k}$ from all the grids and all the trials performed to reduce the effect of the statistical error.

From (4.33), we can obtain

$$e_{q,i,k}^2 = \mu_{q,i}^2 + \sigma_{q,i}^2 \xi_{q,i,k}^2 + 2\mu_{q,i}\sigma_{q,i}\xi_{q,i,k}. \tag{C.1}$$

We take the average of (4.33) and (C.1) over K independent trials

$$\left\langle e_{q,i} \right\rangle^* = \mu_{q,i} + \sigma_{q,i} \frac{1}{K} \sum_{k=1}^{K} \xi_{q,i,k}, \tag{C.2}$$

$$\left\langle e_{q,i}^2 \right\rangle^* = \mu_{q,i}^2 + \sigma_{q,i}^2 \frac{1}{K} \sum_{k=1}^{K} \xi_{q,i,k}^2 + 2\mu_{q,i}\sigma_{q,i} \frac{1}{K} \sum_{k=1}^{K} \xi_{q,i,k}. \tag{C.3}$$

From (C.2), we obtain

$$\begin{aligned} \left\langle e_{q,i} \right\rangle^{*2} &= \mu_{q,i}^2 + \sigma_{q,i}^2 \frac{1}{K^2} \sum_{k=1}^{K} \xi_{q,i,k}^2 \\ &+ 2\mu_{q,i} \cdot \sigma_{q,i} \frac{1}{K} \sum_{k=1}^{K} \xi_{q,i,k} + \sigma_{q,i}^2 \frac{1}{K^2} \sum_{k=1}^{K} \sum_{l=1, l\neq k}^{K} \xi_{q,i,k}\xi_{q,i,l}. \end{aligned} \tag{C.4}$$

The expectation of (C.3) and (C.4) are

$$E\left(\left\langle e_{q,i}^2 \right\rangle^*\right) = \mu_{q,i}^2 + \sigma_{q,i}^2, \tag{C.5}$$

$$E\left(\left\langle e_{q,i} \right\rangle^{*2}\right) = \mu_{q,i}^2 + \frac{\sigma_{q,i}^2}{K}. \tag{C.6}$$

Solving (C.5) and (C.6) for $\mu_{q,i}$, we obtain

$$\mu_{q,i}^2 = \frac{1}{1-1/K}\left(E\left(\left\langle e_{q,i}(\overline{\phi^q})\right\rangle^{*2}\right) - \frac{1}{K}E\left(\left\langle e_{q,i}^2(\overline{\phi^q})\right\rangle^{*}\right)\right). \tag{C.7}$$

Based on (C.7), we can construct an un-biased estimate of $\mu_{q,i}^2$ from the numerical simulation

$$\mu_{q,i}^2 \approx \frac{1}{1-1/K}\left(\left\langle e_{q,i}\right\rangle^{*2} - \frac{1}{K}\left\langle e_{q,i}^2\right\rangle^{*}\right). \tag{C.8}$$

The value of $\mu_{q,i}^2$ is a local measure of the time-stepping error ($\mu_{q,i} \propto \Delta t^p$ for pth order convergence). A global measure of the time-stepping error is defined in (4.34). Apparently, $E\left(\mathcal{E}_{\overline{\phi^q}}\right) \propto \Delta t^p$ for pth order convergence too.

Substituting (C.8) into (4.34), we obtain the un-biased estimate of the global error

$$\mathcal{E}_{\overline{\phi^q}} = \left[\frac{1}{I}\sum_{i=1}^{I}\frac{1}{1-1/K}\left(\left\langle e_{q,i}\right\rangle^{*2} - \frac{1}{K}\left\langle e_{q,i}^2\right\rangle^{*}\right)\right]^{1/2}. \tag{C.9}$$

Note that, in practice, a valid value of $\mathcal{E}_{\overline{\phi^q}}$ may not be obtained because the summation under the square-root in (C.9) may be negative. If this happens, more particles or trials are required.

APPENDIX D

MANUFACTURED SOLUTIONS TO ONE-DIMENSIONAL TEST CASE

For the one-dimensional, periodic, constant-density problem $x \in [0, L_0]$ and $t \in [0, T]$, the manufactured analytical solutions to (4.26) and (4.27) are specified as:

$$\overline{\phi}_m(x,t) = \frac{1}{20} e^{3\varpi t} \cos\left(2\pi\kappa x - \frac{12}{5}\pi\right), \tag{D.1}$$

$$\overline{\phi'^2}_m(x,t) = \frac{1}{8}\left(4 - e^{-3\varpi t}\right)\left[\sin\left(2\pi\kappa x - \frac{12}{5}\pi\right) + 4\right]. \tag{D.2}$$

The second moment of the scalar $\overline{\phi^2}_m(x,t)$ is then

$$\overline{\phi^2}_m(x,t) = \overline{\phi}_m^2(x,t) + \overline{\phi'^2}_m(x,t) \tag{D.3}$$

The velocity, diffusivity and source terms in (4.26) and (4.27) are specified as follows:

$$\overline{u}(x,t) = \frac{1}{10} u_0 e^{4\varpi t}, \tag{D.4}$$

$$\Gamma(x,t) = \Gamma_0 \left\{2 + \frac{2}{5}\left[\sin\left(2\pi\kappa x - \frac{28}{25}\pi\right)\Gamma_x - \Gamma_x + 1\right]\left(\frac{1}{20} e^{4\varpi t} + e^{-4\varpi t}\right)\right\}, \tag{D.5}$$

$$\begin{aligned} S_m(x,t) &= \frac{3}{20}\varpi e^{3\varpi t} \cos\left(2\pi\kappa x - \frac{12}{5}\pi\right) \\ &+ \left[\frac{1}{10} u_0 e^{4\varpi t} - \frac{4}{5}\kappa\pi\Gamma_x\Gamma_0 \cos\left(2\pi\kappa x - \frac{28}{25}\pi\right)\left(\frac{1}{20} e^{4\varpi t} + e^{-4\varpi t}\right)\right] \\ &\times \left[-\frac{1}{10}\kappa\pi e^{3\varpi t} \sin\left(2\pi\kappa x - \frac{12}{5}\pi\right)\right] \\ &+ e^{3\varpi t} \cos\left(2\pi\kappa x - \frac{12}{5}\pi\right) \\ &\times \left\{\frac{R_a}{20} + \frac{2}{5}\Gamma_0\kappa^2\pi^2\left[1 + \frac{1}{5}\left(\sin\left(2\pi\kappa x - \frac{28}{25}\pi\right)\Gamma_x - \Gamma_x + 1\right)\left(\frac{1}{20} e^{4\varpi t} + e^{-4\varpi t}\right)\right]\right\}, \end{aligned} \tag{D.6}$$

$$
\begin{aligned}
S_v(x,t) &= \frac{3}{8}\varpi e^{-3\varpi t}\left[\sin\left(2\pi\kappa x-\frac{12}{5}\pi\right)+4\right] \\
&+ \left[\frac{1}{40}u_0\kappa\pi e^{4\varpi t}-\frac{1}{5}\kappa^2\pi^2\Gamma_x\Gamma_0\cos\left(2\pi\kappa x-\frac{28}{25}\pi\right)\left(\frac{1}{20}e^{4\varpi t}+e^{-4\varpi t}\right)\right] \\
&\times \left(4-e^{-3\varpi t}\right)\cos\left(2\pi\kappa x-\frac{12}{5}\pi\right) \\
&+ \Gamma_0\left\{1+\frac{1}{5}\left[\sin\left(2\pi\kappa x-\frac{28}{25}\pi\right)\Gamma_x-\Gamma_x+1\right]\left(\frac{1}{20}e^{4\varpi t}+e^{-4\varpi t}\right)\right\} \\
&\times \left\{\kappa^2\pi^2\left(4-e^{-3\varpi t}\right)\sin\left(2\pi\kappa x-\frac{12}{5}\pi\right)-\left[-\frac{1}{5}e^{3\varpi t}\sin\left(2\pi\kappa x-\frac{12}{5}\pi\right)\kappa\pi\right]^2\right\} \\
&+ \frac{1}{5}\left[\cos\left(2\pi\varpi t-\frac{1}{5}\pi\varpi\right)+\frac{5}{6}\right]\left[\sin\left(2\pi\kappa x-\frac{28}{25}\pi\right)+\frac{51}{10}\right] \\
&+ \frac{1}{4}R_a\left(4-e^{-3\varpi t}\right)\left[\sin\left(2\pi\kappa x-\frac{12}{5}\pi\right)+4\right], \qquad \text{(D.7)}
\end{aligned}
$$

$$
\begin{aligned}
\Omega(x,t) = &- \frac{1}{10}\left[\cos\left(2\pi\varpi t-\frac{1}{5}\pi\varpi\right)+\frac{6}{5}\right] \\
&\times \left[\sin\left(2\pi\kappa x-\frac{28}{25}\pi\right)+\frac{51}{10}\right]\Big/\overline{\phi'^2}_m(x,t). \qquad \text{(D.8)}
\end{aligned}
$$

From the above specifications, we obtain the SDE coefficients $D(x,t) = \bar{u}(x,t) + d\Gamma(x,t)/dx$ and $b(x,t) = (2\Gamma(x,t))^{1/2}$. The constants are specified as follows:

$$
\varpi = \frac{5}{\pi},\ \ \kappa = \frac{1}{2\pi},\ \ u_0 = \Gamma_0 = \Gamma_x = 1,\ \ R_a = -1,\ \ R_b = 0,\ \ L_0 = 2\pi,\ \ T = \frac{\pi}{5}.
$$

The above functions and constants are specified to minimize the difference of each term of the augmented transport equations for the scalar mean (4.26) and variance (4.27), so that each term has approximately equal contribution to the solutions of the scalar mean and variance. The contour plots of the MMS functions and each term of (4.26) and (4.27) are shown in Fig. D.1.

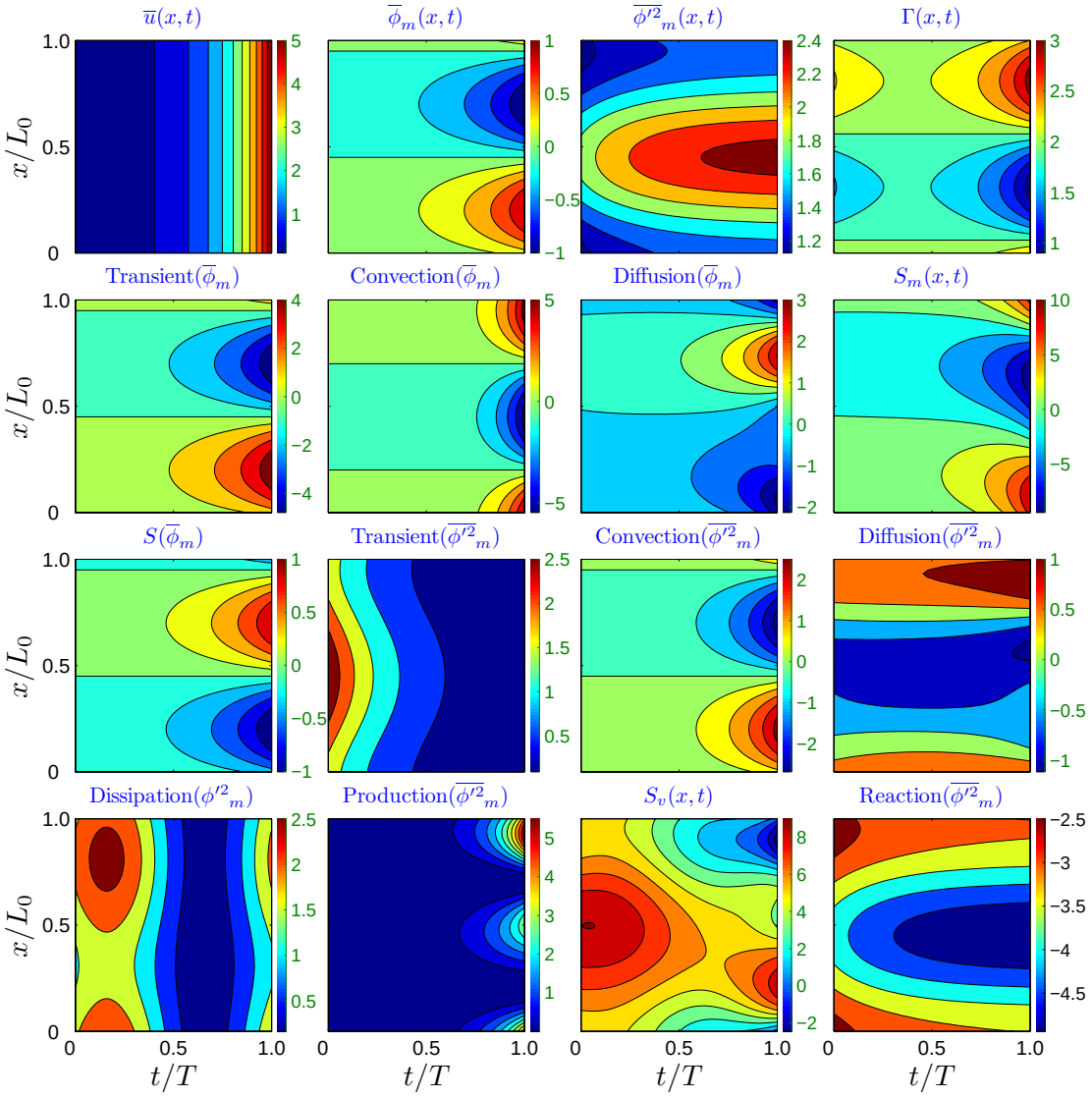

Figure D.1: Contour plots of the MMS functions $\overline{u}(x,t)$, $\overline{\phi}_m(x,t)$, $\overline{\phi'^2}_m(x,t)$, $\Gamma(x,t)$ and each term of the augmented transport equations for the scalar mean (4.26) and variance (4.27) with respect to $(x/L_0, t/T)$

REFERENCES

[1] P.R. Van Slooten, Jayesh, S.B. Pope, Advances in PDF modeling for inhomogeneous turbulent flows, *Phys. Fluids* 10 (1998) 246-265.

[2] R. Cao, S.B. Pope, Numerical integration of stochastic differential equations: weak second-order mid-point scheme for applications in the composition PDF method, *J. Comput. Phys.* 185 (2003) 194-212.